Doctoral Thesis

Field: Information and Communication Sciences and Technologies
Specialization: Electronics, Microelectronics, Nanoelectronics and Microwaves

submitted to the Doctoral School of Science, Technology and Health (ED 585)

at the Université du Littoral Côte d'Opale

by

Qingyu TIAN

to obtain the degree of Doctor of the Université du Littoral Côte d'Opale

Thermal Study of a Multilayer System: Finite Element Modeling and Experimental Characterization by the 3ω Technique

Defended on 23 June 2026, following approval by the reviewers, before the examination committee:

Prof. Nathalie TRANNOY	Université de Reims	Chair of the Jury, Reviewer
Dr. Séverine GOMES	INSA Lyon	Reviewer
Dr. Pierre-Yves CRESSON	Université d'Artois	Examiner
Dr. Aimad KOULALI	IMT Nord Europe	Examiner
Prof. Abdelkrim TALBI	Université de Lille	Co-supervisor
Prof. Michael DEPRIESTER	Université du Littoral Côte d'Opale	Supervisor

Thèse de Doctorat

Mention: Sciences et technologies de l'information et de la communication

Spécialité : Électronique, microélectronique, nanoélectronique et micro-ondes

présentée à l'École Doctorale en Sciences Technologie et Santé (ED 585)

de l'Université du Littoral Côte d'Opale

par

Qingyu TIAN

pour obtenir le grade de Docteur de l'Université du Littoral Côte d'Opale

Étude thermique d'un système multicouches : modélisation par la méthode des éléments finis et caractérisations expérimentales par la technique 3ω

Soutenue le 23 juin 2026, après avis des rapporteurs, devant le jury d'examen :

Mme Nathalie TRANNOY, Pr.	Université de Reims	Présidente du jury, Rapportrice
Mme Séverine GOMES, DR	INSA Lyon	Rapportrice
M. Pierre-Yves CRESSON, MCF	Université d'Artois	Examinateur
M. Aimad KOULALI, MCF	IMT Nord Europe	Examinateur
M. Abdelkrim TALBI, Pr.	Université de Lille	Co-directeur de thèse
M. Michael DEPRIESTER, Pr.	Université du Littoral Côte d'Opale	Directeur de thèse

Acknowledgments

The work presented in this thesis was supported by the China Scholarship Council (CSC). I am deeply grateful for the full scholarship they provided, which enabled me to pursue my doctoral studies and supported my life in France. I would also like to express my sincere appreciation to the Université du Littoral Côte d'Opale (ULCO) for offering outstanding research facilities, experimental platforms, and a stimulating laboratory environment essential to the completion of this work. In addition, I thank the University of Lille for providing experimental samples and valuable academic support that significantly contributed to this research.

First and foremost, I would like to express my deepest gratitude to my supervisor, Michael Depriester. His support was truly comprehensive—he paid attention to every detail of my research and guided me through each obstacle. I am profoundly inspired by his rigorous scientific mindset and relentless spirit of inquiry. Every discussion with him was both intellectually enriching and genuinely enjoyable. His infectious smile and his remarkable personal story—of identifying the cause of his own illness through research—challenged my preconceived notions about specialization. He taught me that the ability to investigate and transfer problem-solving skills transcends disciplinary boundaries. He is not only an academic mentor, but also a role model in life.

I am also sincerely grateful to Abdelkrim Talbi for accepting my PhD application and for his crucial support during the early stages of my journey. His assistance was instrumental in my transition to France and in helping me find a new laboratory. I greatly appreciate his guidance on COMSOL simulations and for providing essential experimental materials.

The atmosphere at UDSMM was more than professional—it was a true community. I will always cherish the memories of our group dinners and the warm, informal conversations that made the laboratory feel like a second home.

My heartfelt thanks go to Abdelhak Hadj Sahraoui for teaching me how to use Calculco. His humility and constant smile created a supportive environment in which I felt both relaxed and encouraged. I also wish to thank Abdellylah Daoudi, director of UDSMM, for his continuous encouragement.

I am grateful to Abdelaziz Elass for his invaluable assistance in setting up my experimental apparatus and designing the software interface. Special thanks to Othmane Marbouh for providing materials and offering strategic solutions during challenging moments. I am deeply thankful to Fabrice Goutier, who was always ready to help with great humility and dedication whenever I encountered difficulties. I also extend my thanks to Wang Suhao and the administrative staff at the secretariat for their professional support.

During my most challenging moments, the conversations I shared with Abir Moghnieh and Shivani Shisodia became my sanctuary. Shivani, thank you for bringing so much joy into our shared experiences and for navigating both work and life alongside me. Abir, thank you for your constant encouragement and support—your kindness helped me through the most difficult times.

I also wish to thank my fellow researchers and friends: Miriam Achkar, Mireille Bader, Soufiane Bahhar, Nouha Drame, Mamadou Barry, Layla Farhat, Karthika Pairadukkam, and Vanishree Bhat.

Living in France, especially in Dunkerque, has been a journey of profound transformation. From the moment I arrived, I was welcomed with warmth and encountered many unexpected acts of kindness. At the same time, this journey included challenges, moments of deep struggle, and periods of self-doubt. Yet, by choosing perseverance, I gradually discovered beauty and meaning in the small

details of everyday life. Over time, I have developed a deep affection for Dunkerque, whose unique character accompanied me throughout my personal growth.

I would like to express my heartfelt gratitude to my dear friends —Zhai Xiaoqin, Zhang Yi, and Chen Yisha. We traveled together, shared our lives like a family, and supported one another through both joyful and difficult moments. Your companionship made this journey warm and meaningful. To Zhang Yi, our conversations on personal growth have been especially meaningful. We encouraged each other and grew together along the way. Every deep conversation with you felt like a form of mental rejuvenation—you always brought fresh and insightful perspectives.

My sincere thanks go to Zhang Wenlong and Chen Yiwen for their invaluable support when I first arrived in France. You helped me adapt to a completely new environment and guided me through the early stages of my life here.

I am also deeply grateful to Hu Yongyong, whose delicious homemade meals often brought comfort, and who always offered help whenever I encountered challenges.

To Zhang Jing, I cherish the quiet and gentle care that came through our friendship—subtle yet deeply touching. To Yu Chongmei, I have always been inspired by your clarity and strength; every meeting with you was filled with joy, whether playing badminton or exploring Paris together.

I would also like to thank the Dai Jiujin family for their unwavering support, generosity, and kindness. You not only provided me with a place to stay, but also offered me opportunities and care that I will always remember.

To Cao Yilin and Zhang Xianwen, I feel so fortunate to have met you all and to have experienced such genuine friendship and kindness.

In addition, I am grateful to the Demazaux family, who allowed me to experience French life and perspectives in a meaningful and enriching way.

I would like to thank Wang Lina and Zhang Xiangxue for always standing by my side, encouraging me and helping me recognize the light and beauty within myself.

I am also grateful to Chen Ruibo, whose insights and sharing of life experiences have broadened my perspective and deepened my understanding of the world.

A very special thanks goes to Huang Xiangyun, my dearest friend. Meeting you has been one of the greatest blessings in my life. Your unwavering support, understanding, and love have meant more to me than I can express. You celebrated my happiness, comforted me in difficult times, and always supported me with clarity and sincerity. You taught me how to love and how to be loved.

Finally, my deepest love and gratitude go to my family.

To my father, Tian Yitong, and my mother, Zhang Xiying—you are my greatest source of strength. In both my darkest moments and my happiest times, it was your unconditional love and patience that sustained me. Thank you for always being my safe haven. To my aunt, Chen Yuxian, take good care of me and cook delicious dish for me.

To my sisters Tian Qingxiu, Qin Zhirong, Tian Xiuzhen, and my brothers Fan Yanwei, Tian Shiwei, and Wang Tianzhi, thank you for your constant support and for believing in me through every decision I have made. Every time I return home, I feel renewed strength.

To my nephews—Tian Zihao, Tian Hao, Tian Yueyue, Fan Yile, Fan Yibo, Wang Shiling, and Wang Zhizhong—you are like little angels who remind me of sincerity, joy, and the beauty of life.

I am deeply grateful for my large and loving family. Each of you is unique, and together you create a home filled with warmth and strength. I love you all.

I wish all of you happiness, health, and a life filled with love and peace.

Contents

Acknowledgments **i**

List of Abbreviations **xvii**

Nomenclature **xix**

I

.I Introduction I
.II Méthodes Expérimentales et Modélisation II
.II.1 Fabrication des échantillons II
.II.2 Méthode de mesure 3ω II
.II.3 Modélisation thermique et stratégie d'analyse IV
.II.4 L'approximation du milieu effectif (EMA) V
.III Résultats et Discussion VII
.III.1 Validation du banc de mesure VII
.III.2 Conductivité thermique du substrat de l'empilement VIII
.III.3 Validation numérique de l'approximation du milieu effectif IX
.III.4 Applicabilité générale et limites de l'approche du milieu effectif X
.III.5 Conductivité thermique effective de l'empilement de couches minces XII
.III.6 Discussion et comparaison avec les modèles théoriques XIII

Conclusion générale **XIV**

General Introduction **1**

1 Heat Conduction in Complex Nanostructured Systems **5**
1.1 Context: The Growing Importance of Thermal Management 5
1.1.1 Moore's Law and the Rise of Power Density in Integrated Circuits 5
1.1.2 Thermal challenges in high-power optoelectronics and other device 7
1.1.3 The role of thermal properties in thermoelectric device efficiency 9
1.2 Problematic: Challenges in thermal property characterization at the nanoscale 11
1.2.1 Breakdown of Fourier's Law at small length scales 11
1.2.2 The emergence of phonon boundary and interface scattering 12
1.2.3 The concept of Thermal Boundary Resistance(TBR) or Kapitza Resistance . 13
1.3 Scientific and Technological Motivation 15
1.3.1 SiO_2 and SiN as key dielectric materials 15
1.3.2 The specific metrological challenge posed by multilayer systems 15
1.3.3 Supplementary Numerical Verification (Appendix A) 16
1.4 Conclusion and Scientific Positioning 17

2 State of the Art: Heat Conduction in Solids and its Metrology **19**
2.1 Fundamentals of Phonon Heat Transport . . . 19
2.1.1 The Macroscopic Picture: Fourier's Law of Heat Conduction . . . 19
2.1.2 The Microscopic Picture:Phonons as Heat Carriers . . . 20
2.1.3 The Concept of Minimum Thermal Conductivity in Amorphous Solids . . . 21
2.2 Thermal Conduction in Nanostructures . . . 24
2.2.1 Size Effects: Phonon-Boundary Scattering in Thin Films . . . 24
2.2.2 Interfacial Thermal Resistance(Kapitza Resistance) . . . 25
2.2.3 Theoretical Models for Interfacial Resistance: AMM and DMM . . . 26
2.2.4 Heat Conduction in Multilayer Systems and Superlattices . . . 27
2.3 Review of Thermal Conductivity Measurement Techniques . . . 28
2.3.1 Overview of Steady-State and Transient Method . . . 29
2.3.2 Advanced Optical Techniques:TDTR and Raman Thermometry . . . 30
2.3.3 Strategic Selection: The 3ω Method . . . 32

3 Experimental and Numerical Methodology **35**
3.1 Theoretical Framework of the 3ω Method . . . 36
3.1.1 Fundamental Principle: Signal Generation . . . 36
3.1.2 Analytical Solution: Internal Line Source in Infinite Cylinder . . . 38
3.1.3 Analytical Solution: Surface Line Source on Semi-Infinite Medium . . . 39
3.1.4 Correction for Finite Heater Width . . . 40
3.1.5 Closed-form Solutions for Layered Structures . . . 42
3.1.6 Limitations of Analytical Approaches and Motivation for Numerical Modeling 45
3.2 The 3-Omega Experimental Setup . . . 48
3.2.1 Principle of Operation: The Metallic Strip as Heater and Thermometer . . . 48
3.2.2 Description of the Experimental Bench: Lock-in Amplifier, Wheatstone Bridge, and Probing . . . 52
3.2.3 Sample Fabrication: Dielectric Stack Deposition and Sensor Patterning . . . 55
3.3 Numerical Modeling with COMSOL Multiphysics . . . 57
3.3.1 Introduction to the Finite Element Method (FEM) for Heat Transfer Problems 57
3.3.2 Model Geometry and Physics . . . 58
3.3.3 Boundary Conditions and Meshing . . . 60
3.3.4 Simulation of the 3ω Signal . . . 62
3.4 Chapter Summary and Outlook to Validation . . . 64

4 Validation and Parametric Study of the Thermal Metrology **67**
4.1 Experimental Validation on Bulk Substrates . . . 68
4.1.1 Initial Characterization: Resistance and TCR . . . 68
4.1.2 3-ω Measurement on Borosilicate Glass . . . 69
4.1.3 3-ω Measurement on Fused Silica . . . 71
4.1.4 Attempted Measurement on SiO_2/Si and Conclusion on Validation . . . 74
4.2 Numerical Investigation and Parametric Study (using COMSOL) . . . 75
4.2.1 Model Validation: 2D FEM vs. Analytical Solutions . . . 75
4.2.2 Parametric Study: Effect of Input Power and Heater Width . . . 78
4.2.3 Numerical Analysis of the Slope Method for a Single Film on a Substrate . . . 79
4.2.4 Parametric Study: Influence of Substrate Thermal Conductivity . . . 83
4.2.5 Further Discussion and Opportunities for Future Simulations . . . 86
4.3 Chapter Summary . . . 87

5 Methodology for the Thermal Characterization of Complex Multilayer Systems 89
5.1 Introduction: From a Simple Measurement to a Complex Inverse Problem 89
5.2 Measuring the Substrate: The First Step of the Decoupling Strategy 91
5.3 First Diagnostic Step: What Does Our Measurement Actually "See"? – Frequency-Dependent Sensitivity Analysis 92
5.3.1 Principle of the Sensitivity Analysis 92
5.3.2 Numerical Procedure 93
5.3.3 Main Results of the Sensitivity Analysis 93
5.4 Building and Validating the Effective Medium Approach (EMA) 95
5.4.1 Theoretical Basis of the EMA 95
5.4.2 Virtual Experiment for EMA Validation 95
5.4.3 Validation on the Baseline Virtual Sample 96
5.5 Testing the Applicability Range of the EMA 97
5.5.1 Design of the Virtual Sample Library 98
5.5.2 Results of the Virtual Sample Library 98
5.5.3 Final Comment on the EMA Applicability 100
5.6 Testing an Alternative High-TBR Interpretation 100
5.6.1 Sensitivity Analysis in a High-TBR Case 100
5.6.2 Comparison Between the EMA Model and a Single Global TBR Model . . . 100
5.6.3 Can Several TBR Values Be Fitted Independently? 101
5.6.4 Conclusion of the Comparison 102
5.7 Final Extraction of the Effective Thermal Conductivity 104
5.8 Final Discussion 105
5.9 Summary and Outlook 106

General Conclusion and Perspectives 107

A Numerical Verification of Effective Medium Theory (EMT) 113
1.1 Theoretical Background and Research Objectives 113
1.2 Structure of the Model 114
1.2.1 The Size of the Model 114
1.2.2 Seebeck Coefficient Simulation 115
1.2.3 Thermal Conductivity Simulation 116
1.2.4 Electrical Conductivity Simulation 117
1.3 Data Analysis and Discussion 118
1.4 Summary of Preliminary Work 121

Abstract/résumé 141

List of Figures

1 (a) Représentation schématique en coupe du système à 5 couches déposé sur un substrat considéré dans l'étude. (b) Vue de dessus de ce même système obtenue par microscopie optique. II

2 Schéma du montage 3ω avec pont de Wheatstone et détection synchrone. III

3 Analyse de sensibilité des paramètres thermiques en fonction de la fréquence. Cette analyse a été réalisée autour des valeurs estimées des paramètres thermiques. Elle montre distinctement les régions où le signal est le plus sensible à la conductivité thermique du substrat et à la conductivité thermique effective de l'empilement de couches minces. L'influence de la résistance thermique d'interface R_{TBR} sur le signal est faible devant les autres paramètres. V

4 Évolution des parties réelle et imaginaire de la tension $V_{3\omega}$ en fonction de $\ln(2\omega)$ pour un verre de borosilicate. Un ajustement via une droite est effectuée sur la partie réelle. La valeur de la pente permet de calculer via l'application successive des relations 1 et 5 la conductivité thermique du matériau sous forme massive. VIII

5 Évolution des parties réelle et imaginaire de la tension $V_{3\omega}$ en fonction de $\ln(2\omega)$ pour un verre de silice. Un ajustement via une droite est effectuée sur la partie réelle. La valeur de la pente permet de calculer via l'application successive des relations 1 et 5 la conductivité thermique du matériau sous forme massive. IX

6 Évolution de la partie réelle de la température $T_{inphase}$ en fonction de $\ln(2\omega)$ pour les deux bandes chauffantes considérées, de a) 6 et b) 8 μm de largeur. Le trait continu représente l'ajustement numérique via une droite dans les « basses fréquences ». . . . X

7 Ajustement par l'approche du milieu effectif des données virtuelles générées concernant le cas A par la méthode des éléments finis. XI

8 Profil de température dans un système avec 1 couche déposée sur un substrat. La bande chauffante est épaisse de 500 nm, la longueur 3 mm et la largeur 3 μm. Elle est traversée par un courant sinusoïdal de 100 mA à une fréquence de 266,9 Hz. a) La conductivité thermique effective de la couche est similaire à celle du substrat, $k_{eff} \approx k_{sub}$. Le flux de température se réparti sous la forme d'une goutte. b) La conductivité thermique de la couche est largement supérieure à celle du substrat ($k_{eff} > k_{sub}$), avec ici k_{eff}=20 W.m^{-1}.K^{-1} . Le flux de chaleur est essentiellement latéral, conduisant à une distribution de température plus aplatie. XIII

9 Évolution expérimentale de la partie réelle de la température en fonction de $\ln(2\omega)$ pour deux bandes chauffantes : l'une de 6 μm (R_0=32,82 Ω) et l'autre de 8 μm de largeur (R_0=25,25 Ω). Les traits représentent les ajustements numériques par l'approche du milieu effectif (AME). XIV

1.1 A semi-log plot illustrating the exponential growth of the number of transistors on integrated circuit chips over the past five decades. The data points represent various Intel microprocessors, showing a doubling of transistor count approximately every two years, consistent with Moore's prediction (Karl (2022)[10], Wikipedia (2022)[11], AppleM1Ultra (2022)[12]). The y-axis shows the number of transistors on a chip (logarithmic scale) versus the year of introduction. 6
1.2 Trends in microprocessor scaling from 1985 to 2010. While transistor count continues to increase exponentially, clock frequency and single-thread performance plateau around 2005 due to power constraints. As a result, performance scaling shifts from frequency increases to multi-core architectures, reflected in the rising number of cores per chip (Fuller ***et al.*** (2011) [17]). 7
1.3 A schematic cross-section of a high-power LED package, illustrating the complex thermal path (Li (2024) [27] and Poppe ***et al.*** (2009) [28]). 8
1.4 LED performance vs. junction temperature 8
1.5 Typical L-I curves of a laser diode at various temperatures showing thermal rollover (Coldren ***et al.*** (2012) [32]). 9
1.6 Power module schematic and thermal resistance network 10
1.7 Conceptual plot of thermoelectric properties (Seebeck coefficient S, electrical conductivity σ, thermal conductivity κ, and figure of merit ZT) as a function of carrier concentration. The interdependence of these parameters limits the maximum ZT to a narrow range of optimal carrier concentration, typically found in heavily doped semiconductors (Adapted from Snyder ***et al.*** (2008) [41]). 10
1.8 Schematic of heat transport regimes (Diffusive, Quasi-Ballistic, Ballistic) defined by the Knudsen number (Kn) (Concept based on Chen (2005) [53]). 12
1.9 Spectral nature of phonon transport in silicon at 300 K. (a) Phonon dispersion curves along the high-symmetry path Γ–X–K–Γ, showing acoustic (LA, TA) and optical (LO, TO) branches. (b) Cumulative thermal conductivity as a function of phonon mean free path (MFP). The results indicate that a significant portion of the thermal conductivity arises from phonons with long mean free paths (on the order of micrometers). Plots are re-drawn based on trends and data from first-principles calculations (Esfarjani ***et al.*** (2011) [59]). 13
1.10 Illustration of specular vs. diffuse phonon scattering. 14
1.11 A schematic plot illustrating the temperature discontinuity (ΔT_{TBR}) at an interface. . 14
1.12 A schematic of a realistic interface, showing features not captured by simple models. 15
1.13 A detailed cross-section of a modern FinFET, highlighting the ubiquitous use of SiO_2 and SiN films (Schematic based on concepts from Duan (2024) [89]). 16
1.14 A diagram defining the inverse problem: determining multiple unknown thermal properties from a single surface measurement. 16

2.1 A multi-panel schematic illustrating the key concepts of phonon-mediated heat transport. (a) One-dimensional lattice model showing atoms as a coupled oscillator system; the quantization of lattice vibrations gives rise to phonons. (b) Representative phonon dispersion relation ω(k) for a diatomic crystal, showing acoustic and optical branches. The slope $\partial\omega/\partial$k defines the phonon group velocity v_g, which governs the propagation speed of vibrational energy. (c) Schematic illustration of major phonon scattering mechanisms: (i) phonon-phonon scattering including Normal (N) and Umklapp (U) processes, (ii) point defect (isotope) scattering, (iii) dislocation scattering, and (iv) boundary scattering. 22

2.2 Schematic plot of Thermal Conductivity vs. Temperature for a typical crystalline solid (e.g., Silicon) and an amorphous glass (e.g., a-SiO2). The plot highlights the contrast between the sharp peak observed in crystals due to phonon scattering and the monotonic, low-conductivity behavior of glasses. The plot is a re-creation based on classic experimental data from Glassbrenner ***et al.*** (1964) [109] for silicon, Zeller ***et al.*** (1971) [110] for a-SiO_2, and the minimum thermal conductivity limit (κ_{min}) described by Cahill ***et al.*** (1989) [103]. 23

2.3 Conceptual illustration of the cross-plane thermal conductivity of a Si/Ge superlattice as a function of period length. The curve illustrates the crossover from incoherent (particle-like) transport at larger periods to coherent (wave-like) transport at short periods. While experiments typically observe the sharp decrease in the incoherent regime (right side) While experiments typically observe the sharp decrease in the incoherent regime (right side), as reported by Lee ***et al.*** (1997) [120], theoretical models predict a rise, forming a U-shaped trend, in the coherent regime (left side), as described by Chen (1998) [56]. The dashed line represents the random alloy limit. . . 28

2.4 A detailed schematic of a typical Time-Domain Thermoreflectance (TDTR) experimental setup. The diagram shows the ultrashort pulse laser, beam splitters, the pump path with an EOM, the probe path with a mechanical delay stage, and the reflected probe beam directed to a photodiode and lock-in amplifier. This schematic is based on the typical configuration described in foundational TDTR methodology papers, such as Cahill (2004) [123]. 31

3.1 A detailed schematic of a typical 3-ω experimental setup. The diagram shows the function generator, current source, sample in a 2-point probe configuration (often with a Wheatstone bridge), and a lock-in amplifier set to measure the 3ω voltage. 37

3.2 Geometry of an infinite circular cylinder with a 1D line heater along its axis. 38

3.3 Plot of the zeroth-order modified Bessel functions of the first kind (I_0) and second kind (K_0) versus the dimensionless argument μ (where $\mu = \gamma r$). The decaying behavior of $K_0(\mu)$ as $\mu \to \infty$ makes it the physically correct solution for an infinite medium. . . . 39

3.4 Geometry of a line heater on the surface of a semi-infinite medium. 39

3.5 Schematic illustrating a finite-width heater (width 2b) on a surface. 40

3.6 Numerically calculated in-phase (blue) and out-of-phase (red) components of the average temperature oscillation (Eq. 3.13) as a function of frequency, showing different regimes. 41

3.7 In-phase and out-of-phase components of the temperature oscillation vs. $\ln(2\omega)$ calculated using the low-frequency approximation (Eq. 3.14) for a bulky material. It illustrates the decreasing linear dependence of the in-phase component and the constant out-of-phase component in this regime. 42

3.8 Schematic of the heater-film-substrate configuration. 42

3.9 Schematic cross-section showing heat flux lines for narrow (left) and wide (right) heaters, illustrating sensitivity to in-plane vs. cross-plane conduction in anisotropic films. 43

3.10 Comparison of the simulated frequency-dependent temperature oscillations (in-phase) for three distinct architectures. The Multilayer Stack (Black Squares) deviates significantly from the linear behavior of the Bare Substrate due to lateral heat spreading in the high-conductivity SiN layers, demonstrating the invalidity of the 1D slope method. 46

3.11 Schematic of the four-wire probe configuration applied to a 3-ω heater/sensor. The two outer pads, labelled I+ and I-, are used to inject the current through the heater line. The two inner pads, labelled V+ and V-, are connected to a high-impedance voltage measurement input and measure only the voltage drop across the active heater section. Because almost no current flows through the voltage leads, the measured voltage is not affected by the contact and lead resistances of the current path. 50
3.12 Schematic of the experimental setup used for TCR calibration. The sample is placed inside a temperature-controlled environmental chamber, while the heater resistance is measured using a four-wire configuration. The resistance acquisition is performed with an Arduino-based ohmmeter controlled by LabVIEW. 51
3.13 Photograph of the custom-built 3-ω experimental setup. Key components shown include the Function Generator (Keysight 33210A), Digital Multimeter (AM-530-EUR), SR7265 Lock-in Amplifier, the custom Wheatstone Bridge circuit, and the sample probing stage. 53
3.14 Example of a 2D computational domain used for the diagnostic FEM simulations, showing the resulting temperature distribution. The model geometry consists of the Ti/Au heater (30 µm wide, 0.5 µm thick) on a one-layer stack. The stack consists of a 0.8 µm Parylene C film (κ = 0.13 W,m^{-1},K^{-1}) on top of a 500 µm × 500 µm borosilicate glass ($BrSiO_2$) substrate (κ = 1.13 W,m^{-1},K^{-1}). In this finite-domain example, a heat flux corresponding to an RMS power P_{rms} = 3.99 W,m^{-1} is applied to the top of the heater, and isothermal conditions are applied to the lateral and bottom boundaries. 59
3.15 Representative mesh used for the 2D diagnostic FEM model. The wide view shows the coarser mesh away from the heater, while the zoomed-in view highlights the refined mesh in the heater/film region, where high thermal gradients must be resolved accurately. 62
3.16 Representative 3D mesh used for one virtual multilayer sample in Chapter 5. The mapped and swept meshing strategy produces regular hexahedral elements along the heater and multilayer stack, while preserving the geometrical resolution required near the thin-film interfaces. 63
3.17 Example of the output of the virtual experiment. The plot shows the simulated in-phase Re(θ_{avg}) and out-of-phase Im(θ_{avg}) components of the heater temperature oscillation as a function of frequency. These curves are the numerical equivalent of the data obtained from the lock-in amplifier after conversion of the measured 3ω voltage into temperature oscillation. 64

4.1 Photographs of the validation samples: (a) $BrSiO_2$ Samples 1 and 2, and (b) fused-silica sample on the left and SiO_2/Si sample on the right. The patterned 3-ω heater/sensor structures can be observed on the sample surfaces. 69
4.2 Representative TCR calibration data. (a) Resistance as a function of temperature for a heater on $BrSiO_2$ Sample 1 Line 8. (b) Resistance as a function of temperature for a heater on fused-silica Sample 3 Line 2. The linear behavior confirms that the heater resistance can be used as a temperature sensor in the investigated range. 71
4.3 Representative TCR calibration data for a heater on the SiO_2/Si sample. The plot shows the resistance as a function of temperature for Sample 4 Line 2. 71
4.4 Experimental validation on borosilicate glass. The plot shows the measured in-phase 3-ω signal, converted to ΔT_{in}, as a function of ln(2ω) for a representative heater line, Sample 1 Line 8. 73
4.5 Experimental validation on fused silica. The plot shows the measured in-phase 3-ω signal as a function of ln(2ω) for a 6 µm-wide heater line. 74

4.6 Self-consistency check of the analytical model. The in-phase temperature response generated from the Cahill approximation is plotted as a function of $\ln(2\omega)$. The linear fit recovers the input thermal conductivity, confirming the internal consistency of the analytical slope method when its assumptions are exactly satisfied. 76
4.7 FEM validation for a high-thermal-conductivity silicon substrate. The simulated in-phase temperature oscillation is plotted as a function of $\ln(2\omega)$. The thermal conductivity extracted from selected frequency windows remains close to the input value of $\kappa_{\mathrm{Si,input}} = 130\ \mathrm{W.m^{-1}.K^{-1}}$. 77
4.8 Numerical study of the effect of heater width. The simulated temperature oscillations for a 20 µm heater and a 25 µm heater on a $BrSiO_2$ substrate are compared. The difference between the two curves shows that finite heater geometry affects the temperature response when the analytical line-source approximation is used. 79
4.9 Schematic representation of the two single-film configurations used to test the analytical film-extraction method. (a) Parylene C film on a $BrSiO_2$ substrate, corresponding to a low-conductivity film on a low-conductivity substrate. (b) SiO_2 film on a silicon substrate, corresponding to a low-conductivity film on a high-conductivity substrate. 80
4.10 Numerical test of the analytical film-extraction method for a Parylene C film on a $BrSiO_2$ substrate. The simulated response of the full film/substrate system is compared with the calculated substrate response. The difference between the two responses is used to estimate the film contribution and to extract the film thermal conductivity. . . 81
4.11 Numerical test of the analytical film-extraction method for a SiO_2 film on a silicon substrate. The simulated response of the full SiO_2/Si system is compared with the calculated silicon substrate response. The difference between the two responses is used to estimate the temperature drop across the SiO_2 film. 82
4.12 Simulated in-phase temperature oscillations for an identical SiO_2 film on three different substrates with $\kappa_{\mathrm{sub}} = 10, 50$, and $131\ \mathrm{W.m^{-1}.K^{-1}}$. (a) Comparison of all three cases. (b) Low-conductivity substrate, $\kappa_{\mathrm{sub}} = 10\ \mathrm{W.m^{-1}.K^{-1}}$. (c) Medium-conductivity substrate, $\kappa_{\mathrm{sub}} = 50\ \mathrm{W.m^{-1}.K^{-1}}$. (d) High-conductivity substrate, $\kappa_{\mathrm{sub}} = 131\ \mathrm{W.m^{-1}.K^{-1}}$. The signal amplitude decreases as the substrate thermal conductivity increases. 84
4.13 Calculated film temperature contribution, ΔT_{film}, for an identical SiO_2 film on three different substrates. (a) Low-conductivity substrate, $\kappa_{\mathrm{sub}} = 10\ \mathrm{W.m^{-1}.K^{-1}}$, showing the largest extraction error. (b) Medium-conductivity substrate, $\kappa_{\mathrm{sub}} = 50\ \mathrm{W.m^{-1}.K^{-1}}$. (c) High-conductivity substrate, $\kappa_{\mathrm{sub}} = 131\ \mathrm{W.m^{-1}.K^{-1}}$, showing the most accurate extraction among the three cases. 85

5.1 Structure of the five-layer Si_3N_4/SiO_2 stack fabricated on a fused silica substrate. (a) Cross-sectional schematic showing the thickness of each layer. (b) Microscope image of the sample. 90
5.2 Experimental in-phase temperature oscillation ΔT_{in} as a function of $\ln(2\omega)$ for the two heater geometries in the low-frequency range from 71 Hz to 266 Hz. (a) Heater width of 6 µm. (b) Heater width of 8 µm. The solid lines correspond to the linear fits used to extract the substrate thermal conductivity κ_{sub}. 92
5.3 Normalized sensitivity coefficients $|S_X|$ of the in-phase 3-ω temperature response with respect to the substrate thermal conductivity κ_{sub}, the effective film thermal conductivity κ_{eff}, and the interface thermal resistance R_{TBR}, as a function of frequency. 94
5.4 EMA inverse fit applied to the virtual in-phase temperature response generated from the full multilayer model of Sample A. The single-layer EMA model reproduces the virtual data in the selected fitting range. 97

5.5 Simulated temperature distribution illustrating the change in heat transport behavior. (a) For Sample A, where κ_{film} is comparable to κ_{sub}, heat mainly penetrates downward into the substrate. (b) When the film is much more conductive, the film spreads heat laterally before the heat enters the substrate. Both simulations are shown at 163 Hz. . 99
5.6 Normalized sensitivity coefficients $|S_X|$ of the in-phase 3-ω response with respect to the substrate thermal conductivity κ_{sub}, the effective film thermal conductivity κ_{eff}, and a high interface thermal resistance $R_{\text{TBR}} = 1.0 \times 10^{-7}$ m^2.K.W^{-1}, as a function of frequency. 101
5.7 Parameter correlation in the multi-TBR inverse fitting test. The fitted response obtained with the multi-TBR model closely matches the virtual data. However, the extracted interface resistances differ from the true input values, showing that a good fit does not necessarily give a unique set of physical parameters. 103
5.8 Final EMA fits applied to the experimental in-phase data for two heater widths, 6 µm and 8 µm, in the selected fitting range from 266 Hz to 898 Hz. 104

A.1 The random and non-overlapping spheres inside the bulk. 115
A.2 The meshing of random and non-overlapping spheres inside the bulk. 116
A.3 3D geometry and boundary condition setup for the Seebeck coefficient simulation. . . 117
A.4 FEM simulated effective electric potential vs. temperature. The linear slope represents the extracted effective Seebeck coefficient. 118
A.5 3D temperature distribution simulation for the effective thermal conductivity calculation. 119
A.6 The extracted temperature vs. length profile from the thermal conductivity simulation. The slope is used to determine the effective thermal conductivity. 120
A.7 3D electric potential simulation profile for the effective electrical conductivity calculation. 121
A.8 Filler loading fraction of the effective thermal conductivity calculated by FEM (blue circle) and by EMT (red line). 122
A.9 A zoom of Figure A.8. 122
A.10 Difference calculated from Figure A.9 between the effective thermal conductivity calculated by FEM and EMT. 123
A.11 Filler loading fraction of the effective electrical conductivity calculated by FEM (blue circle) and by EMT (red line). 123
A.12 A zoom of Figure A.11. 124
A.13 Difference calculated from Figure A.12 between the effective electrical conductivity calculated by FEM and EMT. 124
A.14 Filler loading fraction of the effective ratio electrical conductivity by Seebeck coefficient calculated by FEM(blue circle) and EMT(red line). 125
A.15 A zoom figure of A.14. 125
A.16 Difference calculated from Figure A.15 between the effective ratio electrical conductivity by Seebeck coefficient calculated by FEM and EMT. 126
A.17 Filler loading fraction of the effective ratio thermal conductivity by Seebeck coefficient calculated by FEM(blue circle) and EMT(red line). 126
A.18 A zoom figure of A.17 127
A.19 Difference calculated from Figure A.18 between the effective thermal conductivity/Seebeck coefficient ratio calculated by FEM and EMT. 127
A.20 Comparison between the effective Seebeck coefficient calculated by FEM and by EMT, assuming the relevant transport parameter is σ/S. 128
A.21 Comparison between the effective Seebeck coefficient calculated by FEM and by EMT, assuming the relevant transport parameter is κ/S. 129

A.22 Absolute relative error between the effective Seebeck coefficient calculated by FEM and by EMT, assuming two different assumptions: the relevant transport parameter is σ/S, then κ/S. 130

List of Tables

3 Conditions expérimentales de l'essai de la figure 4 et valeur de la conductivité thermique du borosilicate qui en est déterminée. VII
4 Conditions expérimentales des essais réalisés avec le verre de silice5 et valeurs de la conductivité thermique du borosilicate qui en sont déterminées. VIII
5 Valeurs de la tension appliquée $V_{1\omega}$ et de la résistance ohmique de la bande chauffante R_0 selon la largeur de l'élément chauffant. Les conductivités thermiques du substrat respectives déterminées par ajustement numérique sont également données. IX
6 Paramètres thermiques utilisés pour simuler les signaux virtuels (échantillons A-K) par la méthode des éléments finis. Le cas A concerne le système étudié avec ses paramètres thermiques estimés. XI
7 Résultats des ajustements numériques effectués à l'aide du modèle du milieu effectif pour les signaux générés selon les paramètres du tableau 6. XII
8 Détermination de la conductivité thermique effective transverse ($k_{\text{eff},\perp}$) à partir de l'approche du milieu effectif. Les incertitudes correspondent aux intervalles de confiance à 95% issus de la procédure d'ajustement. XIII

1.1 A comparison of key material properties for power semiconductors. 9

2.1 Summary of Phonon Boundary Scattering Regimes in Thin Films 25
2.2 Comparison of steady-state vs. transient thermal measurement methods for thin films. 30

3.1 Summary of material properties and geometric parameters used in the FEM simulations. Note the minimal thermal contrast between the Oxide layer and the Substrate.(The material properties were obtained from the built-in COMSOL Multiphysics material library.) 46
3.2 Physical interpretation and mathematical expression of the boundary conditions used in the FEM model. 61
3.3 Mesh statistics and quality indicators for a representative 3D virtual sample used in Chapter 5. The element quality was evaluated using the skewness quality measure in COMSOL. 63

4.1 Resistance measurements of heater lines on $BrSiO_2$ Samples 1 and 2 at 20 °C. 70
4.2 Resistance measurements of heater lines on fused-silica Sample 3 at 20 °C. 70
4.3 Resistance measurements of heater lines on the SiO_2/Si sample at 20 °C. 70
4.4 Calibrated TCR values for $BrSiO_2$ Samples 1 and 2. 72
4.5 Calibrated TCR values for fused-silica Sample 3. 72
4.6 Calibrated TCR values for the SiO_2/Si sample. 72
4.7 Estimated linear frequency range for different heater geometries on $BrSiO_2$ samples. 72
4.8 Summary of 3-ω measurement parameters and extracted thermal conductivity values for $BrSiO_2$ Samples 1 and 2. 73

4.9 Estimated linear frequency range for different heater geometries on the fused-silica sample. 73
4.10 Summary of 3-ω measurement parameters and extracted thermal conductivity values for fused-silica Sample 3. 74
4.11 Summary of FEM validation results for bulk substrates using the analytical slope method. 77
4.12 Summary of the FEM-based numerical test of the analytical single-film extraction method. 82
4.13 Influence of substrate thermal conductivity on the analytical extraction of the SiO_2 film thermal conductivity. The input film thermal conductivity is fixed at $\kappa_{f,\text{input}} = 1.40\ \text{W.m}^{-1}\text{.K}^{-1}$. 83

5.1 Slope values obtained from the low-frequency linear fits and extracted substrate thermal conductivity values for the two heater geometries. 92
5.2 Normalized sensitivity coefficients $|S_X|$ of selected thermal parameters at 163.4 Hz. . 94
5.3 Description of the virtual sample library used to test the applicability range of the EMA. 98
5.4 EMA validation results for the virtual sample library. The fitted value $\kappa_{\text{eff},\perp}^{\text{fit}}$ is obtained from the 3D EMA inverse fit and should be interpreted according to the thermal regime of each sample. 99
5.5 Main geometric, electrical, and thermal parameters used in the FEM model for the final EMA inverse fitting. 105
5.6 Final effective cross-plane thermal conductivity values extracted using the EMA model. The reported uncertainties correspond to the 95% confidence intervals obtained from the COMSOL parameter estimation procedure. 105

A.1 Parameters used in the FEM simulation and in the EMT model. 114

List of Abbreviations

Acronym	Definition
1D / 2D / 3D	One- / Two- / Three-Dimensional
3ω	3-Omega (Electro-thermal measurement technique)
AC	Alternating Current
AFM	Atomic Force Microscopy
AMM	Acoustic Mismatch Model
BEOL	Back-End-Of-Line
BTE	Boltzmann Transport Equation
CEF	Critical Electric Field
CMOS	Complementary Metal-Oxide-Semiconductor
COD	Catastrophic Optical Damage
CTE	Coefficient of Thermal Expansion
CVD	Chemical Vapor Deposition
DBC	Direct Bonded Copper
DC	Direct Current
DMM	Diffuse Mismatch Model
EMA	Effective Medium Approach / Effective Medium Theory
EMT	Effective Medium Theory
FDTR	Frequency-Domain Thermoreflectance
FEM	Finite Element Method
FET	Field-Effect Transistor
FinFET	Fin Field-Effect Transistor
GaN	Gallium Nitride
HEMT	High Electron Mobility Transistor
IC	Integrated Circuit
IHCP	Inverse Heat Conduction Problem
IGBT	Insulated Gate Bipolar Transistor
LED	Light-Emitting Diode
L-I	Light-Current

Acronym	Definition
LTE	Local Thermal Equilibrium
MFP	Mean Free Path
PCB	Printed Circuit Board
PECVD	Plasma-Enhanced Chemical Vapor Deposition
PGEC	Phonon-Glass Electron-Crystal
PVD	Physical Vapor Deposition
PSD	Phase Sensitive Detection
RF	Radio Frequency
RMS	Root Mean Square
SEM	Scanning Electron Microscopy
SiC	Silicon Carbide
SiN_x	Silicon Nitride (non-stoichiometric)
SiO_2	Silicon Dioxide
SOI	Silicon-On-Insulator
TBR	Thermal Boundary Resistance (Kapitza Resistance)
TCR	Temperature Coefficient of Resistance
TDTR	Time-Domain Thermoreflectance
TE	Thermoelectric
TEM	Transmission Electron Microscopy
THD	Total Harmonic Distortion
TIM	Thermal Interface Material
WBG	Wide-Bandgap

Nomenclature

Symbol	Description	Unit
b	Half-width of the heater line	m
B	slope	
C_p	Specific heat capacity at constant pressure	J/(kg·K)
C_v	Volumetric heat capacity	J/(m^3·K)
d	Thickness of the film or layer	m
α	Thermal diffusivity	m^2/s
f	Frequency of the electrical current	Hz
I	Electrical current (RMS or amplitude)	A
J	Heat flux density vector	W/m^2
κ	Thermal conductivity	W/(m·K)
κ_{ph}	Phonon thermal conductivity	W/(m·K)
τ	Phonon relaxation time	s
k	Wave vector	m$^-$1
γ	The complex thermal wave vector	m$^-$1
κ_{eff}	Effective thermal conductivity	W/(m·K)
κ_{bulk}	Bulk thermal conductivity	W/(m·K)
κ_s	Thermal conductivity of substrate	W/(m·K)
κ_f	Thermal conductivity of thin film	W/(m·K)
κ_{min}	Minimum thermal conductivity	W/(m·K)
n	Number density of atoms	-
v_i	Speed of sound for the three polarization branches (one longitudinal, two transve)	-
$\Theta_{D,i}$	Debye temperature for each branch	-
Kn	Knudsen number ($Kn = \Lambda/L$)	-
k_B	Boltzmann constant	J/K
l	Length of the heater line or characteristic length	m
p	Specularity parameter (Fuchs-Sondheimer model)	-
P	Electrical power	W

Symbol	Description	Unit
P_l	Linear power density	W/m
q	Heat flux	W/m^2
R	Electrical resistance	Ω
R_0	Electrical resistance at reference temperature T_0	Ω
R_{th}	Thermal resistance	K/W
R_K	Kapitza resistance (Thermal Boundary Resistance)	m^2·K/W
R_{avg}	Resistance at the average operating temperature	m^2·K/W
S	Seebeck coefficient	V/K
S_x	Sensitivity paramenter	
T	Absolute temperature	K
T_0	Reference or ambient temperature	K
v_g	Phonon group velocity	m/s
V	Voltage	V
$V_{1\omega}$	First harmonic voltage component	V
$V_{3\omega}$	Third harmonic voltage component	V
ZT	Thermoelectric figure of merit	-
β	Temperature coefficient of resistance (TCR)	1/K
ΔT	Temperature rise / difference	K
η	Surface roughness parameter	m
Λ	Phonon Mean Free Path (also denoted as λ)	m
λ_{ph}	Phonon wavelength	m
ρ	Mass density	kg/m^3
σ	Electrical conductivity	S/m
ϕ	Phase difference	-
ω	Angular frequency of the current ($2\pi f$)	rad/s
Ω	Electrical resistance unit (Ohm)	-
L_p	Thermal penetration depth	m
$\theta(\mathbf{r})$	The complex amplitude of the temperature oscillationh	m
C	Constant	-
ϵ	Euler constant	-
ξ	The argument of function	-
f_{linear}	The linear frequency window	-
d_f	The thin film thickness	m
t_s	The thickness of substrate	m
$\mathbf{K}$	The global stiffness (conductance) matrix	-

Symbol	Description	Unit
$\mathbf{T}$	The vector of nodal temperatures	-
$\mathbf{F}$	The vector of applied heat loads	-
$Q_{2\omega}$	The amplitude of the volumetric heat source at frequency 2ω	-
θ	The complex temperature field	-
$P'_{2\omega}$	The power per unit length	-

This journey taught me that growth often begins where certainty ends,
and that even in difficulty, life quietly opens new possibilities.

归去，也无风雨也无晴。

Guī qù, yě wú fēng yǔ yě wú qíng.

— Su Shi, *Ding Feng Bo*

Étude thermique d'un système multicouches : modélisation par la méthode des éléments finis et caractérisations expérimentales par la technique 3ω

.I Introduction

Les empilements multicouches diélectriques jouent un rôle crucial dans un large éventail de technologies modernes [1, 2, 3, 4]. Ils constituent des éléments essentiels pour l'isolation électrique et les diélectriques inter-niveaux ou inter-métaux dans les circuits intégrés [2, 3], les couches de passivation et d'encapsulation pour les capteurs et les systèmes microélectromécaniques (MEMS) [4, 5], ainsi que pour les filtres optiques et les réflecteurs distribués de Bragg (DBR) à haute réflectivité utilisés dans les dispositifs photoniques, notamment les lasers à cavité verticale émettant par la surface (VCSEL) [1, 6, 7]. Avec la miniaturisation continue des dispositifs, l'augmentation de la densité d'intégration et de la dissipation de puissance locale rend la gestion thermique efficace essentielle pour garantir les performances, la fiabilité et la durée de vie des appareils [8, 9, 10].

La capacité de ces films multicouches à dissiper la chaleur est gouvernée par leur conductivité thermique effective (k_{eff}). Cependant, à l'échelle nanométrique, la conductivité thermique des films minces peut être de plusieurs ordres de grandeur inférieure à celle de leurs équivalents sous forme massive [11, 12]. Cette réduction est principalement attribuée aux mécanismes de diffusion des phonons, qui deviennent dominants lorsque les dimensions caractéristiques du matériau sont comparables à leur libre parcours moyen [13, 14]. La diffusion des phonons aux surfaces du film et la diffusion interne aux joints de grains et aux défauts entravent fortement le transport de la chaleur [15, 16]. De plus, à l'interface entre deux matériaux différents, une résistance thermique supplémentaire, appelée résistance de Kapitza ou résistance thermique d'interface, apparaît en raison de l'inadéquation des propriétés phononiques des deux matériaux, créant une barrière supplémentaire au flux thermique [17, 18].

Alors que les propriétés thermiques des films fins monocouches de Si_3N_4 et de SiO_2 ont été largement étudiées [19, 20], la caractérisation d'un empilement multicouches complexe représente un défi considérable. Extraire de manière fiable les propriétés thermiques intrinsèques de chaque couche à partir d'un seul jeu de données expérimentales constitue un problème inverse classique de conduction thermique, souvent mal posé et sensible à de fortes corrélations entre les multiples paramètres d'ajustement [21, 22].

Le présent travail vise à relever ce défi en proposant une approche systématique pour caractériser un empilement à 5 couches de Si_3N_4/SiO_2, ensemble utilisé comme éléments isolants électriques dans le domaine de l'électronique. Plusieurs lignes, servant de source de chaleur, de longueur et de largeur différentes sont utilisées afin d'assurer une validation croisée des résultats. La stabilité du modèle d'ajustement multiparamétrique est analysée pour apporter une évaluation quantitative de la sensibilité du signal aux paramètres thermiques. À l'issue de cette démarche, un approche considérant

un unique milieu effectif plus robuste est proposé. Enfin, une valeur de la conductivité thermique effective globale expérimentale de l'empilement est déterminée.

.II Méthodes Expérimentales et Modélisation

.II.1 Fabrication des échantillons

L'échantillon étudié dans cette thèse consiste en un empilement de matériaux diélectriques composé de cinq couches. L'ensemble est déposé sur un substrat, issu du commerce, en silice fondue, d'une épaisseur de 150 µm. Ces couches ont été déposées par dépôt chimique en phase vapeur assisté par plasma (PECVD). Un schéma en coupe de l'échantillon est présenté à la fig. 1 (a), tandis que la fig.1 (b) montre l'image en microscopie optique de l'échantillon. La structure du dispositif en partant du substrat vers le haut, est la suivante : SiO_2 (312 nm), Si_3N_4 (226 nm), SiO_2 (312 nm), SiO_2 (312 nm), et enfin Si_3N_4 (126 nm) en surface. L'épaisseur totale de l'empilement diélectrique est ainsi de 1288 nm. Les échantillons sous forme massive qui ont servi à valider le dispositif sont des *wafers* commerciaux.

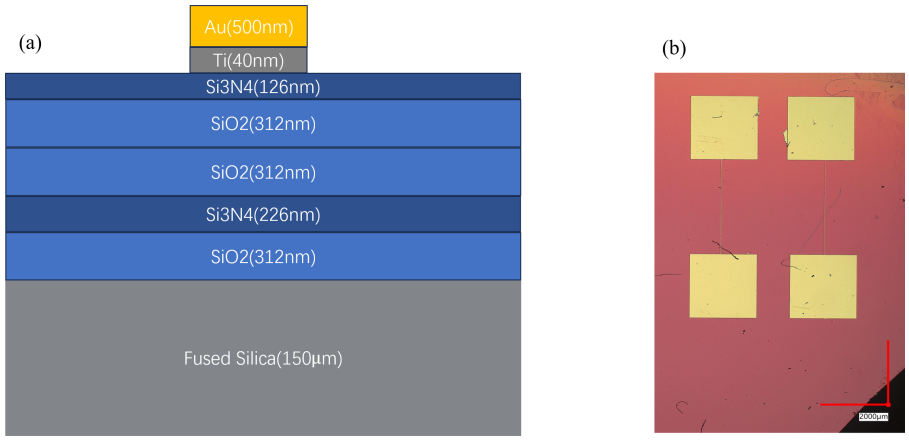


FIGURE 1 – (a) Représentation schématique en coupe du système à 5 couches déposé sur un substrat considéré dans l'étude. (b) Vue de dessus de ce même système obtenue par microscopie optique.

Pour assurer la robustesse de nos mesures, plusieurs bandes métalliques de tailles différentes ont été déposées en surface des échantillons à l'aide de la lithographie par faisceau d'électrons. Lors d'une mesure, une de ces bandes est traversée par un courant électrique assurant un chauffage d'origine ohmique. Les bandes de chauffage sont constituées d'une couche d'adhésion en titane (Ti) de 40 nm, suivie d'une couche d'or (Au) de 500 nm. Dans la suite de ce résumé en français du mémoire, les termes de ligne, capteur, bande de chauffage, élément chauffant ou encore bande métallique seront utilisés indistinctement et se réfèrent à la source de chaleur/capteur de température 3ω en surface de l'échantillon.

.II.2 Méthode de mesure 3ω

Dispositif de caractérisation 3 ω

Les mesures 3ω ont été effectuées à l'aide d'un montage standard, basé sur un amplificateur à détection synchrone, dont le schéma est montré à la fig. 2 [23, 24, 25]. Une tension alternative à la fréquence angulaire ω est appliquée via un générateur de fonctions (Keysight 33210A) à un pont de Wheastone dont une des branches consiste en un élément métallique chauffant déposé sur l'échantillon. Cet élément chauffant joue également le rôle de capteur à partir duquel la température est mesurée. Une variation de température oscillant à la fréquence angulaire 2ω est produite par effet Joule. Le

pont de Wheastone permet de mesurer de manière sensible la faible variation de tension ($V_{3\omega}$) qui en résulte à trois fois la fréquence angulaire de la perturbation électrique appliquée. Cette configuration en pont est essentielle pour annuler la composante du premier harmonique ($V_{1\omega}$) qui viendrait saturer l'entrée de la détection synchrone rendant indétectable le faible signal ($V_{3\omega}$), typiquement trois ordres de grandeur plus petit.

La sortie différentielle du pont est connectée à l'amplificateur à détection synchrone (Signal Recovery, SR7265) afin d'extraire la troisième harmonique de la tension du signal. L'ensemble de l'expérience, y compris le balayage en fréquence et l'acquisition des données, a été automatisé grâce à un instrument virtuel LabVIEW adapté.

Les composantes réelle et imaginaire de la tension au troisième harmonique ($V_{3\omega,\text{in-phase}}$ et $V_{3\omega,\text{out-phase}}$) ont été enregistrées en fonction de la fréquence (f). La résistance de l'élément chauffant métallique et de la tension du premier harmonique à ses bornes ont été mesurées à l'aide d'un multimètre numérique (AM-530-EUR). L'oscillation de la composante réelle de la température ($T_{inphase}$) a ensuite été calculée à partir de la relation bien établie [26] :

$$T_{inphase} = \frac{2V_{3\omega,\text{in-phase}}}{\beta V_{1\omega}}, \tag{1}$$

où $V_{3\omega,\text{in-phase}}$ est la composante réelle de la 3^e harmonique de la tension ($V_{3\omega,\text{in-phase}}$) , β est le coefficient de température pré-calibré de l'élément chauffant mesuré par la méthode 4 fils, et $V_{1\omega}$ est la tension du premier harmonique. Toutes les analyses ultérieures sont effectuées à partir de l'évolution de la composante réelle ainsi calculée de la température.

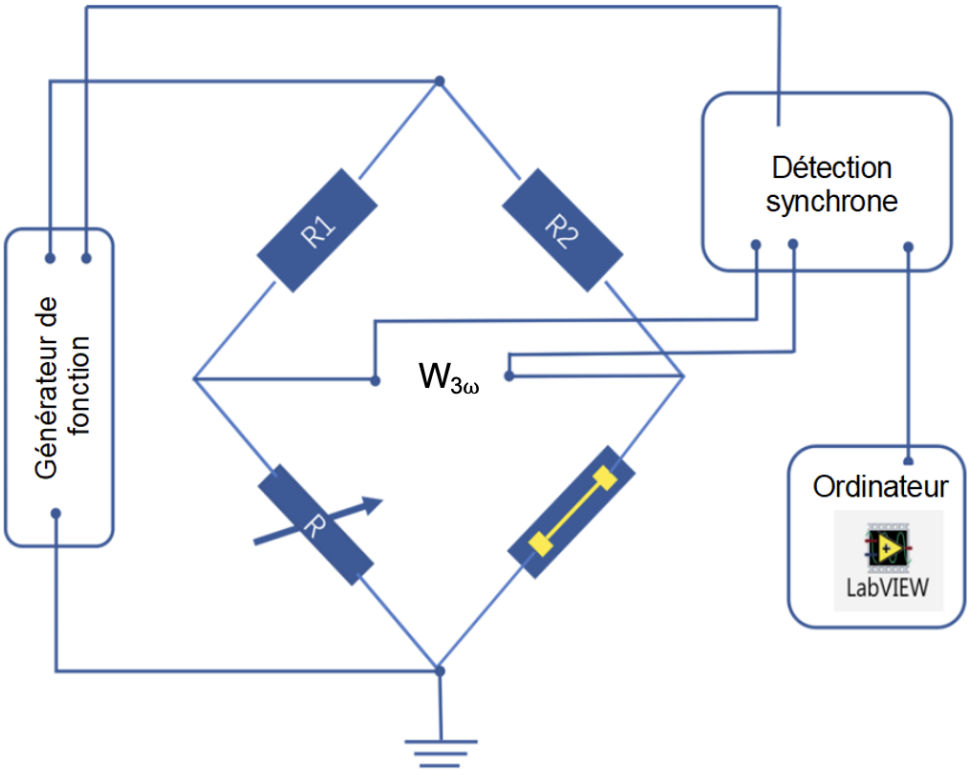


FIGURE 2 – Schéma du montage 3ω avec pont de Wheatstone et détection synchrone.

Détermination du coefficient de température β

Le coefficient de température de résistance (TCR) de la bande chauffante est déterminé par une mesure précise de sa résistance électrique en fonction de la température sous conditions d'équilibre

thermique contrôlé. L'échantillon est placé dans une chambre environnementale thermostatique équipée d'un capteur interne calibré, couvrant une large plage de températures. Il repose sur un support thermiquement conducteur afin d'assurer un bon équilibre thermique.

Un faible courant continu est injecté à travers les contacts externes de la structure quatre fils, tandis que la chute de tension aux bornes internes est mesurée, permettant une détermination précise de la résistance tout en minimisant l'auto-échauffement par effet Joule. Les mesures sont réalisées à l'aide d'un ohmmètre connecté à un Arduino, piloté par LabVIEW. La température est balayée par paliers successifs stabilisés, typiquement autour de la température ambiante, et en chaque point, la température de référence et la résistance sont enregistrées automatiquement.

Les données résistance–température sont ensuite ajustées par régression linéaire, la relation est supposée linéaire sur l'intervalle étudié. La pente dR/dT est extraite de l'ajustement, puis le TCR (β) est calculé à partir de la résistance de référence R_0.

Cette valeur de β, spécifique à chaque élément métallique est utilisée ultérieurement pour convertir la tension V_{3w} en élévation de température $T_{inphase}$ via la relation (1). Une attention particulière doit être portée à la linéarité de la résistance électrique $R(T)$ et à la stabilité thermique, afin de limiter les erreurs systématiques et de garantir la précision des propriétés thermiques qui en sont déduites.

.II.3 Modélisation thermique et stratégie d'analyse

Un modèle basé sur la Méthode des Éléments Finis (MEF) tridimensionnel a été construit dans le logiciel COMSOL Multiphysics® pour résoudre les équations de conduction thermique correspondant à la géométrie de notre échantillon. Bien que des solutions analytiques pour la méthode 3ω existent [17, 27], elles reposent souvent sur l'hypothèse simplificatrice que le substrat est significativement plus conducteur que le film mince ($\kappa_{\text{sub}} \gg \kappa_{\text{film}}$). Cette condition, qui permet de traiter le flux de chaleur dans le film comme une simple résistance thermique unidimensionnelle, n'est pas remplie dans notre système [23, 24, 25, 26]. Le substrat en silice fondue ($\kappa_{\text{sub}} \approx 1,3$ W/(m·K)) possède une conductivité thermique comparable, voire inférieure, à celle attendue pour des films diélectriques. Par conséquent, une approche numérique par éléments finis résolvant les équations complètes de conduction thermique dans les 3 dimensions est nécessaire pour une analyse précise [16, 28].

Notre analyse a suivi une procédure en plusieurs étapes. Dans un premier temps, un modèle multiparamétrique complet considérant les conductivités et capacités thermiques intrinsèques de chacune des couches Si_3N_4 (κ_{Si3N4}) et de SiO_2 (κ_{SiO2}) a été ajusté aux données simulées par ce même modèle. Cette approche s'est révélée particulièrement instable, les paramètres ajustés convergeant vers leurs limites prédéfinies, ou encore de multiples couples de paramètres donnant une même évolution du signal. Ces observations indiquent un problème inverse mal posé.

Pour diagnostiquer l'origine de cette instabilité, une analyse quantitative de sensibilité des paramètres a été réalisée. Le coefficient de sensibilité normalisé est défini comme :

$$S = \left| \frac{\Delta T / T_{\text{base}}}{\Delta p / p_{\text{base}}} \right|. \tag{2}$$

Ce coefficient a été calculé pour chaque paramètre thermique p [21], où $\Delta p / p_{\text{base}}$ représente une petite perturbation fixe appliquée à un paramètre d'entrée unique p (tel que la conductivité thermique d'une couche spécifique ou une résistance d'interface), et $\Delta T / T_{\text{base}}$ est la variation fractionnelle correspondante de l'oscillation de température du modèle. En essence, S quantifie l'influence d'une variation d'un paramètre d'entrée sur le résultat final : une valeur élevée de S indique une forte sensibilité. Pour justifier pleinement notre stratégie d'analyse, ces coefficients de sensibilité ont été calculés sur toute la plage de fréquences de mesure, comme montré à la fig.3. L'analyse révèle trois conclusions critiques : (1) la sensibilité à la conductivité thermique du substrat (k_{sub}) domine à basse fréquence (< 100 Hz) ; (2) la sensibilité aux conductivités effectives des couches minces devient le facteur dominant dans la gamme de fréquences moyenne à haute (> 100 Hz) ; (3) la sensibilité à la

résistance thermique d'interface (R_{TBR}) reste au moins un ordre de grandeur plus faible que les autres paramètres sur tout le spectre.

Cette analyse, dépendante de la fréquence, confirme visuellement que les basses fréquences sont idéales pour extraire les propriétés du substrat, tandis que la gamme de fréquences moyennes constitue la fenêtre optimale pour détecter l'effet des couches minces sur le signal . Le point de croisement observé à environ 1500 Hz, où la sensibilité aux couches minces dépasse celle du substrat, représente physiquement la fréquence à laquelle la profondeur de pénétration thermique devient comparable à l'épaisseur totale de l'empilement.

L'analyse finale a été réalisée selon une stratégie de « découplage » en deux étapes. Premièrement, la conductivité thermique du substrat en silice fondue (k_{sub}) a été déterminée en moyennant les valeurs obtenues à partir de la pente de la droite de la relation $T_{inphase}$ en fonction de $\ln(2\omega)$ dans la région des basses fréquences. Deuxièmement, cette valeur (k_{sub}), statistiquement robuste, a été utilisée comme paramètre d'entrée fixé dans la procédure d'optimisation par MEF. Des ajustements numériques ont ensuite été effectués sur les données expérimentales afin de caractériser thermiquement l'empilement de couches minces. En raison de la dégénérescence entre les paramètres thermiques de ces couches, une approche par milieu effectif est proposée. Elle sera décrite dans la partie suivante.

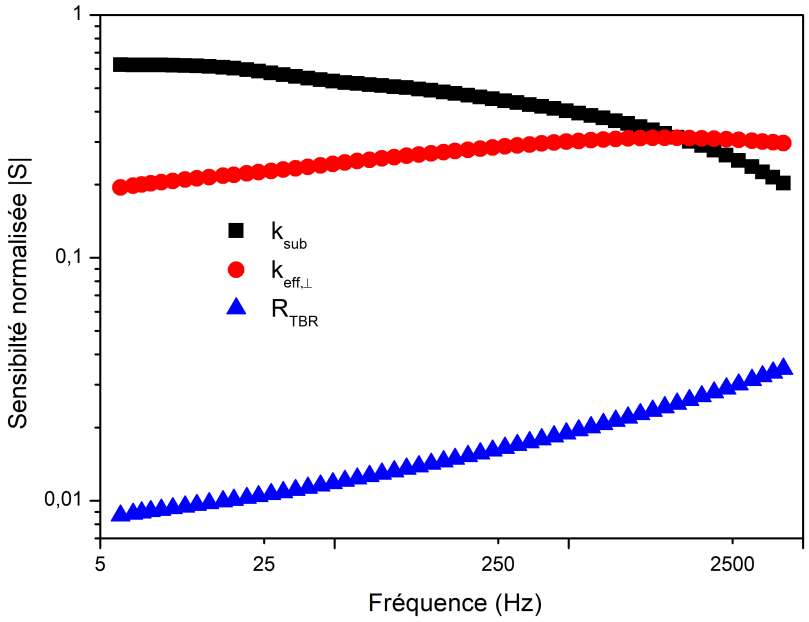


FIGURE 3 – Analyse de sensibilité des paramètres thermiques en fonction de la fréquence. Cette analyse a été réalisée autour des valeurs estimées des paramètres thermiques. Elle montre distinctement les régions où le signal est le plus sensible à la conductivité thermique du substrat et à la conductivité thermique effective de l'empilement de couches minces. L'influence de la résistance thermique d'interface R_{TBR} sur le signal est faible devant les autres paramètres.

.II.4 L'approximation du milieu effectif (EMA)

La simplification du problème : une étape nécessaire

L'analyse de sensibilité a conduit à une conclusion claire : l'ensemble des paramètres physiques caractérisant l'empilement ne peuvent pas être déterminés. Elle offre une opportunité : le signal de mesure est fortement sensible à la performance thermique globale de l'empilement de couches minces.

Cette observation mène directement à la méthodologie centrale de ce travail : l'approche du milieu effectif (*Effective Medium Approach*, EMA).

Le principe fondamental de l'approximation du milieu effectif (EMA) repose sur une simplification [14]. Étant donné que la bande passante expérimentale limite notre capacité à distinguer les contributions individuelles de chaque couche de l'empilement, l'ensemble de la structure complexe (dans notre cas, 5 couches minces et 6 interfaces) est assimilé à une seule couche homogène mathématiquement équivalente.

Cette couche équivalente conserve l'épaisseur totale réelle de l'empilement (dans notre cas, $d_{total} = 1288\,\text{nm}$), mais elle est caractérisée par des propriétés effectives qui homogénéisent l'hétérogénéité sous-jacente. La définition physique de ce milieu équivalent repose sur deux règles d'homogénéisation distinctes, sur la conductivité thermique et la chaleur spécifique, gouvernant respectivement les régimes stationnaire et transitoire. Celles-ci vont être décrites dans les deux paragraphes ci-après.

Conductivité thermique effective (modèle en série)

La conductivité thermique effective en direction transverse ($k_{eff,\perp}$) est définie à partir d'un modèle de résistances thermiques en série. Le flux thermique traversant successivement les différentes couches, l'impédance thermique totale de la couche équivalente est posée égale à la somme des résistances des couches et des interfaces de l'empilement :

$$k_{eff,\perp} = \frac{d_{total}}{\sum_i (d_i/k_i) + \sum_j R_{TBR,j}} \tag{3}$$

où d_i et k_i représentent respectivement l'épaisseur et la conductivité intrinsèque de la i-ième couche, et $R_{TBR,j}$ la résistance thermique d'interface (*Thermal Boundary Resistance*) associée à la j-ième interface. Ce paramètre correspond à une moyenne harmonique intégrant implicitement l'ensemble des résistances thermiques issues des différents processus physiques [17].

Capacité calorifique volumique effective (modèle parallèle)

Contrairement à la conductivité, la réponse thermique transitoire est gouvernée par la masse thermique du système. Afin de conserver strictement la capacité totale de stockage d'énergie thermique de l'empilement, la capacité calorifique volumique effective ($C_{v,eff} = \rho_{eff} c_{p,eff}$) est définie selon une règle de mélange linéaire (moyenne pondérée par le volume) :

$$(\rho c_p)_{eff} = \frac{\sum_i (\rho_i c_{p,i} d_i)}{d_{total}} \tag{4}$$

Cette formulation suit la règle classique des mélanges pour les matériaux composites, garantissant que la constante de temps thermique du milieu effectif reproduit fidèlement l'inertie thermique globale de la structure multicouche réelle [29].

Questions soulevées par l'EMA

L'adoption de l'EMA transforme ainsi un problème initial mal posé de type « n-corps », comportant plus de sept inconnues, en un problème robuste à « corps unique »ne comportant plus qu'une seule inconnue ($k_{eff,\perp}$), la capacité thermique étant fixée par une combinaison, selon une loi de mélange, des propriétés intrinsèques connues des matériaux pris individuellement.

Toutefois, bien que mathématiquement cohérente, cette approche soulève une question scientifique fondamentale : ce modèle simplifié unidimensionnel décrit-il fidèlement l'écoulement thermique tridimensionnel complexe observé dans la réalité physique, en particulier au voisinage des bords du chauffage ? En l'absence d'une validation rigoureuse fondée sur des données objectives, toute conclusion issue de ce modèle reposerait sur une hypothèse non démontrée. Il est donc indispensable de

procéder à une validation numérique approfondie avant d'appliquer l'EMA aux données expérimentales réelles. Cette validation sera entreprise dans la partie .III.3.

.III Résultats et Discussion

.III.1 Validation du banc de mesure

Afin de s'assurer du bon fonctionnement du dispositif et avant de caractériser l'échantillon à bases de 5 couches, des mesures ont été réalisées sur des matériaux épais aux paramètres thermiques connus en vue de valider le banc de mesure. D'abord un verre boroscilicate puis de la silice fondue ont été étudiés.

Verre de borosilicate

Un balayage en fréquence 3ω a été réalisé sur les échantillons de borosilicate ($BrSiO_2$) préalablement calibrés en TCR. Une tension $V_{1\omega}$ a été appliquée à l'élément chauffant, et la composante réelle du troisième harmonique de la tension $V_{3\omega,\text{in-phase}}$ est enregistrée en fonction de la fréquence. Cette tension est ensuite convertie en élévation de température $\Delta T_{\text{in-phase}}$ à l'aide de l'équation 1.

La plage de fréquences appropriée à la caractérisation du matériau sous forme massive $BrSiO_2$ d'épaisseur 1 mm a été calculée à partir de la conductivité thermique de la littérature du matériau selon les différentes géométries d'éléments chauffant rencontrés. La figure 4 montre l'évolution des composantes réelle et imaginaire de la température en fonction de $\ln(2\omega)$ pour un des essais dont les conditions sont données au tableau 3.

L'ajustement numérique de la partie réelle selon une droite permet d'obtenir le coefficient directeur dont la valeur est reliée à la conductivité thermique du matériau sous forme massive selon la relation suivante valide pour une source de chaleur linéaire infiniment longue [25, 26] :

$$k_{\text{sub}} = \frac{P}{2\pi l \cdot B}, \tag{5}$$

où $P = V_{1\omega}^2/(R_0 \cdot l)$ est la puissance électrique par unité de longueur, l la longueur de la bande métallique, et B, la pente, obtenue par l'ajustement linéaire de l'évolution de $T_{inphase}$ en fonction de $\ln(2\omega)$.

R (Ω)	l (mm)	TCR ($°C^{-1}$)	V_ω (V)	Pente (K/m)	κ (W/m K)	Erreur (vs littérature)
25,78	3,6	0,00269	0,1066	-2.6700×10^{-6}	1,016	-10,09%

Table 3 – Conditions expérimentales de l'essai de la figure 4 et valeur de la conductivité thermique du borosilicate qui en est déterminée.

À partir de la pente de la partie réelle de la température de la figure 4, une conductivité thermique κ=1,016 W/m.K a ainsi pu être déterminée. Sur les 2 échantillons étudiés, c'est au total 14 capteurs résistifs 3ω qui ont pu être mis à profit. Sur ces 14 capteurs étudiés, une valeur de conductivité thermique moyenne $k = 1,19 \pm 0,08$ W/m.K est obtenue dont l'intervalle de confiance à 95% est située dans la valeur fournie par la littérature du $BrSiO_2$ (k_{litt}=1,13 W/m.K) [30].

Verre de silice

La même procédure a été appliquée à un matériau en silice fondue épais de 150 µm d'épaisseur, pour différentes géométries du capteur 3ω. La figure 5 montre un des essais effectués. Les paramètres

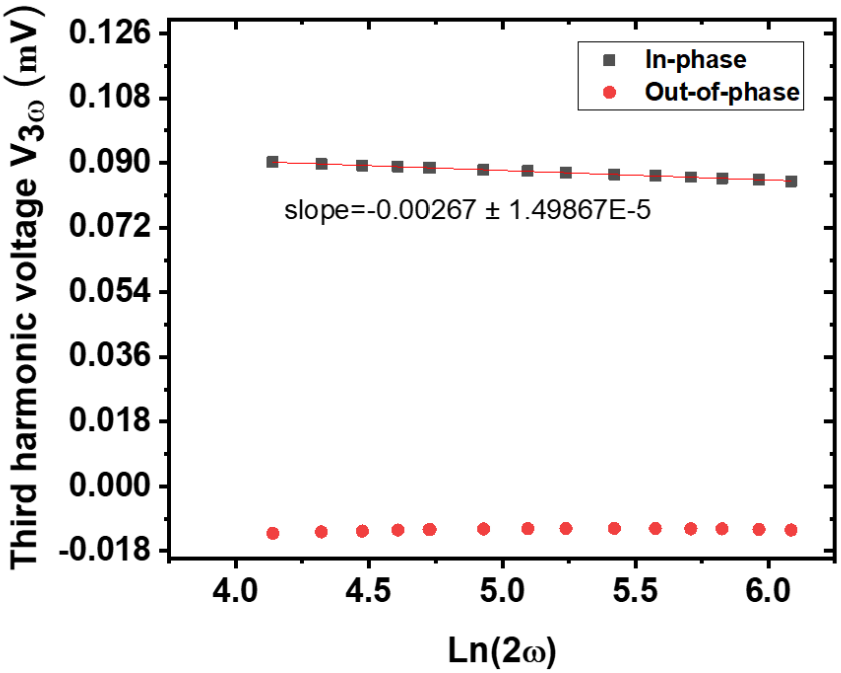


FIGURE 4 – Évolution des parties réelle et imaginaire de la tension $V_{3\omega}$ en fonction de $\ln(2\omega)$ pour un verre de borosilicate. Un ajustement via une droite est effectuée sur la partie réelle. La valeur de la pente permet de calculer via l'application successive des relations 1 et 5 la conductivité thermique du matériau sous forme massive.

physiques associés aux deux lignes utilisées et les valeurs de conductivités thermiques mesurées sont données au tableau 4. La conductivité thermique moyenne mesurée est de $k_{\text{silice fondue}} = 1,41 \pm 0,01$ W/(m K). Cette valeur est en excellent accord (à 2,2 % près) avec la valeur de référence de la littérature, ≈ 1.38 W/(m K) [23], ce qui constitue une seconde confirmation solide du bon fonctionnement de notre banc de mesure.

Ligne	R (Ω)	L (mm)	TCR ($°C^{-1}$)	$V_{1\omega}$ (V)	Pente (B) (K/m)	κ (W/m K)
1	55,42	5	0,00249	0,436	-4.220×10^{-5}	1,409 ± 0,015
2	24,89	3	0,00258	0,305	-5.490×10^{-5}	1,414 ± 0,008

TABLE 4 – Conditions expérimentales des essais réalisés avec le verre de silice5 et valeurs de la conductivité thermique du borosilicate qui en sont déterminées.

.III.2 Conductivité thermique du substrat de l'empilement

Comme expliqué dans la partie .II.3, dans une première étape, la conductivité thermique du substrat en silice fondue (k_{sub}), à la base de l'empilement a été déterminée à partir de la plage basse fréquence (71 Hz–266 Hz) des données issues des expériences 3ω, où la température de surface est principalement dominée par l'influence du substrat. La relation 5 a alors été utilisée pour ce calcul. Tous les éléments chauffant de l'échantillon ont une longueur l=3 mm. Les autres valeurs des paramètres entrant dans la définition de la puissance électrique dissipée P sont rapportées au tableau 5.

Les mesures sur les deux bandes métalliques sélectionnées ont donné des résultats très cohérents (fig. 6 et tableau 5). En moyennant ces valeurs, on obtient une conductivité thermique avec son intervalle de confiance de $k_{\text{sub}} = 1,287 \pm 0,030$ W/(m·K), l'incertitude étant l'écart-type entre les

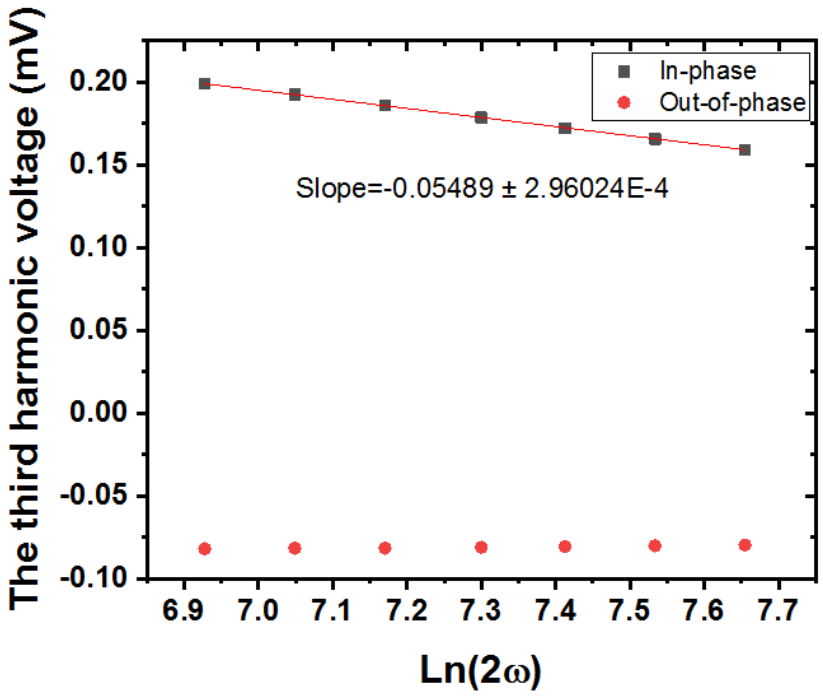


FIGURE 5 – Évolution des parties réelle et imaginaire de la tension $V_{3\omega}$ en fonction de $\ln(2\omega)$ pour un verre de silice. Un ajustement via une droite est effectuée sur la partie réelle. La valeur de la pente permet de calculer via l'application successive des relations 1 et 5 la conductivité thermique du matériau sous forme massive.

deux mesures. Cette valeur a été utilisée comme paramètre fixe pour toutes les analyses ultérieures.

Largeur de la bande	$V_{1\omega}$ (mV)	R_0 (Ω)	k_{sub} ajusté (W/(m·K))
6 μm	256	32,82	1,266 ± 0,017
8 μm	234	25,25	1,308 ± 0,025
Moyenne			1,287 ± 0,030

TABLE 5 – Valeurs de la tension appliquée $V_{1\omega}$ et de la résistance ohmique de la bande chauffante R_0 selon la largeur de l'élément chauffant. Les conductivités thermiques du substrat respectives déterminées par ajustement numérique sont également données.

.III.3 Validation numérique de l'approximation du milieu effectif

Avant d'appliquer le modèle de l'approximation du milieu effectif aux données expérimentales, une validation numérique a été réalisée pour vérifier sa robustesse et sa capacité à extraire correctement la conductivité thermique effective d'un empilement de couches minces.

Des « échantillons virtuels »ont été créés par la MEF avec une géométrie à 5 couches et six résistances thermiques d'interface. Chaque couche possède ses propriétés thermiques intrinsèques issues de la base de données de COMSOL : $k_{\mathrm{Si3N4}} = 2,5$ W/(m·K), $k_{\mathrm{SiO2}} = 1,3$ W/(m·K), et $R_{\mathrm{TBR,Si3N4/SiO2}} = 5,0 \times 10^{-9}$ m^{2}K/W. La conductivité thermique effective théorique de l'empilement est calculée $k_{\mathrm{eff,vraie}} \approx 1,45$ W/(m·K) (modèle en série).

Ce modèle complet a généré des données « expérimentales »sans bruit pour $T_{inphase}$ sur toute la plage de fréquences en pratique accessible. L'ajustement de ces données a ensuite été réalisé

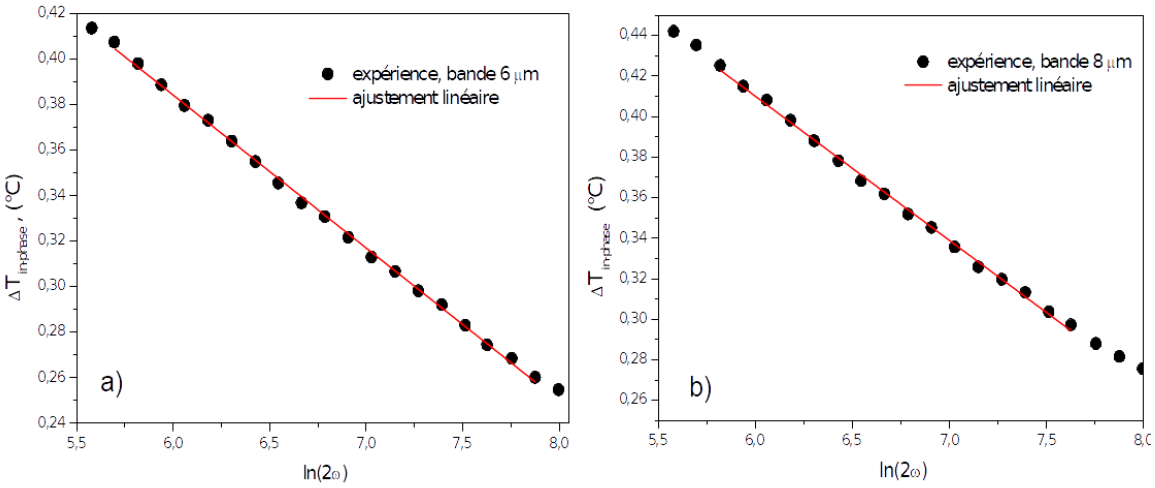


FIGURE 6 – Évolution de la partie réelle de la température $T_{inphase}$ en fonction de $\ln(2\omega)$ pour les deux bandes chauffantes considérées, de a) 6 et b) 8 μm de largeur. Le trait continu représente l'ajustement numérique via une droite dans les « basses fréquences ».

avec l'approche du milieu effectif à une seule couche, dans la fenêtre de fréquences sensibles au film (266–898 Hz). L'ajustement a permis de déterminer une conductivité effective $k_{\text{eff,extrait}} \approx 2.07$ W/(m·K) (fig. 7).

Ce résultat permet de situer :

1. les limites sur la validité et la précision de l'approximation du milieu effectif pour ce type de matériau ;
2. l'importance du flux de chaleur dans les 3 dimensions. En effet, la valeur de la conductivité thermique estimée par l'ajustement d'un modèle à 1 couche équivalente est bien supérieure à la prédiction par transfert thermique purement unidirectionnel (1,45 W/(m·K)) en raison de la dissipation latérale dans les couches Si_3N_4 plus conductrices.

.III.4 Applicabilité générale et limites de l'approche du milieu effectif

Pour évaluer l'applicabilité de l'approche du milieu effectif, une bibliothèque de signaux 3ω issus de la simulation du champ de température au sein de 11 échantillons virtuels avec des propriétés thermiques variées a été construite. Les signaux simulés désignés par les lettres allant de A à K ont pour paramètres physiques d'entrée les valeurs reportées dans le tableau 6.

La conductivité thermique équivalente $k_{eff}(3D)$ a été obtenue par ajustement numérique des signaux simulés à l'aide du modèle de la couche effective équivalente. Les résultats sont présentés dans le tableau 7.

La tendance observée est la suivante : la valeur ajustée de la conductivité thermique effective est systématiquement supérieure à la prédiction issue d'un modèle purement unidimensionnel (1D), ce qui reflète l'effet de la dissipation thermique latérale supplémentaire. Cette dissipation latérale permet une évacuation plus efficace de la chaleur, conduisant à une température de surface plus faible que celle attendue dans un régime strictement unidimensionnel. Tout se passe alors comme si la chaleur se propageait plus facilement, ce qui se traduit par une conductivité thermique apparente plus élevée pour l'empilement multicouche.

Pour les films dont la conductivité thermique est comparable ou inférieure à celle du substrat (échantillons A, B, C et E), la différence entre les approches 3D et 1D reste modérée, typiquement

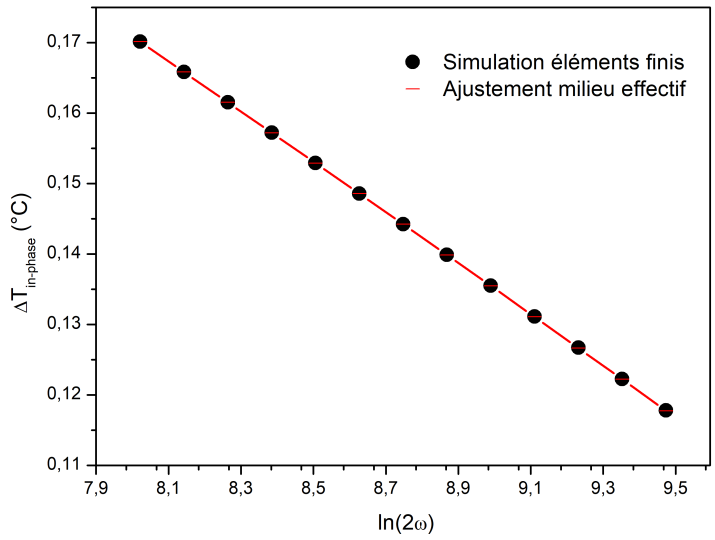


FIGURE 7 – Ajustement par l'approche du milieu effectif des données virtuelles générées concernant le cas A par la méthode des éléments finis.

Échantillon	$k_{Si_3N_4}$ (W/m·K) k_{Sub} (W/m·K)	k_{SiO_2} (W/m·K)	R_{TBR} (m^2·K/W)	
A	2,5	1,3	5,0e-9	1.287
B	2,5	1,3	1,0e-9	1.287
C	2,5	1,3	1,0e-8	1.287
D	10,0	1,3	5,0e-9	1.287
E	0,5	1,3	5,0e-9	1.287
F	2,5	10,0	5,0e-9	1.287
G	10,0	10,0	5,0e-9	1.287
H	2,5	1,3	1,0e-7	1.287
I	0,5	0,5	1,0e-7	1.287
J	0,5	0,5	1,0e-7	10
K	0,5	0,5	1,0e-7	1.287

TABLE 6 – Paramètres thermiques utilisés pour simuler les signaux virtuels (échantillons A-K) par la méthode des éléments finis. Le cas A concerne le système étudié avec ses paramètres thermiques estimés.

comprise entre +35% et +50%. Ce régime correspond à une diffusion thermique tridimensionnelle classique (fig. 8a), dans laquelle le flux thermique est majoritairement dirigé vers le substrat, tandis que la dissipation latérale reste secondaire. Dans ces conditions, l'approche par milieu effectif demeure à la fois numériquement robuste et physiquement pertinente.

En revanche, pour les structures contenant des couches fortement conductrices (échantillons D, F et G), la différence entre les résultats 3D et 1D devient nettement plus importante, atteignant jusqu'à +113%. Cette augmentation traduit un changement de régime de transport thermique, caractérisé par une propagation latérale dominante de type quasi bidimensionnel (fig. 8b). Dans cette situation, la chaleur se répartit largement dans le plan avant de pénétrer dans le substrat, ce qui remet en question l'interprétation d'une conductivité thermique effective strictement verticale.

En présence de résistances thermiques interfaciales élevées (échantillons H et K), un second régime

Échantillon virtuel	$k_{eff}(1D)$ théorique ($W.m^{-1}.K^{-1}$)	$k_{eff}(3D)$ ajusté ($W.m^{-1}.K^{-1}$)	Erreur %
A	1,45	1.996	+37.7
B	1,49	2,09	+40.3
C	1,41	2.05	+45.4
D	1,65	3,52	+113,3
E	0.89	1,32	+48.3
F	4.97	8.16	+64.2
G	8.38	10.47	+24.9
H	1.02	1.70	+66.7
I	0.43	0,61	+41.9
J	0.43	0,55	+27.9
K	0.0303	0,0497	+64.0

TABLE 7 – Résultats des ajustements numériques effectués à l'aide du modèle du milieu effectif pour les signaux générés selon les paramètres du tableau 6.

limite apparaît. La forte résistance aux interfaces freine la propagation thermique en profondeur et confine l'énergie thermique dans les couches supérieures du système. Ce confinement entraîne une élévation de la température locale et favorise le développement de gradients thermiques latéraux près du transducteur. Le modèle 3D prédit alors toujours une conductivité effective plus élevée que le modèle 1D, non pas en raison d'un transport vertical amélioré, mais du fait d'une redistribution latérale accrue de la chaleur.

Le cas de l'échantillon J apporte un éclairage complémentaire. Bien que la conductivité du substrat y soit significativement augmentée, la différence entre les modèles 3D et 1D reste modérée (+27.9%) et du même ordre de grandeur que pour les autres systèmes à faible conductivité. Ce résultat montre clairement que l'augmentation de la conductivité du substrat n'entraîne pas nécessairement une domination du transport thermique par celui-ci, dans les conditions de mesure considérées. La réponse thermique reste principalement gouvernée par la résistance globale du système multicouche et des interfaces, tandis que l'effet du substrat apparaît comme une correction secondaire.

Ainsi, l'approche par milieu effectif fournit un résultat physiquement significatif tant que la différence entre les modèles 3D et 1D reste modérée et que le transport thermique demeure principalement vertical. Plus généralement, la méthodologie est robuste tant que le système ne bascule pas vers un régime dominé par un mécanisme unique, qu'il s'agisse d'une diffusion latérale importante (échantillons D–F–G) ou de résistance(s) interfaciale(s) dominante(s) (échantillons H–K). Dans ces conditions, la conductivité thermique effective extraite conserve une signification physique en tant que paramètre homogénéisé décrivant la réponse thermique globale du système, ce qui correspond précisément au cas de notre échantillon expérimental.

.III.5 Conductivité thermique effective de l'empilement de couches minces

En utilisant la valeur de k_{sub} précédemment déterminée, combinée à l'approche du milieu effectif, deux ajustements indépendants ont été effectués pour extraire k_{eff} à partir des données recueillies lors des essais effectués sur les deux éléments chauffant de 6 et 8 μm. La plage de fréquence « idéale »(266–793 Hz) a été utilisée, conformément à l'analyse de sensibilité (fig. 3). Les ajustements montrent un excellent accord avec les données expérimentales (fig. 9). Les résultats sont cohérents entre les deux dispositifs (tableau 3), donnant une conductivité effective de la couche

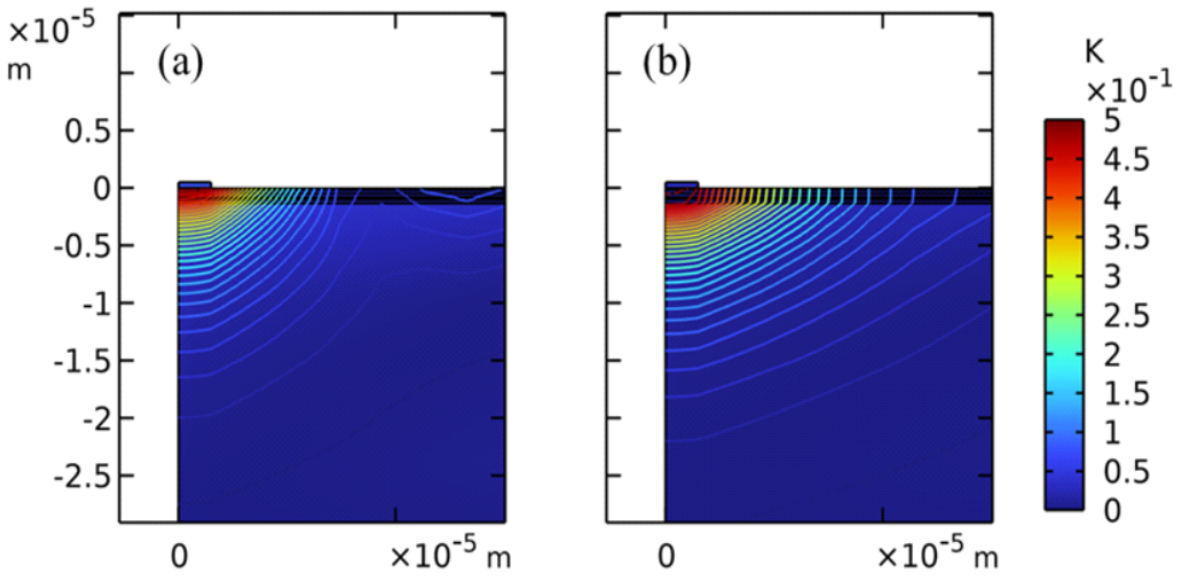


FIGURE 8 – Profil de température dans un système avec 1 couche déposée sur un substrat. La bande chauffante est épaisse de 500 nm, la longueur 3 mm et la largeur 3 μm. Elle est traversée par un courant sinusoïdal de 100 mA à une fréquence de 266,9 Hz. a) La conductivité thermique effective de la couche est similaire à celle du substrat, $k_{eff} \approx k_{sub}$. Le flux de température se réparti sous la forme d'une goutte. b) La conductivité thermique de la couche est largement supérieure à celle du substrat ($k_{eff} > k_{sub}$), avec ici k_{eff}=20 W.m^{-1}.K^{-1} . Le flux de chaleur est essentiellement latéral, conduisant à une distribution de température plus aplatie.

$k_{\text{eff}} = 0,62 \pm 0,03$ W/(m·K).

TABLE 8 – Détermination de la conductivité thermique effective transverse ($k_{\text{eff},\perp}$) à partir de l'approche du milieu effectif. Les incertitudes correspondent aux intervalles de confiance à 95% issus de la procédure d'ajustement.

Largeur de l'élément chauffant (µm)	$k_{\text{eff},\perp}$ mesurée (W m^{-1} K^{-1})	Intervalle de confiance à 95%
6	0,624	±0, 027
8	0,615	±0, 030
Moyenne	**0,62**	±0, 03

.III.6 Discussion et comparaison avec les modèles théoriques

La valeur expérimentale $k_{\text{eff}} = 0,62$ W/(m·K) est nettement inférieure à la prédiction théorique (1,45 W/(m·K)), démontrant que les films PECVD réels diffèrent des prédictions sur des films idéalisés où seuls les paramètres thermiques de la littérature des constituants seraient pris en compte. Cette différence peut résulter des mécanismes de diffusion phononique et des non-idéalités du procédé (stœchiométrie non parfaite, microstructure amorphe, défauts d'interface) [13, 18, 31].

La valeur expérimentale étant inférieure à k_{eff} confirme que notre échantillon est dans le régime $k_{\text{film}} < k_{\text{sub}}$, où l'approche du milieu effectif est rigoureusement applicable, renforçant la confiance dans nos résultats.

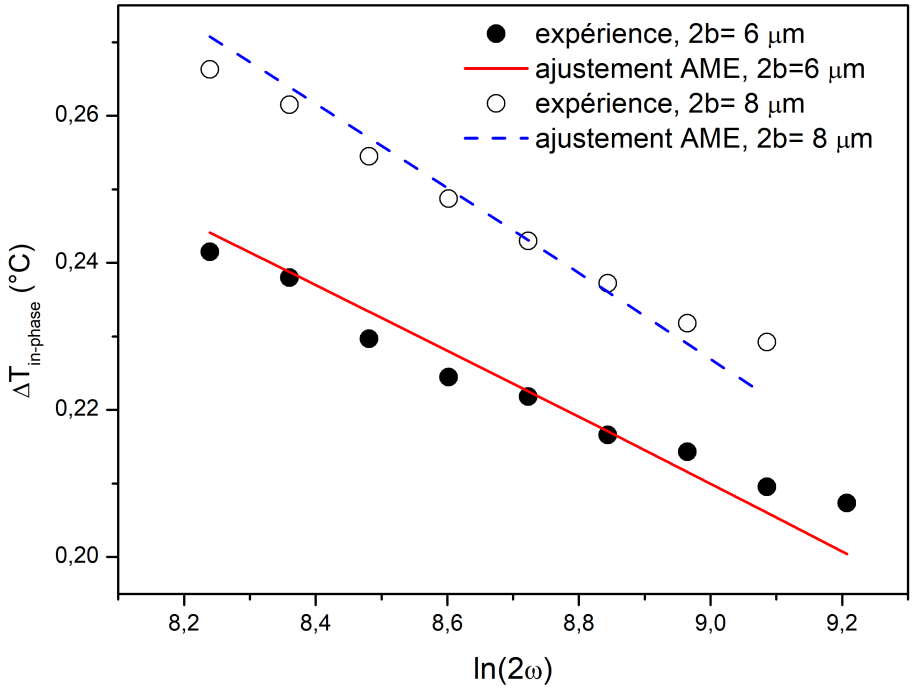


FIGURE 9 – Évolution expérimentale de la partie réelle de la température en fonction de $\ln(2\omega)$ pour deux bandes chauffantes : l'une de 6 μm (R_0=32,82 Ω) et l'autre de 8 μm de largeur (R_0=25,25 Ω). Les traits représentent les ajustements numériques par l'approche du milieu effectif (AME).

Conclusion générale

Cette thèse s'est attachée à relever un défi majeur de la microélectronique contemporaine : la caractérisation thermique précise de films diélectriques multicouches complexes. Dans un contexte de miniaturisation continue des dispositifs électroniques et photoniques, le contrôle du transfert thermique constitue désormais un verrou critique en termes de performance et de fiabilité. Les matériaux isolants tels que le dioxyde de silicium et le nitrure de silicium, indispensables à l'isolation électrique, représentent simultanément des barrières thermiques significatives. Lorsqu'ils sont intégrés sous forme d'empilements nanométriques, leurs propriétés diffèrent sensiblement de celles des matériaux massifs, rendant leur caractérisation thermique particulièrement délicate.

Contributions majeures

Le principal apport de ce travail réside dans le développement d'un cadre méthodologique hybride couplant la technique expérimentale 3ω à un modèle numérique fondé sur la méthode des éléments finis (FEM). Cette approche permet de dépasser les limitations des modèles analytiques traditionnels, qui peinent à décrire fidèlement l'écoulement thermique dans des structures multicouches hétérogènes. Le modèle FEM agit comme un véritable « jumeau numérique » de l'expérience, reproduisant la géométrie réelle du chauffage ainsi que la stratification détaillée de l'échantillon.

Une contribution méthodologique déterminante concerne l'analyse critique du problème inverse de conduction thermique appliqué aux empilements diélectriques. L'étude de sensibilité fréquentielle a mis en évidence le caractère mal posé de l'extraction simultanée des conductivités intrinsèques des couches et des résistances thermiques d'interface (TBR). Face à cette corrélation paramétrique, une approche fondée sur le milieu effectif (EMA) a été adoptée et validée numériquement. Cette stratégie

permet de transformer un problème multi-paramétrique à solution non unique en une détermination robuste de la conductivité thermique effective transverse.

Sur le plan scientifique, l'application de ce cadre validé à un empilement Si_3N_4/SiO_2 à cinq couches a permis de quantifier expérimentalement sa conductivité thermique effective k_{eff}. La conductivité thermique du substrat en silice fondue a été déterminée à $k_{\text{sub}} = 1,287 \pm 0,03$ W/(m·K). La conductivité thermique effective globale perpendiculaire au plan de l'empilement des couches diélectriques d'épaisseur totale 1288 nm a été déterminée à $k_{\text{eff}} = 0,62 \pm 0,03$ W/(m·K), résultat validé par la cohérence observée entre plusieurs dispositifs indépendants. L'écart significatif de cette valeur par rapport aux estimations théoriques met en évidence le rôle prépondérant de la microstructure dépendante du procédé dans la détermination des propriétés thermiques des films PECVD.

Les résultats montrent une réduction significative par rapport aux valeurs massives des matériaux constitutifs, attribuable à l'accumulation des phénomènes de diffusion phononique aux interfaces internes de l'échantillon. Ces résultats fournissent des données essentielles pour la modélisation thermique des circuits intégrés et démontrent que l'utilisation de valeurs massives ou monocouches conduit à une sous-estimation potentiellement critique des températures de fonctionnement.

En conclusion, cette thèse a permis de développer et de valider un outil robuste de métrologie thermique à l'échelle nanométrique. Elle apporte une contribution méthodologique ainsi que des résultats scientifiques quantitatifs sur le comportement thermique des empilements diélectriques multicouches. Elle établit ainsi une base solide pour de futures recherches en transport thermique à l'échelle nanométrique.

Limites de l'étude

Certaines limites doivent toutefois être soulignées. Le modèle numérique repose sur une approximation bidimensionnelle, négligeant certains effets tridimensionnels aux extrémités des lignes de chauffage. La méthodologie actuelle ne permet pas de déconvoluer individuellement les résistances thermiques d'interface, la conductivité extraite constituant un paramètre effectif global. Les matériaux ont été supposés isotropes, hypothèse raisonnable mais susceptible d'être discutée selon les procédés de dépôt. Enfin, les mesures ont été réalisées à température ambiante uniquement, alors que les propriétés thermiques présentent une dépendance intrinsèque à la température.

Perspectives

Plusieurs perspectives prometteuses découlent de ce travail. L'extension de la méthodologie à d'autres systèmes technologiques critiques, tels que les diélectriques « faible-k », les matériaux à changement de phase ou les revêtements pour barrières thermiques, constitue une voie immédiate. Des mesures dépendantes de la température permettraient d'approfondir la compréhension des mécanismes de transport phononique. Enfin, l'extension du cadre expérimental-numérique à l'étude de conductivités thermiques anisotropes représenterait une avancée méthodologique significative.

Références du résumé

[1] H. Angus MacLeod. *Thin-Film Optical Filters*. 4e éd. Boca Raton : CRC Press, 2010. ISBN : 9781420073034. DOI : 10.1201/9781420073034.

[2] M. Morgen et al. « Low Dielectric Constant Materials for ULSI Interconnects ». In : *Annual Review of Materials Science* 30 (2000), p. 645-680. DOI : 10.1146/annurev.matsci.30.1.645.

[3] A. Grill. « Progress in the Development and Understanding of Advanced Low-k and Ultralow-k Dielectrics for Very Large-Scale Integrated Interconnects : State of the Art ». In : *Applied Physics Reviews* 1.1 (2014), p. 011306. DOI : 10.1063/1.4861876.

[4] Stephen D. Senturia. *Microsystem Design*. 1re éd. Springer Book Archive. Springer New York, NY, 2001. 715 p. ISBN : 978-0-7923-7246-2. DOI : 10.1007/b117574. URL : https://doi.org/10.1007/b117574.

[5] Marc J. Madou. *Fundamentals of Microfabrication and Nanotechnology*. 3rd. CRC Press, 2011.

[6] Kenichi Iga. « Surface-Emitting Laser : Its Birth and Generation of New Optoelectronics Field ». In : *IEEE Journal of Selected Topics in Quantum Electronics* 6.6 (2000), p. 1201-1215. DOI : 10.1109/2944.902168.

[7] Rainer Michalzik, éd. *VCSELs : Fundamentals, Technology and Applications of Vertical-Cavity Surface-Emitting Lasers*. T. 166. Springer Series in Optical Sciences. Berlin, Heidelberg : Springer, 2013. ISBN : 9783642249853. DOI : 10.1007/978-3-642-24986-0.

[8] Gordon E. Moore. « Cramming More Components Onto Integrated Circuits ». In : *IEEE Solid-State Circuits Society Newsletter* 11.3 (2006). Reprinted from Electronics, vol. 38, no. 8, Apr. 19, 1965, p. 33-35. DOI : 10.1109/N-SSC.2006.4785860.

[9] Eric Pop. « Energy dissipation and transport in nanoscale devices ». In : *Nano Research* 3.2 (2010), p. 147-169. DOI : 10.1007/s12274-010-1019-z.

[10] David G. Cahill et al. « Nanoscale thermal transport. II. 2003–2012 ». In : *Applied Physics Reviews* 1.1 (2014), p. 011305. DOI : 10.1063/1.4832615.

[11] Arun Majumdar. « Microscale Heat Conduction in Dielectric Thin Films ». In : *Journal of Heat Transfer* 115.1 (fév. 1993), p. 7-16. DOI : 10.1115/1.2910673.

[12] Gang Chen. *Nanoscale Energy Transport and Conversion : A Parallel Treatment of Electrons, Molecules, Phonons, and Photons*. Online edition, Oxford Academic, 31 Oct. 2023. New York, NY, USA : Oxford University Press, 2005. ISBN : 9780195159424. DOI : 10.1093/oso/9780195159424.001.0001.

[13] David G. Cahill et al. « Nanoscale thermal transport ». In : *Journal of Applied Physics* 93.2 (2003), p. 793-818. DOI : 10.1063/1.1524305.

[14] G. Chen. « Thermal conductivity and ballistic-phonon transport in the cross-plane direction of superlattices ». In : *Physical Review B* 57.23 (juin 1998), p. 14958-14973. DOI : 10.1103/PhysRevB.57.14958.

[15] Yongho Sungtaek Ju et Kenneth E. Goodson. « Phonon scattering in silicon films with thickness of order 100 nm ». In : *Applied Physics Letters* 74.20 (1999), p. 3005-3007. DOI : 10.1063/1.123994. URL : https://doi.org/10.1063/1.123994.

[16] Jung Hun Kim, Albert Feldman et Donald Novotny. « Application of the three omega thermal conductivity measurement method to a film on a substrate of finite thickness ». In : *Journal of Applied Physics* 86.7 (oct. 1999), p. 3959-3963. DOI : 10.1063/1.371314.

[17] E. T. Swartz et R. O. Pohl. « Thermal boundary resistance ». In : *Reviews of Modern Physics* 61.3 (juill. 1989), p. 605-668. doi : 10.1103/RevModPhys.61.605.

[18] Patrick E. Hopkins. « Thermal Transport across Solid Interfaces with Nanoscale Imperfections : Effects of Roughness, Disorder, Dislocations, and Bonding on Thermal Boundary Conductance ». In : *International Scholarly Research Notices* 2013 (2013), p. 682586. doi : 10.1155/2013/682586.

[19] S.-M. Lee et David G. Cahill. « Heat transport in thin dielectric films ». In : *Journal of Applied Physics* 81.6 (mars 1997), p. 2590-2595. doi : 10.1063/1.363923.

[20] L. Griffin et al. « Phonon scattering in amorphous solids and at interfaces ». In : *Physical Review B* 83 (2011), p. 195414.

[21] James V. Beck et Kenneth J. Arnold. *Parameter Estimation in Engineering and Science*. New York, NY : John Wiley & Sons, 1977. isbn : 9780471061854.

[22] Tao Tong et Arun Majumdar. « Reexamining the 3-omega technique for thin film thermal characterization ». In : *Review of Scientific Instruments* 77.10 (oct. 2006), p. 104902. doi : 10.1063/1.2349601.

[23] David G. Cahill. « Thermal conductivity measurement from 30 to 750 K : the 3ω method ». In : *Review of Scientific Instruments* 61.2 (fév. 1990), p. 802-808. doi : 10.1063/1.1141498.

[24] Chris Dames. « Measuring the Thermal Conductivity of Thin Films : 3ω and Related Electrothermal Methods ». In : *Annual Review of Heat Transfer*. T. 16. Begell House, 2013, p. 7-49. doi : 10.1615/AnnualRevHeatTransfer.v16.20.

[25] N. Al-Khudary et al. « Inkjet printing technology for polymer thermal conductivity measurement by the three omega method ». In : *Polymer Testing* 40 (2014), p. 187-195. issn : 0142-9418. doi : 10.1016/j.polymertesting.2014.09.008.

[26] A. A. Guermoudi, P. Y. Cresson, A. Ouldabbes et al. « Thermal conductivity and interfacial effect of parylene C thin film using the 3-omega method ». In : *Journal of Thermal Analysis and Calorimetry* 145 (2021), p. 1-12. doi : 10.1007/s10973-020-09612-z.

[27] T. Borca-Tasciuc, A. R. Kumar et G. Chen. « Data reduction in 3ω method for thin-film thermal conductivity determination ». In : *Review of Scientific Instruments* 72.4 (avr. 2001), p. 2139-2147. doi : 10.1063/1.1353189.

[28] National Research Council. *The Future of Computing Performance : Game Over or Next Level ?* Sous la dir. de Samuel H. Fuller et Lynette I. Millett. Includes data adapted from M. Horowitz et al. Washington, DC : The National Academies Press, 2011. isbn : 978-0-309-15951-7. doi : 10.17226/12980. url : https://www.nap.edu/catalog/12980/the-future-of-computing-performance-game-over-or-next-level.

[29] H. S. Carslaw et J. C. Jaeger. *Conduction of Heat in Solids*. 2nd. Oxford University Press, 1959.

[30] Jörg Schröder et Paulo Pimenta, éd. *Novel Finite Element Technologies for Solids and Structures*. T. 91. Lecture Notes in Applied and Computational Mechanics. Cham, Switzerland : Springer Nature, 2020. isbn : 978-3-030-33519-9. doi : 10.1007/978-3-030-33520-5.

[31] W. A. P. Claassen et al. « Characterization of Plasma Silicon Nitride Layers ». In : *Journal of The Electrochemical Society* 130.12 (déc. 1983), p. 2419-2425. doi : 10.1149/1.2119600. url : https://doi.org/10.1149/1.2119600.

General Introduction

Thermal management has become a major challenge in modern microelectronic, optoelectronic, and power electronic devices. Over the past decades, device dimensions have continuously decreased, while the number of components integrated in a given area has increased. This evolution has improved electrical performance, but it has also increased local power density and made heat dissipation more difficult. As a result, thermal effects now directly influence device performance, reliability, and lifetime.

In many electronic systems, heat is no longer only a packaging issue considered at the end of device design. It must be considered together with electrical performance, material selection, and device architecture. This has led to the development of electro-thermal or thermo-electric co-design approaches, where heat generation and heat dissipation are treated as central design constraints [1, 2].

The importance of thermal management can be observed in several technological fields. In silicon-based integrated circuits, excessive heat generation limits clock frequency, increases leakage current, and can force processors to reduce their operating speed in order to avoid overheating [3, 4]. In data centers, the energy required for cooling represents an important part of the total energy consumption, making heat dissipation a major issue for both performance and energy efficiency [5].

The thermal challenge is also important in high-power radio-frequency devices based on gallium nitride (GaN). In GaN high-electron-mobility transistors, high local power densities can produce strong self-heating and localized hot spots. Channel temperatures can exceed 250 °C, which accelerates degradation and reduces device lifetime [6]. Heat can contribute to current collapse, reduced carrier mobility, contact degradation, metal diffusion, and thermomechanical stress in the surrounding layers and packaging materials [7, 8]. In these devices, the thermal properties of the active material, the substrate, and the surrounding dielectric layers are all important for predicting and improving reliability.

Dielectric thin films such as SiO_2 and SiN_x are widely used in electronic devices as passivation, insulation, or barrier layers. Although they play an essential electrical role, they can also limit heat dissipation because their thermal conductivity is generally much lower than that of semiconductors or metals. At the nanoscale, their thermal properties can differ from bulk values due to phonon boundary scattering, defects, non-ideal microstructure, and thermal boundary resistance at interfaces. These effects become especially important in multilayer systems, where several thin films and interfaces contribute together to the measured thermal response.

For this reason, the accurate characterization of thermal transport in dielectric thin films and multilayer stacks is essential. However, this characterization is difficult because the measured signal is usually influenced by several coupled contributions: the substrate, the heater geometry, the individual films, and the interfaces. A central challenge is therefore to determine what can be reliably extracted from the measurement, and what requires numerical modeling or an effective description.

The Growing Importance of Thermal Management

Thermal management is a central issue in modern technology because heat directly affects performance, efficiency, and reliability. In microelectronics, increasing device density and power density

make heat removal more difficult. In optoelectronic and power electronic systems, local heating can reduce efficiency and accelerate failure mechanisms. In thermoelectric materials, the situation is different but equally important: controlling and reducing heat flow is necessary to improve energy conversion efficiency.

These examples show that thermal transport must be understood at the material level. As device dimensions decrease and the number of interfaces increases, classical bulk descriptions of heat conduction become less sufficient. Thin films, interfaces, and multilayer stacks require specific measurement and modeling approaches. This thesis addresses this need by combining the 3-ω experimental method with finite element modeling.

Thesis Objectives

The objective of this doctoral work is to develop and validate a combined experimental and numerical approach for the thermal characterization of dielectric thin films and multilayer structures. The main objectives are:

— to implement and optimize the 3-ω method for measuring dielectric thin films and multilayer systems with weak thermal responses;

— to develop a finite element method (FEM) model able to reproduce the thermal response of the 3-ω experiment and to assist in parameter extraction;

— to validate the experimental setup and the FEM model using reference materials and controlled numerical cases;

— to investigate the limits of analytical extraction methods for thin films and multilayer structures;

— to analyze the inverse problem associated with complex multilayer stacks, where several layers and interfaces contribute to the same measured signal;

— to extract the effective cross-plane thermal conductivity of a five-layer SiN_x/SiO_2 dielectric stack using a validated Effective Medium Approach (EMA).

Thesis Outline

This thesis is organized into five main chapters, followed by a general conclusion and an appendix.

Chapter 1: Heat Conduction in Complex Nanostructured Systems. This chapter introduces the scientific context of the thesis. It presents the growing importance of thermal management in modern devices and discusses why heat transport becomes more difficult to describe at the nanoscale. Particular attention is given to dielectric thin films, multilayer systems, phonon boundary scattering, and thermal boundary resistance. The chapter also introduces the metrological challenge of extracting thermal properties from a measured response that contains several coupled contributions.

Chapter 2: State of the Art: Heat Conduction in Solids and its Metrology. This chapter reviews the theoretical and experimental foundations of heat conduction in solids. It begins with macroscopic heat conduction based on Fourier's law and then introduces microscopic heat transport in terms of phonons. The chapter also reviews thermal conductivity measurement techniques, including steady-state and transient methods. Particular emphasis is placed on the 3-ω method, which is selected in this work for the thermal characterization of dielectric thin films and multilayer structures.

Chapter 3: Experimental and Numerical Methodology. This chapter presents the experimental and numerical framework developed in this thesis. It first introduces the theoretical basis of the 3-ω method, including signal generation and analytical solutions for idealized geometries. It then describes the experimental setup, including the metallic heater, the Wheatstone bridge, the lock-in detection, and the TCR calibration procedure. Finally, the chapter presents the FEM modeling strategy implemented

in COMSOL Multiphysics, including geometry, material properties, boundary conditions, meshing, and the simulation of the complex temperature response.

Chapter 4: Validation and Parametric Study of the Thermal Metrology. This chapter validates the measurement and modeling framework. The experimental setup is first tested on reference bulk substrates, including borosilicate glass and fused silica. The measured thermal conductivities are compared with literature values in order to evaluate the reliability of the experimental procedure. The FEM model is then validated against analytical solutions and used for parametric studies. These studies examine the influence of input power, heater width, and substrate thermal conductivity, and they clarify the limits of simplified analytical models for thin-film extraction.

Chapter 5: Methodology for the Thermal Characterization of Complex Multilayer Systems. This chapter applies the validated framework to the five-layer SiN_x/SiO_2 stack. It first shows why direct multi-parameter fitting is not reliable for this system, due to strong parameter correlation and limited sensitivity to individual interfaces. A frequency-dependent sensitivity analysis is then used to identify the parameters that can be reliably detected by the 3-ω signal. Based on this diagnosis, an Effective Medium Approach is introduced and validated using virtual FEM experiments. The method is then applied to the experimental data in order to extract the effective cross-plane thermal conductivity of the complete multilayer stack.

General Conclusion and Perspectives. The final section summarizes the main results of the thesis, including the validation of the 3-ω platform, the development of the FEM model, the analysis of the inverse problem, and the extraction of the effective thermal conductivity of the multilayer stack. It also discusses the limitations of the present work and proposes directions for future research.

Appendix A: Numerical Verification of Effective Medium Theory (EMT). Additional work not included in the main body of the thesis is presented in Appendix A. This appendix provides a numerical verification of Effective Medium Theory for estimating effective transport properties, including thermal conductivity, electrical conductivity, and the Seebeck coefficient, in heterogeneous thermoelectric materials.

Chapter 1

Heat Conduction in Complex Nanostructured Systems

While the General Introduction highlighted the macroscopic thermal management crisis in modern electronics—from throttling processors to overheating power amplifiers—solving these technological bottlenecks requires a fundamental understanding of heat transport at the microscopic level. The reliability of a device is ultimately dictated by how efficiently phonons, the quanta of lattice vibrations, can navigate through the complex, nanostructured materials that constitute the device.

This chapter transitions from the broad technological context to the specific physical mechanisms governing heat conduction in solids. We will focus particularly on the dielectric materials (SiO_2 and Si_3N_4) central to this study. We will explore why classical Fourier diffusion fails at the nanoscale, how interfaces act as dominant scattering centers (Kapitza resistance), and why characterizing these properties in multilayer stacks presents a unique "inverse problem." This theoretical foundation is essential for understanding the metrological challenges addressed in the subsequent chapters.

1.1 Context: The Growing Importance of Thermal Management

This section examines the growing importance of thermal management across several high-impact technological domains. We begin with silicon-based integrated circuits, where the continued scaling predicted by Moore's Law has led to a dramatic increase in power density, making heat dissipation a critical bottleneck. We then extend the discussion to high-power optoelectronic and power electronic systems, where localized heating and thermal reliability pose major challenges. Finally, we consider thermoelectric systems, in which the objective is not to dissipate heat, but to control and impede its flow.

Through these examples, it becomes evident that thermal transport is not merely a secondary effect, but a fundamental factor governing device performance. This motivates the need for precise characterization and modeling of heat conduction, particularly in materials and structures where nanoscale effects and interfaces dominate.

1.1.1 Moore's Law and the Rise of Power Density in Integrated Circuits

For over five decades, the semiconductor industry has been propelled by the empirical observation known as Moore's Law, which famously predicted the doubling of transistors on an integrated circuit (IC) approximately every two years [9]. This exponential scaling has been the primary engine of the digital revolution, enabling the delivery of exponentially increasing computational power at decreasing costs. This historical trend of transistor integration is visually summarized in Figure 1.1, which plots the transistor count of microprocessors against their year of introduction, clearly illustrating the logarithmic growth trajectory.

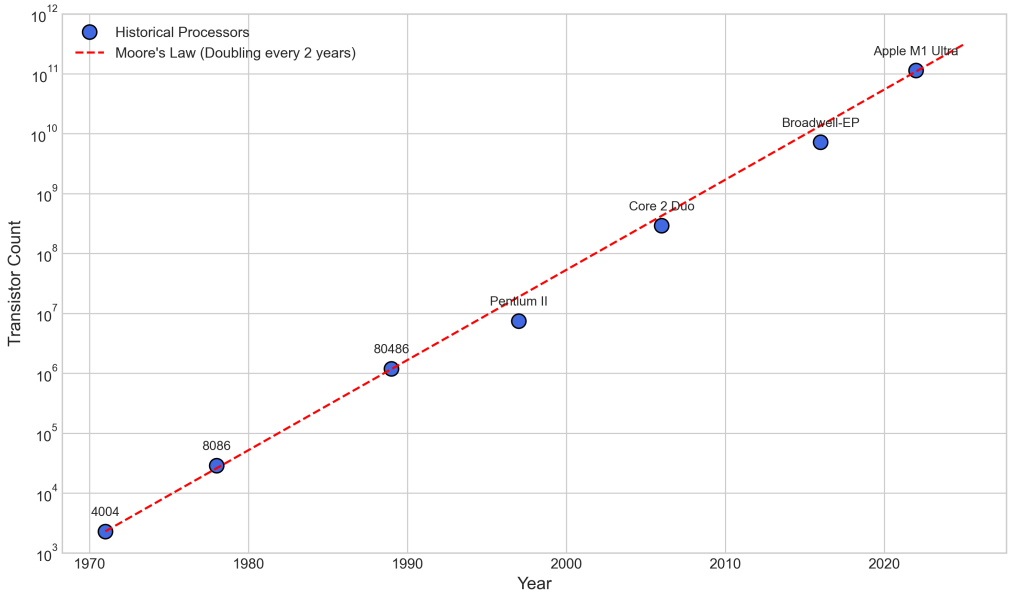


Figure 1.1 – A semi-log plot illustrating the exponential growth of the number of transistors on integrated circuit chips over the past five decades. The data points represent various Intel microprocessors, showing a doubling of transistor count approximately every two years, consistent with Moore's prediction (Karl (2022)[10], Wikipedia (2022)[11], AppleM1Ultra (2022)[12]). The y-axis shows the number of transistors on a chip (logarithmic scale) versus the year of introduction.

For many years, this geometric scaling was accompanied by the principles of Dennard scaling [13], which stated that as transistors got smaller, their power density stayed constant, so the power use stayed in proportion with area. This allowed performance (clock frequency) to increase without a corresponding penalty in power consumption. However, around the mid-2000s, Dennard scaling effectively broke down due to fundamental physical limitations at the nanoscale, primarily leakage currents and threshold voltage scaling limits [14, 15].

The consequences of this breakdown are clearly illustrated in Figure 1.2. While transistor count continues to grow steadily in accordance with Moore's Law, the historical trend of increasing clock frequency begins to plateau around 2004–2005. Prior to this point, frequency scaling had been the dominant driver of performance improvements. However, as power consumption rises and approaches a practical limit on the order of 100 W, further increases in clock frequency become unsustainable. This phenomenon, commonly referred to as the power wall, effectively marks the end of the frequency-scaling era.

As a result, improvements in single-thread performance also begin to slow, no longer benefiting directly from higher clock speeds. Instead, the continued growth in transistor budgets is increasingly utilized to replicate processing units rather than accelerate them. This shift is evident in Figure 1.2, where the number of cores per chip remains roughly constant until the mid-2000s and then begins to increase. Consequently, performance gains are achieved through parallelism rather than higher operating frequencies, signaling a fundamental transition in computer architecture design.

Although Figure 1.2 depicts total chip power rather than power density, the implications extend beyond absolute power consumption. As more transistors are integrated within a fixed chip area under strict power constraints, the effective power density increases, exacerbating thermal challenges. This trend has been associated with the emergence of the so-called thermal wall [1], which further constrains performance scaling and accelerates reliability concerns. In response, modern architectures must balance performance, power, and thermal limits, giving rise to challenges such as efficient parallelization and the underutilization of available transistors, often referred to as dark silicon [16].

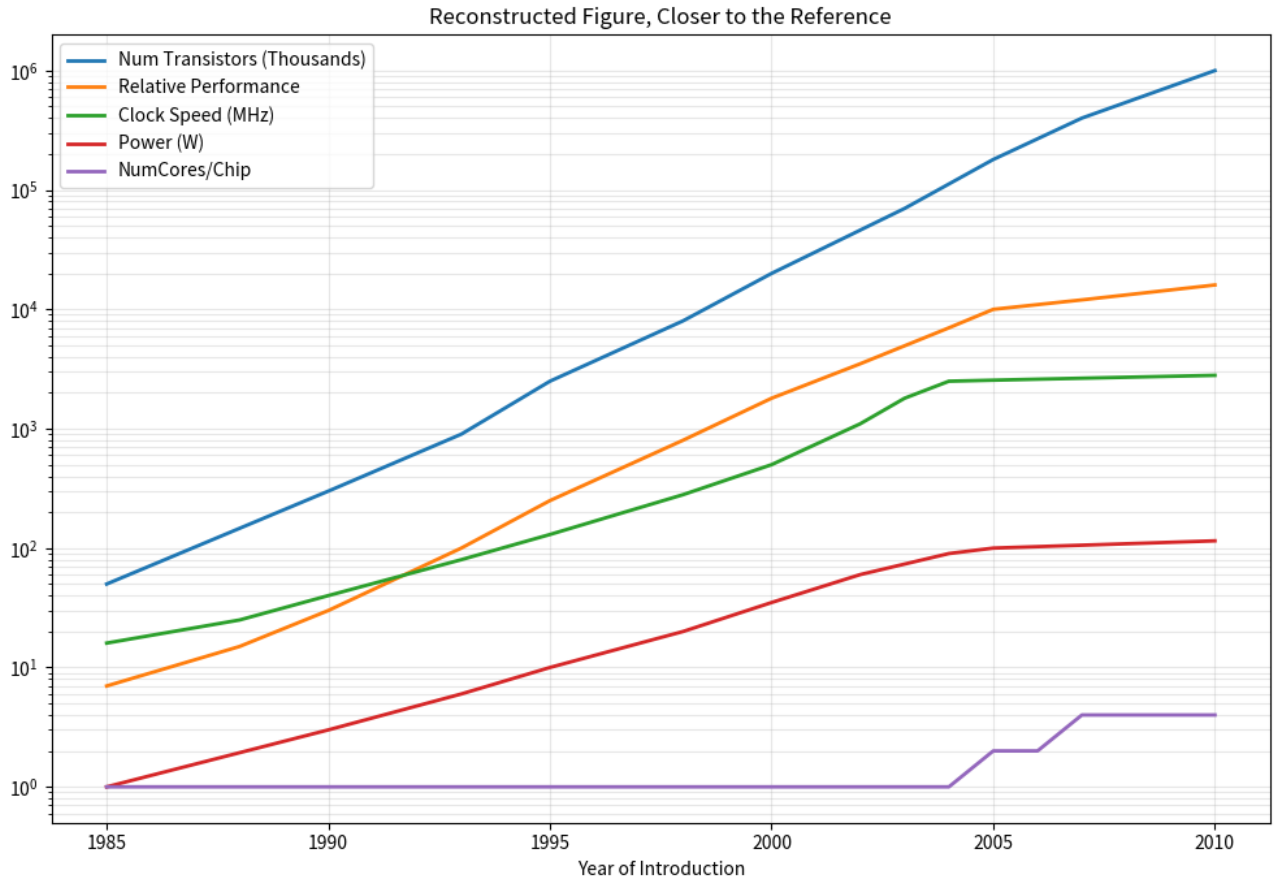


Figure 1.2 – Trends in microprocessor scaling from 1985 to 2010. While transistor count continues to increase exponentially, clock frequency and single-thread performance plateau around 2005 due to power constraints. As a result, performance scaling shifts from frequency increases to multi-core architectures, reflected in the rising number of cores per chip (Fuller ***et al.*** (2011) [17]).

1.1.2 Thermal challenges in high-power optoelectronics and other device

The imperative for advanced thermal management extends far beyond microprocessors, posing equally significant challenges in optoelectronics and power electronics where heat generation is an intrinsic consequence of the primary energy conversion process.

Thermal Management in Solid-State Lighting: The High-Brightness LED

High-brightness LEDs, despite their favorable efficiency, convert a substantial fraction of electrical power into heat [18]. This leads to an "efficiency droop," where the internal quantum efficiency decreases as temperature rises [19, 20, 21, 22]. Figure 1.3 shows a schematic cross-section of a high-power LED, illustrating the critical heat flow path. The heat generated at the junction must be extracted through a complex stack, including the LED chip itself, the die attach, the submount, and the Thermal Interface Material (TIM), before reaching the final heat sink. This unwanted heat is a primary performance limiter; as Figure 1.4 demonstrates, key metrics such as luminous flux and forward voltage decrease significantly as the junction temperature rises. For white LEDs, thermal quenching of the phosphor also degrades performance and color quality [23, 24]. Thermomechanical stress from Coefficient of Thermal Expansion (CTE) mismatches is a primary cause of catastrophic failure [25, 26].

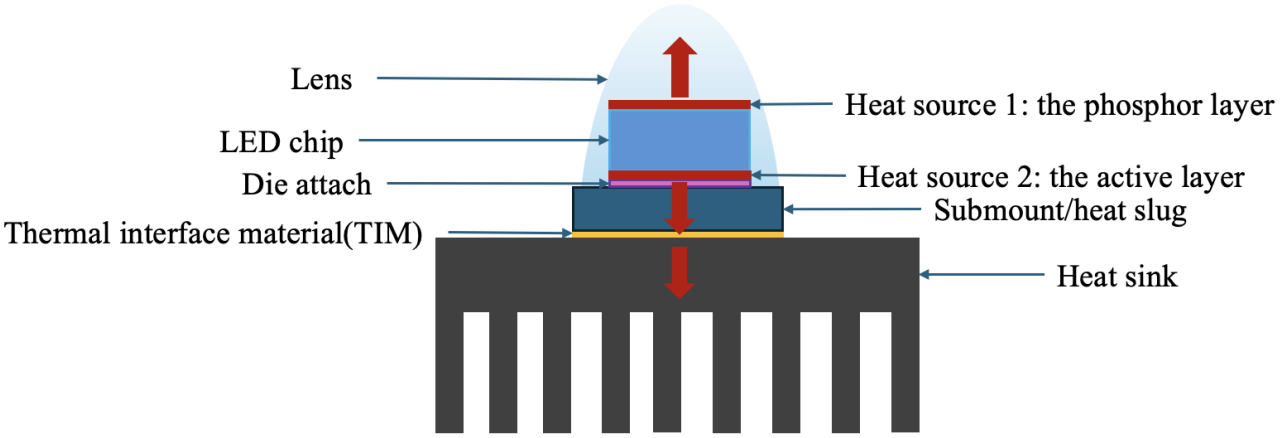


Figure 1.3 – A schematic cross-section of a high-power LED package, illustrating the complex thermal path (Li (2024) [27] and Poppe ***et al.*** (2009) [28]).

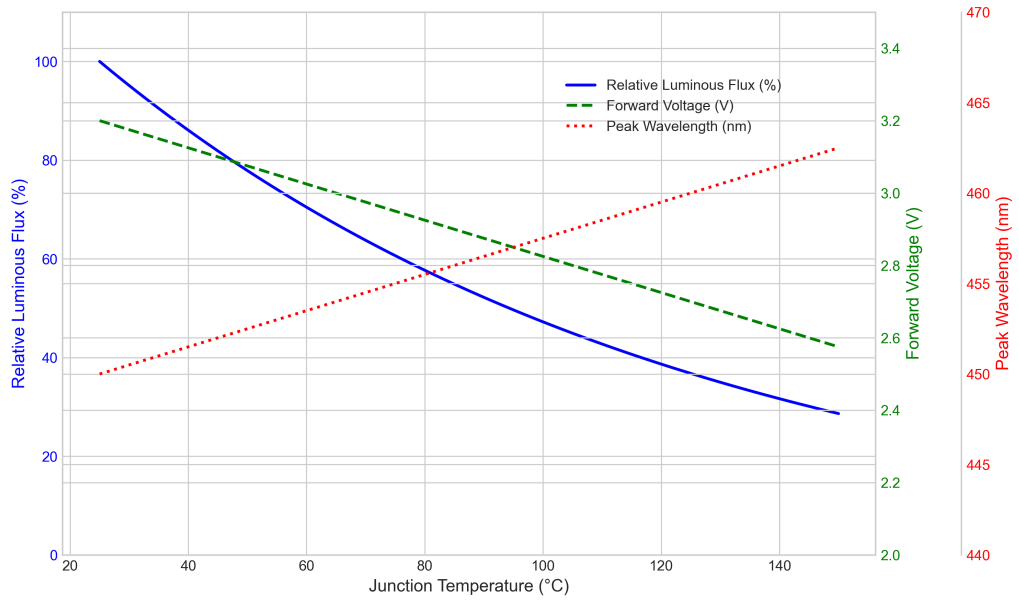


Figure 1.4 – Key performance metrics decrease significantly as junction temperature rises. Data supported by studies on efficiency droop (Piprek ***et al.*** (2010) [19] and Shen ***et al.*** (2007) [21]) and phosphor thermal quenching (Nishiura ***et al.*** (2011) [29]).

Thermal Management in High-Power Laser Diodes

High-power laser diodes face a severe thermal barrier. Key performance parameters are highly sensitive to temperature, which can lead to “thermal rollover” [30, 31, 32]. Figure 1.5 clearly illustrates this effect by plotting the typical Light-Current (L-I) curve at different operating temperatures. As the temperature increases from 25°C to 75°C, the slope efficiency (optical power per amp) decreases, and the maximum achievable power is significantly reduced, demonstrating the "rollover" phenomenon. Wavelength stability is also compromised by temperature fluctuations [33], and the ultimate failure is often a catastrophic optical damage (COD), or a thermal runaway process [34].

Thermal Management in Wide-Bandgap Power Electronics

Wide-Bandgap (WBG)semiconductors like SiC and GaN enable more efficient power devices but also generate extreme localized heat fluxes [35, 36]. Table 1.1 provides a direct comparison of key properties for these materials. It highlights that, compared to traditional Silicon (Si), WBG materials

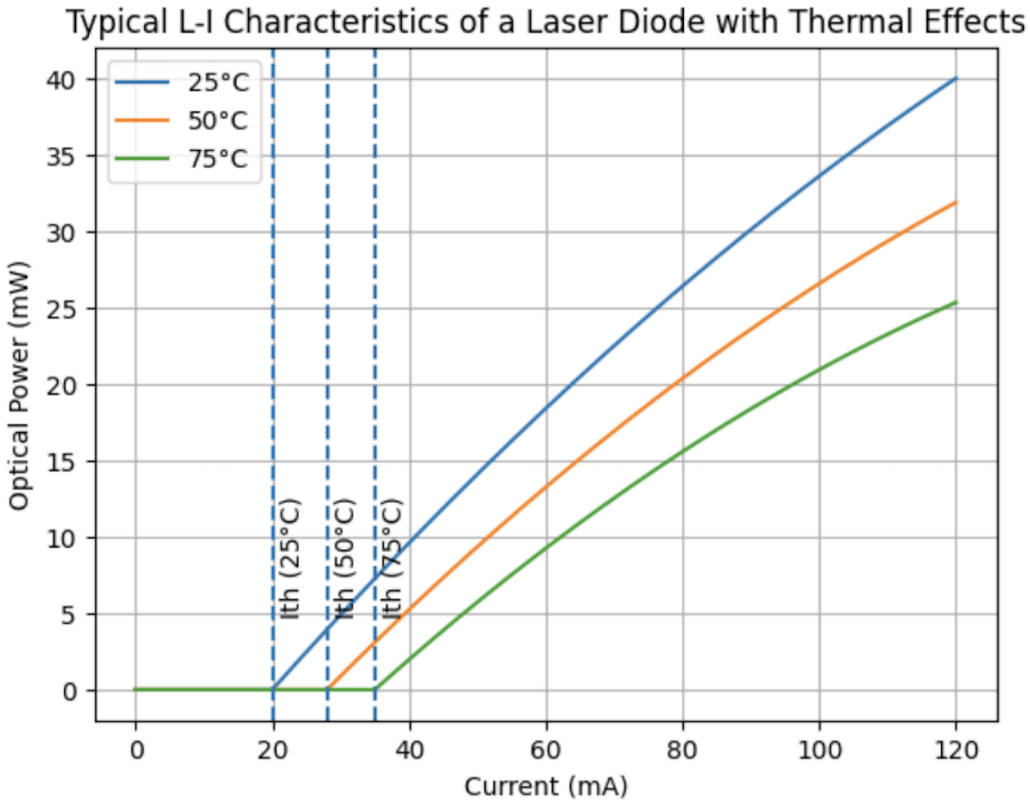


Figure 1.5 – Typical L-I curves of a laser diode at various temperatures showing thermal rollover (Coldren ***et al.*** (2012) [32]).

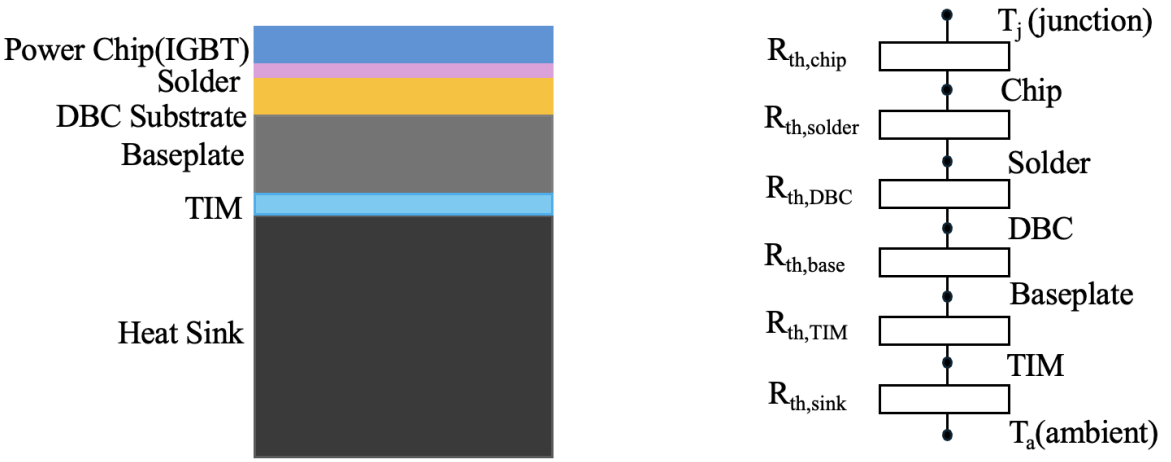
like 4H-SiC and GaN have vastly superior electrical properties, such as a higher Bandgap and Critical Electric Field (CEF). However, their thermal conductivities—which are critical for dissipating the heat from these high-power operations—vary significantly. Although WBG materials have high intrinsic thermal conductivity (as shown for 4H-SiC in Table 1.1), the packaging often becomes the bottleneck. Figure 1.6(a) illustrates a typical power module stack, showing the multiple layers (Thermal Interface Material (TIM), Direct Bonded Copper (DBC) substrate, solder, Power Chip(Insulated Gate Bipolar Transistor)) that heat must traverse. This entire assembly can be modeled as an equivalent thermal resistance network, shown in Figure 1.6(b), where the total thermal resistance (R_{th}) from the junction to the ambient air dictates the device's operating temperature. Self-heating can lead to performance degradation and reliability issues [7, 8, 37, 38].

Table 1.1 – A comparison of key material properties for power semiconductors.

Property	**Si**	**4H-SiC**	**GaN**
Bandgap (eV)	1.12	3.26	3.4
Critical Electric Field (MV/cm)	0.3	2.2	3.3
Thermal Conductivity (W/m·K)	150	370	130-200

1.1.3 The role of thermal properties in thermoelectric device efficiency

In contrast to heat dissipation, thermoelectric (TE) devices actively utilize thermal gradients for energy conversion [39, 40]. The efficiency is governed by the figure of merit, $ZT = (S^2\sigma/k)T$, where T is the absolute temperature. To maximize ZT, a material requires the paradoxical combination of a high Seebeck coefficient (S), high electrical conductivity (σ) and low thermal conductivity (κ) [41].



(a) Power Module Stack (b) Equivalent Thermal Resistance Network

Figure 1.6 – Thermal management in WBG power modules. (a) Schematic cross-section of a typical power module packaging stack (chip, solder, DBC, baseplate, TIM). (b) Equivalent one-dimensional thermal resistance network model ($R_{th,j-a}$) (Adapted from Baliga (2019) [35] and She ***et al.*** (2017) [36]).

Figure 1.7 provides a conceptual plot of these competing properties, showing how they depend on carrier concentration. The individual parameters (S, σ, κ) are interdependent, causing the figure of merit (ZT) to be optimized only within a narrow band of carrier concentration, typically found in heavily doped semiconductors.

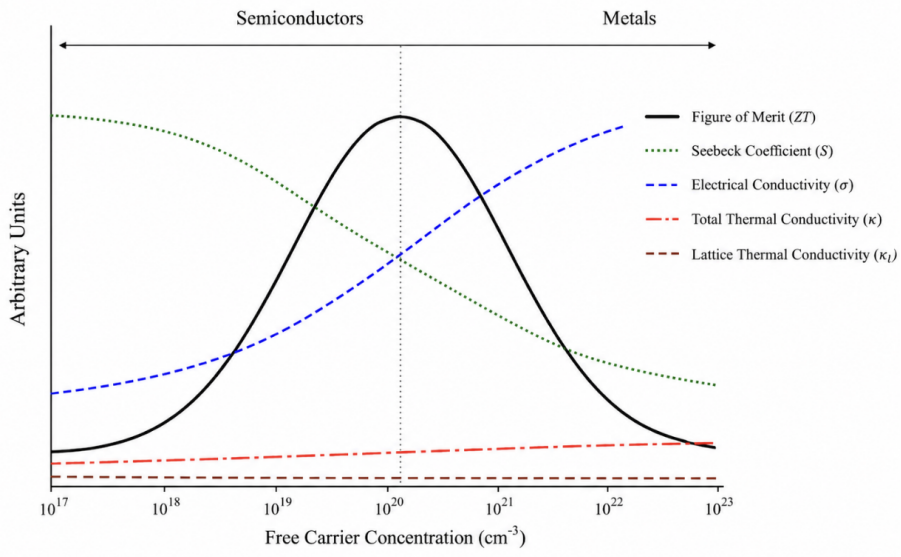


Figure 1.7 – Conceptual plot of thermoelectric properties (Seebeck coefficient S, electrical conductivity σ, thermal conductivity κ, and figure of merit ZT) as a function of carrier concentration. The interdependence of these parameters limits the maximum ZT to a narrow range of optimal carrier concentration, typically found in heavily doped semiconductors (Adapted from Snyder ***et al.*** (2008) [41]).

The key strategy is to reduce the lattice thermal conductivity (k_L) without harming the electronic properties, a concept encapsulated by the "phonon-glass electron-crystal" (PGEC) paradigm [40]. This has been achieved through nanostructuring techniques such as superlattices [42, 43, 44], nanocomposites [45], and materials with complex crystal structures [46, 47]. Advanced methods include band structure engineering [48] and energy filtering [49].

1.2 Problematic: Challenges in thermal property characterization at the nanoscale

As device dimensions shrink, the classical continuum understanding of heat flow becomes insufficient.

1.2.1 Breakdown of Fourier's Law at small length scales

The classical continuum understanding of heat flow is embodied by Fourier's Law of heat conduction ($J = -\kappa \nabla T$). While highly effective for macroscale engineering, this diffusive model relies on the assumption of Local Thermal Equilibrium (LTE) and the treatment of the medium as a continuum [50, 51, 52]. Physically, this validity rests on the promise that heat carriers—in dielectrics, phonons—scatter frequently and sufficiently within the medium to establish a local temperature [53, 54]. This scattering frequency is spatially characterized by the phonon mean free path (MFP, λ), defined as the average distance a phonon travels between successive scattering events.

In bulk materials, where the characteristic length scale of the system (L) is significantly larger than the phonon MFP ($L \gg \lambda$), phonons undergo numerous internal scattering events. This process randomizes their momenta, establishing a diffusive transport regime where Fourier's Law accurately predicts thermal behavior.

However, as device dimensions shrink to become comparable to or smaller than the phonon MFP ($L \sim \lambda$ or $L < \lambda$), the continuum assumption breaks down. Phonons are no longer guaranteed to scatter thoroughly within the device volume; instead, they are increasingly likely to travel "ballistically" from boundary to boundary. In this regime, the local temperature gradient becomes ill-defined, and the effective thermal conductivity deviates significantly from bulk values [55, 56].

This transition is governed by the Knudsen number, defined as $Kn = \lambda/L$. The transport regimes are classified by this ratio, as illustrated conceptually in Figure 1.8:

(a) Diffusive Regime ($Kn \ll 1$): When the device dimension L is much larger than the mean free path λ, phonon transport is dominated by internal scattering (phonon-phonon or phonon-impurity). Their motion is randomized, resembling a random walk, and the transport is accurately described by Fourier's Law.

(b) Quasi-Ballistic Regime ($Kn \approx 1$): This is the intermediate case where L and λ are comparable, transport is a hybrid of internal diffusion and boundary scattering. Neither the diffusion equation nor purely ballistic models suffice; the Boltzmann Transport Equation (BTE) is required to capture the non-equilibrium effects [53, 57].

(c) Ballistic Regime ($Kn \gg 1$): When L is much smaller than λ, phonons travel directly between boundaries with negligible internal scattering, similar to photons in a transparent medium or bullets. The thermal conductance is then limited purely by the boundary resistance (Casimir limit) rather than intrinsic material properties.

When $Kn \geq 1$ (i.e., in the quasi-ballistic or ballistic regimes), transport is no longer diffusive, and Fourier's law fails, requiring more fundamental models such as the Boltzmann Transport Equation (BTE)[55, 53, 57].

The failure of Fourier's law is fundamentally rooted in the *spectral* nature of phonon transport [58, 59, 60, 61]. In crystalline materials like silicon, heat is carried by a broad spectrum of phonon modes, each possessing a distinct frequency ω, group velocity $v_g(\omega)$, and most critically, a frequency-dependent MFP $\lambda(\omega)$. The total thermal conductivity k_{bulk} is an integral over this spectrum: $k = \frac{1}{3} \int C(\omega) v_g(\omega) \lambda(\omega) d\omega$.

Figure 1.9 provides critical evidence for the spectral nature of phonon transport in silicon. Figure 1.9(a) shows the phonon dispersion relations, which define the fundamental properties of phonon modes. More importantly, Figure 1.9(b) presents the thermal conductivity accumulation as a function

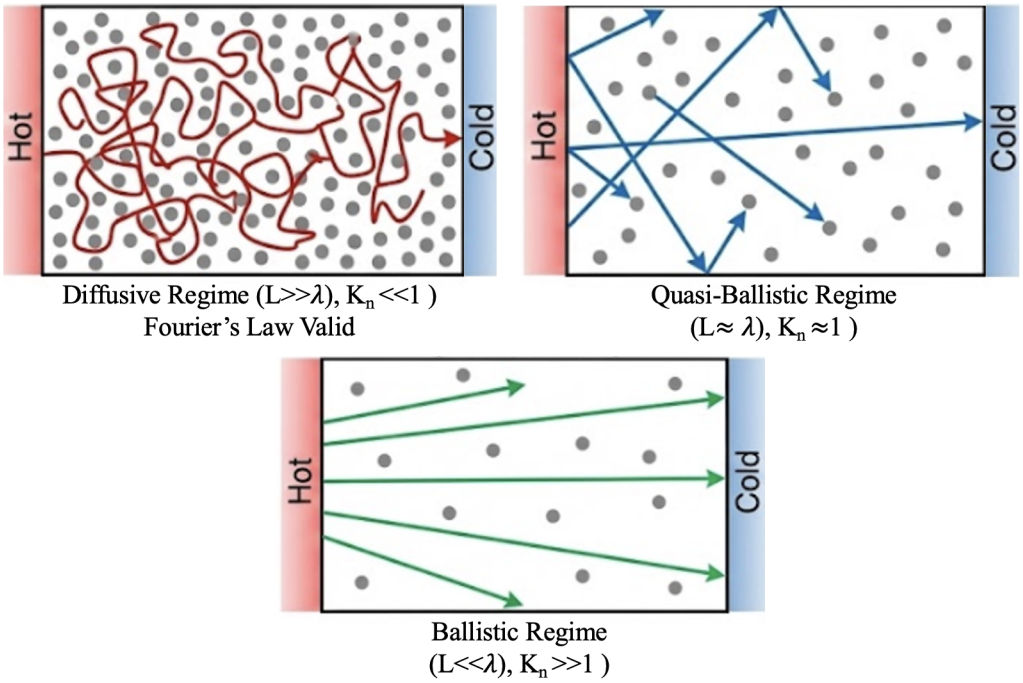


Figure 1.8 – Schematic of heat transport regimes (Diffusive, Quasi-Ballistic, Ballistic) defined by the Knudsen number (Kn) (Concept based on Chen (2005) [53]).

of phonon mean free path (MFP), quantifying the fraction of total thermal conductivity contributed by phonons with MFPs below a given length scale.

This plot reveals that, in order to recover the full bulk thermal conductivity of silicon (150 W/m·K at 300 K), phonons with MFPs spanning several orders of magnitude—from nanometers to microns—must be included [59]. Notably, approximately half of the total thermal conductivity is contributed by phonons with MFPs on the order of microns, corresponding primarily to low-frequency acoustic modes.

This directly explains the strong length-scale dependence of the effective thermal conductivity. For example, in a silicon thin film with thickness (L = 100) nm, boundary scattering will strongly suppress phonons with intrinsic MFPs larger than (L). As indicated by Figure 1.9(b), this removes a substantial fraction of the dominant heat-carrying phonons, leading to a significantly reduced effective thermal conductivity compared to the bulk value. This spectral "cutoff" effect, which is beyond the scope of Fourier's law, has been experimentally validated in numerous studies [61, 62, 63, 64].

1.2.2 The emergence of phonon boundary and interface scattering

In nanostructures, extrinsic scattering from boundaries becomes dominant [65, 66]. The Fuchs-Sondheimer model, using a specularity parameter p, describes this reduction in effective MFP [67]. The specularity depends on the surface roughness relative to the phonon wavelength [53, 65].

This boundary scattering can be broadly classified by comparing the surface roughness (symbolized by η) to the phonon wavelength (λ_{ph}) [65, 66], leading to two distinct types, as illustrated in Figure 1.10.

Figure 1.10(a) Specular Scattering: Occurs at interfaces that are "smooth" ($\eta \ll \lambda_{ph}$). The phonon reflects light like a mirror, preserving its momentum (in the plane) and its phase coherence. This is a wave-like interaction.

Figure 1.10(b) Diffuse Scattering: Occurs at interfaces that are "rough" relative to the phonon wavelength ($\eta \geq \lambda_{ph}$). The phonon scatters randomly in all directions, losing its phase information. This is best described as a particle-like interaction. Where $p = 1$ to fully specular scattering (Fig.

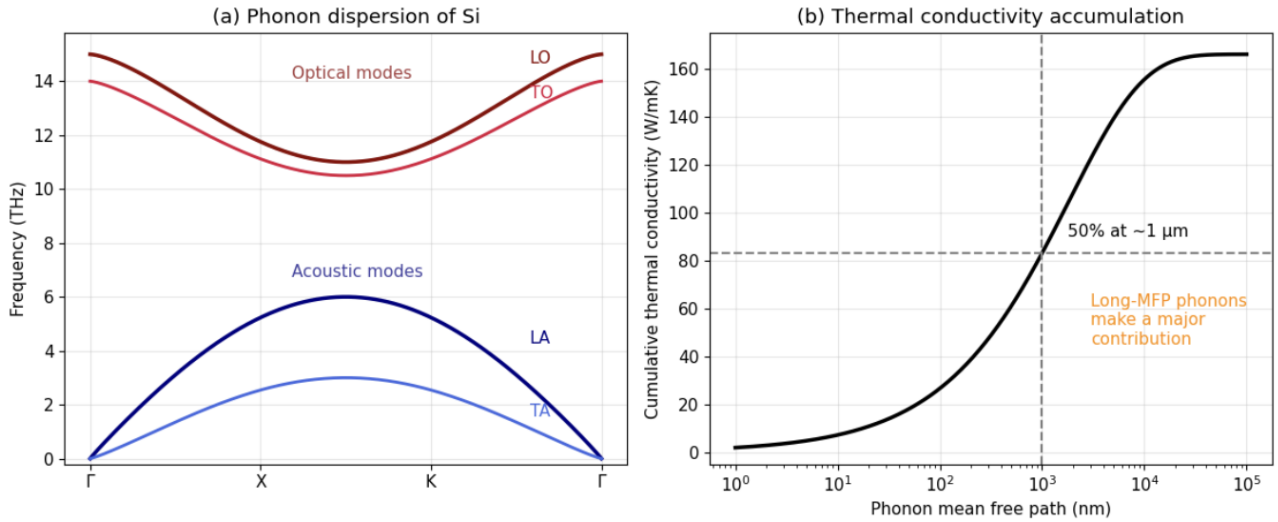


Figure 1.9 – Spectral nature of phonon transport in silicon at 300 K. (a) Phonon dispersion curves along the high-symmetry path Γ–X–K–Γ, showing acoustic (LA, TA) and optical (LO, TO) branches. (b) Cumulative thermal conductivity as a function of phonon mean free path (MFP). The results indicate that a significant portion of the thermal conductivity arises from phonons with long mean free paths (on the order of micrometers). Plots are re-drawn based on trends and data from first-principles calculations (Esfarjani ***et al.*** (2011) [59]).

1.10a) and $p = 0$ corresponds to fully diffuse scattering (Fig. 1.10b) [67].

This fundamental distinction between particle-like diffuse scattering and wave-like specular scattering also governs heat transport in periodic structures like superlattices. This leads to two different transport regimes:

Incoherent Transport: In superlattices with rough interfaces, phonons scatter diffusely (as in Fig. 1.10b) at each boundary. The phonon phase is destroyed at every interface. Transport is dominated by the particle-like behavior of phonons, and the total thermal resistance is a simple sum of the individual layer resistances and their associated Thermal Boundary Resistances (TBR).

In high-quality, periodic superlattices with atomically smooth interfaces, phonons can maintain their wave-like nature (as in Fig. 1.10a) as they traverse the structure, this behavior is called coherent transport. This "coherence" allows the phonon wave to interfere with its own reflections from the periodic interfaces. When the superlattice period is comparable to the phonon wavelength, destructive interference can occur, forbidding phonons of specific frequencies from propagating. This phenomenon creates phononic bandgaps—ranges of frequencies where heat transport is almost completely suppressed—leading to a very strong reduction in thermal conductivity[68, 69, 70].

1.2.3 The concept of Thermal Boundary Resistance(TBR) or Kapitza Resistance

At the interface between two materials, a temperature discontinuity arises, as schematically plotted in Figure 1.11. This jump in temperature, denoted as ΔT_{TBR}, occurs even under a steady-state heat flux q. This phenomenon is known as the Thermal Boundary Resistance (TBR), or sometimes Kapitza Resistance [71, 72]. defined as $R_{bd} = \Delta T/q$.

Historically, this effect was first observed at the interface between superfluid helium and copper, where it is specifically termed the Kapitza Resistance [71, 73]. In modern nanoscale thermal transport, the term Kapitza resistance is often used interchangeably with TBR to describe the intrinsic resistance arising from the acoustic mismatch of energy carriers (phonons or electrons) at a widely perfect interface[72, 74], whereas TBR encompasses both intrinsic mismatch and extrinsic factors such as

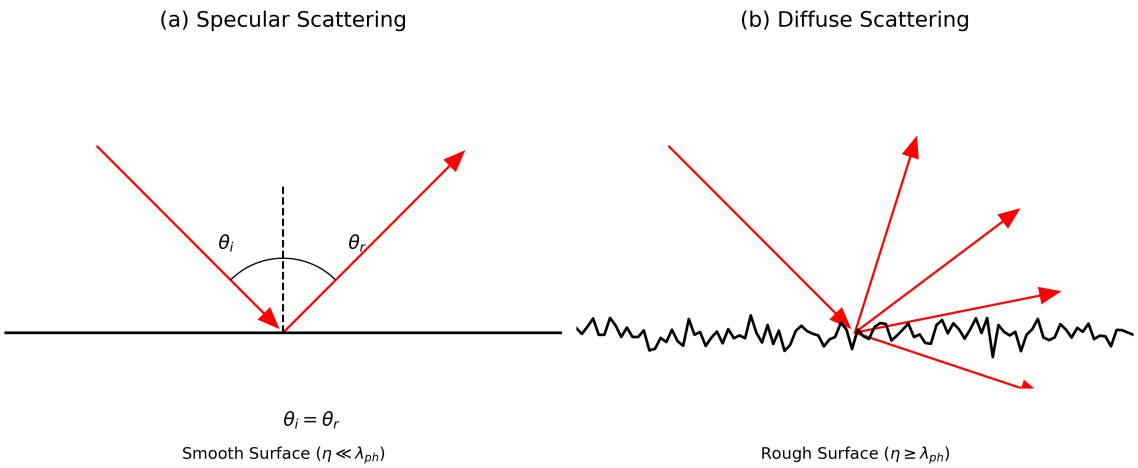


Figure 1.10 – Illustration of specular vs. diffuse phonon scattering.

surface roughness or defects.

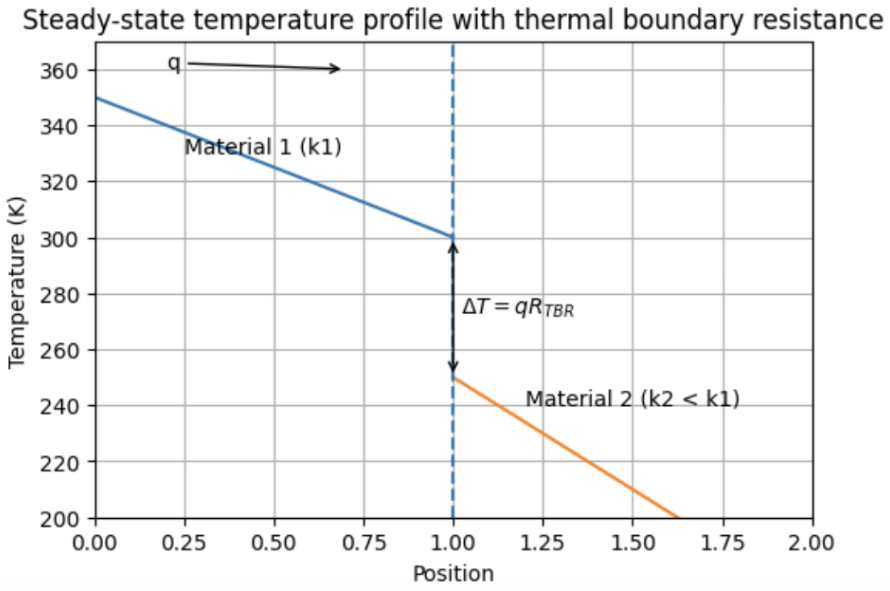


Figure 1.11 – A schematic plot illustrating the temperature discontinuity (ΔT_{TBR}) at an interface.

Classical models like the Acoustic Mismatch Model (AMM) and the Diffuse Mismatch Model (DMM) attempt to predict TBR based on the mismatch in phonon properties, assuming a perfect, atomically sharp interface [74]. However, these models often fail to capture the complexity of real-world interfaces, which is schematically shown in Figure 1.12. As the diagram illustrates, a real interface is not a perfect 2D plane, but rather a disordered 3D volume containing a combination of interface roughness, atomic mixing, impurity atoms, dislocations, and voids [75, 76, 77, 78, 79]. Each of these imperfections acts as an additional scattering center for phonons, further impeding heat transport and increasing the measured TBR beyond the predictions of simple mismatch models.

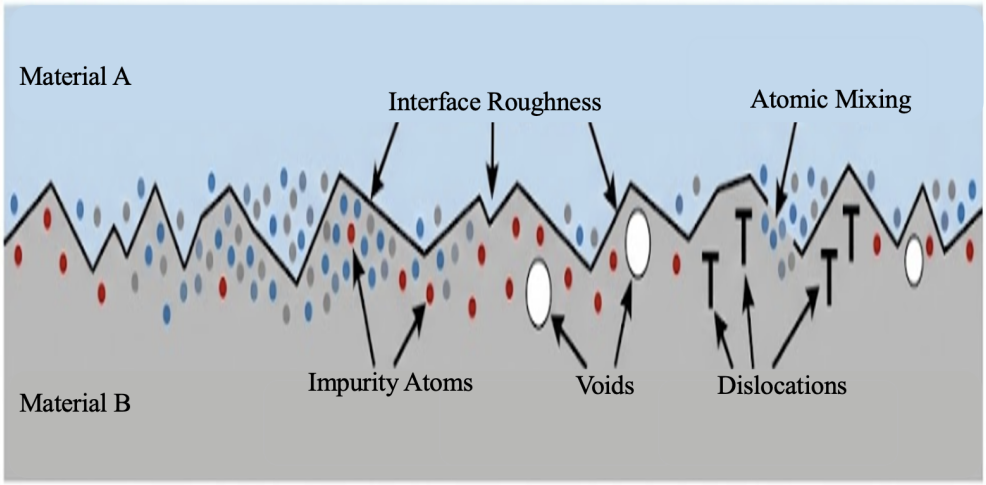


Figure 1.12 – A schematic of a realistic interface, showing features not captured by simple models.

1.3 Scientific and Technological Motivation

Having established the fundamental challenges of nanoscale heat transport in Section 1.2—such as the breakdown of Fourier's Law and the emergence of Thermal Boundary Resistance (TBR)—this section now connects these concepts to the specific technological problem driving this dissertation. This problem is the accurate thermal characterization of SiO_2 and SiN dielectric films, which are critical materials in modern electronics.

1.3.1 SiO_2 and SiN as key dielectric materials

Silicon dioxide (SiO_2) and silicon nitride (Si_3N_4) are indispensable dielectrics in semiconductor fabrication, used primarily for their excellent electrical insulation properties as dielectrics [80, 81]. This creates a fundamental thermo-electric challenge: while these layers are required to prevent electrical current leakage, their inherently low thermal conductivities ($\kappa \approx 1.4$ W/m·K for SiO_2) are in direct conflict with the need to dissipate heat. Indeed, a high thermal conductivity would be preferable for efficient heat removal.

Therefore, their low κ is 'critical' because it acts as a major thermal barrier, impeding heat flow from active device regions. Figure 1.13 provides a clear example of this problem, showing a modern FinFET where the active device (the "Silicon Fin") is surrounded by these low-κ oxide and nitride layers (e.g., in the Back-End-of-Line (BEOL) stack). Heat generated in the fin must travel through these thermal bottlenecks to reach the heat sink, making their low conductivity a critical factor that negatively impacts device performance and reliability [82, 83, 84, 85, 86, 87, 88].

1.3.2 The specific metrological challenge posed by multilayer systems

The core challenge is solving the inverse heat conduction problem (IHCP) for multilayer films [90]. Figure 1.14 illustrates the nature of this problem. In a "Forward Problem" (which is used in simulations), one starts with known material properties (like $\kappa_1, \kappa_2, R_{TBR}$) and a known heat flux $q(t)$ to calculate the temperature response $\Delta T(\omega)$. In the "Inverse Problem" (which is what we do in an experiment), the situation is reversed: we measure the effect (the surface temperature $\Delta T(\omega)$) and must work backward to find the multiple unknown properties ($\kappa_1, \kappa_2, R_{TBR}, ...$). This deconvolution of individual layer properties becomes what is known as an "ill-posed problem" when the solution is not unique. This often happens due to strong parameter correlation [1, 52].

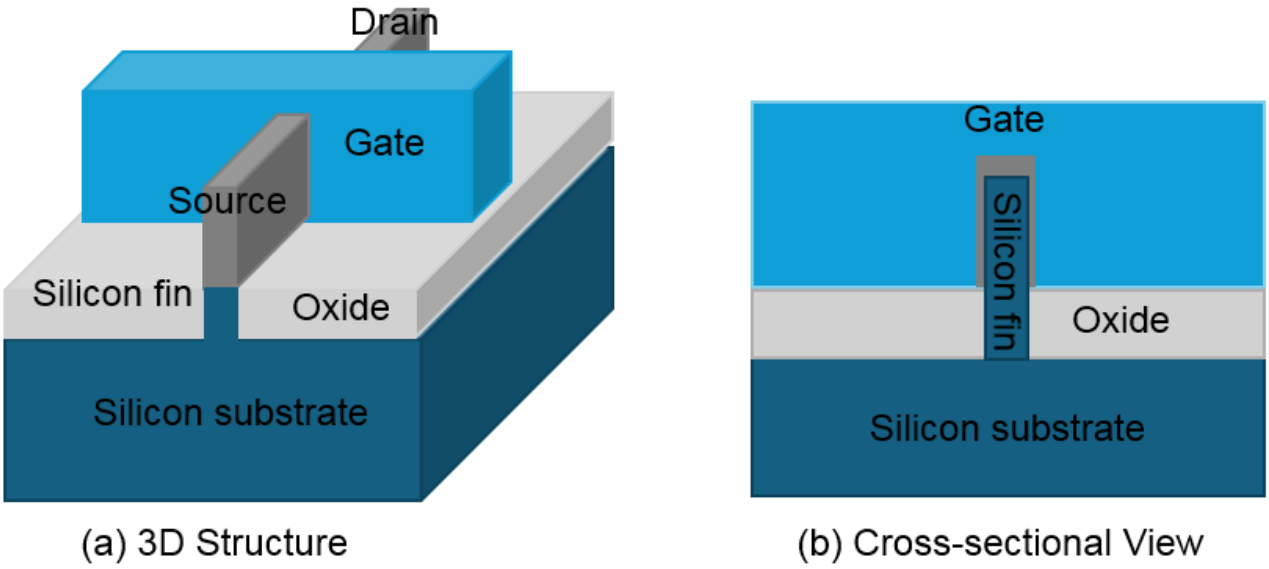


Figure 1.13 – A detailed cross-section of a modern FinFET, highlighting the ubiquitous use of SiO_2 and SiN films (Schematic based on concepts from Duan (2024) [89]).

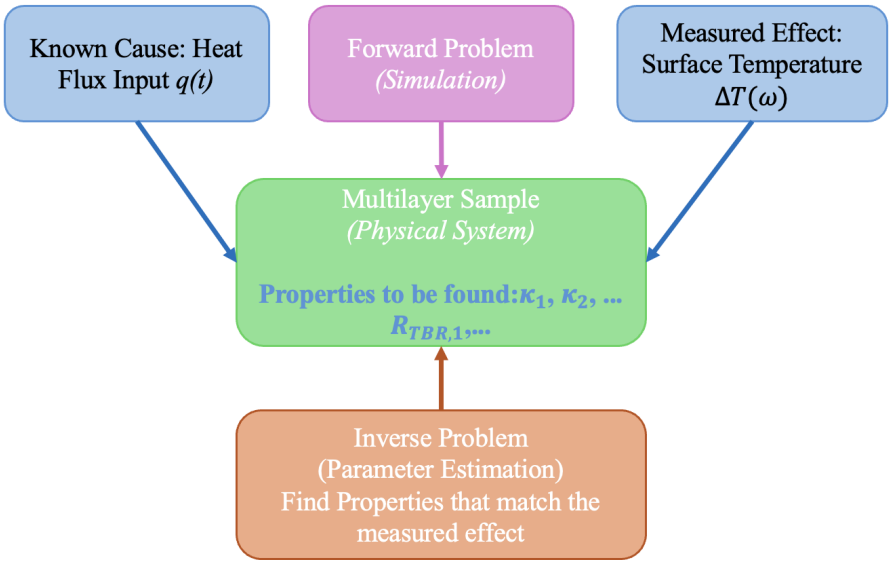


Figure 1.14 – A diagram defining the inverse problem: determining multiple unknown thermal properties from a single surface measurement.

1.3.3 Supplementary Numerical Verification (Appendix A)

While the main body of this thesis focuses on the experimental characterization and theoretical modeling of the multilayer thin films, a fundamental question remains regarding the validity of the mixing laws used in the Effective Medium Theory (EMT), especially those concerning the Seebeck coefficient. To address this, we have conducted a dedicated numerical study, which is presented in detail in **Appendix A**.

This appendix details the construction of a 3D Finite Element Method (FEM) model using COMSOL Multiphysics ®. The model simulates a composite matrix containing randomly distributed, non-overlapping spherical inclusions, which are the initial simplifying assumptions at the basis of the effective medium theory [91], to mimic the heterogeneous nature of the material at the microscale.

By applying specific boundary conditions, we extracted the effective physical properties—specifically thermal conductivity (κ), electrical conductivity (σ), and the Seebeck coefficient (S)—and compared them with the predictions of standard analytical EMT models.

The primary objective of this supplementary work is to simulate by FEM the local flux densities in phase separated alloys, knowing the individual component transport parameter values. From these simulations, effective transport parameters(Seebeck coefficient, electrical and thermal conductivities) of the whole composite extracted. These transport parameter values are compared with those established by EMT. The calculation of the effective Seebeck coefficient in a point of discussion raised by J. Sonntag [92]. These simulations provide the necessary computational evidence to support the use of the EMT framework applied in the subsequent chapters.

1.4 Conclusion and Scientific Positioning

As reviewed in the preceding sections, the management of heat in modern electronics has evolved from a macroscopic packaging issue to a fundamental microscopic challenge. While the theory of heat transport in bulk materials is well-established, transport in nanostructured dielectrics is dominated by non-diffusive phenomena and interface scattering.

For the specific SiO_2/SiN multilayer systems central to this thesis, these factors create a "perfect storm" of characterization difficulties. The inverse problem is inherently ill-posed due to the high thermal impedance and the strong correlation between the intrinsic film conductivity and the interface resistance.

Consequently, relying on literature values or simplified analytical inversions is no longer sufficient. There is a clear need for a robust metrology framework that can:

1. Experimentally measure small temperature oscillations with high signal-to-noise ratio.
2. Numerically interpret these measurements using models that fully account for 3D heat spreading.
3. Rigorously decouple the "effective" thermal conductivity from interface artifacts.

The following chapter (Chapter 2) will therefore detail the development and optimization of the 3-omega experimental setup and the associated Finite Element Method (FEM) models designed to meet these specific challenges.

Chapter 2

State of the Art: Heat Conduction in Solids and its Metrology

Having established in the previous chapter the critical and ubiquitous role of thermal management in modern technology, this chapter now delves into the foundational knowledge required to understand and address these challenges. It serves as a comprehensive review of the state of the art, filling the gap between fundamental solid-state physics and the practical science of thermal metrology. The primary objective of this chapter is twofold. First, it aims to provide a rigorous theoretical framework for understanding heat conduction in the materials of interest—dielectric solids—from both macroscopic and microscopic perspectives. We will trace the evolution of our understanding from the classical continuum model of Fourier to the quantum mechanical picture of phonons, paying special attention to the phenomena that emerge at the nanoscale. Second, this chapter will critically survey the landscape of experimental techniques developed to measure thermal properties. This review will culminate in a detailed examination of the 3-ω method, the experimental cornerstone of this thesis. By thoroughly exploring its principles, historical development, and, most importantly, its inherent limitations when applied to complex structures, we will construct a compelling and undeniable justification for the novel hybrid experimental-numerical methodology developed in this work. This chapter, therefore, not only summarizes the work of those who came before but also precisely defines the scientific gap that this dissertation aims to fill.

2.1 Fundamentals of Phonon Heat Transport

This section lays the theoretical groundwork for all subsequent discussions of thermal transport in this thesis. We will begin by revisiting the classical, macroscopic law of heat conduction, which, despite its limitations at the nanoscale, remains the cornerstone of thermal engineering. From there, we will transition to the microscopic, quantum mechanical picture, introducing phonons as the primary heat carriers in dielectric solids and exploring the kinetic theory that governs their collective behavior. Finally, we will address the special case of amorphous materials, like the silicon dioxide central to this study, by introducing the concept of a minimum thermal conductivity, which provides a theoretical lower bound for heat transport in disordered systems.

2.1.1 The Macroscopic Picture: Fourier's Law of Heat Conduction

At length scales significantly larger than the mean free path of the underlying energy carriers, the transport of thermal energy in solids is accurately and elegantly described by the empirical law of heat conduction formulated by Jean-Baptiste Joseph Fourier in his seminal 1822 work, *Théorie analytique de la chaleur* [93]. Fourier's law is a phenomenological vector relationship that states that the local heat flux density, $\mathbf{J}$ (with units of W/m^2), is directly proportional to the negative of the local

temperature gradient, ∇T:

$$\mathbf{J} = -k\nabla T \tag{2.1}$$

The constant of proportionality, κ, is the thermal conductivity, a second-rank tensor for anisotropic materials, which simplifies to a scalar for isotropic materials like the amorphous films studied in this work. It is an intrinsic material property that quantifies a substance's ability to conduct heat. The negative sign signifies that heat flows "downhill," from a region of higher temperature to a region of lower temperature, in accordance with the second law of thermodynamics.

Fourier's law is fundamentally a diffusive equation. Its mathematical form is identical to Fick's first law of diffusion for particles and Ohm's law for electrical charge, and it is built on similar physical assumptions. The law implicitly presumes that the medium is a continuum and that a state of local thermal equilibrium (LTE) exists everywhere within the material. The LTE assumption implies that even though the system as a whole may have a temperature gradient and be out of equilibrium, any sufficiently small volume element can be considered to be in thermal equilibrium and can be assigned a well-defined local temperature. This assumption is valid only when the fundamental energy carriers—in our case, phonons—undergo frequent scattering events within that small volume element. This intense scattering effectively randomizes the energy and momentum of the carriers, leading to the random-walk-like transport process that is mathematically captured by a diffusion equation [94, 95].

For centuries, Fourier's law has served as the bedrock of thermal science and engineering, enabling the design of everything from heat engines to building insulation to the cooling systems for early computers. Its validity in the macroscopic world is undisputed. However, as was foreshadowed in Chapter 1, the core assumption of LTE, and thus the validity of Fourier's law itself, breaks down when the characteristic length scales of the system (L) become comparable to or smaller than the mean free path (λ) of the heat carriers. In this nanoscale regime, which is the central focus of modern electronics and this thesis, a more fundamental, microscopic description of heat transport is required.

2.1.2 The Microscopic Picture:Phonons as Heat Carriers

In electrically insulating (dielectric) and semiconducting solids, heat is predominantly carried by collective vibrations of the atoms that constitute the crystal lattice. In a classical picture, one can imagine the atoms connected by springs, and thermal energy is the kinetic and potential energy stored in these coupled oscillations. From a quantum mechanical perspective, the allowed energies of these vibrational modes are quantized. A quantum of lattice vibrational energy is called a phonon, a concept first introduced by Igor Tamm and later adopted by Yakov Frenkel [96, 97]. In direct analogy to photons being the quanta of the electromagnetic field, phonons are the quasi-particles of the crystal's vibrational field. These phonons can be treated as a "gas" of particles that propagate through the crystal, carrying energy, and occasionally scattering off one another or from imperfections in the lattice [50, 98].

This "phonon gas" picture, conceptually illustrated in Figure 2.1, allows for the derivation of thermal conductivity from a microscopic standpoint, using an approach analogous to the kinetic theory of gases. Figure 2.1(a) shows the classical picture of atoms connected by springs, whose collective vibrations (lattice vibrations) are quantized. A quantum of this vibrational energy is a phonon. These phonons propagate through the crystal, carrying energy. Their propagation is defined by the phonon dispersion relation (the relationship between frequency ω and wave vector k), shown schematically in Figure 2.1(b). From this dispersion, we can define the phonon group velocity $v_g = \partial\omega/\partial\mathrm{k}$, which represents the speed at which thermal energy propagates. In this kinetic theory framework, the thermal conductivity of phonon (κ_{ph}) can be expressed in its most common form as:

$$\kappa_{ph} = \frac{1}{3}C_v v_g^2 \tau = \frac{1}{3}C_v v_g \lambda \tag{2.2}$$

Here, each term has a distinct physical meaning:

— C_v is the specific heat capacity at constant volume per unit volume. It represents the energy carrying capacity of the phonon gas—i.e., how much thermal energy is stored in the lattice vibrations for a given increase in temperature. The temperature dependence of C_v is well-described by the Debye model, which predicts a T^3 dependence at low temperatures and saturation at the classical Dulong-Petit value of $3Nk_B$ at high temperatures [99].

— v_g is the phonon group velocity, defined as the derivative of the angular frequency ω with respect to the wave vector k from the phonon dispersion relation, $v_g = \partial\omega/\partial\mathrm{k}$. It represents the speed at which a packet of vibrational energy propagates through the crystal. For simplicity, it is often approximated by the average speed of sound in the material.

— τ is the phonon relaxation time, which is the average time between successive scattering events.

— λ is the phonon mean free path (MFP), the average distance a phonon travels between scattering events, given by $\lambda = v_g\tau$.

This equation elegantly bridges the macroscopic, experimentally measurable property (κ) with the microscopic properties of the heat carriers (C_v, v_g, λ). It makes clear that a material will have a high thermal conductivity if its lattice can store a large amount of energy per unit temperature (high C_v), if that energy propagates quickly (high v_g), and if the energy carriers can travel a long distance before being scattered (long λ).

The mean free path, λ, is arguably the most complex and sensitive of these parameters, as it is limited by a multitude of competing scattering mechanisms, such as those depicted in Figure 2.1(c). The total scattering rate ($1/\tau$) is found by summing the rates of all individual scattering processes, according to Matthiessen's rule:

$$\frac{1}{\tau_{total}} = \sum_i \frac{1}{\tau_i} = \frac{1}{\tau_{ph-ph}} + \frac{1}{\tau_{defect}} + \frac{1}{\tau_{boundary}} + \dots \tag{2.3}$$

The most important intrinsic scattering mechanism in a pure crystal is phonon-phonon scattering. These three-phonon processes, which arise from the anharmonicity of the interatomic potential, can be classified into two types: Normal (N) processes, which conserve the total phonon momentum, and Umklapp (U) processes, which do not. It was Rudolf Peierls who first showed that only U-processes provide a direct source of thermal resistance[100]. This is because, unlike N-processes which conserve the total phonon crystal momentum, U-processes can effectively reverse the direction of phonon momentum (by adding a reciprocal lattice vector, G). This "backward" scattering of phonons is the fundamental microscopic mechanism that impedes the net flow of heat and thus gives rise to intrinsic thermal resistance. At high temperatures (above the Debye temperature), U-process scattering rates are proportional to temperature, leading to the characteristic $\kappa \propto 1/T$ behavior of most crystalline dielectrics.

Extrinsic scattering mechanisms include:

— **Point Defect/Isotope Scattering:** Mass differences in the lattice, such as isotopes or impurity atoms, act as scattering centers. This type of scattering is most effective for high-frequency (short-wavelength) phonons and has a scattering rate that scales with frequency as ω^4 [66, 101].

— **Dislocation Scattering:** The strain fields around dislocations are effective at scattering mid-frequency phonons.

— **Boundary Scattering:** As will be discussed in great detail in Section 2.2, scattering from the physical boundaries of the material becomes dominant when the material's dimensions shrink to the nanoscale.

2.1.3 The Concept of Minimum Thermal Conductivity in Amorphous Solids

The phonon gas model described above is built on the premise of a periodic crystal lattice, which gives rise to well-defined wave vectors and phonon dispersion relations. As illustrated in Figure

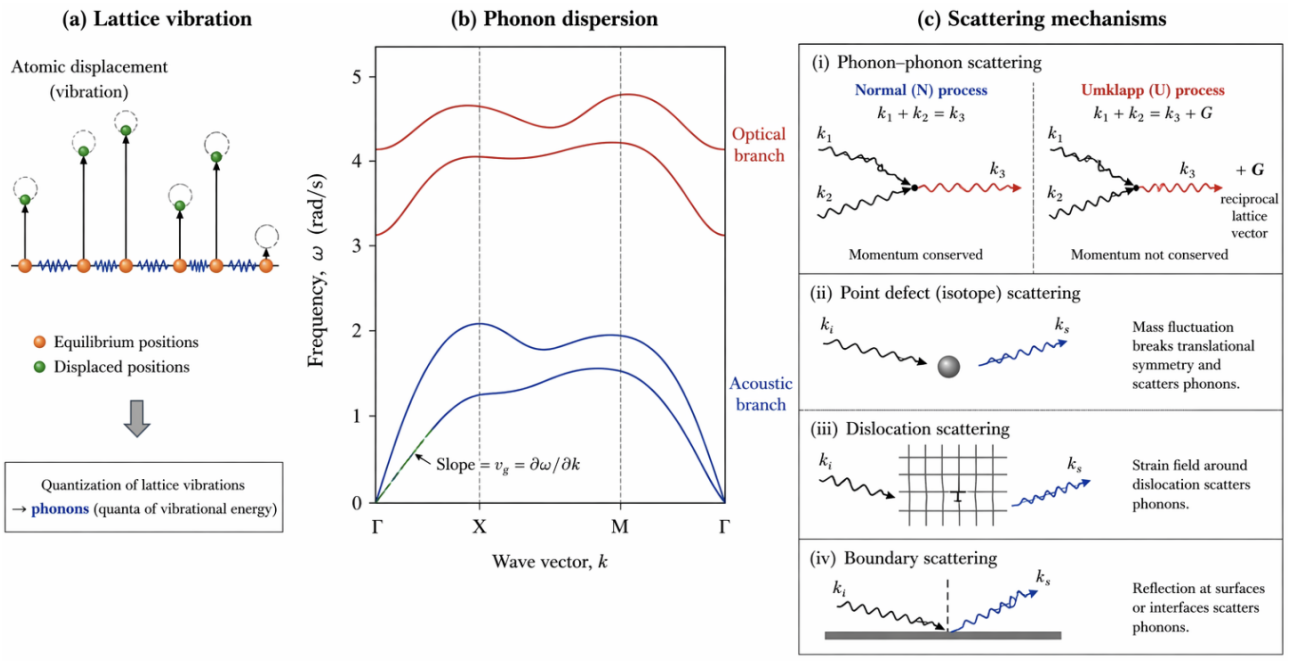


Figure 2.1 – A multi-panel schematic illustrating the key concepts of phonon-mediated heat transport. (a) One-dimensional lattice model showing atoms as a coupled oscillator system; the quantization of lattice vibrations gives rise to phonons. (b) Representative phonon dispersion relation ω(k) for a diatomic crystal, showing acoustic and optical branches. The slope $\partial\omega/\partial$k defines the phonon group velocity v_g, which governs the propagation speed of vibrational energy. (c) Schematic illustration of major phonon scattering mechanisms: (i) phonon-phonon scattering including Normal (N) and Umklapp (U) processes, (ii) point defect (isotope) scattering, (iii) dislocation scattering, and (iv) boundary scattering.

2.2, the thermal conductivity of a typical crystal (such as Silicon) rises sharply at low temperatures (following a T^3 dependence) until it reaches a sharp peak. This peak marks the crossover where the phonon mean free path is limited by the crystal boundaries. At higher temperatures, intrinsic phonon-phonon (Umklapp) scattering becomes dominant, causing the conductivity to decrease (typically as T^{-1}).

In amorphous materials, such as the silicon dioxide (SiO_2) and silicon nitride (SiN) that are central to this study, the absence of long-range periodic order fundamentally alters the nature of heat transport. Figure 2.2 contrasts this behavior with that of the crystal: the amorphous curve (a-SiO_2) shows no sharp peak. Instead, it exhibits a much lower magnitude and a monotonic rise in thermal conductivity. The vibrational modes are no longer propagating plane waves (phonons) that extend throughout the material. Instead, at higher frequencies, the modes become spatially localized, a phenomenon known as Anderson localization [102]. This strong scattering and localization mean that the concept of a phonon mean free path becomes ill-defined and is believed to be restricted to a length scale on the order of the interatomic spacing.

This observation led to the development of the concept of a "minimum thermal conductivity" (κ_{min}), a theoretical lower limit for the thermal conductivity of a material in its dense, disordered state. The idea was that heat could not be transported less efficiently than by a mechanism where vibrational energy hops randomly from one localized oscillator to the next. Several models have been proposed to quantify this limit. One of the earliest and most intuitive is the Einstein model, where each atom is treated as an independent 3D quantum harmonic oscillator vibrating at a single frequency ω_E. While this model fails for crystals, it provides a surprisingly reasonable picture for glasses[103, 104].

The most widely accepted and utilized model for κ_{min} was developed by Cahill, Watson, and Pohl, building on earlier ideas from Slack and Einstein [103, 104, 105]. The Cahill-Pohl model posits

that the mean free path for these vibrational modes cannot be shorter than half of their wavelength, a constraint known as the Ioffe-Regel limit for phonons[103, 106, 107]. By integrating over all vibrational modes (using a Debye density of states) and assuming this minimum scattering length, they derived an expression for the minimum thermal conductivity:

$$\kappa_{min} = \left(\frac{\pi}{6}\right)^{1/3} k_B n^{2/3} \sum_{i=1}^{3} v_i \left(\frac{T}{\Theta_{D,i}}\right)^2 \int_0^{\Theta_{D,i}/T} \frac{x^3 e^x}{(e^x - 1)^2} dx \tag{2.4}$$

where n is the number density of atoms, v_i is the speed of sound for the three polarization branches (one longitudinal, two transverse), and $\Theta_{D,i}$ is the Debye temperature for each branch. k_B is the Boltzmann constant, which provides the fundamental link between temperature and energy in statistical physics. It sets the characteristic thermal energy scale $k_B T$ associated with lattice vibrations and determines how phonon populations are distributed as a function of temperature. In the context of thermal transport, k_B governs the energy carried by each vibrational mode and ensures the correct conversion between microscopic energy scales and macroscopic quantities such as thermal conductivity. The numerical value of the Boltzmann constant is $k_B = 1.380\,649 \times 10^{-23}$ J K^{-1}.This model successfully predicts both the magnitude and the weak, glass-like temperature dependence of the thermal conductivity for a wide range of amorphous solids and disordered crystals. For SiO_2, this model predicts a room-temperature thermal conductivity of ~1.3 W/m·K, in excellent agreement with the experimentally measured value for bulk fused silica [108]. The concept of κ_{min} provides a crucial theoretical benchmark for the amorphous materials studied in this thesis and suggests that their thermal conductivity is fundamentally limited by their disordered atomic structure.

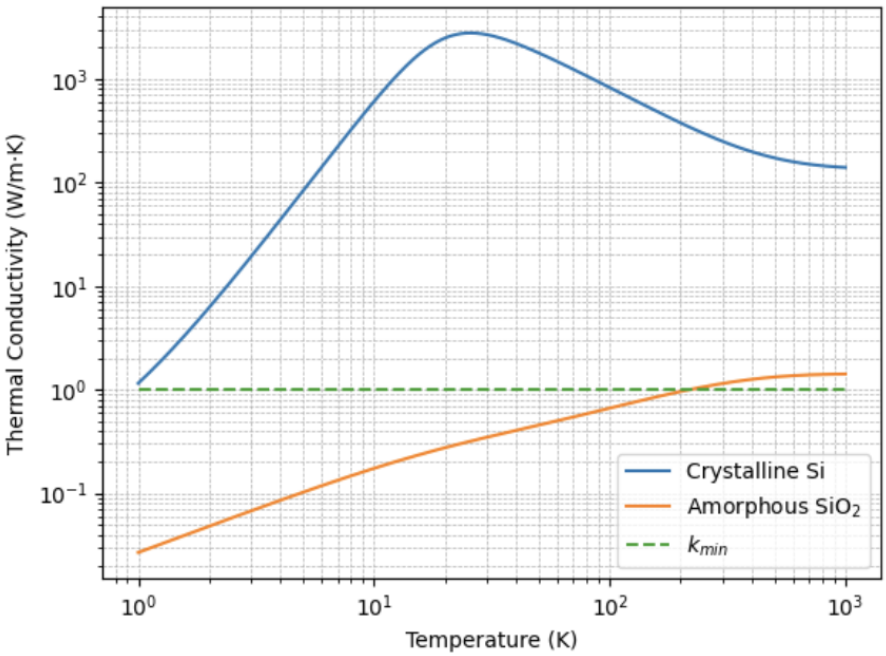


Figure 2.2 – Schematic plot of Thermal Conductivity vs. Temperature for a typical crystalline solid (e.g., Silicon) and an amorphous glass (e.g., a-SiO2). The plot highlights the contrast between the sharp peak observed in crystals due to phonon scattering and the monotonic, low-conductivity behavior of glasses. The plot is a re-creation based on classic experimental data from Glassbrenner ***et al.*** (1964) [109] for silicon, Zeller ***et al.*** (1971) [110] for a-SiO_2, and the minimum thermal conductivity limit ($\kappa_{\min}$) described by Cahill ***et al.*** (1989) [103].

2.2 Thermal Conduction in Nanostructures

When one or more dimensions of a material are reduced to a scale comparable to the mean free path of its heat carriers, its thermal properties can deviate dramatically from those of the bulk[52, 53]. This is the domain of nanoscale heat transport, where the extrinsic geometry of the system—its surfaces, boundaries, and interfaces—begins to play a dominant, and often controlling role in the thermal conduction process. The classical rules and intrinsic material properties defined in the previous section are no longer sufficient. This section explores the key phenomena that govern heat flow in nanostructures. We will first examine the classical size effect in thin films and nanowires, where phonon-boundary scattering leads to a significant reduction in thermal conductivity. We will then provide a more detailed treatment of the critical role of interfaces, introducing the concept of thermal boundary resistance (TBR) and reviewing the classical models used to describe it. Finally, we will discuss how these effects manifest in more complex systems like multilayer films and superlattices, where wave-like phonon behavior can emerge, leading to phenomena such as coherent transport and phononic bandgaps.

2.2.1 Size Effects: Phonon-Boundary Scattering in Thin Films

The most direct and widely studied manifestation of nanoscale heat transport is the reduction of thermal conductivity in thin films and nanowires due to phonon-boundary scattering. As first articulated by Casimir in his work on low-temperature thermal conductivity [111], when a material's characteristic dimension L (e.g., film thickness or wire diameter) becomes comparable to or smaller than the phonon mean free path λ_{bulk}, phonons are more likely to scatter off the system's boundaries than from intrinsic mechanisms (like Umklapp scattering). This introduces a powerful new scattering channel that shortens the effective mean free path, λ_{eff}, and consequently suppresses the thermal conductivity, κ_{eff}.

This phenomenon can be quantitatively understood by extending the kinetic theory of gases [50, 99], where thermal conductivity is given by $\kappa = \frac{1}{3}C_v v_g \lambda$. Under the relaxation time approximation (RTA), as formulated in the Callaway model [112], the total effective scattering rate (τ_{eff}^{-1}) can be expressed using Matthiessen's rule as the sum of the intrinsic bulk scattering rate and the boundary scattering rate [1, 111]:

$$\frac{1}{\tau_{eff}} = \frac{1}{\tau_{bulk}} + \frac{1}{\tau_{boundary}} \tag{2.5}$$

Converting relaxation times to mean free paths via the group velocity v_g (where $\lambda = v_g \tau$), we obtain the effective mean free path, λ_{eff}:

$$\frac{1}{\lambda_{eff}} = \frac{1}{\lambda_{bulk}} + \frac{1}{\lambda_{boundary}} \tag{2.6}$$

For a simple estimation, the boundary-limited mean free path, $\lambda_{boundary}$, is often taken to be on the order of the characteristic dimension, L. This simple approximation already captures the essential physics: as L becomes very small, $1/L$ becomes large, making λ_{eff} approach L and causing a significant reduction in effective thermal conductivity κ_{eff}. Consequently, the effective thermal conductivity is suppressed significantly below the bulk value.

A more rigorous treatment of boundary scattering requires solving the Boltzmann Transport Equation (BTE) with appropriate boundary conditions. This was notably achieved by the Fuchs-Sondheimer (F-S) model [67, 113], originally developed for electron transport in metal films but later adapted for phonons, most notably by Ziman [65]. The F-S model introduces a phenomenological specularity parameter, p ($0 \leq p \leq 1$), to describe the nature of the scattering event at the interface:Specular Scattering ($p \to 1$): The boundary acts as a perfect mirror. The parallel component of the phonon

wavevector is conserved, and the scattering does not impede the heat flux along the film. In this limit, size effects are suppressed. Diffuse Scattering ($p \to 0$): The phonon loses all memory of its incoming direction and is scattered randomly (isotropic distribution). This corresponds to the Casimir limit, where thermal resistance is maximized. The magnitude of p is not a free parameter but is physically determined by the surface roughness relative to the phonon wavelength. According to Ziman's theory, for a surface with root-mean-square (RMS) roughness η, the specularity parameter for a phonon with wavelength λ_{ph} (or wavevector k) is dependent on the angle of incidence θ:

$$p(k,\theta) = \exp\left(-16\pi^2 \frac{\eta^2}{\lambda_{ph}^2} \cos^2\theta\right) \tag{2.7}$$

This relationship highlights that "roughness" is a relative concept; a surface may appear smooth (specular) to long-wavelength acoustic phonons at low temperatures but rough (diffuse) to short-wavelength thermal phonons at room temperature.

Numerous experimental studies have validated these theoretical predictions. Classic measurements on single-crystal silicon thin films [58, 114, 115] have demonstrated that as film thickness decreases from a few micrometers to tens of nanometers, the room-temperature thermal conductivity drops by more than an order of magnitude compared to the bulk silicon value (~148 W/m·K). These experimental data points generally fall between the theoretical curves predicted by the F-S model for diffuse and partially specular boundaries. Table 2.1 summarizes the distinct regimes of boundary scattering and their impact on thermal transport.

Table 2.1 – Summary of Phonon Boundary Scattering Regimes in Thin Films

Scattering Regime	**Specularity Parameter (p)**	**Physical Mechanism**	**Impact on Thermal Conductivity (κ)**
Casimir Limit (Fully Diffuse)	$p = 0$	Phonons scatter in random directions upon hitting the boundary; momentum is randomized.	Maximum Reduction: κ is strictly limited by the film thickness L.
Ziman Regime (Partially Specular)	$0 < p < 1$	Dependent on surface roughness η. Transition region where $p = \exp(-16\pi^2\eta^2/\lambda^2)$.	Moderate Reduction: High-frequency (short λ) phonons scatter diffusely; low-frequency (long λ) phonons scatter specularly.
Specular Limit	$p = 1$	Mirror-like reflection; parallel momentum component is conserved.	No Size Effect: Boundaries do not resist heat flow; κ approaches κ_{bulk} regardless of thickness.

2.2.2 Interfacial Thermal Resistance(Kapitza Resistance)

While boundary scattering describes how surfaces affect transport within a material, an equally important phenomenon governs transport across the junction of two different materials. At any interface, a thermal resistance arises, which manifests as a finite temperature discontinuity, ΔT, even under a steady-state heat flux, J. This resistance is known as the Thermal Boundary Resistance (TBR)

or, historically, the Kapitza Resistance, and is defined as:

$$R_{TBR} = \frac{\Delta T}{J} \tag{2.8}$$

The units of TBR are typically $m^2 \cdot K/W$. This resistance acts in series with the intrinsic thermal resistances of the adjoining materials and, in many multilayered nanostructures, the sum of these TBR contributions can dominate the total thermal resistance of the entire stack [53, 77]. The physical origin of TBR lies in the difficulty of phonons, the primary heat carriers in dielectrics, to transmit from one material to another. This difficulty arises from two main sources:

— **Mismatch in Vibrational Properties:** The two materials on either side of the interface generally have different crystal structures, atomic masses, and interatomic bond strengths. This results in different phonon dispersion relations and phonon densities of states. A phonon propagating from material A to the interface may not find an available vibrational mode with a matching frequency and momentum in material B, making it likely to scatter back into material A rather than transmit. This concept forms the physical basis for the classic models of interfacial transport, such as the Acoustic Mismatch Model (AMM) and the Diffuse Mismatch Model (DMM) [**Swartz1989** , 53, 72].

— **Interface Imperfections:** Real interfaces are never atomically perfect. They contain a mixture of physical roughness, dislocations, point defects, vacancies, chemical mixing, and even amorphous interlayers. These imperfections act as powerful scattering centers that disrupt the transmission of phonons across the interface, further increasing the TBR[74, 78, 116].

The discovery of this phenomenon is credited to Pyotr Kapitza, who, in his 1941 experiments, observed a surprisingly large temperature jump at the interface between solid copper and superfluid liquid helium at cryogenic temperatures [71]. This observation could not be explained by classical heat transfer theories and spurred the development of microscopic models of interfacial heat transport.

2.2.3 Theoretical Models for Interfacial Resistance: AMM and DMM

To explain and predict TBR, two classical theoretical models were developed, both of which are based on the concept of phonon transmission probability across an interface.

— **The Acoustic Mismatch Model (AMM)**, first developed by Khalatnikov and later refined by Little, provides the simplest picture [72, 117]. The AMM treats phonons as plane waves in a continuous elastic medium and assumes a perfectly flat and ordered interface. In this framework, the transmission and reflection of phonons are treated analogously to acoustic waves, governed by Snell's law and determined by the acoustic impedances ($Z = \rho v$, where ρ is the density and v is the speed of sound) of the two materials. The transmission probability for a phonon incident at an angle θ_1 is given by:

$$\alpha_{1\to2}(\theta_1) = \frac{4Z_1 Z_2 \cos\theta_1 \cos\theta_2}{(Z_1 \cos\theta_1 + Z_2 \cos\theta_2)^2} \tag{2.9}$$

The total heat conductance (inverse of resistance) is then found by integrating this probability over all incident angles and phonon modes. The AMM correctly predicts that a large mismatch in acoustic impedance will lead to high reflectivity and thus a high TBR. However, it is only valid at very low temperatures where only long-wavelength acoustic phonons are excited and the assumption of a perfect, specular interface holds. At room temperature, the AMM often severely underestimates the experimentally measured TBR, sometimes by an order of magnitude or more, because it completely neglects scattering from interface defects and the contribution of the full phonon spectrum [74].

— **The Diffuse Mismatch Model (DMM)** provides an alternative picture that is often more applicable at higher temperatures and for more disordered interfaces [74]. The DMM abandons the assumption of a perfect interface and instead posits that any phonon incident on the interface is scattered diffusely, completely losing its memory of its original momentum and mode. The phonon is then assumed to be elastically re-emitted into either material 1 or 2 with a probability that is simply determined by the relative availability of phonon states (density of states) on each side. The transmission probability from material 1 to 2 is then given by:

$$\alpha_{1\to 2} = \frac{\sum_j v_{g,2,j}^{-2} N_{2,j}(\omega)}{\sum_i v_{g,1,i}^{-2} N_{1,i}(\omega) + \sum_j v_{g,2,j}^{-2} N_{2,j}(\omega)} \tag{2.10}$$

where the sum is over all phonon modes, and $N(\omega)$ is the phonon density of states. The DMM generally provides better agreement with experimental data for non-ideal interfaces at moderate to high temperatures because it implicitly accounts for the crucial effect of interface disorder. However, it is also an idealized model, as it assumes that all phonon scattering at the interface is both 100% diffuse (fully random) and purely elastic (no change in phonon frequency), which is not always the case. More advanced models and molecular dynamics (MD) simulations have shown that real interfaces often exhibit partial specular scattering and, crucially, that inelastic phonon scattering can play a significant role in thermal transport across dissimilar materials [74, 78, 79, 116].

The real physics of phonon transport at an interface is far more complex, often involving a combination of specular and diffuse scattering, as well as inelastic scattering processes. This highlights the critical need for direct experimental measurement of TBR for technologically relevant interfaces.

2.2.4 Heat Conduction in Multilayer Systems and Superlattices

When multiple thin films are stacked together to form a multilayer system or a superlattice (a periodic multilayer structure), the thermal transport properties become even more complex and interesting. The total thermal resistance of such a stack is a combination of the intrinsic resistance of each layer (which is already reduced by boundary scattering) and the TBR of each interface. In many cases, especially when the layers are very thin, the sum of the interface resistances can be the dominant contributor to the total thermal impedance of the structure [118].

Furthermore, in highly ordered superlattices with flat, sharp interfaces and a repeating period, a fascinating transition can occur between incoherent and coherent phonon transport.

— **Incoherent Transport:** When the layer thicknesses are much larger than the phonon wavelengths and the interfaces are rough, phonons can be treated as classical particles. They propagate within each layer and scatter incoherently at the interfaces. In this regime, the thermal conductivity of the superlattice can be approximated by a series resistor model that simply sums the resistances of the layers and their interfaces.

— **Coherent Transport (Phonon Wave Effects):** When the layer thicknesses become comparable to the dominant phonon wavelengths and the interfaces are atomically sharp and periodic, the wave-like nature of phonons becomes the predominant transport mechanism. That is, phonons maintain their phase coherence as they propagate and reflect from the multiple interfaces. This coherence leads to wave-like interference phenomena, much like light in a Bragg reflector or electrons in a crystal lattice. This coherence can lead to the modification of the material's phonon dispersion relation, causing the original dispersion curves to "fold" into a smaller superlattice Brillouin zone, which creates "minibands" and opens up "phononic bandgaps" [68, 119]. These bandgaps can flatten the dispersion curves (reducing group velocities) and even forbid the propagation of phonons in certain frequency ranges altogether.

The transition from incoherent to coherent transport implies a crossover in phonon physics, which is schematically plotted in Figure 2.3 for a Si/Ge superlattice. This curve exhibits a theoretical "U-shape" defined by two competing regimes. In the incoherent "particle" regime (typically period $L > 10$ nm), decreasing the superlattice period increases the density of interfaces. Each interface introduces a Thermal Boundary Resistance (TBR), effectively impeding heat flow. Consequently, the effective thermal conductivity decreases monotonically with period thickness, a trend well-documented in experimental studies [120]. Conversely, in the coherent "wave" regime (short periods), theoretical models predict that as the period becomes comparable to the phonon coherence length, phonons propagate as waves through a new effective crystal structure (minibands) [56]. This coherence should theoretically reduce scattering, causing the thermal conductivity to rise again after reaching a minimum. It is important to note that while the bulk thermal conductivities of Si ($\approx$ 148 W m$^{-1}\kappa^{-1}$) and Ge ($\approx$ 60 W m$^{-1}\kappa^{-1}$) are high at room temperature [109], the thermal conductivity of their superlattices can fall significantly below the "Alloy Limit" (dashed line). Although the "U-shaped" recovery is difficult to observe experimentally due to interface roughness destroying coherence, the concept of a minimum conductivity remains critical for understanding the physical limits of heat conduction. While the amorphous multilayer films studied in this thesis are not expected to support coherent transport, understanding the powerful and multifaceted role of interfaces in dictating the thermal properties of layered systems is a universally critical concept.

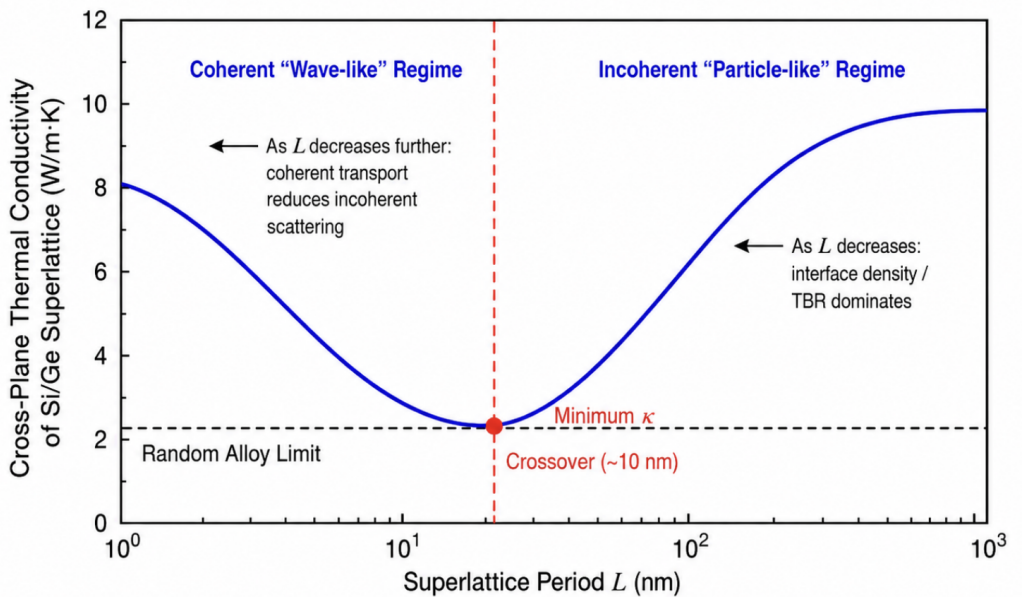


Figure 2.3 – Conceptual illustration of the cross-plane thermal conductivity of a Si/Ge superlattice as a function of period length. The curve illustrates the crossover from incoherent (particle-like) transport at larger periods to coherent (wave-like) transport at short periods. While experiments typically observe the sharp decrease in the incoherent regime (right side) While experiments typically observe the sharp decrease in the incoherent regime (right side), as reported by Lee ***et al.*** (1997) [120], theoretical models predict a rise, forming a U-shaped trend, in the coherent regime (left side), as described by Chen (1998) [56]. The dashed line represents the random alloy limit.

2.3 Review of Thermal Conductivity Measurement Techniques

The accurate experimental determination of thermal properties, particularly for thin films and nanostructures, represents a significant metrological challenge. The minute physical dimensions of these materials mean that the resulting temperature differences are often minuscule, making them difficult to measure accurately and prone to environmental noise. Furthermore, the property of

interest is often buried beneath other layers, making it inaccessible to direct probing. Over the past several decades, a sophisticated suite of experimental techniques has been developed to overcome these challenges. This section provides a critical review of these methods, classifying them into broad categories, discussing their underlying principles, and evaluating their respective strengths and weaknesses. This survey will begin with a general overview of steady-state versus transient techniques, followed by a detailed look at prominent modern optical methods, and will culminate in an in-depth analysis of the 3-ω method, which forms the experimental foundation of this thesis.

2.3.1 Overview of Steady-State and Transient Method

Thermal conductivity measurement techniques can be broadly classified into two main families: steady-state and transient methods.

Steady-State Methods

Steady-state methods are the most direct application of Fourier's law of heat conduction ($J = -\kappa\nabla T$). In a steady-state experiment, a constant, time-invariant heat flux (J) is applied to the sample, and the system is allowed to reach thermal equilibrium, where a stable, unchanging temperature gradient (∇T) is established. By measuring both J and ∇T, the thermal conductivity κ can be calculated directly. Classic examples for bulk materials include the guarded hot-plate method [121] and the Searle's bar experiment[122]. While conceptually simple and straightforward, steady-state methods are notoriously difficult to implement for thin-film samples. The primary challenges include:

— **Parasitic Heat Loss:** Accurately measuring the heat flux that flows only through the sample is extremely difficult. Unwanted heat losses to the surroundings via convection and radiation can be significant, leading to a systematic overestimation of the thermal conductivity. While techniques like guarding can mitigate this for bulk samples, it is nearly impossible for thin films.

— **Temperature Measurement:** Measuring the small temperature difference across a film that may be only nanometers thick is a formidable challenge. Attaching physical sensors like thermocouples would dominate the thermal properties of the film itself.

— **Substrate Effects:** Thin films must be supported by a substrate, which is typically much thicker and more thermally conductive. The vast majority of the applied heat will therefore bypass the film and flow through the substrate, making it exceedingly difficult to isolate the thermal resistance of the film alone.

Due to these severe limitations, steady-state methods are rarely used for the characterization of thin dielectric films, although some specialized microfabricated structures have been developed to attempt such measurements [51].

Transient Methods

Transient methods, in contrast, have become the standard for thin-film thermometry. In a transient experiment, a time-varying thermal excitation—either a short pulse or a periodic wave—is applied to the sample, and the resulting time-dependent temperature response is monitored. Instead of measuring absolute temperatures and heat fluxes, these methods typically measure the temporal evolution of the temperature field. The data is then fitted to a solution of the transient heat diffusion equation[94]:

$$\rho c_p \frac{\partial T(\mathbf{r},t)}{\partial t} = \nabla \cdot [\kappa \nabla T(\mathbf{r},t)] + g(\mathbf{r},t) \tag{2.11}$$

where ρc_p is the mass specific heat capacity and $g(\mathbf{r},t)$ is the time-varying heat source term. Transient methods often measure the thermal diffusivity, $\alpha = \kappa/(\rho c_p)$, which describes how quickly

the material responds to a change in temperature. If the heat capacity is known, the thermal conductivity can be readily calculated. The key advantages of transient methods over their steady-state counterparts include:

— **Reduced Sensitivity to Heat Loss:** Because the measurements are typically performed over short timescales (microseconds to picoseconds), the effects of slow, quasi-static heat losses to the environment are greatly minimized.

— **High Sensitivity and Signal-to-Noise:** By using periodic heating and lock-in detection, it is possible to extract extremely small temperature oscillation signals from a noisy background, enabling high-precision measurements.

— **Depth Profiling:** In periodic heating methods, the frequency of the thermal wave can be varied. The thermal penetration depth, $L_p \approx \sqrt{\alpha/\omega}$, is frequency-dependent. This allows one to probe different depths within the sample, making it possible to separate the thermal properties of a thin film from its underlying substrate.

Table 2.2 summarizes the key differences between these two classes of measurement techniques, highlighting why transient methods are preferred for thin-film applications.

Table 2.2 – Comparison of steady-state vs. transient thermal measurement methods for thin films.

Method Type	**Principle**	**Key Advantages**	**Key Disadvantages (for Thin Films)**
Steady-State	Direct application of Fourier's Law ($J = -\kappa\nabla T$) by measuring a constant heat flux and the resulting stable temperature gradient.	Conceptually simple; direct measurement of thermal conductivity κ.	Highly susceptible to parasitic heat loss; difficult to measure ΔT across thin films; substrate shunting effect is severe.
Transient	Application of a time-varying heat source and measurement of the time-dependent temperature response. Data is fit to the heat diffusion equation.	Insensitive to slow heat losses; high signal-to-noise ratio (e.g., with lock-in); allows for depth profiling via frequency dependence.	Typically measures thermal diffusivity α; requires knowledge of heat capacity to find κ; often more complex experimental setup and analysis.

2.3.2 Advanced Optical Techniques:TDTR and Raman Thermometry

Among the many transient methods, non-contact optical techniques have emerged as particularly powerful and versatile tools for probing nanoscale heat transport, as they avoid the issue of placing physical sensors on the sample.

Time-Domain Thermoreflectance (TDTR)

Time-Domain Thermoreflectance (TDTR) is arguably the most sensitive and widely used pump-probe technique for measuring the thermal properties of thin films and interfaces [123]. A detailed schematic of a typical TDTR experimental setup is shown in Figure 2.4. The typical TDTR setup utilizes an ultrashort pulse laser (typically a Ti:Sapphire laser producing ~100 fs pulses) whose output is split into two beams: a "pump" beam and a much lower-power "probe" beam. The pump beam power

is kept relatively high compared to the probe to induce heating, but must be kept low in an absolute sense. This is critical to avoid a large steady-state temperature rise (ΔT_{DC}) at the sample surface, which could induce nonlinear effects (since thermal properties like κ are themselves temperature-dependent, $\kappa = \kappa(T)$). The entire measurement relies on this linear perturbation assumption. Before reaching the sample, the pump beam is passed through an electro-optic modulator (EOM) to impose a high-frequency modulation (typically 1–20 MHz) for lock-in detection. The probe beam is passed through a mechanical delay stage that adjusts its optical path length. Since the speed of light is constant, this change in path length translates into a precise temporal delay relative to the pump pulse. Both beams are focused onto the same spot on the sample surface, which must first be coated with a thin (50–100 nm) metal film (e.g., Al, Au, or Pt) that acts as a thermoreflectance transducer.

The measurement proceeds as follows: the modulated pump pulse is absorbed by the metal film, causing a rapid, periodic heating event. This heat then diffuses through the underlying thin film(s) and into the substrate. The probe pulse, which is delayed in time, measures the temperature of the metal film surface by detecting the minute change in its reflectivity (ΔR), as the reflectivity of a metal is weakly dependent on temperature. This is known as the thermoreflectance effect. By systematically varying the delay time of the probe pulse from picoseconds to several nanoseconds, one can precisely map out the temperature decay curve of the surface. The shape of this decay curve is exquisitely sensitive to the thermal properties of the underlying layers. The experimental data (typically the ratio of the in-phase to out-of-phase signals from the lock-in amplifier as a function of delay time) is then fit to a multi-parameter thermal model that solves the heat diffusion equation for the multilayer stack.

The key strengths of TDTR are its exceptional time resolution (~ps), which allows for the direct observation of non-equilibrium thermal processes, and its very high sensitivity to thermal boundary resistance, making it the gold standard for TBR measurements [78, 52]. However, it also has limitations: the setup is complex and expensive, the analysis requires a multi-parameter fit where some parameters (like the heat capacity and thermal conductivity of the metal transducer) must be known accurately, and the required deposition of a metal film can alter the very surface or interface that one wishes to study.

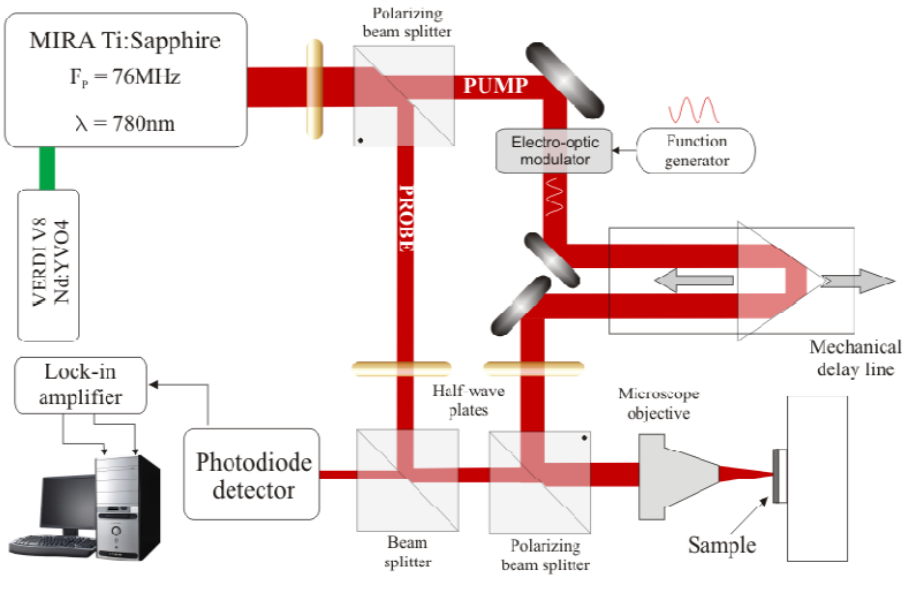


Figure 2.4 – A detailed schematic of a typical Time-Domain Thermoreflectance (TDTR) experimental setup. The diagram shows the ultrashort pulse laser, beam splitters, the pump path with an EOM, the probe path with a mechanical delay stage, and the reflected probe beam directed to a photodiode and lock-in amplifier. This schematic is based on the typical configuration described in foundational TDTR methodology papers, such as Cahill (2004) [123].

Raman Thermometry

Raman Thermometry is another powerful non-contact optical technique that leverages the inelastic scattering of light by phonons [52]. When a monochromatic laser is focused on a sample, most of the light is scattered elastically (Rayleigh scattering), but a small fraction is scattered inelastically, either losing energy by creating a phonon (Stokes scattering) or gaining energy by absorbing a phonon (anti-Stokes scattering). The energy shift of the scattered light corresponds to the energy of specific optical phonon modes in the material. The temperature of the material can be determined in several ways from the Raman spectrum:

— **Stokes/Anti-Stokes Ratio:** The ratio of the integrated intensities of the Stokes and anti-Stokes peaks is directly related to the phonon population and thus to the absolute temperature.

— **Peak Position:** As the material heats up, thermal expansion and anharmonic effects cause the phonon energies to change, resulting in a shift (typically a redshift) of the Raman peak position.

— **Peak Width:** Increased temperature leads to shorter phonon lifetimes due to increased phonon-phonon scattering, which results in a broadening of the Raman peak (linewidth).

By using the laser as both a local heat source and the excitation source for the temperature measurement, one can perform a thermal conductivity measurement. In this technique, the Raman scattered light—which is generated by the interaction of the laser with the sample's phonons—acts as the true temperature probe. The laser power is varied, and the corresponding temperature rise at the center of the laser spot is measured via one of the methods above. This relationship between laser power and temperature rise is then fit to a solution of the heat diffusion equation to extract the thermal conductivity of the material [124]. The key advantages of Raman thermometry are its high spatial resolution (sub-micron) and its ability to probe the temperature of the material directly without a transducer layer. Its primary limitations are a generally lower temperature resolution compared to TDTR or 3-ω, the requirement of a strong and temperature-sensitive Raman peak in the material of interest, and potential complications from laser-induced stress, which can also shift the Raman peak.

2.3.3 Strategic Selection: The 3ω Method

While the optical techniques discussed in the previous section (Section 2.3.2), such as Time-Domain Thermoreflectance (TDTR), offer excellent temporal resolution for ultrafast thermal phenomena, the 3-omega (3ω) method was selected as the primary characterization tool for this research. This electro-thermal technique has established itself as the "gold standard" for measuring the thermal conductivity of dielectric materials, particularly amorphous thin films. The method was originally pioneered by Cahill et al. for bulk glasses and subsequently adapted for thin-film measurements by Lee and Cahill[85]. Their work demonstrated that by manipulating the frequency of the driving current, the thermal penetration depth could be precisely controlled, allowing for the separation of the film's intrinsic thermal properties from the substrate effects.

The decision to employ the 3-omega method in this study, rather than optical alternatives like the Flash method or TDTR, is driven by several critical advantages relevant to the dielectric multilayers under investigation:

— **High Sensitivity for Low-κ Materials:** The 3-omega method provides an exceptional signal-to-noise ratio specifically for low-thermal-conductivity materials (such as silicon nitride and oxide), where optical methods often struggle with sensitivity.

— **Suppression of Radiative Losses:** Unlike steady-state methods that are susceptible to radiative heat losses, particularly at high temperatures, the frequency-domain nature of the 3-omega technique effectively minimizes blackbody radiation errors. This ensures high accuracy across the wide temperature ranges explored in this thesis.

— **Interface Characterization:** A key requirement for this work is the ability to distinguish between the intrinsic thermal conductivity of the layers and the thermal boundary resistance (TBR) at interfaces. The frequency-dependent nature of the 3-omega signal allows for a "thermal depth profiling" approach, which is instrumental in isolating these interface effects.

It is acknowledged that the 3-omega method imposes stricter requirements on sample preparation—specifically the need for complex micro-fabrication of heater patterns—compared to non-contact optical techniques. However, the benefits in measurement precision and the ability to probe sub-surface thermal transport outweigh these fabrication challenges for the samples studied here.

In recent years, the 3-omega method has been extensively utilized to investigate phonon scattering mechanisms in amorphous solids. For instance, Zink and Hellman[125] successfully applied this technique to study the specific heat and thermal conductivity of amorphous silicon nitride, providing critical insights into heat transport in disordered lattices. Furthermore, the method's compatibility with numerical modeling—as demonstrated by Jacquat et al. [126]—allows for the extraction of thermal properties even in complex geometries where analytical solutions are limited. Given the multilayered nature of the samples in this thesis, this compatibility with Finite Element Method (FEM) simulations is a decisive advantage.

In summary, the 3-omega method represents the most robust and appropriate tool for this study. The detailed theoretical framework, including the mathematical derivation of the signal generation, the heat diffusion models, and the discussion on validity limits (such as thermal penetration depth constraints), will be comprehensively presented in Chapter 3 (Section 3.1). The experimental implementation, including the micro-fabrication process and the detailed description of the measurement bench (e.g., Wheatstone bridge circuit and lock-in amplifier setup), will be detailed in Chapter 3 (Section 3.2).

Chapter 3

Experimental and Numerical Methodology

Having established the technological imperative for accurate thermal property data in the preceding chapters, this chapter transitions from the *why* to the *how*. It details the comprehensive methodology employed in this thesis for the thermal characterization of thin dielectric films and complex multilayer stacks, centered around the 3-omega (3ω) technique. The accurate measurement of these properties is essential for the effective thermal management of modern electronic and optoelectronic devices. While the 3ω method is a powerful and widely used technique, conventional analytical models often fall short when applied to the intricate, multi-layered systems that are the focus of this research. This limitation necessitates a more robust and versatile approach.

To overcome these challenges, this chapter details a hybrid methodology developed to deconvolve the thermal properties of complex dielectric systems with high precision. This framework forms the cornerstone of the research, tightly coupling high-precision physical measurements with sophisticated Finite Element Method (FEM) computational modeling to create a powerful analytical tool. This chapter serves as the practical and technical foundation of the entire research effort, providing a complete and transparent account of the tools and procedures used to generate the results presented in subsequent chapters.

The chapter is structured logically to provide a foundational "how-to" for the research presented.

First, it provides an extensive exploration of the theoretical framework of the 3ω method. This includes a detailed derivation of the signal generation principle from fundamental heat diffusion concepts, followed by a thorough review of the key analytical solutions developed for various sample geometries. Crucially, this section also explicitly discusses the assumptions and inherent limitations of these analytical models, thereby establishing the clear motivation for adopting numerical simulation.

Next, the chapter details the experimental implementation. This encompasses the complete workflow for sample fabrication, from substrate preparation and dielectric film deposition (specifically the PECVD process) to the microfabrication steps (photolithography, metallization, lift-off) used to pattern the metallic heater/sensor structures. It then provides a detailed description of the custom-built 3ω experimental bench, including the specific instrumentation (e.g., lock-in amplifier, Wheatstone bridge), their configuration, and the critical process of Temperature Coefficient of Resistance (TCR) calibration for each sensor.

Finally, the chapter introduces the numerical modeling approach used to overcome the limitations of analytical solutions. This section details the implementation of a high-fidelity "virtual twin" of the 3ω experiment using COMSOL Multiphysics ®. It covers the model setup, the governing equations for frequency-domain heat transfer, the implementation of boundary conditions (including heat source, far-field conditions, and interface thermal resistance), and the meshing strategies employed to ensure numerical accuracy. This detailed forward model is the essential prerequisite for the inverse fitting method used to extract the final thermal property data.

Together, these sections provide a complete account of the theoretical underpinnings, experimental procedures, and numerical techniques that form the methodological backbone of this dissertation,

ensuring the rigor and reproducibility of the results.

3.1 Theoretical Framework of the 3ω Method

The 3ω method is a well-established AC electrothermal technique renowned for its sensitivity in measuring the thermal properties of thin films and bulk materials [84, 127]. This section delves into the detailed theoretical foundation, starting from basic heat diffusion principles, deriving the signal generation mechanism, exploring analytical solutions for various geometries, and critically evaluating their limitations. The derivations presented here largely follow the detailed analysis conducted in the preliminary work associated with this thesis.

3.1.1 Fundamental Principle: Signal Generation

The core idea relies on using a microfabricated metallic strip simultaneously as a localized AC heater and a sensitive resistance thermometer.

Small Temperature Variations and Resistance: For small temperature changes (ΔT) around a reference temperature T_0, the resistance of the metallic strip (R_0 at T_0) changes linearly:

$$R(T) = R_0(1 + \beta\Delta T) \tag{3.1}$$

where $\beta = (1/R_0)(dR/dT)$ is the Temperature Coefficient of Resistance (TCR).

Joule Heating and 2ω Power Oscillation: An alternating current

$$I(t) = I_0 \cos(\omega t) \tag{3.2}$$

is driven through the metallic strip. The instantaneous power dissipated due to Joule heating is $P(t) = I(t)^2 R(t)$. Assuming the resistance change is small, $R(t) \approx R_0$, the power becomes: $P(t) \approx I(t)^2 R_0 = I_0^2 R_0 \cos^2(\omega t)$. Using the identity $\cos^2(x) = \frac{1}{2}(1 + \cos(2x))$, the power can be written as:

$$P(t) = \frac{1}{2} I_0^2 R_0 + \frac{1}{2} I_0^2 R_0 \cos(2\omega t) = P_{DC} + P_{AC}(t) \tag{3.3}$$

The heating power oscillates at exactly twice the driving frequency (2ω) via the term $P_{AC}(t) = P_{2\omega} \cos(2\omega t)$, where $P_{2\omega} = \frac{1}{2} I_0^2 R_0$ is the root mean square(rms) power dissipated in the heater in W. This decomposition reveals both a steady heating effect and a periodic fluctuation in power dissipation, which are crucial for precise temperature control and thermal measurement application.

Heat Diffusion and Temperature Response: This periodic heating ($P_{AC}(t)$) acts as a source term driving heat diffusion into the sample. The fundamental equation governing heat conduction is Fourier's law ($\mathbf{q} = -\kappa \nabla T$) and the heat diffusion equation derived from energy conservation is written as:

$$\frac{\partial T}{\partial t} = \frac{k}{\rho C_p} \nabla^2 T + \frac{g}{\rho C_p} = \alpha \nabla^2 T + \frac{g}{\rho C_p} \tag{3.4}$$

Here, $g(\mathbf{r}, t)$ represents the volumetric heat generation rate (e.g., Joule heating). In the passive substrate layers where no internal heat is generated, g is taken as zero, reducing the equation to the homogeneous diffusion form. And κ is thermal conductivity, ρc_p is volumetric heat capacity, and α is thermal diffusivity. Since the heating source is sinusoidal at 2ω, the resulting temperature field will also oscillate at 2ω after reaching a quasi-steady state. We can express the temperature change

as $T(\mathbf{r}, t) = T_{dc}(\mathbf{r}) + \theta(\mathbf{r})e^{i2\omega t}$, where $\theta(\mathbf{r})$ is the complex amplitude of the temperature oscillation. Substituting this into the heat equation yields the time-harmonic (Helmholtz) form:

$$(i2\omega)\rho c_p \theta(\mathbf{r}) = \nabla \cdot (\kappa \nabla \theta(\mathbf{r})) + Q_{2\omega}(\mathbf{r}) \tag{3.5}$$

The solution $\theta(\mathbf{r})$ contains both amplitude and phase information. For the heater itself, the average temperature oscillation is $\Delta T(t) = \Delta T_{DC} + \Delta T_{2\omega} \cos(2\omega t + \phi)$.

Resistance Oscillation and 3ω Voltage Generation: The 2ω temperature oscillation causes a 2ω resistance oscillation: $R(t) \approx R_{avg}(1 + \beta \Delta T_{2\omega} \cos(2\omega t + \phi))$, where R_{avg} is the resistance at the average operating temperature. The voltage across the heater is $V(t) = I(t)R(t) = [I_0 \cos(\omega t)] \times [R_{avg}(1 + \beta \Delta T_{2\omega} \cos(2\omega t + \phi))]$. Expanding this product yields terms at ω and 3ω. The crucial third-harmonic component is:

$$V_{3\omega}(t) = \frac{1}{2} I_0 R_{avg} \beta \Delta T_{2\omega} \cos(3\omega t + \phi) \tag{3.6}$$

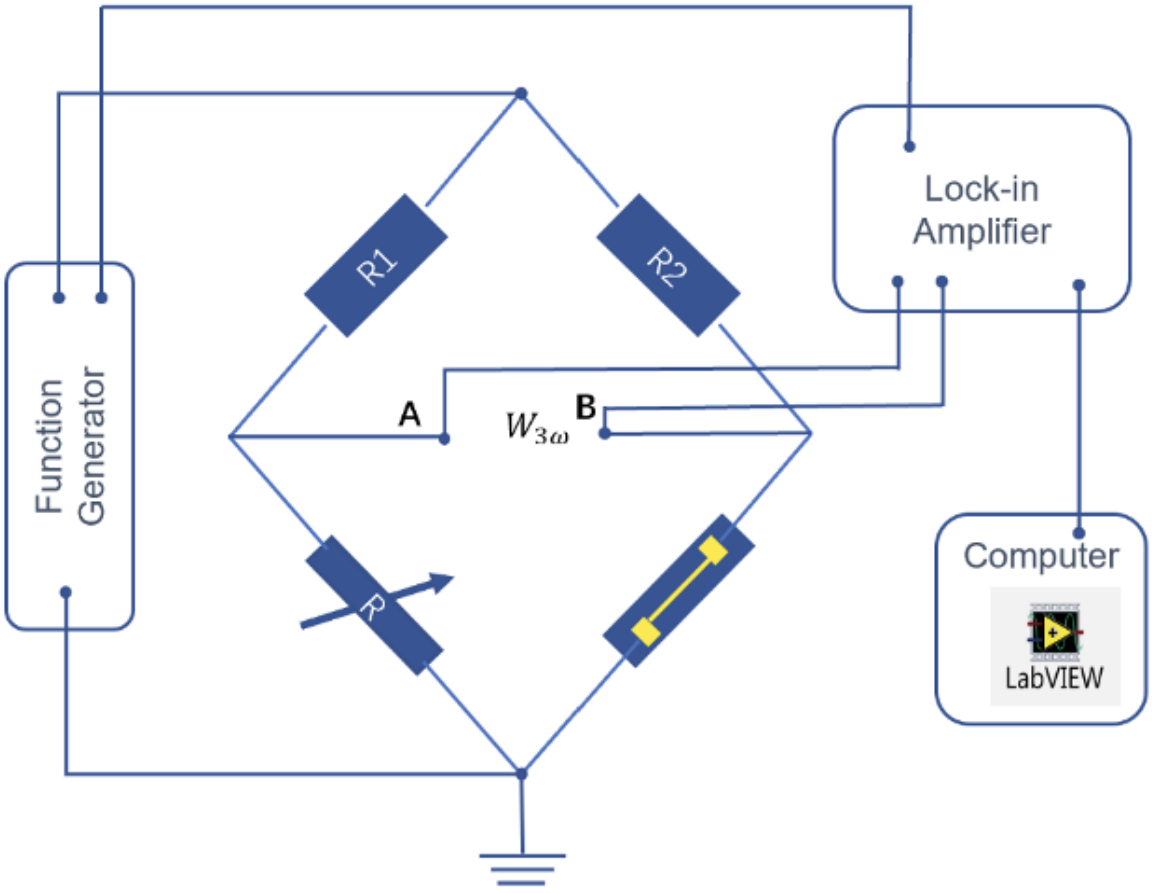


Figure 3.1 – A detailed schematic of a typical 3-ω experimental setup. The diagram shows the function generator, current source, sample in a 2-point probe configuration (often with a Wheatstone bridge), and a lock-in amplifier set to measure the 3ω voltage.

This tiny third-harmonic voltage, $V_{3\omega}$, is the key signal in the 3-ω experiment. Its amplitude is directly proportional to the amplitude of the temperature oscillation, $\Delta T_{2\omega}$. However, this small signal (typically nanovolts to microvolts) must be extracted from the much larger 1ω signal (typically millivolts to volts). A typical experimental setup designed to solve this challenge is shown schematically

in Figure 3.1. The system is driven by a Function Generator (at frequency ω). A Wheatstone Bridge circuit (composed of the sample, a variable resistor R, and two fixed resistors R1, R2) is used to cancel out, or "null," the majority of the large $V_{1\omega}$ voltage. The remaining small differential voltage, which contains the $V_{3\omega}$ signal, is then fed into a Lock-in Amplifier that is phase-locked to the 3ω frequency. This phase-sensitive detection allows the amplitude and phase of the $V_{3\omega}$ signal to be extracted with extremely high precision. The amplitude and phase of this extracted signal are, in turn, dictated by how efficiently the heat generated by the line diffuses into the underlying sample, and are therefore a sensitive function of the sample's thermal properties. The amplitude $|V_{3\omega}| = \frac{1}{2} I_0 R_{avg} \beta \Delta T_{2\omega}$ is directly proportional to $\Delta T_{2\omega}$. Measuring $V_{3\omega}$ (complex amplitude) allows determination of the complex temperature oscillation $\Delta T_{2\omega}$ using the relation:

$$\Delta T_{2\omega} \approx \frac{2V_{3\omega}}{V_{1\omega}} \frac{1}{\beta} \tag{3.7}$$

where $V_{1\omega} \approx I_0 R_{avg}$ is the complex amplitude of the fundamental voltage. This $\Delta T_{2\omega}$ is the primary experimental quantity related to the sample's thermal properties.

3.1.2 Analytical Solution: Internal Line Source in Infinite Cylinder

To understand the spatial decay of the thermal wave, it is useful to first consider the idealized case of an infinitely long line heater embedded along the axis ($r = 0$) of an infinite cylinder as shown in Figure 3.2.

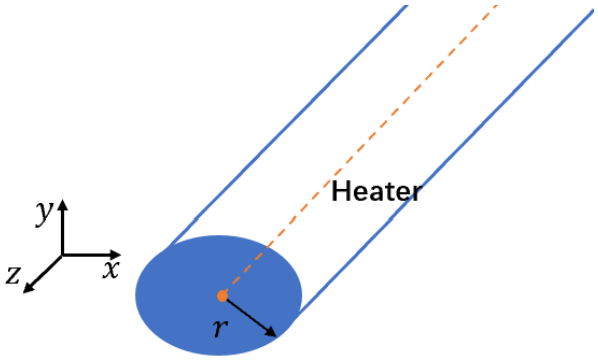


Figure 3.2 – Geometry of an infinite circular cylinder with a 1D line heater along its axis.

The heat diffusion equation in cylindrical coordinates for the complex temperature oscillation $\theta(r)$ is:

$$\frac{d^2\theta}{dr^2} + \frac{1}{r}\frac{d\theta}{dr} - \gamma^2\theta = 0 \tag{3.8}$$

where $\gamma = \sqrt{i2\omega/\alpha} = (1+i)\sqrt{\omega/\alpha}$ is the complex thermal wave vector. This is the modified Bessel equation of order zero. The general mathematical solution is a linear combination of the two modified Bessel functions, $I_0(\gamma r)$ and $K_0(\gamma r)$. As plotted in Figure 3.3, the I_0 function diverges to infinity as r increases, which is physically unrealistic for a temperature in an infinite medium. Therefore, the only physical solution is the one that decays to zero, which is the function of the second kind, K_0 [94]:

$$\theta(r) = CK_0(\gamma r) \tag{3.9}$$

The constant C is determined by applying the heat flux boundary condition near the source. For a line source emitting AC power amplitude $P_{2\omega}$ per unit length, the flux through a small cylinder of radius r_0 must equal the source power: $-\kappa(d\theta/dr)|_{r_0}(2\pi r_0) = P_{2\omega}$. Using the properties $dK_0(\xi)/d\xi =$

$-K_1(\xi)$ and the small argument limit $K_1(\xi) \approx 1/\xi$ (where ξ is the argument of the function), we find $C = P_{2\omega}/(2\pi k)$. Thus, the temperature oscillation is:

$$\theta(r) = \frac{P_{2\omega}}{2\pi k} K_0(\gamma r) \tag{3.10}$$

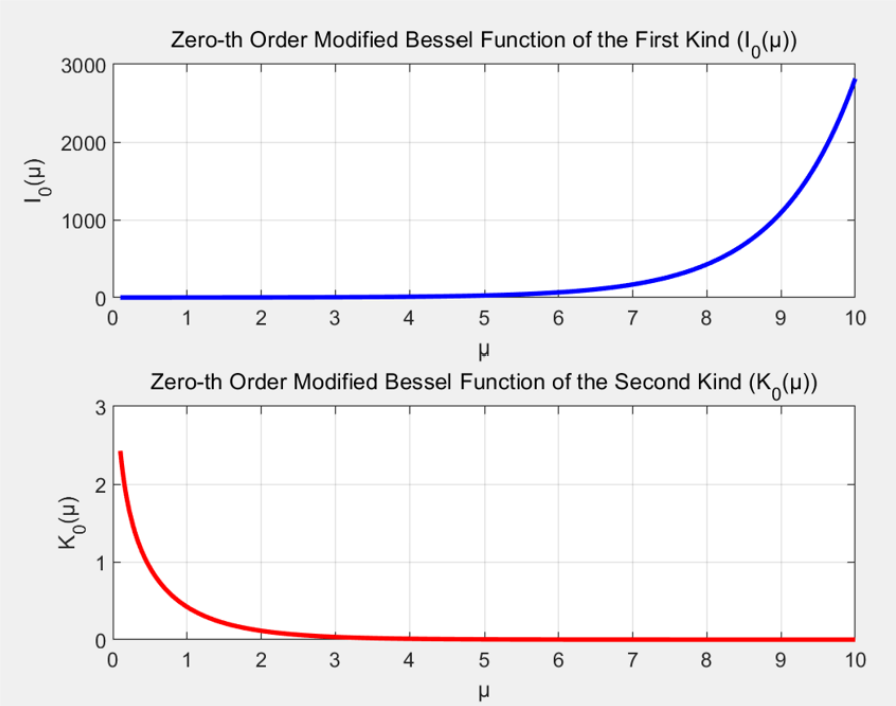


Figure 3.3 – Plot of the zeroth-order modified Bessel functions of the first kind (I_0) and second kind (K_0) versus the dimensionless argument μ (where $\mu = \gamma r$). The decaying behavior of $K_0(\mu)$ as $\mu \to \infty$ makes it the physically correct solution for an infinite medium.

3.1.3 Analytical Solution: Surface Line Source on Semi-Infinite Medium

The configuration more relevant to the 3-ω experiment is a line heater placed on the surface ($y = 0$) of a semi-infinite medium ($y > 0$) as shown in Figure 3.4.

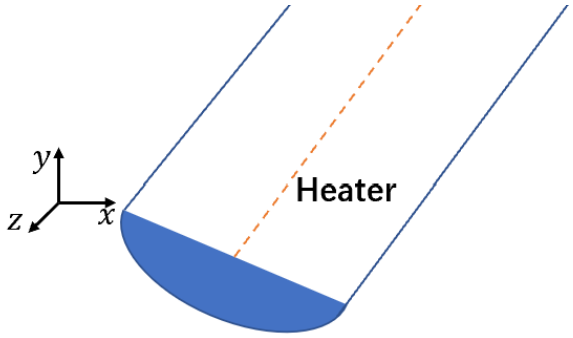


Figure 3.4 – Geometry of a line heater on the surface of a semi-infinite medium.

Due to symmetry (or by considering an image source), the heat flux is directed only into the medium ($y > 0$). This effectively doubles the temperature rise at the surface compared to the embedded source case for the same power input. Therefore, the complex temperature oscillation at a distance r from the line source on the surface is:

$$\theta(r) = \frac{P_{2\omega}}{\pi \kappa} K_0(\gamma r) \tag{3.11}$$

3.1.4 Correction for Finite Heater Width

Real heaters possess a finite width, $2b$, which is described in Figure 3.5. The effect of this finite width on the measured average temperature oscillation across the heater is significant and must be accounted for, especially at higher frequencies.

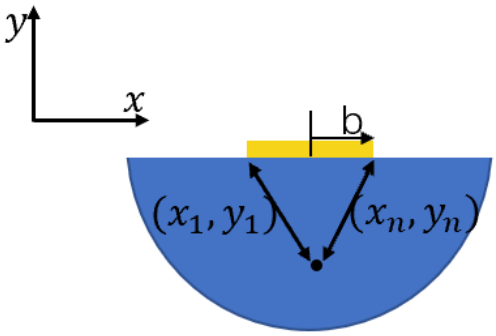


Figure 3.5 – Schematic illustrating a finite-width heater (width 2b) on a surface.

The temperature distribution $\theta(x)$ on the surface due to a finite-width heater can be found by treating the heater as a continuous distribution of line sources from $x = -b$ to $x = b$. This is elegantly solved using Fourier transforms [84].

Fourier Transform Approach: The temperature distribution in Fourier space (η) for the finite-width heater is:

$$\tilde{\theta}_{finite}(\eta) = \frac{P_{2\omega}}{2\kappa} \frac{\sin(\eta b)}{\eta b \sqrt{\eta^2 + \gamma^2}} \tag{3.12}$$

Average Temperature Integral: The experimentally relevant quantity is the temperature oscillation averaged across the heater width. Applying the inverse Fourier transform and averaging $\theta(x)$ from $x = -b$ to $x = b$ yields the exact integral expression [84]:

$$\theta_{avg} = \frac{P_{2\omega}}{\pi\kappa} \int_0^\infty \frac{\sin^2(\eta b)}{(\eta b)^2 \sqrt{\eta^2 + \gamma^2}} d\eta \tag{3.13}$$

This integral must generally be solved numerically.

As shown in Figure 3.6, the solution exhibits different behaviors depending on the relationship between the thermal penetration depth ($L_p = 1/|\gamma| = \sqrt{\alpha/\omega}$) and the heater half-width (b).

Low-Frequency Approximation (Slope Method for Bulk): In the crucial low-frequency limit where $L_p \gg b$ (or $|\gamma b| \ll 1$), the integral (Eq. 3.13) can be approximated. This leads to the key result [84, 85]:

$$\theta_{avg} \approx -\frac{P_{2\omega}}{2\pi\kappa} \left[\ln\left(\frac{b^2}{\alpha}\right) + \ln(2\omega) + 2\epsilon \right] - i\frac{P_{2\omega}}{4\kappa} \tag{3.14}$$

where $\epsilon \approx 0.923$ is related to the Euler constant. The in-phase component $\Delta T_{in-phase} = \mathrm{Re}[\theta_{avg}]$ varies linearly with $\ln(\omega)$:

$$\Delta T_{in-phase} \approx -\frac{P_{2\omega}}{2\pi\kappa} \ln(2\omega) + \text{Constant} \tag{3.15}$$

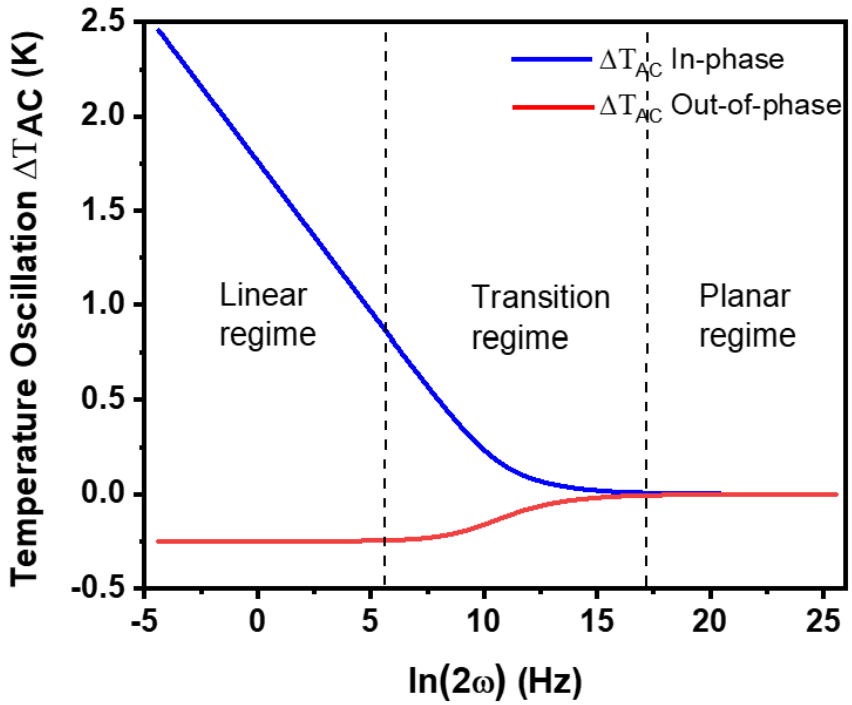


Figure 3.6 – Numerically calculated in-phase (blue) and out-of-phase (red) components of the average temperature oscillation (Eq. 3.13) as a function of frequency, showing different regimes.

This linear relationship allows the determination of the thermal conductivity κ of a bulk substrate using the slope method:

$$\kappa = -\frac{P_{2\omega}}{2\pi}\left(\frac{d(\Delta T_{in-phase})}{d(\ln(2\omega))}\right)^{-1} \tag{3.16}$$

The validity of the slope method approximation strictly relies on defining a specific spatial window for the thermal diffusion length, L_p. Based on the established "5-times" rule derived from the boundary conditions [84], L_p must be large enough to satisfy the line-source approximation ($L_p > 5b$) yet small enough to maintain the semi-infinite medium assumption ($t_s > 5L_p$). These geometric constraints can be expressed as:

$$5b \ll L_p \ll \frac{t_s}{5} \tag{3.17}$$

where b is the half-width of the heater and t_s is the thickness of the substrate.

By substituting the definition of the thermal diffusion length, $L_p = \sqrt{\frac{\alpha}{4\pi f}}$, into Eq. 3.17, we can translate these spatial limits into a measurable frequency range. Solving for the frequency f, we obtain the upper and lower limits of the linear regime:

$$\frac{25\alpha}{4\pi t_s^2} \leq f_{linear} \leq \frac{\alpha}{100\pi b^2} \tag{3.18}$$

where α represents the thermal diffusivity of the substrate. This frequency window (f_{linear}) defines the valid measurement range where the temperature oscillation is linear with respect to the logarithm of frequency, allowing for the accurate extraction of thermal conductivity.

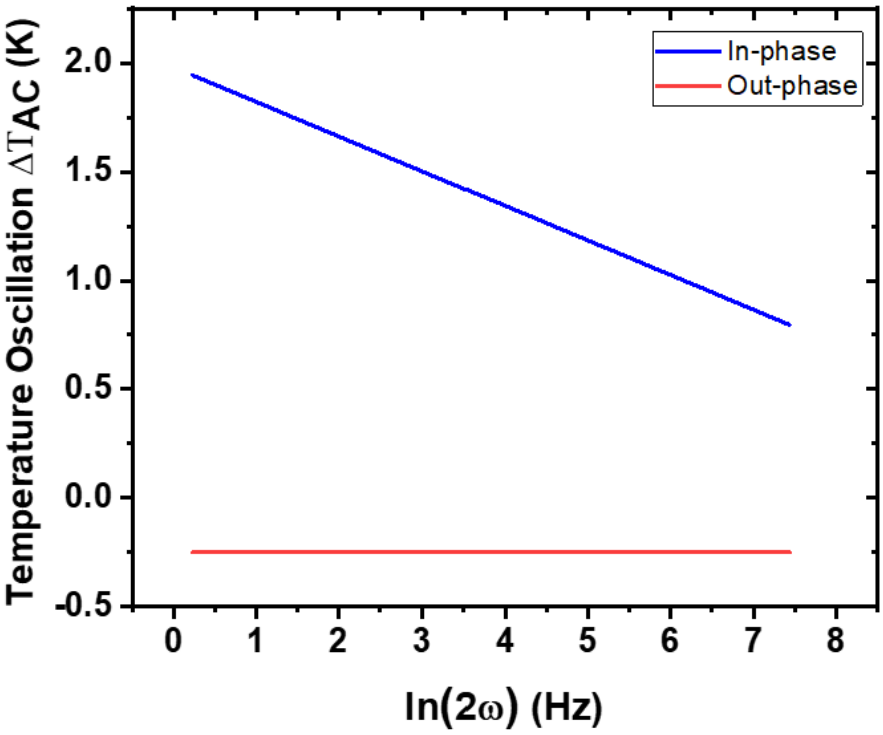


Figure 3.7 – In-phase and out-of-phase components of the temperature oscillation vs. $\ln(2\omega)$ calculated using the low-frequency approximation (Eq. 3.14) for a bulky material. It illustrates the decreasing linear dependence of the in-phase component and the constant out-of-phase component in this regime.

3.1.5 Closed-form Solutions for Layered Structures

When thin films are present on the substrate, obtaining exact closed-form solutions becomes significantly more complex as heat diffusion occurs through multiple media with different properties.

Single Isotropic Film on Substrate

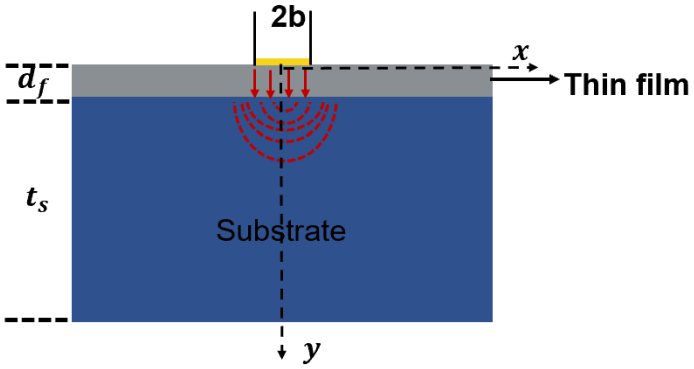


Figure 3.8 – Schematic of the heater-film-substrate configuration.

Exact solutions typically involve solving the heat equation in both the film and substrate domains and matching boundary conditions (temperature and flux continuity, possibly including TBR) at the interface, often using integral transform methods [128, 129].

A common simplification, the differential or slope method, is applicable under restrictive conditions: a film thickness (d_f) much smaller than the heater width ($d_f \ll 2b$) and a film much more thermally resistive than the substrate ($\kappa_f \ll \kappa_s$),the describtion is shown in Figure 3.8. κ_f is thermal conductivity of thin film and κ_s is thermal conductivity of substrate. In this limit, the film acts primarily as a 1D thermal resistance added in series to the substrate response [84, 85]:

$$\Delta T_{2\omega,film+sub} \approx \Delta T_{2\omega,sub}(\text{surface}) + \Delta T_f \tag{3.19}$$

where ΔT_f is the temperature drop across the film, approximated as frequency-independent:

$$\Delta T_f \approx \frac{P_{2\omega} d_f}{2b\kappa_f} \tag{3.20}$$

This allows κ_f to be extracted by subtracting the substrate's temperature response (measured or calculated) from the total measured response:

$$\kappa_f \approx \frac{P_{2\omega} d_f}{2b(\Delta T_{film+sub} - \Delta T_{sub})} \tag{3.21}$$

Limitation: This 1D approximation (Eq. 3.19) is only valid under the restrictive conditions $\kappa_f \ll \kappa_s$ and $d_f \ll 2b$. The model fails when these inequalities are no longer met. The approximation fails significantly when $\kappa_f \geq \kappa_s$ (the film is no longer a significant thermal barrier compared to the substrate) or $d_f \geq 2b$ (the film is geometrically "thick" relative to the heater). In either of these failure cases, lateral heat spreading within the film, which is ignored in the 1D assumption, becomes non-negligible.

Single Anisotropic Film on Substrate

Heat conduction can be anisotropic ($\kappa_x \neq \kappa_y$). Borca-Tasciuc et al. extended the analysis to handle anisotropy [130]. The temperature rise now depends on both κ_x and κ_y. By using heaters of different widths (narrow vs. wide, see Figure 3.9), the sensitivity to in-plane (κ_x) versus cross-plane (κ_y) conduction can be varied, theoretically allowing for the deconvolution of both components. However, the analysis involves complex integrals and still requires careful fitting.

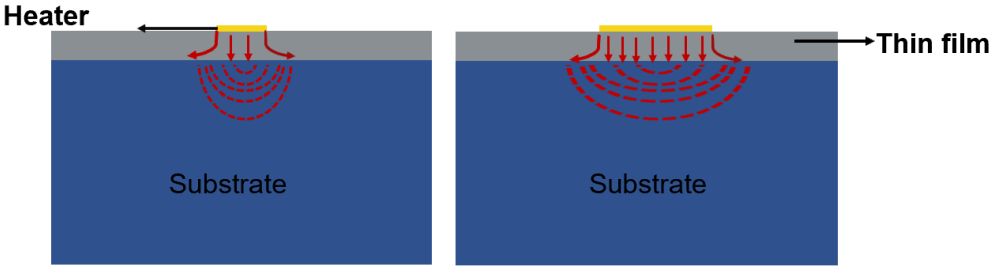


Figure 3.9 – Schematic cross-section showing heat flux lines for narrow (left) and wide (right) heaters, illustrating sensitivity to in-plane vs. cross-plane conduction in anisotropic films.

General Anisotropic Multilayers (Borca-Tasciuc Model)

To address the limitations of the slope method in handling finite thickness and distinct thermal properties of multilayer stacks, Borca-Tasciuc et al. derived a rigorous analytical solution based on the Fourier transform method [130, 131]. This model generalizes the heat diffusion equation for an arbitrary stack of N layers, explicitly accounting for the cross-plane (κ_y) and in-plane (κ_x) thermal conductivities of each layer, as well as the thermal interface resistances.

The Integral Solution For a heater of half-width b dissipating a peak electrical power per unit length P/l, the complex temperature rise at the surface (ΔT) is given by the integration of the thermal response over the spatial frequency spectrum. Neglecting the thermal mass of the heater itself, the solution is expressed as:

$$\Delta T = -\frac{P}{\pi l \kappa_{y,1}} \int_0^\infty \frac{1}{A_1 B_1} \frac{\sin^2(b\eta)}{(b\eta)^2} d\eta \tag{3.22}$$

where:

— $\kappa_{y,1}$ is the cross-plane thermal conductivity of the top layer (Layer 1).

— η is the integration variable (spatial wavenumber).

— The term $\frac{\sin^2(b\eta)}{(b\eta)^2}$ represents the Fourier transform of the heat source distribution (assuming a uniform heat flux across the heater width $2b$).

Recursive Matrix Algorithm The core of this model lies in the terms A_1 and B_1, which capture the thermal response of the entire stack. These are determined using a recursive algorithm that propagates the thermal boundary conditions from the bottom substrate (Layer n) up to the surface (Layer 1).

The thermal wave vector B_j for the j-th layer is defined as:

$$B_j = \left(\kappa_{xy,j} \cdot \eta^2 + \frac{i2\omega}{\alpha_{y,j}} \right)^{1/2} \tag{3.23}$$

where $\alpha_{y,j}$ is the thermal diffusivity, ω is the angular frequency, and $\kappa_{xy,j} = \kappa_{x,j}/\kappa_{y,j}$ represents the anisotropy ratio of the j-th layer.

The coefficient A_j relates the temperature and heat flux at the interface between layers. It is calculated recursively from the bottom layer ($j = n$) upwards using the relation:

$$A_{j-1} = \frac{A_j \frac{\kappa_{y,j} B_j}{\kappa_{y,j-1} B_{j-1}} - \tanh(\phi_{j-1})}{1 - A_j \frac{\kappa_{y,j} B_j}{\kappa_{y,j-1} B_{j-1}} \tanh(\phi_{j-1})} \tag{3.24}$$

where $\phi_j = B_j d_j$, and d_j is the thickness of the j-th layer.

Boundary Conditions at the Substrate The recursion must be initialized at the bottom-most layer (the substrate, $j = n$). The value of A_n depends on the physical boundary condition at the back of the substrate:

— **Semi-infinite Substrate:** If the substrate is treated as infinitely thick (thermal wave does not reach the bottom), $A_n = -1$.

— **Finite Substrate (Adiabatic):** If the backing materials is infinitely thermally insulating (e.g., vacuum is an acceptable approximation of this case), $A_n = -\tanh(B_n d_n)$.

— **Finite Substrate (Isothermal):** If the back surface is held at a constant temperature (perfect heat sink), $A_n = -1/\tanh(B_n d_n)$.

By solving this recursion from $j = n$ to $j = 2$, the surface coefficients A_1 and B_1 are obtained, allowing the numerical evaluation of the integral in Eq. 3.22. This model provides a theoretically exact solution for 1D/2D heat flow in idealized multilayer structures, serving as a critical benchmark for validating our FEM simulations.

3.1.6 Limitations of Analytical Approaches and Motivation for Numerical Modeling

While the analytical solutions derived in the previous sections—particularly the slope method (Eq. 3.15)—provide a fundamental understanding of the thermal diffusion process, they rely on idealized assumptions that are rarely met in complex multilayered devices. This section critically analyzes the breakdown of these analytical models when applied to the specific materials and geometries investigated in this thesis, establishing the imperative for a rigorous Finite Element Method (FEM) framework.

Breakdown of the Slope Method: The Constraint of Thermal Contrast

The most immediate limitation is observed in the frequency response of the multilayer stacks. The classic slope method, widely used for bulk substrates, assumes that the thermal wave propagates primarily in a direction perpendicular to the surface (quasi-1D flow) into a semi-infinite medium. This assumption leads to the well-known linear relationship between the in-phase temperature oscillation $\Delta T_{in-phase}$ and the logarithm of the heating frequency $\ln(2\omega)$.

However, the validity of this 1D approximation is strictly contingent upon a specific thermal contrast constraint: the thermal conductivity of the substrate must be significantly higher than that of the film ($\kappa_{sub} \gg \kappa_{film}$). Under this condition, the film acts merely as a thermal resistance, and the heat flow remains vertical.

Failure in Low-Contrast and Inverted Regimes: Our specific experimental architecture violates this constraint in two fundamental ways, rendering the slope method mathematically invalid:

1. **Low Contrast Violation ($\kappa_{film} \approx \kappa_{sub}$):** The SiO_2 layers in our stack possess thermal conductivities ($\sim$ 1.4 W/mK) that are comparable to the fused silica substrate. In this regime, the thermal wave implies a complex interaction volume where the substrate signal cannot be simply subtracted from the total response using the differential method.
2. **Inverted Contrast Violation ($\kappa_{film} \gg \kappa_{sub}$):** More critically, the Si_3N_4 layers exhibit a thermal conductivity ($\sim$ 20 W/mK) that is an order of magnitude higher than the substrate. This creates an "inverted" thermal structure where the high-κ layers act as **lateral heat spreaders**. Heat flux is no longer 1D; instead, it is preferentially channeled horizontally through the nitride layers (the "fin effect").

This theoretical breakdown is confirmed by simulation data. As shown in Figure 3.10, we compared the thermal response of different architectures. While the Bare Substrate (Blue Triangles) follows the classic linear trend, the Multilayer Stack (Black Squares) shows a suppressed amplitude and significant curvature. This non-linearity is the direct signature of lateral heat spreading, which the simple slope method fails to capture.

The thermophysical properties assigned to each domain are listed in Table 3.1. The substrate thickness is fixed at 150 µm to match the experimental wafer specifications. The metallic heater (Gold) is modeled with a length of $L = 3$ mm, a width of $2b = 6$ µm, and a thickness of $t_h = 50$ nm.

The thermal wave is excited by a Joule heating source applied to the gold heater domain. The volumetric power density, $Q(t)$, is defined as a function of the electrical driving frequency f and the peak power density is set to $Q_0 = 2.4 \times 10^{11}$ W/m^3. For Single Film on Substrate, the structure is a single dielectric layer (SiO_2, $\kappa = 1.4W \cdot m^{-1} \cdot K^{-1}$) deposited on the Fused Silica substrate ($\kappa = 1.38W \cdot m^{-1} \cdot K^{-1}$). This configuration specifically targets the "Low Contrast Regime," where the film is nearly thermally indistinguishable from the substrate, posing a stringent test for the extraction algorithm. For Multilayer Stack, the target experimental structure, comprising a five-layer composite stack of alternating SiO_2 and Silicon Nitride (SiN, $\kappa = 20.0W \cdot m^{-1} \cdot K^{-1}$) layers. Three distinct behaviors are observed from the simulation results:

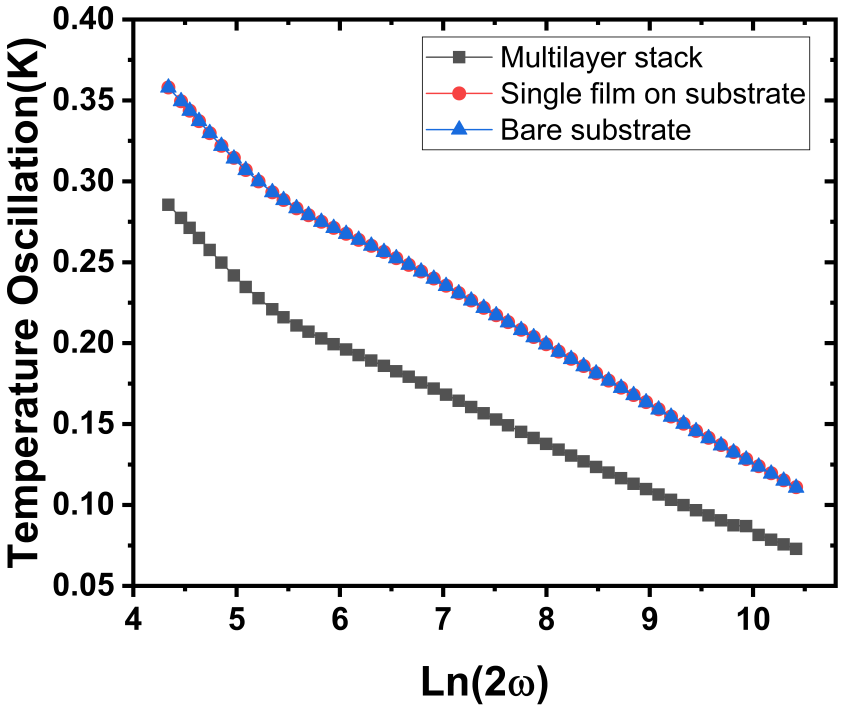


Figure 3.10 – Comparison of the simulated frequency-dependent temperature oscillations (in-phase) for three distinct architectures. The Multilayer Stack (Black Squares) deviates significantly from the linear behavior of the Bare Substrate due to lateral heat spreading in the high-conductivity SiN layers, demonstrating the invalidity of the 1D slope method.

Table 3.1 – Summary of material properties and geometric parameters used in the FEM simulations. Note the minimal thermal contrast between the Oxide layer and the Substrate.(The material properties were obtained from the built-in COMSOL Multiphysics material library.)

Domain	**Material**	**Thermal Conductivity** κ ($W \cdot m^{-1} \cdot K^{-1}$)	**Heat Capacity** C_p ($J \cdot kg^{-1} \cdot K^{-1}$)	**Density** ρ ($kg \cdot m^{-3}$)
Substrate	Fused Silica	1.38	740	2203
Thin Films				
Oxide Layer	SiO_2(bulk)	1.40	730	2200
Nitride Layer	SiN(bulk)	20.0	700	3100
Sensor	Gold (Au)	317	129	19300

— **Bare Substrate (Blue Triangles):** The response follows a strictly linear trend across the frequency range. This behavior is characteristic of a semi-infinite, homogeneous medium and is consistent with the classical analytical line-source solution derived by Cahill. It serves as a baseline for validating the simulation procedure.

— **Single Film on Substrate (Red Circles):** The curve for the single film (representing a low-conductivity dielectric like SiO_2 on a fused silica substrate) closely follows the substrate response. This similarity indicates a low thermal contrast between the film and the substrate. In such scenarios, the additional thermal resistance provided by the film is small relative to the substrate's impedance, making the accurate extraction of film properties challenging without the precision of a numerical model to account for spreading resistance.

— **Multilayer Stack (Black Squares):** Crucially, the multilayer stack exhibits a markedly different response. The temperature oscillation amplitude is significantly lower than that of both the bare substrate and the single film case. This reduction implies that the effective thermal impedance of the stack is lower than that of the substrate alone. This phenomenon is driven by the silicon nitride (SiN) layers within the stack. Since SiN typically possesses a higher thermal conductivity than the surrounding SiO_2 layers, it acts as a thermal spreader, facilitating lateral heat flow away from the heater. The distinct curvature observed in this plot signifies the complex, frequency-dependent interplay between the thermal penetration depth and the multiple layers, validating the necessity of a full 2D/3D numerical model.

Inadequacy of Advanced Analytical Integrals

One might argue that more sophisticated analytical solutions, such as the integral model developed by Borca-Tasciuc et al. [131], could resolve the dimensionality issue since they explicitly account for 2D anisotropic heat flow. While these models are superior to the slope method, they still suffer from geometric and physical simplifications that introduce systematic errors when applied to the specific low-conductivity stacks studied here.

1. Limitations regarding Heater Thermal Shunting (The Geometric Limitation) While the standard Borca-Tasciuc formalism significantly improves upon the slope method by explicitly accounting for the heater's heat capacity, it still relies on analytical approximations regarding the heat flux distribution. A critical challenge arises when applying this 2D analytical model to systems with high thermal contrast.

In our experiments, the gold heater possesses a finite thickness ($\approx 50nm$) and a high thermal conductivity ($\kappa_{Au} \approx 317W/mK$). On high-conductivity substrates (like Silicon), the lateral heat flow within the heater is negligible compared to the vertical flow into the substrate. However, on the low-conductivity substrates (Fused Silica, $\kappa \approx 1.4W/mK$) used in this work, the metallic heater acts as a significant "thermal shunt." A non-negligible fraction of the heat flux flows laterally through the metallic strip (the "fin effect") and axially toward the contact pads (3D end effects) rather than entering the sample. Standard analytical integrals, which typically assume an infinitely long heater with an idealized flux distribution, may fail to fully capture the magnitude of this parasitic lateral loss, potentially leading to an overestimation of the sample's thermal conductivity. Our FEM model, by treating the heater as a fully meshed physical domain, naturally solves this conjugate heat transfer problem without such approximations.

2. Challenges in Discrete Interface Decoupling (The Physical Limitation) Analytical models typically employ transfer matrix methods that treat the multilayer stack as a sequence of homogeneous, infinite planes. While mathematically elegant, this approach often lumps interface effects into effective layer properties or assumes perfect planarity. However, a primary objective of this thesis is to separate the intrinsic thermal conductivity of the thin films (κ_{int}) from the discrete interface resistances (R_{TBR}). Analytical models lack the geometric flexibility to investigate how non-ideal features—such as edge effects, sidewall contacts, or localized defects—impact the extraction of these specific interface parameters. Consequently, a numerical approach is preferred to explicitly define and verify the physical location of these resistive boundaries within the complex device geometry.

The Challenge of the Ill-Posed Inverse Problem

Beyond the physics of heat flow, the mathematical nature of the data analysis presents a formidable challenge. We are solving an Inverse Heat Transfer Problem: inferring multiple unknown parameters (layer conductivities and interface resistances) from a single frequency-response curve.

In multilayer stacks, this inverse problem is often ill-posed due to parameter correlation. For instance, a decrease in the intrinsic conductivity of a layer can produce a signal indistinguishable from an increase in the resistance of its adjacent interface.

— **Analytical Limitations:** Analytical formulas act as "black boxes" that output a temperature for a given input. They do not easily facilitate the calculation of **Sensitivity Coefficients** required to quantify these correlations.

— **Numerical Advantage:** A numerical framework allows for a rigorous **Sensitivity Analysis** (detailed in Chapter 5). By systematically perturbing each material property in the simulation, we can determine which parameters are linearly independent and thus uniquely solvable, and which are correlated.

Motivation for Finite Element Method (FEM)

Consequently, to overcome the combined challenges of complex geometry, lateral heat spreading, thermal shunting, and parameter correlation, a comprehensive numerical approach is mandatory. The Finite Element Method (FEM), detailed in the following Section 3.3, provides the necessary capabilities:

1. **Geometric Fidelity:** Unlike most analytical models, our FEM approach explicitly models the gold heater as a 3D physical domain with finite thickness and properties. This accurately captures the thermal shunting effect inherent to low-conductivity substrates.
2. **Physics Completeness:** FEM solves the full heat diffusion equation without restricting assumptions regarding thermal contrast, correctly handling the lateral spreading in the high-κ SiN layers.
3. **Discrete Interface Modeling:** The method allows for the distinct definition of bulk domains and thin resistive layers, enabling the physical separation of intrinsic conductivity from interface resistance.
4. **Inverse Problem Solver:** The FEM model serves as a robust forward engine for the iterative optimization algorithms, allowing for the precise extraction of thermal properties even in the presence of complex parameter interactions.

In summary, while analytical models form the theoretical basis (Chapter 3.1) and are used for validation (Chapter 4), FEM constitutes the essential tool for the accurate analysis of the complex multilayer stacks presented in this work.

3.2 The 3-Omega Experimental Setup

This section provides a comprehensive description of the physical implementation of the 3-ω (3ω) method as utilized in this work. We begin by revisiting the core operational principle from a practical standpoint, focusing on the critical role of the metallic transducer. We then proceed to a detailed "tour" of the experimental bench, describing each piece of instrumentation and its specific function within the measurement chain. Finally, we provide a thorough account of the sample preparation and the microfabrication processes used to create the heater/sensor structures, as the quality and precise geometry of these structures are paramount to the accuracy of the final measurement.

3.2.1 Principle of Operation: The Metallic Strip as Heater and Thermometer

As introduced in Chapter 2, the elegance of the 3ω method lies in its use of a single, microfabricated metallic strip to function as both a periodic heat source and a sensitive in-situ thermometer. To achieve this dual role with high precision, several practical considerations regarding the choice of material and the electrical measurement configuration are critical.

Transducer Material Selection

The choice of metal for the heater/sensor strip is a crucial design decision, driven by a need to balance several material properties:

— **High Temperature Coefficient of Resistance (TCR, β):** The TCR is the figure of merit for the sensor's sensitivity. A high β value means that a small change in temperature will produce a large, easily measurable change in resistance, which in turn generates a larger $V_{3\omega}$ signal. Metals like Platinum (Pt, $\beta \approx 0.0039$ K^{-1}) and Nickel (Ni, $\beta \approx 0.006$ K^{-1}) are excellent in this regard. Gold (Au, $\beta \approx 0.0034$ K^{-1}) and Aluminum (Al, $\beta \approx 0.0043$ K^{-1}) are also very common choices.

— **Linear and Stable Resistance-Temperature Behavior:** The resistance-temperature relationship, $R(T) = R_0(1 + \beta\Delta T)$, must be highly linear over the range of temperature oscillations encountered in the experiment. The material should also be chemically stable and resistant to oxidation over time and during thermal cycling to ensure that the calibration remains valid. Platinum and Gold are superior in this respect.

— **Fabrication Compatibility:** The metal must adhere well to the dielectric films being studied and be compatible with standard photolithography and lift-off or etching processes. While Gold has poor adhesion to SiO_2 and SiN, a thin adhesion layer of Titanium (Ti) or Chromium (Cr) is universally used to overcome this issue. This direct-patterning approach is valid because the samples studied in this thesis (SiO_2/SiN) are strong electrical insulators. It is critical to note that this standard 3-omega configuration will fail if the sample itself is electrically conductive(e.g., a Silicon substrate or a metal film). In such cases, the drive current (I_ω) would short-circuit through the sample, corrupting the signal and violating the "line source" heating model. To measure a conductive sample, an intermediate, thin, electrically insulating layer (such as SiO_2) must first be deposited to isolate the metal heater from the sample.

— **Low Electromigration:** The metal line must be able to withstand the AC current densities required for heating without significant degradation due to electromigration.

In this work, Gold (Au) with a Titanium (Ti) adhesion layer was chosen as the primary transducer material, offering a favorable combination of a reasonably high TCR, excellent chemical stability, and a well-established fabrication process.

Four-Wire Probe Configuration for Accurate Resistance Measurement

Accurately determining the resistance of the metallic heater strip, and particularly its small, temperature-induced changes, is fundamental to the 3-ω method. However, when measuring the resistance of small structures like thin-film metal lines using a simple two-wire method (where current is injected and voltage is measured through the same contacts), the measurement is inevitably corrupted by unwanted series resistances. These parasitic resistances arise from the measurement probes themselves, the contact resistance between the probes and the device pads, and the resistance of the wider metal leads connecting the pads to the narrow central heater element.

To overcome this critical issue, the four-wire probe configuration, also known as the Kelvin sensing method, developed by Lord Kelvin, is employed [132, 133] (see Figure 3.11). This technique elegantly separates the path for current injection from the path for voltage measurement.

As illustrated in Figure 3.11, the AC current (I) is sourced through two outer contact pads (I+, I-). This current flows through the outer leads and the entire length of the heater element. The voltage drop (V) is then measured using a separate pair of inner contact pads (V+, V-), which are positioned precisely at the ends of the narrow, active heater/sensor section. These inner pads are connected to a high-impedance voltage measurement instrument (such as the input stage of the lock-in amplifier).

Because the voltmeter has a very high input impedance (typically $> 10\,\mathrm{M\Omega}$), negligible current flows through the voltage sensing probes and leads (V_+, V_-). According to Ohm's law ($V = IR$), if the

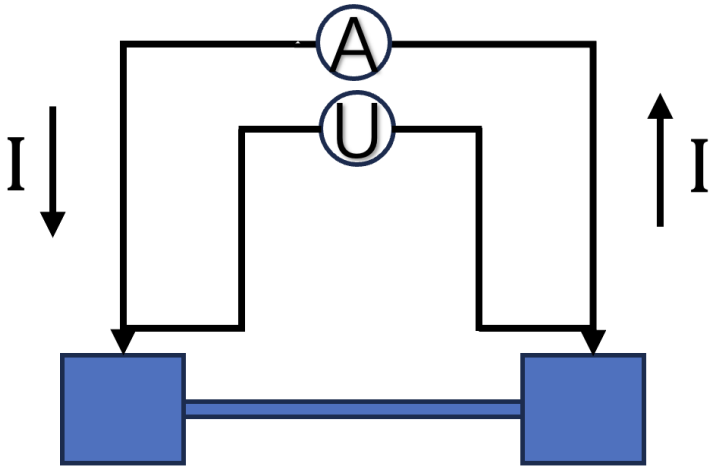


Figure 3.11 – Schematic of the four-wire probe configuration applied to a 3-ω heater/sensor. The two outer pads, labelled I+ and I-, are used to inject the current through the heater line. The two inner pads, labelled V+ and V-, are connected to a high-impedance voltage measurement input and measure only the voltage drop across the active heater section. Because almost no current flows through the voltage leads, the measured voltage is not affected by the contact and lead resistances of the current path.

current through the voltage leads is practically zero, then the voltage drop across these leads and their contact resistances is also essentially zero [132].

Therefore, the voltage measured between V+ and V- corresponds exclusively to the potential drop across the defined central segment of the heater/sensor element, completely eliminating the influence of all parasitic series resistances associated with the current injection path.

This sensing technique is thus critically important for the 3-ω method. It ensures that the measured fundamental voltage ($V_{1\omega}$) and, more importantly, the tiny third-harmonic voltage ($V_{3\omega}$), accurately reflect the electrical potential difference and resistance changes occurring only within the active heating and sensing region. This allows for a precise determination of the heater resistance R_0, its temperature coefficient β, and ultimately, the accurate calculation of the temperature oscillation $\Delta T_{2\omega}$ from the measured $V_{3\omega}$ signal [84, 127].

Temperature Coefficient of Resistance (TCR) Calibration

The accurate conversion of the measured third-harmonic voltage ($V_{3\omega}$) into the physically meaningful temperature oscillation amplitude ($\Delta T_{2\omega}$) is a critical step underpinning the entire 3-ω method. This conversion relies fundamentally on the precise knowledge of the Temperature Coefficient of Resistance (TCR) of the metallic heater/sensor strip, typically denoted by β.

Definition and Importance: The TCR quantifies the fractional change in the electrical resistance (R) of a material per unit change in temperature (T). For the relatively small temperature variations (ΔT) encountered in 3-ω experiments around a reference temperature T_0 (where the resistance is R_0), the resistance $R(T)$ can be accurately described by a linear relationship:

$$R(T) = R_0(1 + \beta\Delta T) \tag{3.25}$$

where $\Delta T = T - T_0$. From this linear approximation, the TCR is defined as the slope of the normalized resistance change with temperature:

$$\beta = \frac{1}{R_0}\frac{dR}{dT} \tag{3.26}$$

(Units: K^{-1} or $°C^{-1}$)

The accuracy of the thermal conductivity determination hinges directly on the precision with which this TCR value, β, is known. It serves as the crucial calibration factor linking the measured electrical signal ($V_{3\omega}$) to the desired thermal quantity ($\Delta T_{2\omega}$), according to the relationship derived in section 3.1 [84, 127]:

$$\Delta T_{2\omega} = \frac{2V_{3\omega}}{V_{1\omega}}\frac{1}{\beta} = \frac{2V_{3\omega}}{I_{1\omega}R_0\beta} \tag{3.27}$$

where $V_{1\omega}$ and $I_{1\omega}$ are the amplitude of the fundamental voltage and current across the heater, respectively. Any error in β will propagate directly into the calculated $\Delta T_{2\omega}$ and subsequently into the determined thermal conductivity.

Necessity of In-Situ Calibration: It is crucial to emphasize that the TCR value for the heater/sensor cannot simply be adopted from bulk material handbooks. The electrical properties, including TCR, of thin metallic films are known to be highly sensitive to the specific deposition method (e.g., evaporation, sputtering), film thickness, resulting microstructure (grain size, crystal orientation, defects), adhesion layers used (e.g., Ti or Cr for Au), and any post-deposition annealing treatments [134, 135]. Relying on bulk values, which do not account for these thin-film specific factors, can introduce significant systematic errors (potentially >10%) into the final thermal conductivity measurement [127]. Consequently, each fabricated heater/sensor device must be individually calibrated in-situ to determine its specific and accurate TCR value.

Calibration Procedure and Setup: The calibration was performed by measuring the electrical resistance of each heater line as a function of temperature under controlled equilibrium conditions.

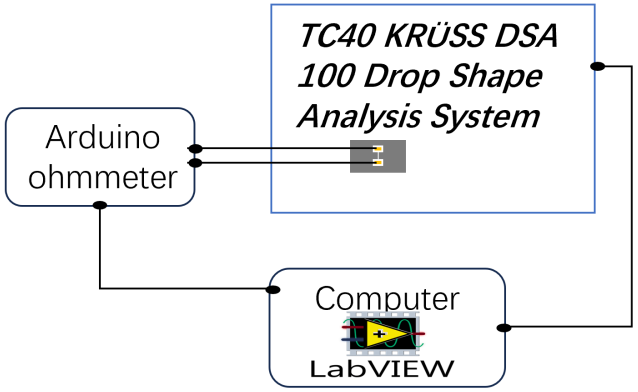


Figure 3.12 – Schematic of the experimental setup used for TCR calibration. The sample is placed inside a temperature-controlled environmental chamber, while the heater resistance is measured using a four-wire configuration. The resistance acquisition is performed with an Arduino-based ohmmeter controlled by LabVIEW.

As illustrated in Figure 3.12, the sample was placed inside a temperature-controlled chamber (TC40, part of the KRÜSS DSA 100 Drop Shape Analysis System), equipped with a calibrated internal temperature sensor. The sample rested on a thermally conductive stage in order to promote thermal equilibrium between the chamber, the substrate, and the metallic heater.

During the calibration, a small DC current was applied through the outer pads (I+, I-) of the four-wire structure. This current was kept sufficiently low to make Joule self-heating negligible compared

with the imposed temperature variation. The voltage drop across the inner pads (V+, V-) was then measured and converted into the heater resistance. In this work, the resistance acquisition was carried out using an Arduino-based ohmmeter controlled by a LabVIEW interface. The LabVIEW program synchronized the temperature setpoint, the stabilization time, and the resistance recording.

The temperature was increased stepwise with a temperature increment of 2 °C. At each temperature setpoint, a stabilization time of 5 min was applied before recording the resistance. This waiting time was chosen to ensure that the chamber, substrate, and metallic transducer reached thermal equilibrium before each data point was acquired. At each stable temperature point, the chamber temperature and the four-wire resistance of the heater were recorded automatically.

The resulting resistance-temperature curve was fitted using a linear regression:

$$R(T) = R_0 + \frac{dR}{dT}(T - T_0) \tag{3.28}$$

The reference resistance R_0 and the slope dR/dT were obtained from the fit, and the TCR was then calculated using Eq. (3.26). The uncertainty in R_0 and β was estimated from the standard errors of the fitted parameters obtained from the linear regression performed in Origin. This uncertainty was subsequently taken into account in the conversion of the measured $V_{3\omega}$ signal into the temperature oscillation $\Delta T_{2\omega}$.

This individual calibration was performed for each heater line used in the thermal measurements. It is an essential step because the TCR of thin Au/Ti metallic films depends on the deposition conditions, film thickness, adhesion layer, and microstructure, and therefore cannot be accurately replaced by the bulk value of gold.

3.2.2 Description of the Experimental Bench: Lock-in Amplifier, Wheatstone Bridge, and Probing

The successful implementation of the 3-ω method hinges on the precise generation of a pure AC heating signal and the highly sensitive detection of the resulting third-harmonic voltage ($V_{3\omega}$), which is typically orders of magnitude smaller than the fundamental voltage ($V_{1\omega}$). Figure 3.13 shows a photograph of the actual experimental bench constructed and utilized in this work, highlighting the key instruments and their arrangement. The underlying electrical schematic and working principle, previously illustrated in Figure 3.1, are realized using this specific hardware configuration. This section details the function of each component within our setup.

Signal Generation and Driving Circuit

The experiment is initiated with a highly stable, low-distortion sinusoidal AC voltage signal generated by a digital function generator (Keysight 33210A), as labeled in Figure 3.13. The spectral purity of this source signal is critical; any intrinsic third-harmonic distortion present in the function generator's output would directly add to the measured $V_{3\omega}$ signal, potentially creating a significant systematic error, particularly at low signal levels.

To mitigate this, the Keysight 33210A was specifically selected for its minimal harmonic content. According to the manufacturer's specifications, the instrument exhibits a Total Harmonic Distortion (THD) of less than 0.04% and suppresses spurious harmonic components to below −70 dBc within the operating frequency range (DC to 20 kHz). This ensures that the electrical source contribution to the third harmonic is orders of magnitude lower than the thermal signal generated by the sample, rendering source-induced artifacts negligible.

The output of the function generator serves two essential purposes: it provides the fundamental frequency (ω) reference signal required by the lock-in amplifier for phase-sensitive detection, and it supplies the driving voltage for the heating source.

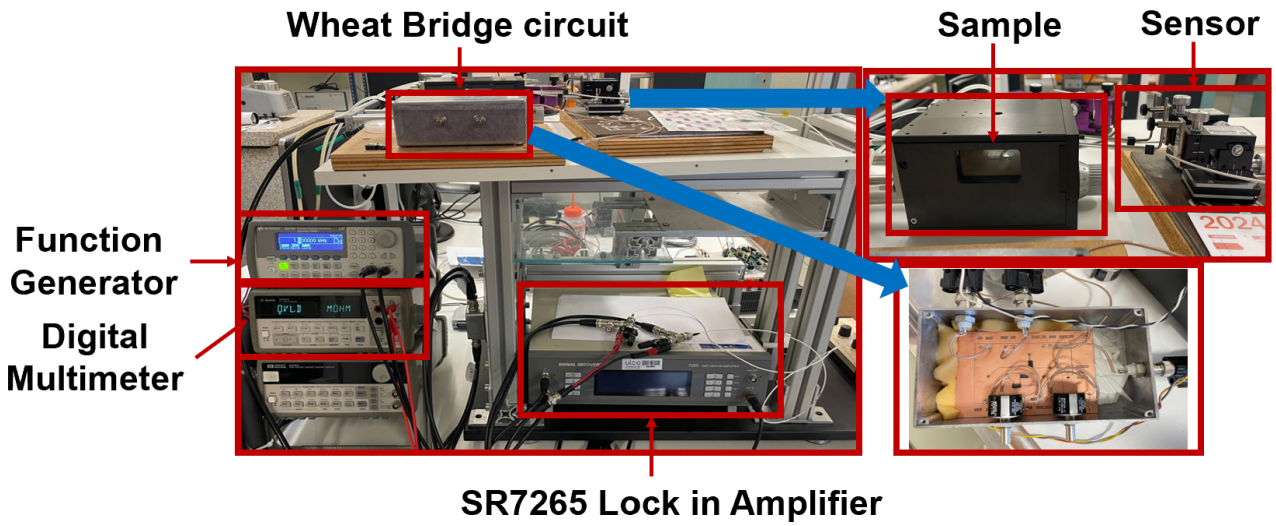


Figure 3.13 – Photograph of the custom-built 3-ω experimental setup. Key components shown include the Function Generator (Keysight 33210A), Digital Multimeter (AM-530-EUR), SR7265 Lock-in Amplifier, the custom Wheatstone Bridge circuit, and the sample probing stage.

To ensure that the heating power ($P = I^2R$) remains constant even if the sample resistance (R) fluctuates slightly during the experiment (e.g., due to the average DC temperature rise or minor drifts), it is generally preferable to drive the sample with a controlled AC current source rather than a voltage source. While our experimental setup utilizes a voltage source (Keysight 33210A) rather than a dedicated Voltage-Controlled Current Source (VCCS), a stable current drive is effectively achieved through the circuit design.

As established in the foundational work by Cahill [84], the inclusion of a series limitation resistor (often the upper arm of the Wheatstone bridge) that is significantly larger than the sample resistance ($R_{series} \gg R_{sample}$) creates a quasi-constant current condition. Under this configuration, the total impedance of the driving loop is dominated by the series resistor. Consequently, the small thermal fluctuations in the sample resistance induce negligible variations in the loop current, fulfilling the constant-current assumption required for the valid extraction of the $V_{3\omega}$ signal without the need for active current regulation. The AC voltage from the function generator, operating at an angular frequency ω, is applied across the Wheatstone bridge, causing Joule heating within the metallic heater strip at the second harmonic frequency, 2ω.

Signal Conditioning: The Wheatstone Bridge for 1ω Cancellation

A major practical challenge in 3-ω measurements is the immense difference in magnitude between the fundamental voltage ($V_{1\omega}$) across the heater (typically millivolts to volts) and the desired third-harmonic signal ($V_{3\omega}$) arising from the temperature oscillation (typically nanovolts to microvolts). The ratio $V_{3\omega}/V_{1\omega}$ is often between 10^{-3} and 10^{-6}. If the large $V_{1\omega}$ signal were fed directly into the lock-in amplifier, it would easily saturate the instrument's sensitive input stages, rendering accurate measurement of the tiny $V_{3\omega}$ impossible.

To overcome this critical issue, a Wheatstone bridge circuit is employed as a crucial signal conditioning step to null out, or cancel, the majority of the large $V_{1\omega}$ component before it reaches the lock-in amplifier [84]. As shown in Figure 3.13, our circuit consists of the two-point-probed sample ($R_s(T)$) integrated as one arm of the bridge, a precision variable resistor (R_{var} between 450 Ω to 2460 Ω) in an adjacent arm, and two high-precision, stable, fixed resistors ($R_1 = 100\,\Omega$ and $R_2 = 5\,\text{k}\Omega$ in our specific implementation) in the other two arms. In the specific Wheatstone bridge circuit configuration utilized for this work, the adjustment range allows for the balancing of sample heater

resistances (R_s) spanning from 9 Ω to 49.2 Ω. The bridge is excited by the AC signal from the function generator applied across two opposing vertices. The voltage output is measured differentially across the other two opposing vertices (the detection nodes).

Before initiating a frequency sweep, the bridge must be carefully balanced at the fundamental frequency (at 1ω). This balancing is achieved by meticulously adjusting the variable resistor R_{var} until the bridge condition is met, meaning the ratio of resistances in the upper arms equals the ratio in the lower arms ($R_s/R_2 \approx R_{var}/R_1$). When the bridge is balanced, the AC potential at the two voltage taps is nominally equal at the fundamental frequency ω, and consequently, the differential $V_{1\omega}$ signal output across these taps is minimized, ideally driven close to zero (often attenuated by 40 dB to 60 dB or more).

Critically, this balancing act, which targets the fundamental frequency, does not cancel the desired $V_{3\omega}$ signal. The $V_{3\omega}$ voltage is actively generated only within the sample resistor, $R_s(T)$, as a direct consequence of its temperature- and hence resistance-oscillations at 2ω. The other three resistors in the bridge (R_1, R_2, R_{var}) are standard passive components selected for their low temperature coefficients; their resistance does not oscillate significantly at 2ω under the experimental conditions. Therefore, they generate no intrinsic 3ω voltage. The $V_{3\omega}$ signal produced by the sample thus appears as a differential voltage across the bridge output terminals and is passed on, relatively unattenuated by the balancing, to the lock-in amplifier. By effectively removing the overwhelming $V_{1\omega}$ background, the Wheatstone bridge allows the lock-in amplifier's input sensitivity to be significantly increased without saturation, enabling a much higher signal-to-noise ratio and greater precision in the final $V_{3\omega}$ measurement. In some ultra-high precision setups, a low-noise differential preamplifier might be added between the bridge output and the lock-in input for further signal gain and impedance matching.

Signal Detection: The Lock-In Amplifier

The heart of the detection system is a dual-phase, digital lock-in amplifier (Model 7265, SIGNAL RECOVERY, AMETEK), also depicted schematically in Figure 3.1. The lock-in amplifier is a sophisticated instrument specifically designed to perform phase-sensitive detection (PSD). This technique allows for the extraction of extremely weak AC signals at a specific frequency and phase, even when buried within a background noise level that is orders of magnitude larger [136, 137].

The operational principle of PSD as applied in the 3-ω method is as follows: The input signal received from the Wheatstone bridge, which ideally contains primarily the tiny $V_{3\omega}$ component plus residual noise (the large $V_{1\omega}$ having been mostly cancelled), is first multiplied internally by a pure sinusoidal reference signal oscillating precisely at the third-harmonic frequency, 3ω. This 3ω reference signal is typically generated internally by the lock-in amplifier itself; it achieves this by phase-locking its internal oscillator to the fundamental frequency (ω) reference signal provided externally by the function generator and then digitally synthesizing the third harmonic.

The multiplication of the input signal (containing the term $V_{3\omega} \propto \cos(3\omega t + \phi)$, where ϕ is the phase shift relative to the heating signal) with the internal reference signal (e.g., $\propto \cos(3\omega t)$) yields, via trigonometric identities, terms containing sum and difference frequencies. Specifically, the product includes a DC component (frequency $3\omega - 3\omega = 0$) whose magnitude is proportional to the amplitude of the input $V_{3\omega}$ and the cosine of the phase difference (ϕ), and a high-frequency component oscillating at 6ω ($3\omega + 3\omega$). This resulting mixed signal is then passed through a steep internal low-pass filter with a user-selectable time constant (τ, typically chosen such that $1/\tau \ll 3\omega$). This filter aggressively attenuates the 6ω component and virtually all other frequency noise (e.g., 50 ,60 Hz mains hum which is pervasive electromagnetic noise originating from the building's main AC power lines picked up by wiring, broadband thermal noise), leaving only a stable DC component at the output. The magnitude of this DC output is directly proportional to the amplitude of the original $V_{3\omega}$ signal component that is in-phase with the internal reference signal.

To capture the full signal information, the lock-in amplifier employs a second internal reference

signal that is phase-shifted by exactly 90° (quadrature) relative to the first. It performs a parallel PSD operation using this quadrature reference. The resulting DC output from this second channel is proportional to the amplitude of the $V_{3\omega}$ signal component that is out-of-phase with the main reference. Thus, the lock-in amplifier provides two simultaneous DC outputs: the in-phase component ($V_{3\omega,in-phase}$ or X) and the out-of-phase component ($V_{3\omega,out-of-phase}$ or Y). These two orthogonal components contain the complete amplitude ($|V_{3\omega}| = \sqrt{X^2 + Y^2}$) and phase ($\phi = \arctan(Y/X)$) information of the third-harmonic signal relative to the heating cycle, which are directly related through thermal modeling to the thermal properties of the sample.

Key settings on the lock-in amplifier—such as input coupling (AC or DC), input sensitivity (voltage range), time constant (filtering bandwidth/measurement time), filter slope (e.g., 6, 12, 18, 24 dB/octave), and dynamic reserve (the instrument's ability to tolerate large off-frequency noise or residual fundamental signal without saturating)—must be carefully selected and optimized to achieve the best balance between measurement speed, precision, and noise rejection for the specific signal levels and frequency range encountered in the experiment.

Data Acquisition and Automation

The entire experimental procedure was automated using a custom-built LabVIEW virtual instrument running on a personal computer, as indicated in Figure 3.1. The program controlled the frequency sweep of the function generator, allowed the lock-in amplifier signal to stabilize over several time constants, and recorded the in-phase (X) and out-of-phase (Y) components of the third-harmonic voltage $V_{3\omega}$.

The fundamental voltage $V_{1\omega}$ across the heater was measured using a separate digital multimeter (AM-530-EUR). This choice was made to keep the lock-in amplifier dedicated to the third-harmonic detection during the measurement. Measuring $V_{1\omega}$ with the lock-in amplifier would require changing the detection harmonic or modifying the measurement configuration, which could disturb the optimized 3ω detection chain. The use of an independent digital multimeter therefore provides a direct measurement of the fundamental voltage while preserving the lock-in settings used for the weak $V_{3\omega}$ signal.

The reference heater resistance R_0 was measured independently before the frequency sweep and was used together with the calibrated TCR β to convert the measured $V_{3\omega}$ signal into the temperature oscillation $\Delta T_{2\omega}$ using Eq. (3.27). The recorded quantities for each measurement were therefore the frequency f, the in-phase and out-of-phase components of $V_{3\omega}$, the fundamental voltage $V_{1\omega}$, and the reference resistance R_0.

The noise level of the voltage measurement was evaluated from the fluctuations of the lock-in amplifier outputs after stabilization at each frequency. This noise directly affects the uncertainty of $V_{3\omega}$ and therefore propagates to the calculated temperature oscillation. In first approximation, the relative uncertainty in $\Delta T_{2\omega}$ can be expressed as:

$$\frac{\delta(\Delta T_{2\omega})}{\Delta T_{2\omega}} \simeq \sqrt{\left(\frac{\delta V_{3\omega}}{V_{3\omega}}\right)^2 + \left(\frac{\delta V_{1\omega}}{V_{1\omega}}\right)^2 + \left(\frac{\delta \beta}{\beta}\right)^2} \tag{3.29}$$

This relation highlights the importance of both a stable $V_{3\omega}$ detection and an accurate TCR calibration.

3.2.3 Sample Fabrication: Dielectric Stack Deposition and Sensor Patterning

The successful implementation and accurate analysis of the 3-ω method are critically contingent upon the quality, uniformity, and dimensional fidelity of the test structures. This thesis involved the fabrication and characterization of several distinct sample types to validate the methodology and investigate the target multilayer system. The fabrication process for all samples involved two major

stages: first, the preparation or deposition of the material(s) of interest onto a suitable substrate, and second, the subsequent patterning of the metallic heater/sensor structure onto the top surface. Both stages require systematic and well-controlled microfabrication processes performed in a cleanroom environment.

Overview of Fabricated Samples

Several types of samples were prepared and measured during the course of this work:

— **Bulk Validation Samples:**

  — *Borosilicate Glass* ($BrSiO_2$): Commercially obtained borosilicate glass wafers (~1 mm thick) were used directly as substrates for sensor fabrication. These served as initial validation standards. (Measurements presented in Chapter 4).

  — *Fused Silica:* High-purity fused silica wafers (150 µm thick) were used both as validation standards and as the substrate for the primary multilayer sample. (Measurements presented in Chapter 4).

— **Single Film on Substrate Sample:**

  — *SiO_2 on Silicon* (SiO_2/Si):A thin film of SiO_2 (nominally ~1 µm thick) was deposited onto a standard silicon wafer (~380 µm thick). This sample was intended for validation, however, a detailed analysis of its measurement results is deferred to Section 4.1.4, where the experimental limitations of this specific configuration are discussed.

— **Primary Multilayer Sample:**

  — *Five-Layer Si_3N_4/SiO_2 Stack:* This is the central sample of the thesis, consisting of the dielectric stack [SiO_2(312 nm)/Si_3N_4(226 nm)/SiO_2(312 nm)/SiO_2(312 nm)/SiN(126 nm)] deposited via PECVD onto a 150 µm fused silica substrate. (Detailed fabrication below; analysis in Chapter 5).

The following subsections detail the general procedures used for substrate cleaning, the specific PECVD deposition process for the multilayer stack, and the sensor patterning steps common to all samples.

Substrate Preparation and Dielectric Thin Film Deposition (PECVD for Multilayer Sample)

The foundation for high-quality thin-film deposition is a pristine substrate surface. For the bulk validation samples ($BrSiO_2$, Fused Silica), commercially polished wafers were used after undergoing a rigorous cleaning procedure involving sonication in sequential baths of Acetone and Isopropanol, followed by a final cleaning/drying step noted as SVC-14, 15 min @ 100 °C. The wafers were rinsed with deionized water and dried before sensor fabrication.

For the primary multilayer sample, the same cleaning procedure was applied to the 150 µm fused silica substrate before loading into the Plasma-Enhanced Chemical Vapor Deposition (PECVD) system. PECVD allows for high-quality dielectric film deposition at relatively low temperatures [138]. The deposition proceeded sequentially in the vacuum chamber onto the heated substrate electrode to form the stack structure: Substrate / SiO_2(312 nm) / Si_3N_4(226 nm) / SiO_2(312 nm) / SiO_2(312 nm) / SiN(126 nm). Key process parameters (precursor gases like SiH_4, N_2O, NH_3; flow rates; temperature 200 °C to 400 °C; RF power 13.56 MHz; pressure) were precisely controlled. Following deposition, the thickness of each layer was verified using spectroscopic ellipsometry [139], confirming the total stack thickness of 1288 nm.

Sensor Patterning via Photolithography and Lift-off (Common Process)

Once the substrate was prepared (either bare for validation samples or coated with the dielectric stack), the metallic heater/sensor pattern was created using a standard positive photolithography and lift-off process [140]. This process was applied uniformly to all sample types mentioned above. The specific steps were as follows:

(a) **Photoresist Coating:** Coating with AZ 1512 photoresist (Spin: 2500 rpm, Accel: 1000 rpm/s^2, Time: 12 s), followed by a soft bake (110 °C, 1 min).

(b) **Exposure:** Pattern transfer using laser lithography.

(c) **Development:** Immersion in MIF 326 developer (45 s), followed by rinse and dry.

(d) **Metallization:** Deposition in a high-vacuum sputtering system: 40 nm Titanium (Ti) adhesion layer followed by 500 nm Gold (Au).

(e) **Lift-Off:** Dissolving the resist stencil in a suitable solvent, potentially using the "SVC-14" process (100 °C, 2.5 hours), leaving the patterned Ti/Au structures.

Final Inspection and Geometrical Characterization

After lift-off, all fabricated devices underwent inspection via optical microscopy. The critical geometrical dimensions (width $2b$, length L) of the heater lines for each successfully fabricated device across all sample types were accurately measured using a calibrated optical microscope system. These dimensions are essential input parameters for the subsequent thermal modeling and analysis presented in Chapters 4 and 5.

3.3 Numerical Modeling with COMSOL Multiphysics

As established in Chapter 2, analytical models for the 3-ω method are elegant and effective for simple and idealized structures. However, they become insufficient when applied to multilayer systems involving finite heater geometry, lateral heat spreading, multiple interfaces, and strong correlations between thermal parameters. To overcome these limitations, a hierarchical finite element modelling strategy was developed using COMSOL Multiphysics®.

In this chapter, the numerical formulation is introduced mainly through a two-dimensional (2D) cross-sectional model of the 3-ω experiment. This 2D model describes heat diffusion in the plane perpendicular to the heater length and is used for model validation, parametric studies, and analysis of the limitations of simplified analytical approaches. For the final analysis of the five-layer dielectric stack presented in Chapter 5, the modelling framework is extended to a three-dimensional (3D) FEM model including infinite element domains. The 3D model is used as the forward model in the virtual experiment protocol and in the inverse fitting procedure for extracting the effective thermal conductivity of the multilayer structure. Therefore, the 2D model presented in this chapter should be understood as a diagnostic and validation tool, whereas the 3D model is used for the final multilayer extraction.

3.3.1 Introduction to the Finite Element Method (FEM) for Heat Transfer Problems

The Finite Element Method is a numerical technique for finding approximate solutions to boundary value problems governed by partial differential equations [141, 142]. It is particularly well suited to problems involving complex geometries, heterogeneous materials, and non-trivial boundary conditions, all of which are present in this work. The core idea of FEM is discretization: instead of seeking a single analytical expression over the entire domain, the computational domain is divided into a large

number of smaller, non-overlapping finite elements, such as triangles, quadrilaterals, tetrahedra, or hexahedra.

Within each element, the temperature field is approximated using simple interpolation functions, also called shape functions. The heat diffusion equation is then reformulated in weak form and assembled over all elements, leading to a system of algebraic equations. In matrix form, this system can be written schematically as

$$\mathbf{KT} = \mathbf{F} \tag{3.30}$$

where $\mathbf{K}$ is the global conductance matrix, $\mathbf{T}$ is the vector of nodal temperatures, and $\mathbf{F}$ is the vector of applied heat loads. The numerical solution gives the temperature field throughout the domain. The accuracy of the FEM solution depends strongly on the mesh density and quality; a finer mesh generally improves accuracy but increases computational time and memory requirements [143].

3.3.2 Model Geometry and Physics

The construction of the FEM model requires a careful translation of the physical experiment into a numerical problem. This includes the choice of model dimensionality, the definition of material domains, and the specification of the governing heat-transfer equation.

$2D$ and $3D$ Model Setup and Symmetry Considerations

A full three-dimensional model of the 3-ω heater on a chip provides the most complete representation of the experimental geometry. However, it is computationally demanding because the heater length (l) is much larger than both its width ($2b$) and the thicknesses of the deposited layers. In a typical 3-ω configuration, l is on the order of millimetres, whereas $2b$ is on the order of several micrometres, leading to a length-to-width aspect ratio of about 100 : 1 or higher. Owing to this large aspect ratio, the thermal response in the central part of the heater can be considered nearly invariant along the heater length. Far from the heater ends and contact pads, end effects are negligible, and heat spreading is mainly governed by the cross-sectional plane perpendicular to the heater length. This approximation justifies the use of a $2D$ model for validation and parametric analysis [84].

In the present work, the $2D$ model was constructed from the complete cross-section of the experimental structure, including the heater, the thin-film stack, and the substrate, as shown in Figure 3.14. No geometrical symmetry reduction was applied in the $2D$ simulations. For the $3D$ model used in Chapter 5, a symmetry simplification was introduced to reduce the computational cost. Since the heater geometry, the multilayer stack, and the thermal excitation are symmetric with respect to the vertical plane passing through the centre of the heater along its length, only one half of the 3D structure was simulated.

On this symmetry plane, a zero normal heat flux condition was imposed:

$$-\mathbf{n} \cdot \mathbf{q} = 0. \tag{3.31}$$

This boundary condition is a direct consequence of mirror symmetry. The two sides of the symmetry plane are physically identical and are subjected to the same thermal excitation. Therefore, any heat flux that would tend to cross the plane from one side would have an identical mirror counterpart tending to cross it in the opposite direction. These two contributions cancel each other exactly.

As a result, the net heat flux through the symmetry plane must be zero. In other words, heat may still flow along the symmetry plane, but it cannot cross it. Thus, the condition $-\mathbf{n} \cdot \mathbf{q} = 0$ does not represent an external adiabatic boundary. It simply enforces the fact that no net heat crosses the central mirror plane of the full structure.

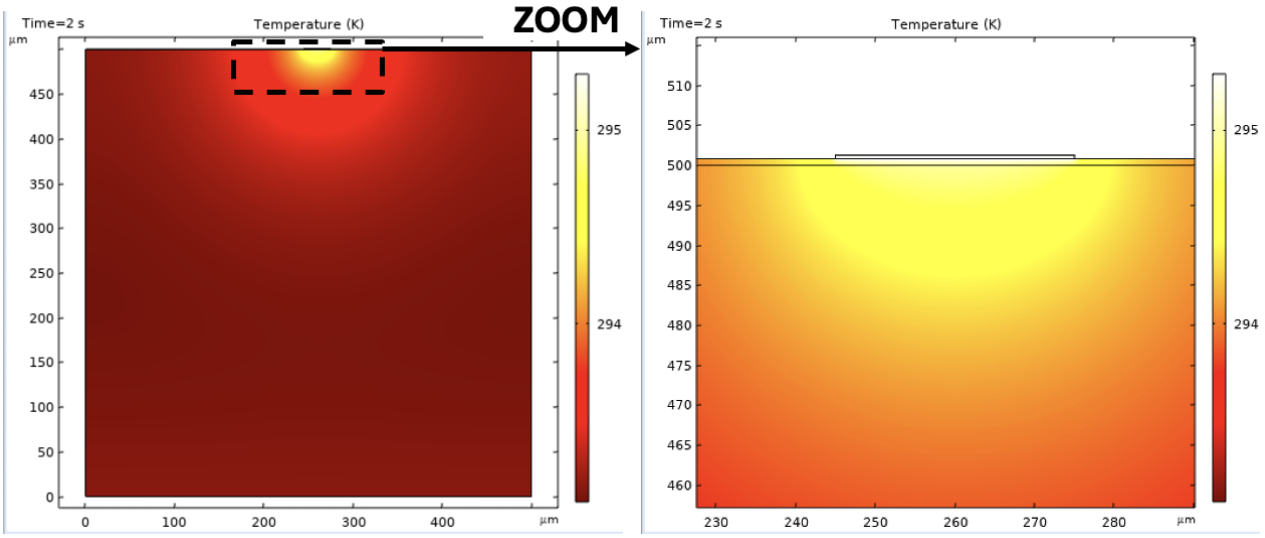


Figure 3.14 – Example of a 2D computational domain used for the diagnostic FEM simulations, showing the resulting temperature distribution. The model geometry consists of the Ti/Au heater (30 µm wide, 0.5 µm thick) on a one-layer stack. The stack consists of a 0.8 µm Parylene C film (κ = 0.13 W,m^{-1},K^{-1}) on top of a 500 µm × 500 µm borosilicate glass ($BrSiO_2$) substrate (κ = 1.13 W,m^{-1},K^{-1}). In this finite-domain example, a heat flux corresponding to an RMS power P_{rms} = 3.99 W,m^{-1} is applied to the top of the heater, and isothermal conditions are applied to the lateral and bottom boundaries.

Governing Equation: Frequency-Domain Heat Transfer

As derived in Section 3.1, the metallic heater in the 3-ω experiment generates Joule heating at the second harmonic frequency, 2ω. The corresponding temperature field therefore also oscillates at 2ω. Instead of solving the transient heat equation in the time domain, the problem can be solved more efficiently in the frequency domain.

Assuming a time-harmonic temperature field of the form

$$T(\mathbf{r}, t) = T_{\text{dc}}(\mathbf{r}) + \theta(\mathbf{r})e^{i2\omega t} \tag{3.32}$$

where $\theta(\mathbf{r})$ is the complex amplitude of the temperature oscillation, the governing equation solved in COMSOL is:

$$\rho c_p(i2\omega)\theta + \nabla \cdot (-\kappa\nabla\theta) = Q_{2\omega}. \tag{3.33}$$

Here, ρ is the mass density, c_p is the mass specific heat capacity, and ρc_p is therefore the volumetric heat capacity. The parameter κ is the thermal conductivity of each material, i is the imaginary unit, and $Q_{2\omega}$ is the amplitude of the heat source at frequency 2ω. The term $(i2\omega)\rho c_p\theta$ represents the cyclic storage of thermal energy. By solving Eq. (3.33), COMSOL directly computes the complex temperature field, from which the amplitude and phase of the thermal oscillation can be extracted.

Modeling Multilayer Structures and Interfaces

The primary advantage of the FEM approach is its ability to handle heterogeneous multilayer geometries. The multilayer stack is constructed by defining adjacent solid domains, each assigned the material properties of the corresponding physical layer, such as the thermal conductivity κ_i and volumetric heat capacity $\rho_i c_{p,i}$.

For ideal interfaces, temperature and normal heat flux are assumed to be continuous across the boundary:

$$T_1 = T_2, \qquad \mathbf{n} \cdot \mathbf{q}_1 = \mathbf{n} \cdot \mathbf{q}_2. \tag{3.34}$$

When a Thermal Boundary Resistance (TBR) is considered, the interface is modeled in COMSOL using the *Thermal Contact* feature with the contact model set to *Equivalent thin resistive layer*. In this formulation, the interface is not represented as a volumetric layer with an explicit thickness. Instead, it is introduced as a boundary resistance, defined by a layer resistance R_{eq} with units of $\mathrm{K, m^2, W^{-1}}$. In the present model, this layer resistance is identified with the thermal boundary resistance:

$$R_{\mathrm{eq}} = R_{\mathrm{TBR}}. \tag{3.35}$$

The thermal contact condition imposes a temperature discontinuity across the interface, proportional to the normal heat flux J_n:

$$\Delta T = R_{\mathrm{TBR}} J_n. \tag{3.36}$$

Here, ΔT is the temperature jump across the interface and J_n is the heat flux normal to the interface. The radiative conductance term in the COMSOL thermal contact feature was set to zero, so that only conductive interfacial resistance was considered.

This formulation allows the interfacial resistance R_{TBR} to be treated as an independent thermal parameter. It is therefore useful for analysing multilayer systems and for investigating the parameter correlations discussed in Chapter 5.

3.3.3 Boundary Conditions and Meshing

The accuracy of the FEM model depends on two essential aspects: the definition of boundary conditions that correctly translate the physical experiment into mathematical constraints, and a mesh sufficiently refined to resolve the thermal gradients in the heater, thin films, interfaces, and substrate. In the present work, each boundary condition was assigned according to its physical meaning in the 3-ω experiment.

Heat Source and Thermal Boundary Conditions

In the physical experiment, heat is generated by Joule dissipation in the metallic heater. Since the electrical current oscillates at the angular frequency ω, the Joule heating power contains a component at 2ω, which is responsible for the temperature oscillation measured by the 3-ω method. In the 2D model, the total heating power is expressed per unit heater length, $P'_{2\omega} = P_{2\omega}/l$, and is applied as a heat flux on the heater surface:

$$-\mathbf{n} \cdot \mathbf{q} = q_{2\omega}^{2D} = \frac{P'_{2\omega}}{2b} = \frac{P_{2\omega}}{2bl} = \frac{I_{\mathrm{rms}}^2 R_0}{2bl}. \tag{3.37}$$

Here, $\mathbf{n}$ is the outward normal vector, $\mathbf{q}$ is the conductive heat flux vector, $2b$ is the heater width, l is the heater length, I_{rms} is the RMS current, and R_0 is the reference heater resistance.

For normalized simulations, the input power per unit length can be set to $1\ \mathrm{W.m^{-1}}$. The calculated temperature response then has units of $\mathrm{K.m.W^{-1}}$ and represents the thermal impedance of the structure.

The main thermal boundary conditions used in the FEM model are summarized in Table 3.2. This table explicitly links each physical assumption to the corresponding mathematical expression used in the model.

For the 2D diagnostic and validation models, the computational domain was chosen sufficiently large with respect to the heater width and to the thermal penetration depth in the selected frequency range. In finite-domain examples, isothermal boundaries were applied to the lateral and bottom boundaries to reproduce a finite-size substrate configuration. For the final 3D multilayer model used in Chapter 5, infinite element domains were introduced around the substrate. These domains allow the complex temperature field to decay smoothly away from the heater and reduce artificial effects associated with the truncation of the computational domain.

Table 3.2 – Physical interpretation and mathematical expression of the boundary conditions used in the FEM model.

Physical situation	**Mathematical expression**	**Use in the model**
Periodic Joule heating in the metallic strip	$-\mathbf{n} \cdot \mathbf{q} = q_{2\omega}$	Applied on the heater surface or heater domain, depending on the model dimensionality
Symmetry plane in the 3D model	$-\mathbf{n} \cdot \mathbf{q} = 0$	Used when only one half of the 3D geometry is simulated
Top surface not covered by the heater	$\mathbf{n} \cdot \mathbf{q} = 0$	Neglects convection and radiation losses to air
Finite lateral and bottom boundaries in 2D diagnostic models	$T = T_0$ or $\theta = 0$	Represents an isothermal boundary at ambient temperature for finite-domain validation cases
Interface between two solid layers without TBR	$T_1 = T_2$, $\mathbf{n} \cdot \mathbf{q}_1 = \mathbf{n} \cdot \mathbf{q}_2$	Ensures temperature and heat-flux continuity
Interface with thermal boundary resistance	$\Delta T = R_{\mathrm{TBR}} J_n$	Represents a temperature jump proportional to the normal heat flux
Outer boundaries with infinite element domains	Smooth decay of θ away from the heater	Used in the final 3D multilayer model to reduce artificial boundary effects

The top surface not covered by the heater was treated as thermally insulated. This assumption is justified because, under the present experimental conditions, heat transfer by natural convection and radiation toward the surrounding air is much smaller than heat conduction into the substrate and the multilayer stack. These losses were therefore neglected in the main thermal model.

Meshing Strategy and Convergence

A non-uniform meshing strategy was employed to balance numerical accuracy and computational cost. The mesh was strongly refined in the heater, thin-film stack, and interface regions, where the thermal gradients are the steepest. A progressively coarser mesh was used farther from the heater, where the temperature field varies more slowly.

The meshing strategy used in this work can be summarized as follows:

— **Refined mesh near the heater and interfaces:** the heater, the dielectric layers directly beneath it, and the interfaces were meshed with small elements in order to resolve steep local thermal gradients.

— **Layered or swept mesh through thin films:** in the thin-film stack, a structured or swept mesh was used whenever possible to preserve the layer geometry and avoid poorly shaped elements across nanometer-scale thicknesses.

— **Coarser mesh in the substrate and outer domains:** in regions far from the heater, where thermal gradients are weaker, a coarser mesh was used to reduce the total number of degrees of freedom.

Figure 3.15 shows a representative mesh used for the 2D diagnostic model. The left view illustrates the global mesh distribution, while the zoomed view highlights the strong refinement in the heater and thin-film region. This 2D mesh is used to support the validation and parametric studies discussed in Chapters 3 and 4.

In addition to mesh refinement, the mesh quality was evaluated using the quality indicators available in COMSOL. The mesh quality factor is a dimensionless indicator ranging from 0 to 1.

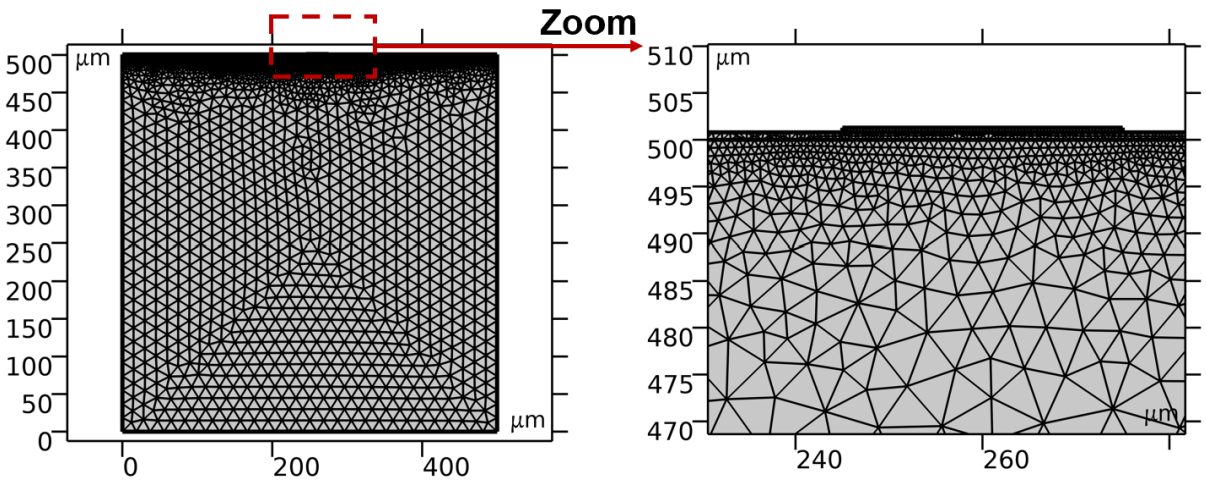


Figure 3.15 – Representative mesh used for the 2D diagnostic FEM model. The wide view shows the coarser mesh away from the heater, while the zoomed-in view highlights the refined mesh in the heater/film region, where high thermal gradients must be resolved accurately.

Values close to 1 correspond to well-shaped elements, whereas values close to 0 indicate highly distorted elements. The minimum element quality, the average element quality, the element aspect ratio, and the distribution of distorted elements were checked both globally and locally. Particular attention was paid to the heater, the thin dielectric layers, and the interfaces, since numerical errors in these regions directly affect the calculated heater temperature response.

The mesh convergence was evaluated by refining the mesh and comparing the averaged complex temperature response of the heater, θ_{avg}, which is the quantity directly used for comparison with the experimental 3-ω signal. The mesh was considered sufficiently refined when further refinement produced negligible changes in both the in-phase and out-of-phase components of θ_{avg} over the frequency range used for fitting. In the parameter estimation procedure, this convergence check ensures that the retrieved thermal parameters are governed by the physical model and experimental data, rather than by the numerical discretization.

As a representative example of the 3D discretization, Figure 3.16 shows the mesh used for one virtual multilayer sample in the virtual experiment protocol discussed in Chapter 5. This second example complements the 2D mesh shown in Figure 3.15: the former illustrates the simplified cross-sectional model used for validation and parametric analysis, whereas the latter illustrates the 3D modelling strategy used for the multilayer inverse problem.

The corresponding mesh statistics are reported in Table 3.3. This example illustrates the mapped and swept meshing strategy adopted for the 3D models. The mesh mainly consists of regular hexahedral elements, which are well adapted to the layered geometry of the heater, dielectric stack, and substrate.

3.3.4 Simulation of the 3ω Signal

Once the geometry, material properties, boundary conditions, and mesh are defined, the simulation is performed over the same frequency range as the experiment.

Implementation of Frequency-Domain Analysis

The model is solved as a parametric sweep over the electrical heating frequency f, with $\omega = 2\pi f$. At each frequency, the heat source oscillates at 2ω, and COMSOL computes the complex temperature field θ. In the 2D model, this field is written as $\theta(x, y)$; in the 3D model, it is written as $\theta(x, y, z)$. This

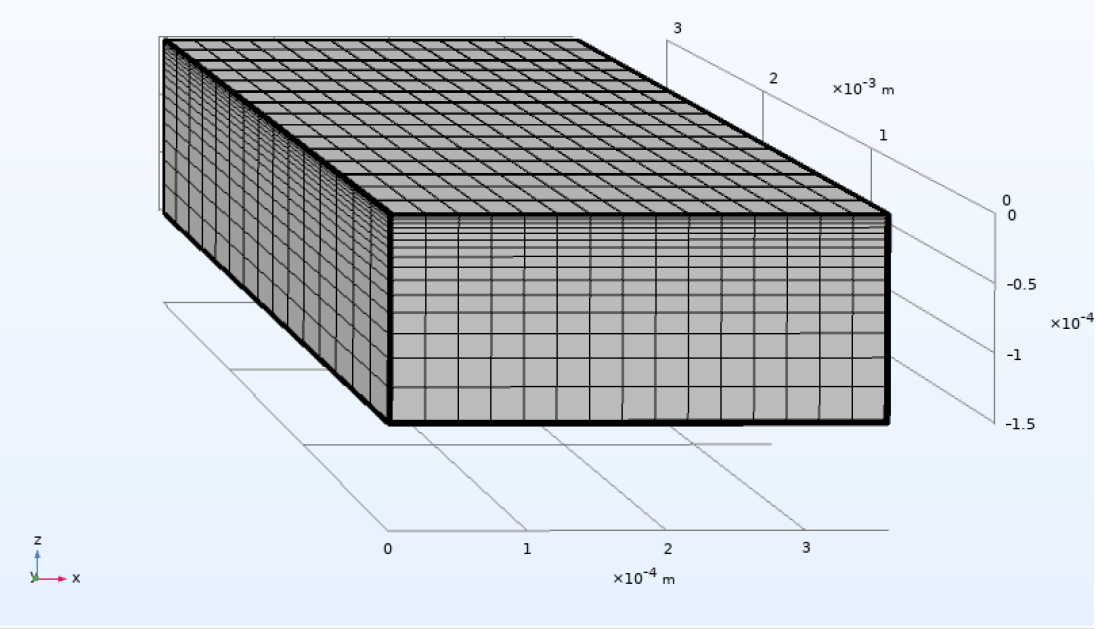


Figure 3.16 – Representative 3D mesh used for one virtual multilayer sample in Chapter 5. The mapped and swept meshing strategy produces regular hexahedral elements along the heater and multilayer stack, while preserving the geometrical resolution required near the thin-film interfaces.

Table 3.3 – Mesh statistics and quality indicators for a representative 3D virtual sample used in Chapter 5. The element quality was evaluated using the skewness quality measure in COMSOL.

Mesh quantity	**Value**
Mesh vertices	14080
Hexahedral elements	12210
Quadrilateral boundary elements	4898
Edge elements	691
Vertex elements	34
Minimum element quality	1.0
Average element quality	1.0
Element volume ratio	1.304×10^{-5}
Mesh volume	1.634×10^{-10} m^3

procedure generates a virtual dataset directly comparable to the in-phase and out-of-phase components measured by the lock-in amplifier.

Extraction of Temperature Oscillation and Comparison with Experiment

The key output quantity is the average complex temperature oscillation of the heater, because the measured 3ω voltage is generated by the temperature-dependent resistance of the metallic transducer.

For the 2D cross-sectional model, the heater is assumed invariant along its length. The average temperature is therefore calculated along the top boundary of the heater in the cross-section. In the half-domain representation, this gives:

$$\theta_{\mathrm{avg}}^{2D} = \frac{1}{b} \int_0^b \theta(x, y = y_{\mathrm{h}}), dx. \tag{3.38}$$

This line average is not an arbitrary simplification; it is the 2D analogue of averaging the temperature over the active heater region, under the assumption that the temperature is uniform along the heater length away from the end effects.

For the 3D model used in Chapter 5, the corresponding quantity is the surface average over the active heater area:

$$\theta_{\text{avg}}^{3D} = \frac{1}{A_{\text{h}}} \int_{A_{\text{h}}} \theta(x, y, z), dA, \tag{3.39}$$

where A_{h} is the active top surface area of the heater included in the simulated domain. When symmetry is used, the integration is performed over the simulated heater surface and normalized by the corresponding simulated area.

The computed average temperature is a complex quantity. Its real part, $\text{Re}(\theta_{\text{avg}})$, corresponds to the in-phase component of the temperature oscillation, while its imaginary part, $\text{Im}(\theta_{\text{avg}})$, corresponds to the out-of-phase component. These two components are the numerical counterparts of the X and Y components of the measured 3ω signal.

By performing this calculation at each frequency, two simulated curves are obtained:

$$\Delta T_{\text{in-phase}}(f) = \text{Re}\left[\theta_{\text{avg}}(f)\right], \qquad \Delta T_{\text{out-of-phase}}(f) = \text{Im}\left[\theta_{\text{avg}}(f)\right] \tag{3.40}$$

These curves constitute the output of the forward model. They are compared with the experimentally measured temperature oscillation curves during the inverse fitting process described in Chapter 5. The unknown thermal parameters are then obtained by minimizing the difference between the simulated and experimental responses, typically in a least-squares sense.

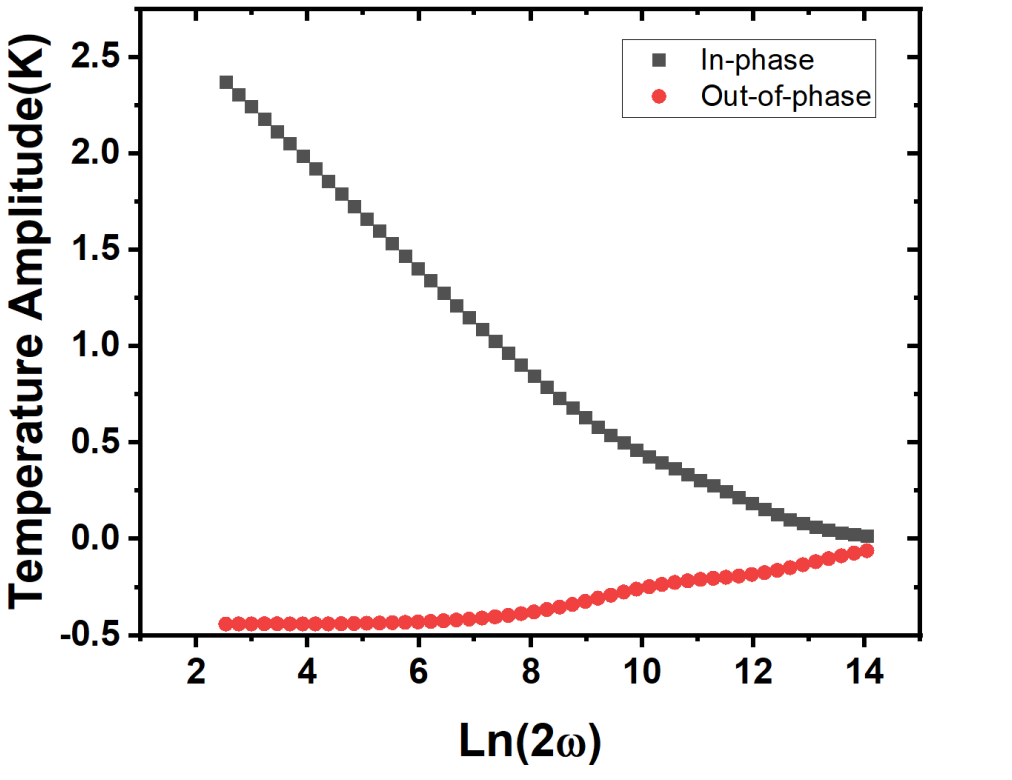


Figure 3.17 – Example of the output of the virtual experiment. The plot shows the simulated in-phase $\text{Re}(\theta_{\text{avg}})$ and out-of-phase $\text{Im}(\theta_{\text{avg}})$ components of the heater temperature oscillation as a function of frequency. These curves are the numerical equivalent of the data obtained from the lock-in amplifier after conversion of the measured 3ω voltage into temperature oscillation.

3.4 Chapter Summary and Outlook to Validation

This chapter has comprehensively detailed the three foundational pillars of the methodology employed in this dissertation: the theoretical framework of the 3-ω method, the practical implementation

of the experimental apparatus, and the development of a high-fidelity numerical model.

Section 3.1 refers to the main sections of this methodology chapter as outlined in the introduction. It established the fundamental physics of the 3-ω signal, deriving its generation from the 2ω Joule heating and the temperature-dependent resistance of the sensor. A thorough review of the classical analytical solutions for various geometries (from bulk substrates to complex multilayers) was presented. This theoretical exploration concluded by critically highlighting the severe limitations of these analytical models, particularly their reliance on restrictive assumptions (e.g., $\kappa_f \ll \kappa_s$) and, most importantly, their inability to resolve the ill-posed inverse problem inherent in multilayer systems with parameter correlations.

Section 3.2 detailed the practical realization of the measurement. This included a full description of the sample fabrication process, covering all steps from substrate cleaning and PECVD film deposition to the sensor patterning via photolithography, sputtering, and lift-off. It also provided a detailed walkthrough of the custom-built experimental bench, identifying the specific instrumentation (Keysight function generator, SR7265 lock-in amplifier), the function of the Wheatstone bridge for 1ω cancellation, and the critical importance of the four-wire probe (Kelvin) configuration. The rigorous in-situ TCR calibration procedure, which is essential for converting measured voltage into temperature, was also established.

Section 3.3 detailed the development of the numerical modelling framework in COMSOL Multiphysics ®. A hierarchical modelling strategy was introduced: a 2D cross-sectional model was used for validation and parametric analysis, while the final multilayer extraction relies on a 3D FEM model presented in Chapter 5. The governing frequency-domain heat-transfer equation was formulated, and the implementation of heat sources, thermal boundary conditions, interface thermal resistances, and mesh refinement strategies was described. Particular attention was paid to the extraction of the averaged complex heater temperature, which provides the numerical counterpart of the experimentally measured 3ω signal.

In summary, this chapter has constructed a complete, hybrid methodological framework. We have established the "rules of the game" through theory, built the physical apparatus to conduct the experiment, and developed the virtual simulation tool to accurately analyze the results. This integrated toolbox, combining analytical theory, experimental hardware, and numerical power, is now fully established.

The immediate next step, however, is to rigorously validate this entire framework before applying it to our primary scientific problem. The following chapter, Chapter 4, is dedicated to precisely this critical validation process. We will use the experimental setup to test known standards ($BrSiO_2$ and Fused Silica) and use the numerical model to explore parametric sensitivities, thereby building the final layer of confidence required before the methodology is applied to the complex multilayer stack in Chapter 5.

Chapter 4

Validation and Parametric Study of the Thermal Metrology

The previous chapter introduced the theoretical basis of the 3-ω method, the experimental platform developed in this work, and the numerical modeling strategy implemented in COMSOL Multiphysics ®. These three elements form the methodological basis of this thesis. However, before applying this combined experimental and numerical approach to the complex Si_3N_4/SiO_2 multilayer stack studied in Chapter 5, it is necessary to verify that the method gives reliable results under well-controlled conditions.

The objective of this chapter is therefore to validate the thermal characterization procedure and to study the main parameters that influence the 3-ω response. This validation step is important for two reasons. First, it checks whether the experimental setup can correctly measure the thermal conductivity of materials whose properties are already known. Second, it allows the numerical model to be tested against analytical solutions and then used to explore situations that are difficult to investigate experimentally. In this way, the chapter provides the link between the theoretical and experimental developments of Chapter 3 and the inverse analysis of the multilayer sample presented in Chapter 5.

The chapter is divided into two main parts, corresponding to the two complementary aspects of the methodology.

Experimental validation, Section 4.1: The 3-ω experimental setup is first tested using reference bulk materials. Borosilicate glass and fused silica were selected because they are homogeneous, isotropic, and have well-documented thermal conductivities. These materials therefore provide suitable test cases for evaluating the complete experimental chain. The validation includes the fabrication and calibration of the metal heater, the measurement of the temperature coefficient of resistance, the acquisition of the third-harmonic voltage, and the extraction of the thermal conductivity using the analytical slope method given in Eq. (3.16). The extracted values are then compared with literature values in order to evaluate the accuracy and repeatability of the experimental platform.

Numerical validation and parametric study, Section 4.2: The FEM model is then used to reproduce the 3-ω thermal response under controlled numerical conditions. The first objective is to validate the numerical model by comparing simulated results with the analytical solutions introduced in Chapter 3. This comparison is performed for simple configurations, such as bulk substrates and single-film systems, where analytical descriptions are available. Once this validation is established, the FEM model is used to perform a parametric study. Several parameters are varied, including the heater width, the input power, the substrate properties, the film thermal conductivity, and the contrast between the film and the substrate. The purpose is to identify how these parameters affect the temperature response, the sensitivity of the method, and the range in which simplified analytical models can still be used.

This chapter therefore has a double role. On the experimental side, it demonstrates that the 3-ω setup developed in this work can provide consistent thermal conductivity values for reference materials. On the numerical side, it shows that the FEM model can reproduce the expected behavior of the 3-ω method and can be used to analyze more complex cases. The parametric study also highlights the limits of the classical analytical approach, especially when the thermal response is affected by finite heater width, thin-film effects, substrate influence, or strong contrasts between layers.

These results prepare the analysis presented in Chapter 5. In particular, they show why a direct analytical treatment is not sufficient for the final multilayer sample and why an FEM-based inverse fitting approach is required. The validation and parametric study presented here therefore provide the necessary basis for extracting an effective thermal conductivity from the complex Si_3N_4/SiO_2 multilayer stack.

4.1 Experimental Validation on Bulk Substrates

The first step in validating the 3-ω setup is to test it on reference materials with known thermal properties. For this purpose, 3-ω heater/sensors were fabricated on two amorphous glass substrates: borosilicate glass ($BrSiO_2$) and fused silica. The fabrication process of the heater/sensors was described in Section 3.2.3. These two materials were chosen because they are homogeneous, isotropic, and have well-documented thermal conductivity values.

The experimental data were analyzed using the analytical slope method derived in Chapter 3, Eq. (3.16). This method is suitable for bulk substrates when the frequency range satisfies the conditions required for the linear regime. The objective of this section is therefore to verify that the complete experimental chain, including sensor fabrication, electrical calibration, third-harmonic voltage measurement, and thermal conductivity extraction, gives consistent results on reference samples before applying the method to more complex multilayer structures.

4.1.1 Initial Characterization: Resistance and TCR

Before performing the 3-ω thermal measurements, the baseline electrical properties of the fabricated heater/sensors were characterized at room temperature, approximately 20 °C. The resistance of each heater line was measured using the four-wire probe method described in Section 3.2.1. Figure 4.1 shows photographs of the validation samples. Figure 4.1(a) shows the $BrSiO_2$ samples, while Figure 4.1(b) shows the fused-silica sample on the left and the SiO_2/Si sample on the right.

The measured resistances for all heater lines on the validation samples are presented in Tables 4.1, 4.2, and 4.3.

The Temperature Coefficient of Resistance (TCR), denoted by β, was then calibrated for each heater line using the procedure described in Section 3.2.1. The resistance was measured as a function of temperature using the TC40 environmental chamber. In these measurements, the temperature was increased step by step over a typical range from 20 °C to 60 °C. The resistance-temperature relation was then fitted by a linear function.

Figure 4.2 shows representative TCR calibration results. Figure 4.2(a) corresponds to $BrSiO_2$ Sample 1 Line 8, and Figure 4.2(b) corresponds to fused-silica Sample 3 Line 2.

For the SiO_2 thin film on a silicon substrate, the same procedure was also applied. Figure 4.3 shows the resistance-temperature relation obtained for this sample.

The slope of the linear fit, dR/dT, was used to calculate the TCR according to: $\beta = \frac{1}{R_0}\frac{dR}{dT}$.

The resulting TCR values are summarized in Tables 4.4, 4.5, and 4.6.

These R_0 and β values are essential for converting the raw electrical signals into thermal quantities. The resistance R_0 is used to determine the Joule heating power generated in the metal strip, while the TCR β is used to convert the measured third-harmonic voltage into the temperature oscillation of the heater.

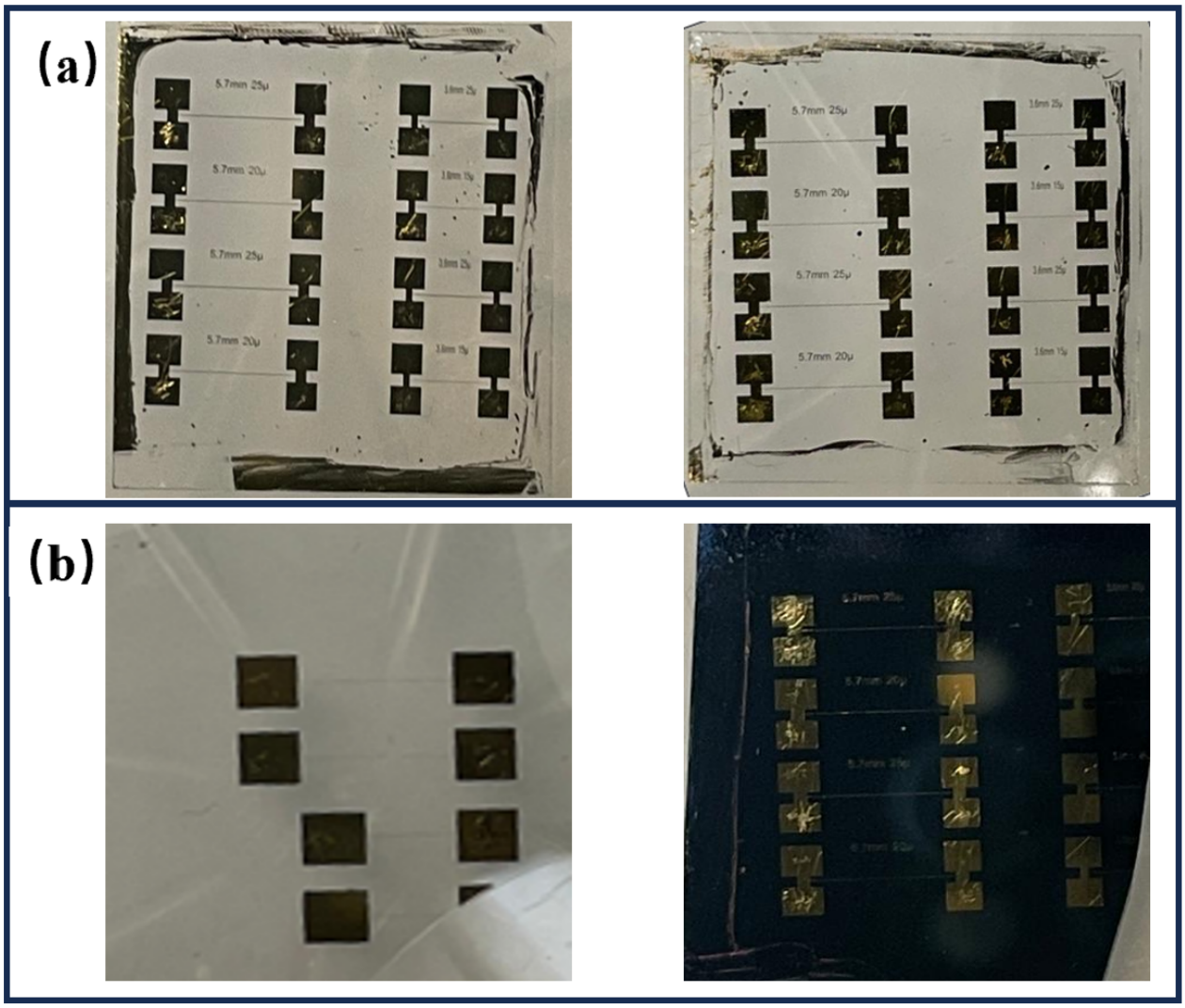


Figure 4.1 – Photographs of the validation samples: (a) $BrSiO_2$ Samples 1 and 2, and (b) fused-silica sample on the left and SiO_2/Si sample on the right. The patterned 3-ω heater/sensor structures can be observed on the sample surfaces.

4.1.2 3-ω Measurement on Borosilicate Glass

The 3-ω frequency sweep was first performed on the calibrated $BrSiO_2$ samples. For each selected heater line, an AC voltage at the fundamental frequency was applied to the metal strip, and the resulting in-phase third-harmonic voltage, $V_{3\omega,\mathrm{in}}$, was recorded as a function of frequency. This voltage was then converted into the in-phase temperature oscillation, ΔT_{in}, using Eq. (3.6).

Before extracting the thermal conductivity, the appropriate linear frequency range was estimated from the thermal penetration depth conditions introduced in Chapter 3. For a bulk substrate, the heater should behave as a line heat source, while the thermal wave should not reach the bottom of the substrate. These conditions define a frequency window in which the analytical slope method can be applied. For the $BrSiO_2$ samples, with a substrate thickness of 1 mm, the calculated frequency ranges depend on the heater width and are summarized in Table 4.7.

A representative experimental result for $BrSiO_2$ is shown in Figure 4.4. The in-phase temperature oscillation varies linearly with $\ln(2\omega)$ in the selected frequency range, as expected from the analytical 3-ω model for bulk substrates.

The thermal conductivity of the substrate, κ_s, was extracted from the slope of the linear fit. If the

Table 4.1 – Resistance measurements of heater lines on $BrSiO_2$ Samples 1 and 2 at 20 °C.

Sample	Line	R_0 (Ω)	Width (µm)	Length (mm)
Sample 1	1	22.15	25	5.7
	2	27.88	20	5.7
	3	21.87	25	5.7
	4	27.92	20	5.7
	5	14.55	25	3.6
	6	25.51	15	3.6
	8	25.78	15	3.6
Sample 2	1	22.02	25	5.7
	2	27.59	20	5.7
	3	22.69	25	5.7
	4	28.93	20	5.7
	5	14.73	25	3.6
	7	14.50	25	3.6
	8	25.58	15	3.6

Table 4.2 – Resistance measurements of heater lines on fused-silica Sample 3 at 20 °C.

Line	R_0 (Ω)	Width (µm)	Length (mm)
1	55.42	6	5
2	24.89	8	3

Table 4.3 – Resistance measurements of heater lines on the SiO_2/Si sample at 20 °C.

Line	R_0 (Ω)	Width (µm)	Length (mm)
1	24.88	20	5.7
2	20.44	25	5.7
3	28.51	20	5.7

slope is denoted by:

$$B = \frac{d\Delta T_{\text{in}}}{d\ln(2\omega)} \tag{4.1}$$

the thermal conductivity is obtained using:

$$\kappa_s = -\frac{P'}{2\pi B} \tag{4.2}$$

where P' is the heating power per unit length. The negative sign is required because the measured in-phase temperature decreases with increasing frequency, leading to a negative slope. The input parameters and extracted thermal conductivity values for all measured lines are summarized in Table 4.8.

The extracted thermal conductivity values are generally close to the literature value of approximately 1.13 $W.m^{-1}.K^{-1}$ for borosilicate glass [144]. Some dispersion is observed between the different heater lines, which can be attributed to differences in heater geometry, electrical contact quality, signal level, and uncertainty in the selected fitting range. Most of the reliable values are located around 1.14 – 1.21 $W.m^{-1}.K^{-1}$, which confirms that the experimental setup and the analytical slope method provide reasonable results for bulk amorphous glass substrates.

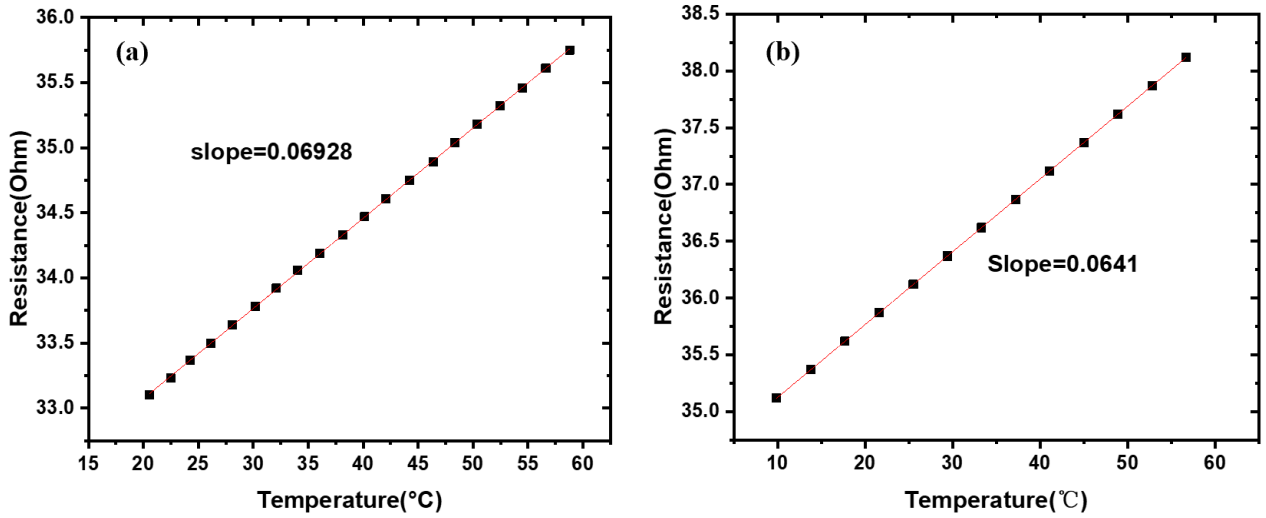


Figure 4.2 – Representative TCR calibration data. (a) Resistance as a function of temperature for a heater on $BrSiO_2$ Sample 1 Line 8. (b) Resistance as a function of temperature for a heater on fused-silica Sample 3 Line 2. The linear behavior confirms that the heater resistance can be used as a temperature sensor in the investigated range.

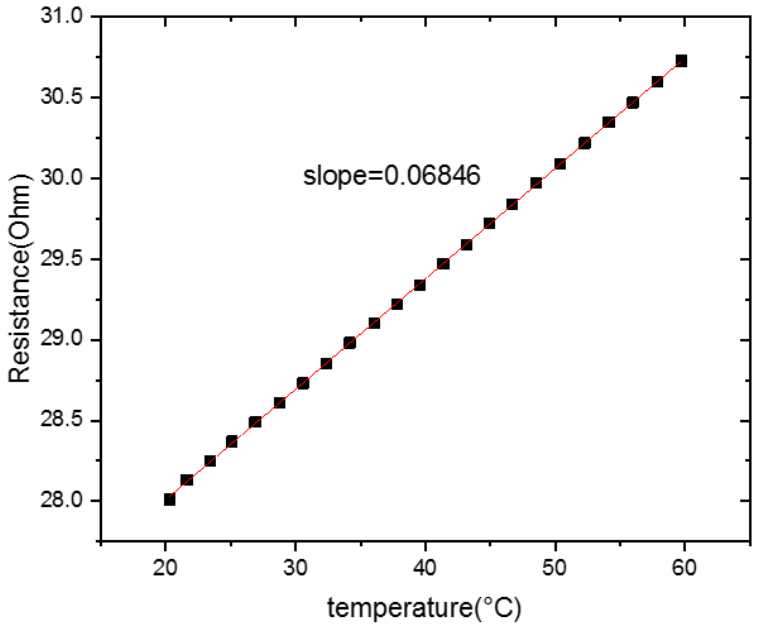


Figure 4.3 – Representative TCR calibration data for a heater on the SiO_2/Si sample. The plot shows the resistance as a function of temperature for Sample 4 Line 2.

The measurements on $BrSiO_2$ also show the importance of heater geometry. For a given substrate thickness, the heater width affects the accessible linear frequency range through the thermal penetration depth condition. Therefore, the heater geometry must be taken into account when selecting the frequency window used for the thermal conductivity extraction.

4.1.3 3-ω Measurement on Fused Silica

The same validation procedure was then applied to the fused-silica sample. Compared with the $BrSiO_2$ samples, the fused-silica substrate used here was thinner, with a thickness of 150 µm. Therefore, the frequency range satisfying the thermal penetration depth conditions is shifted to higher

Table 4.4 – Calibrated TCR values for $BrSiO_2$ Samples 1 and 2.

Sample	Line	$\Delta R/\Delta T$ ($\Omega\,°C^{-1}$)	β ($°C^{-1}$)
Sample 1	1	0.0563	0.00254
	2	0.0694	0.00249
	3	0.0566	0.00259
	4	0.0711	0.00255
	5	0.0376	0.00258
	6	0.0653	0.00256
	8	0.0693	0.00269
Sample 2	1	0.0587	0.00266
	2	0.0716	0.00259
	3	0.0591	0.00260
	4	0.0755	0.00261
	5	0.0395	0.00268
	7	0.0391	0.00269
	8	0.0664	0.00259

Table 4.5 – Calibrated TCR values for fused-silica Sample 3.

Line	$\Delta R/\Delta T$ ($\Omega\,°C^{-1}$)	β ($°C^{-1}$)
1	0.1379	0.00249
2	0.0641	0.00258

Table 4.6 – Calibrated TCR values for the SiO_2/Si sample.

Line	$\Delta R/\Delta T$ ($\Omega\,°C^{-1}$)	β ($°C^{-1}$)
1	0.0680	0.00273
2	0.0572	0.00280
3	0.0685	0.00240

Table 4.7 – Estimated linear frequency range for different heater geometries on $BrSiO_2$ samples.

Sample	Heater lines	Linear frequency range (Hz)
1 and 2	1 and 3	1.34–13.69
1 and 2	2 and 4	1.34–21.39
1 and 2	5 and 7	1.34–13.69
1 and 2	6 and 8	1.34–38.03

frequencies.

The estimated linear frequency ranges for the two heater lines are summarized in Table 4.9. For Line 1, the calculated linear range is approximately 77 Hz to 173 Hz, while for Line 2 it is approximately 77 Hz to 308 Hz.

A representative fused-silica measurement is shown in Figure 4.5. The measured in-phase 3-ω response follows a linear dependence with $\ln(2\omega)$ in the selected frequency range, which confirms that the slope method can be applied to this sample.

The input parameters and extracted thermal conductivity values are summarized in Table 4.10.

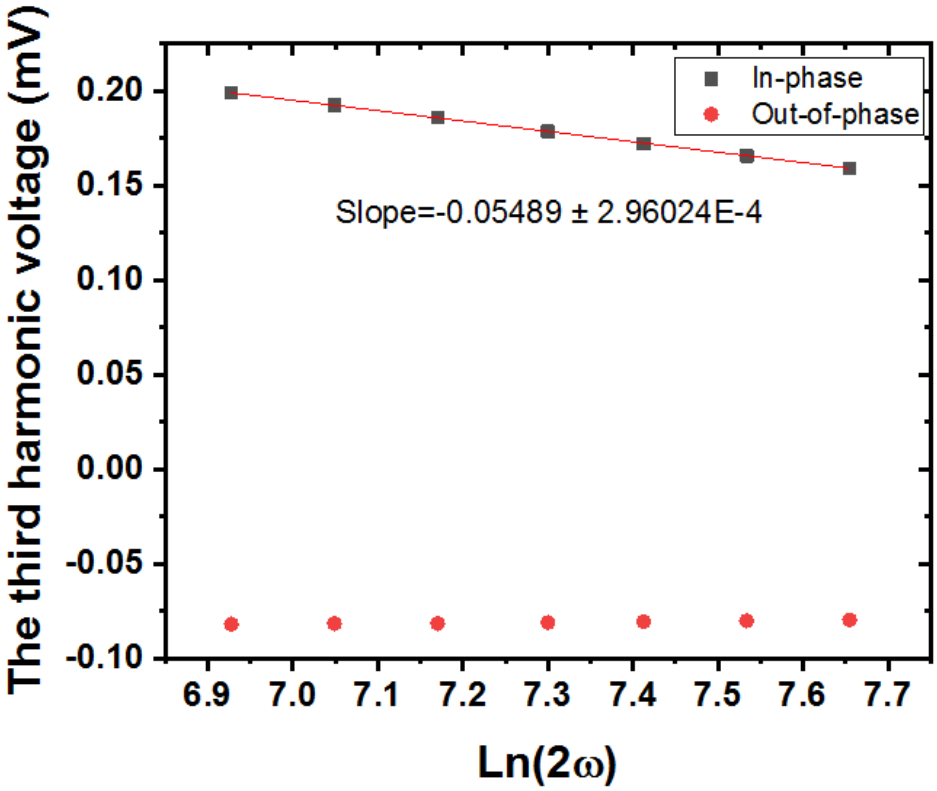


Figure 4.4 – Experimental validation on borosilicate glass. The plot shows the measured in-phase 3-ω signal, converted to ΔT_{in}, as a function of $\ln(2\omega)$ for a representative heater line, Sample 1 Line 8.

Table 4.8 – Summary of 3-ω measurement parameters and extracted thermal conductivity values for $BrSiO_2$ Samples 1 and 2.

Sample	Line	R_0 (Ω)	L (mm)	β ($^\circ C^{-1}$)	V_ω (V)	Slope ($\times 10^{-6}$)	κ ($W.m^{-1}.K^{-1}$)	Error vs. literature
1	1	22.15	5.7	0.00254	0.0919	-1.01	1.232	9.03%
1	2	27.88	5.7	0.00249	0.1112	-1.41	1.216	7.61%
1	3	21.87	5.7	0.00259	0.0897	-1.10	1.086	-3.89%
1	4	27.92	5.7	0.00255	0.1135	-1.63	1.144	1.24%
1	5	14.55	3.6	0.00258	0.0927	-2.58	1.240	9.73%
1	6	25.51	3.6	0.00256	0.0996	-1.84	1.343	18.85%
1	8	25.78	3.6	0.00269	0.1066	-2.67	1.016	-10.09%
2	1	22.02	5.7	0.00266	0.0947	-1.305	1.019	-9.82%
2	2	27.59	5.7	0.00259	0.1838	-5.398	1.508	33.45%
2	3	22.69	5.7	0.00260	0.0929	-1.114	1.152	1.95%
2	4	28.93	5.7	0.00261	0.1705	-5.163	1.210	7.08%
2	5	14.73	3.6	0.00268	0.0745	-1.364	1.217	7.70%
2	7	14.50	3.6	0.00269	0.0734	-1.423	1.141	0.97%
2	8	25.58	3.6	0.00259	0.1206	-3.303	1.188	5.13%

Table 4.9 – Estimated linear frequency range for different heater geometries on the fused-silica sample.

Line	Linear frequency range (Hz)
1	77–173
2	77–308

The two heater lines give very close thermal conductivity values: 1.409 $W.m^{-1}.K^{-1}$ and 1.414 $W.m^{-1}.K^{-1}$. The average value is therefore:

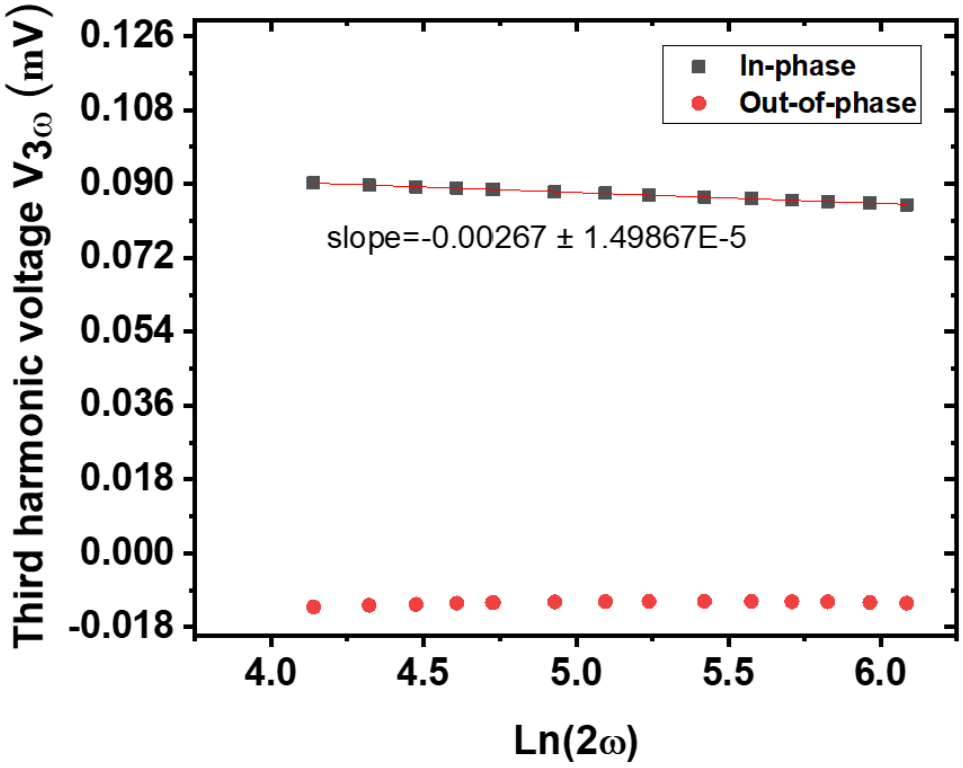


Figure 4.5 – Experimental validation on fused silica. The plot shows the measured in-phase 3-ω signal as a function of $\ln(2\omega)$ for a 6 µm-wide heater line.

Table 4.10 – Summary of 3-ω measurement parameters and extracted thermal conductivity values for fused-silica Sample 3.

Line	R_0 (Ω)	L (mm)	w (µm)	β (K^{-1})	$V_{1\omega}$ (V)	Slope ($\times 10^{-6}$)	κ ($W.m^{-1}.K^{-1}$)
1	55.42	5	6	0.00249	0.436	-4.22	1.409 ± 0.015
2	24.89	3	8	0.00258	0.305	-5.49	1.414 ± 0.008

$\kappa_{\text{fused silica}} \approx 1.41 \pm 0.01$ $W.m^{-1}.K^{-1}$. This value is close to the commonly reported thermal conductivity of fused silica, approximately 1.38 $W.m^{-1}.K^{-1}$ [84]. This second reference sample confirms the validity of the experimental procedure.

4.1.4 Attempted Measurement on SiO_2/Si and Conclusion on Validation

An additional experiment was performed on a SiO_2 thin film deposited on a highly conductive silicon substrate. The same electrical calibration procedure was first applied to the heater lines, as shown previously in Tables 4.3 and 4.6. Then, 3-ω frequency sweeps were performed in order to extract the thermal response of the film/substrate system.

However, a reliable value for the SiO_2 film thermal conductivity could not be extracted from this sample. The main difficulty comes from the high thermal conductivity and high thermal diffusivity of the silicon substrate. Heat is rapidly evacuated into the substrate, which strongly reduces the temperature oscillation of the heater. As a result, the measured 3-ω signal becomes weak and difficult to separate from noise and parasitic contributions.

This unsuccessful extraction is useful because it identifies the practical limits of the present experimental configuration. Three main limitations were observed:

— **Signal-to-noise limitation.** At low driving voltage, the third-harmonic signal was close to the

noise floor. Increasing the driving voltage improved the signal level, but it also increased the risk of parasitic third-harmonic distortion from the function generator.

— **Thermal penetration depth limitation.** The analytical slope method requires the heater to behave approximately as a line heat source, which means that the thermal penetration depth must be larger than the heater half-width. At the same time, the substrate must behave as semi-infinite, which requires the thermal penetration depth to remain smaller than the substrate thickness. For the silicon substrate, because of its high thermal diffusivity, it was difficult to find a frequency range that satisfies both conditions while keeping a measurable signal.

— **High thermal contrast.** The large contrast between the thin SiO_2 film and the highly conductive silicon substrate makes the film contribution difficult to isolate using the present analytical treatment. In this configuration, the measured response is strongly influenced by the substrate.

Therefore, the difficulty encountered with the SiO_2/Si sample does not indicate a failure of the 3-ω method itself. Rather, it shows that the method must be applied within a suitable experimental window, where the signal level, heater geometry, substrate thickness, and thermal penetration depth are compatible.

Conclusion on Experimental Validation The measurements performed on $BrSiO_2$ and fused silica validate the experimental 3-ω setup developed in this work. For both reference substrates, the extracted thermal conductivity values are close to literature values. The $BrSiO_2$ measurements confirm that the platform can measure bulk amorphous glass substrates over a suitable low-frequency range. The fused-silica measurements provide an additional validation on a thinner substrate and give very repeatable results between two heater geometries.

The attempted measurement on the SiO_2/Si sample further shows that the choice of substrate and frequency window is critical. In particular, high-conductivity substrates can reduce the temperature oscillation and make the extraction of thin-film thermal properties difficult with the simple analytical slope method. This observation motivates the use of FEM modeling and inverse analysis for more complex configurations, as discussed in the next sections.

4.2 Numerical Investigation and Parametric Study (using COMSOL)

Having established the reliability of our physical experiment, we now leverage the FEM model as a "virtual laboratory" to validate the model itself and, more importantly, to systematically probe the limitations of the analytical models used in Section 4.1.

4.2.1 Model Validation: 2D FEM vs. Analytical Solutions

The first numerical step is to validate the 2D FEM model against analytical solutions. This validation is necessary because the FEM model will later be used to study situations where the analytical model becomes difficult to apply directly. The aim here is not yet to extract an unknown property, but to verify that the numerical model reproduces the expected 3-ω thermal response for simple and well-defined systems.

Two types of validation were performed. First, the analytical model was checked by generating theoretical data from the Cahill approximation and then reapplying the slope method to this generated data. Second, the FEM model was used to simulate bulk substrates with known input thermal conductivities, and the simulated data were analyzed using the same slope method as for the experimental data.

Analytical self-consistency check As a first check, theoretical temperature data were generated using the analytical approximation introduced in Chapter 3, Eq. (3.14). The generated in-phase temperature response was plotted as a function of $\ln(2\omega)$ and fitted using the analytical slope method. The result is shown in Figure 4.6.

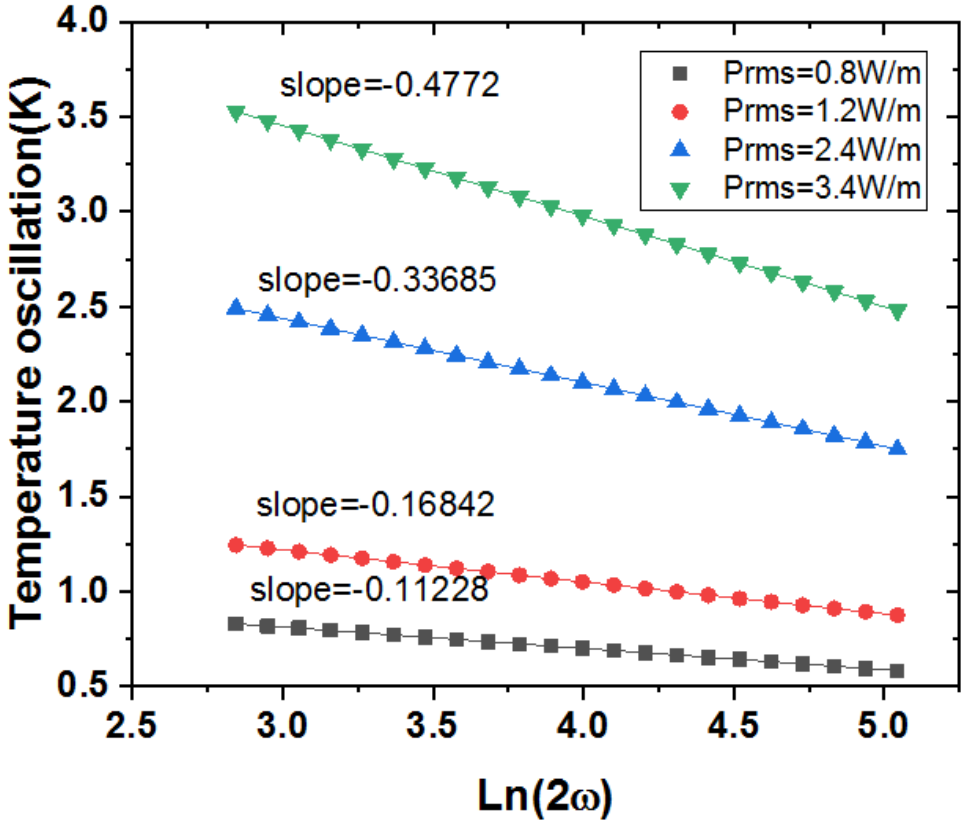


Figure 4.6 – Self-consistency check of the analytical model. The in-phase temperature response generated from the Cahill approximation is plotted as a function of $\ln(2\omega)$. The linear fit recovers the input thermal conductivity, confirming the internal consistency of the analytical slope method when its assumptions are exactly satisfied.

This first test confirms that the analytical formula and the fitting procedure are implemented correctly. When the data are generated from the same assumptions as the analytical model, the input thermal conductivity is recovered. This provides a useful reference before testing the FEM model, where the heater has a finite width and thickness.

FEM validation on bulk substrates The second validation step was performed using the 2D FEM model. Bulk substrates with known thermal conductivities were simulated, and the resulting temperature response was analyzed using the analytical slope method. Two representative materials were considered: borosilicate glass, representing a low-thermal-conductivity amorphous substrate, and silicon, representing a high-thermal-conductivity crystalline substrate. For the borosilicate glass case, the input thermal conductivity was set to: $\kappa_{BrSiO_2,input} = 1.13$ W.m^{-1}.K^{-1}. After applying the analytical slope method to the FEM-generated data, the extracted value was approximately: $\kappa_{BrSiO_2,fit} \approx 1.17$ W.m^{-1}.K^{-1}.

The difference between the input and extracted values is about 3–4%. The same validation was then applied to silicon. Silicon is a useful benchmark because its high thermal conductivity produces a much smaller temperature oscillation and requires a careful choice of frequency window. The input thermal conductivity was: $\kappa_{Si,input} = 130$ W.m^{-1}.K^{-1}.

As shown in Figure 4.7, the simulated in-phase temperature oscillation decreases with increasing frequency, and a linear region can be selected for the slope analysis.

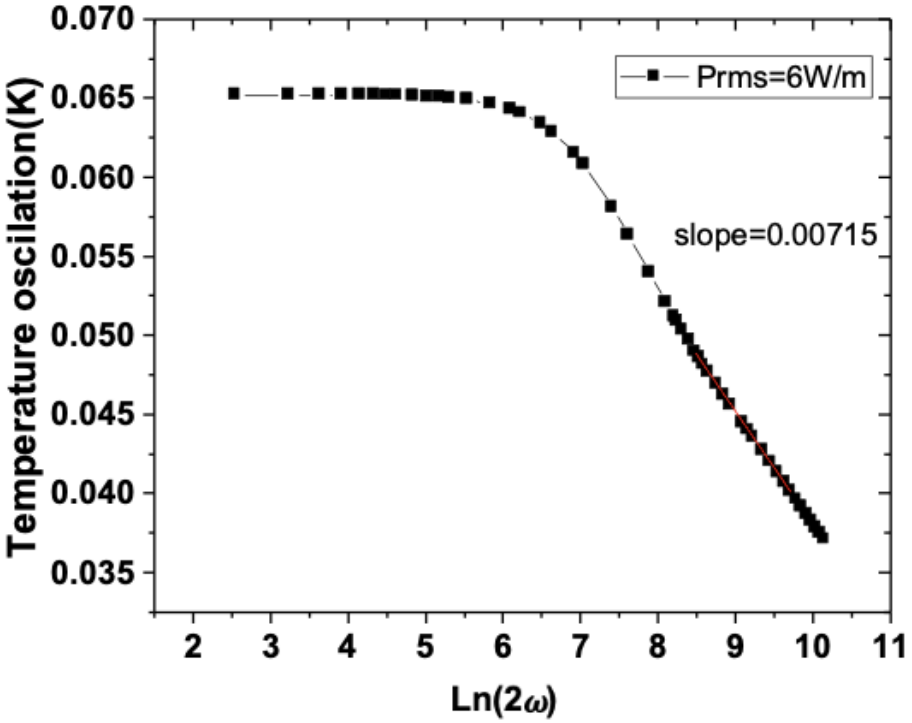


Figure 4.7 – FEM validation for a high-thermal-conductivity silicon substrate. The simulated in-phase temperature oscillation is plotted as a function of $\ln(2\omega)$. The thermal conductivity extracted from selected frequency windows remains close to the input value of $\kappa_{\mathrm{Si,input}} = 130$ W.m^{-1}.K^{-1}.

The extracted values for silicon are summarized in Table 4.11. Depending on the selected frequency range, the fitted thermal conductivity remains between approximately 133.6 W.m^{-1}.K^{-1} and 135 W.m^{-1}.K^{-1}, corresponding to a deviation below about 4% from the input value.

Table 4.11 – Summary of FEM validation results for bulk substrates using the analytical slope method.

Material	Input κ (W.m^{-1}.K^{-1})	Frequency range (Hz)	Extracted κ (W.m^{-1}.K^{-1})
$BrSiO_2$	1.13	1.34–13.69	≈ 1.17
Si	130	1100–1600	135.0
Si	130	380–1300	133.56

These results show that the FEM model reproduces the expected 3-ω response for both low- and high-thermal-conductivity bulk substrates. The remaining deviation of a few percent does not indicate a failure of the FEM model. It mainly comes from the difference between the simplified analytical assumptions and the more realistic FEM geometry. In the analytical model, the heater is treated as an ideal line heat source. In the FEM model, the heater has a finite width and thickness, and the heat flow near the metal strip is therefore more realistic.

This comparison is important for the rest of the thesis. It shows that the FEM model is consistent with the analytical theory in simple cases, while also capturing geometry-related effects that are not included in the analytical slope method. Therefore, the FEM model can be used as a reliable numerical tool for studying more complex film/substrate and multilayer configurations.

4.2.2 Parametric Study: Effect of Input Power and Heater Width

After validating the FEM model on bulk substrates, the model was used to study how selected experimental parameters affect the simulated 3-ω response. Two parameters were considered in this step: the input power applied to the heater and the heater width. These two parameters are important because they are directly controlled during the experiment and strongly influence the signal level and the validity of the analytical assumptions.

Effect of input power The first parameter studied was the input power. In the linear heat-transfer regime, the temperature oscillation generated by the heater is proportional to the applied power. Therefore, if the material properties are assumed to be temperature independent, the relation between the temperature response and the input power can be written as:

$$\Delta T_{2\omega}(f) \propto P, \tag{4.3}$$

where (P) is the time-averaged Joule heating power per unit length. As a result, the normalized thermal response, or thermal impedance, is independent of the power level:

$$Z_{\text{th}}(f) = \frac{\Delta T_{2\omega}(f)}{P}. \tag{4.4}$$

The FEM simulations confirmed this linear behavior. When the input power was varied, the amplitude of the temperature oscillation changed proportionally, but the shape of the frequency response remained the same after normalization by the input power. Therefore, the thermal conductivity extracted from the slope method did not depend on the power level, as long as the system remained in the linear regime.

This result is important for the experimental design. A higher input power increases the measured ($V_{3\omega}$) signal and improves the signal-to-noise ratio. However, the power cannot be increased without limit. If the temperature oscillation becomes too large, the material properties and the heater resistance may no longer remain constant over the temperature range of the oscillation. This would introduce nonlinear effects and violate the assumptions of the analytical and numerical models. In practice, the input power must therefore be chosen as a compromise: it should be high enough to obtain a measurable signal, but low enough to keep the temperature rise within the linear regime.

For the $BrSiO_2$ validation case, the simulations and experiments indicate that a temperature oscillation of the order of a few kelvin is suitable. This range gives a measurable third-harmonic signal while avoiding excessive self-heating of the heater and the surrounding material.

Effect of heater width The second parameter studied was the heater width. In the analytical 3-ω model, the heater is often approximated as a line heat source. This approximation is valid when the heater half-width (b) is much smaller than the thermal penetration depth. In practice, the heater has a finite width and thickness, and this finite geometry modifies the temperature field near the heater.

To evaluate this effect, FEM simulations were performed for two heater widths on the same $BrSiO_2$ substrate. The comparison is shown in Figure 4.8. The two simulated temperature responses are close, but not identical. This difference shows that the heater width affects the measured temperature response and therefore the thermal conductivity extracted using the simplified analytical slope method.

The results confirm the trend observed experimentally: narrower heaters give extracted values that are slightly closer to the expected thermal conductivity. This is because a narrower heater better satisfies the line-source approximation used in the analytical model. In contrast, a wider heater produces stronger finite-width effects, which are not fully described by the analytical slope method.

This does not mean that wide heaters cannot be used. Wider heaters can provide a stronger signal and are easier to fabricate reliably. However, their geometry must be taken into account when high accuracy is required. This is one of the reasons why FEM modeling is useful: it can include the

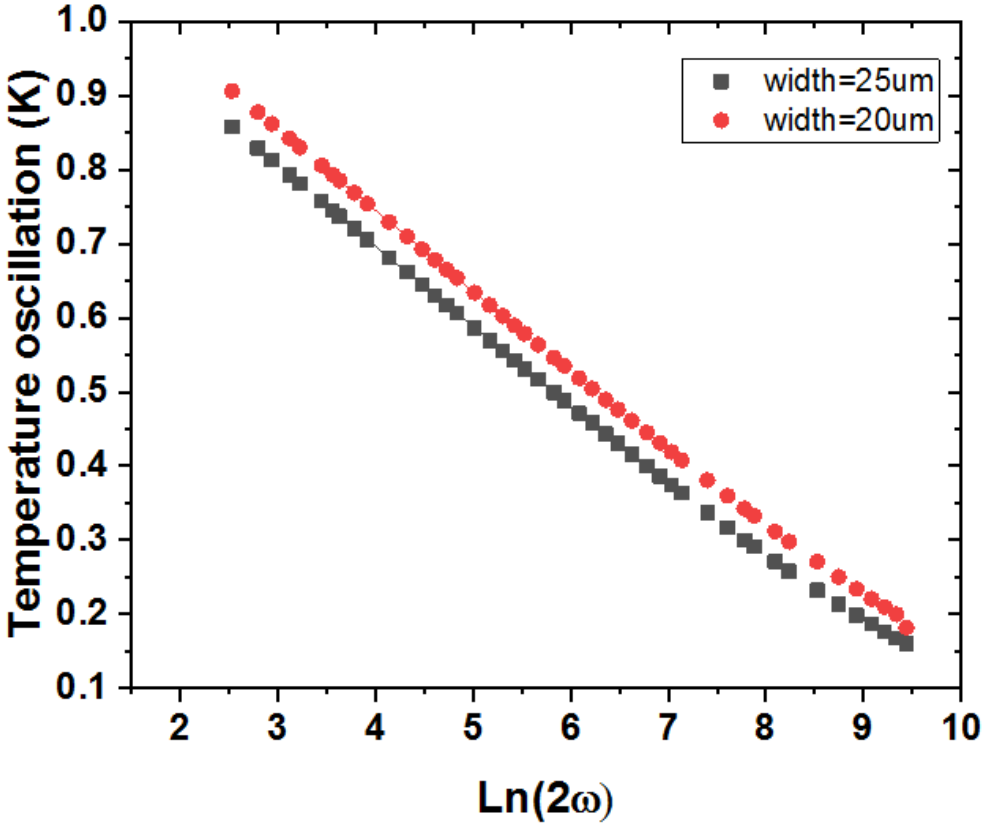


Figure 4.8 – Numerical study of the effect of heater width. The simulated temperature oscillations for a 20 µm heater and a 25 µm heater on a $BrSiO_2$ substrate are compared. The difference between the two curves shows that finite heater geometry affects the temperature response when the analytical line-source approximation is used.

real heater dimensions and therefore reduce the systematic error associated with the ideal line-source approximation.

Conclusion The parametric study of input power and heater width provides two practical guidelines for the 3-ω measurements. First, the input power should be selected within the linear regime, where the temperature response scales proportionally with power and the extracted thermal conductivity remains independent of power. Second, the heater width should be chosen carefully because it affects the validity of the analytical line-source approximation. These results support the use of FEM modeling as a complementary tool for interpreting experimental data obtained with real heater geometries.

4.2.3 Numerical Analysis of the Slope Method for a Single Film on a Substrate

The previous numerical studies validated the FEM model for bulk substrates. The next step is to test whether the standard analytical film-extraction method can be applied to a film deposited on a substrate. This point is important because the final samples studied in this thesis are not bulk materials, but thin-film stacks supported by a substrate.

For a single film on a substrate, the classical analytical approach assumes that the total temperature oscillation measured by the heater can be separated into two contributions:

$$\Delta T_{\text{total}} \approx \Delta T_{\text{sub}} + \Delta T_{\text{film}} \tag{4.5}$$

where ΔT_{sub} is the temperature oscillation of the substrate and ΔT_{film} is the additional temperature drop caused by the film.

In this approach, the film contribution is assumed to be mainly one-dimensional and perpendicular to the sample surface. Under this approximation, the temperature drop across the film can be written as:

$$\Delta T_{\text{film}} \approx \frac{P' d_f}{2b\kappa_f} \tag{4.6}$$

where P' is the heating power per unit length, d_f is the film thickness, $2b$ is the heater width, and κ_f is the film thermal conductivity. The film thermal conductivity can then be extracted as:

$$\kappa_f \approx \frac{P' d_f}{2b\,(\Delta T_{\text{total}} - \Delta T_{\text{sub}})} \tag{4.7}$$

This method is simple and useful, but it relies on several assumptions. In particular, it assumes that heat crosses the film mainly in the vertical direction, and that the substrate response can be accurately calculated or measured separately. These assumptions may not be fully satisfied when the heater has a finite width, when the substrate has a strong influence, or when the thermal contrast between the film and the substrate is large.

To test the validity of this method, two virtual film/substrate systems were simulated using the validated FEM model. The two configurations are shown schematically in Figure 4.9. The first configuration is a low-conductivity Parylene C film on a low-conductivity $BrSiO_2$ substrate. The second configuration is a SiO_2 film on a high-conductivity silicon substrate. These two cases were selected to evaluate the behavior of the extraction method under two different substrate conditions.

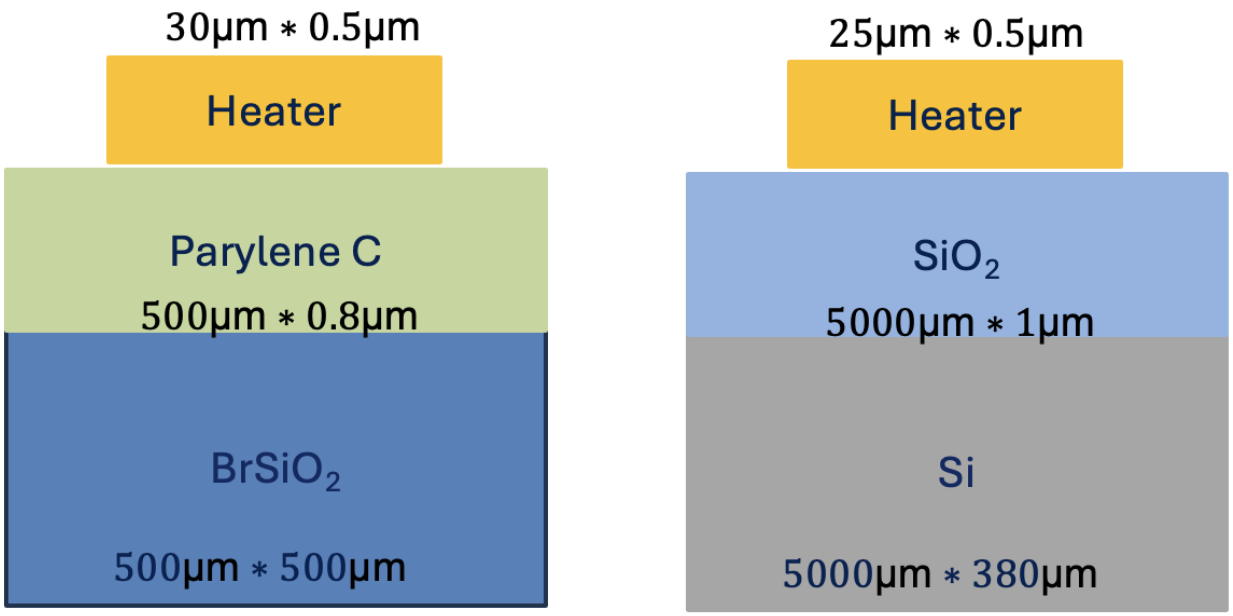


Figure 4.9 – Schematic representation of the two single-film configurations used to test the analytical film-extraction method. (a) Parylene C film on a $BrSiO_2$ substrate, corresponding to a low-conductivity film on a low-conductivity substrate. (b) SiO_2 film on a silicon substrate, corresponding to a low-conductivity film on a high-conductivity substrate.

Case 1: Parylene C on $BrSiO_2$ The first virtual sample consisted of a 0.8 µm Parylene C film deposited on a $BrSiO_2$ substrate. The input thermal conductivity of the film was: $\kappa_{\text{Parylene,input}} = 0.13\,\text{W.m}^{-1}\text{.K}^{-1}$. The input thermal conductivity of the substrate was: $\kappa_{\text{BrSiO}_2\text{,input}} = 1.13\,\text{W.m}^{-1}\text{.K}^{-1}$. The heater width was (2b=30 µm), the heater thickness was 0.5 µm, and the injected RMS power per unit length was $3.99\,\text{W m}^{-1}$.

The FEM simulation first provided the total temperature oscillation of the film/substrate system, ΔT_{total}. Then, the substrate contribution, ΔT_{sub}, was estimated using the analytical line-source model. The difference between these two quantities gave the film contribution: $\Delta T_{\text{film}} = \Delta T_{\text{total}} - \Delta T_{\text{sub}}$. Using Eq. (4.7), the extracted film thermal conductivity was: $\kappa_{\text{Parylene,ext}} = 0.119$ W.m^{-1}.K^{-1}. Compared with the input value of 0.13 W.m^{-1}.K^{-1}, this corresponds to a relative error of approximately (8.46%).

The result is shown in Figure 4.10. The full film/substrate response is higher than the bare-substrate response because the low-conductivity Parylene C film adds an additional thermal resistance between the heater and the substrate.

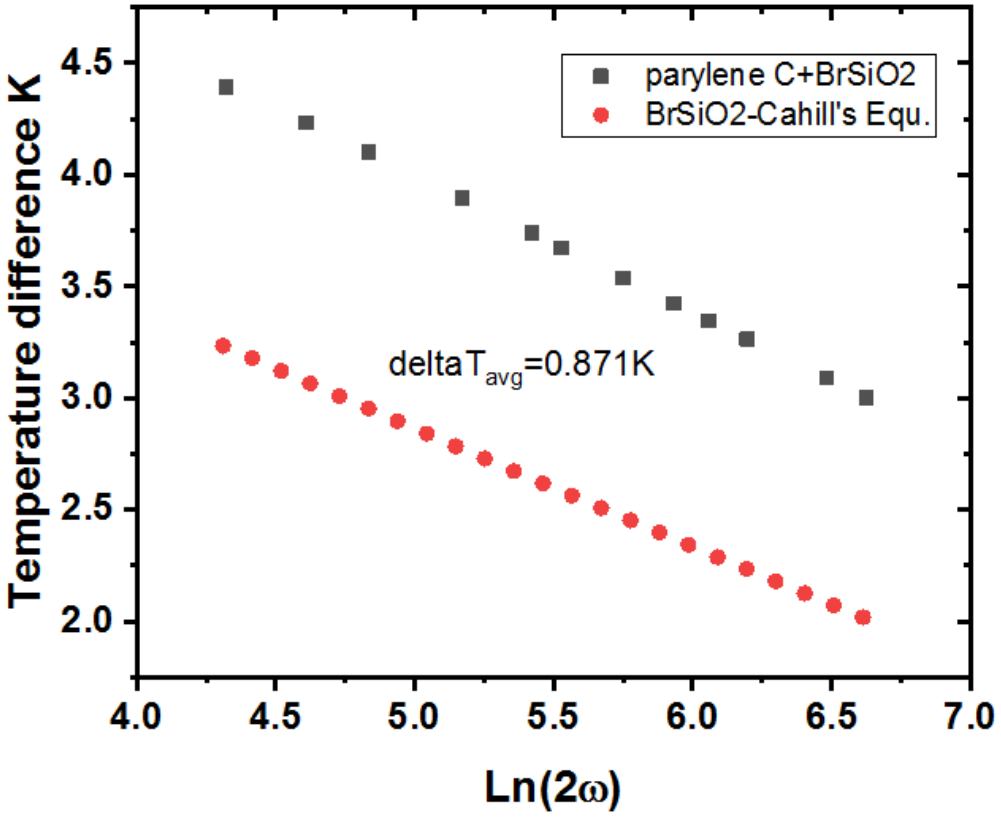


Figure 4.10 – Numerical test of the analytical film-extraction method for a Parylene C film on a $BrSiO_2$ substrate. The simulated response of the full film/substrate system is compared with the calculated substrate response. The difference between the two responses is used to estimate the film contribution and to extract the film thermal conductivity.

Case 2: SiO_2 on silicon The second virtual sample consisted of a 1 µm SiO_2 film deposited on a 380 µm silicon substrate. The input thermal conductivity of the film was: $\kappa_{\text{SiO}_2\text{,input}} = 1.40$ W.m^{-1}.K^{-1}. The input thermal conductivity of the silicon substrate was: $\kappa_{\text{Si,input}} = 130$ W.m^{-1}.K^{-1}. The heater width was 25 µm, the heater thickness was 0.5 µm, and the injected RMS power per unit length was 6 W m^{-1}.

The same extraction procedure was applied. The FEM model provided the total temperature oscillation of the SiO_2/Si system. The substrate contribution was then estimated using the analytical model for silicon, and the difference was attributed to the SiO_2 film. The extracted film thermal conductivity was: $\kappa_{\text{SiO}_2\text{,ext}} = 1.472$ W.m^{-1}.K^{-1}. Compared with the input value of 1.40 W.m^{-1}.K^{-1}, this corresponds to a relative error of approximately (5.0%).

The result is shown in Figure 4.11. In this case, the additional temperature drop caused by the film is smaller than in the Parylene C case, because the silicon substrate removes heat very efficiently.

Nevertheless, the film contribution remains visible in the numerical data.

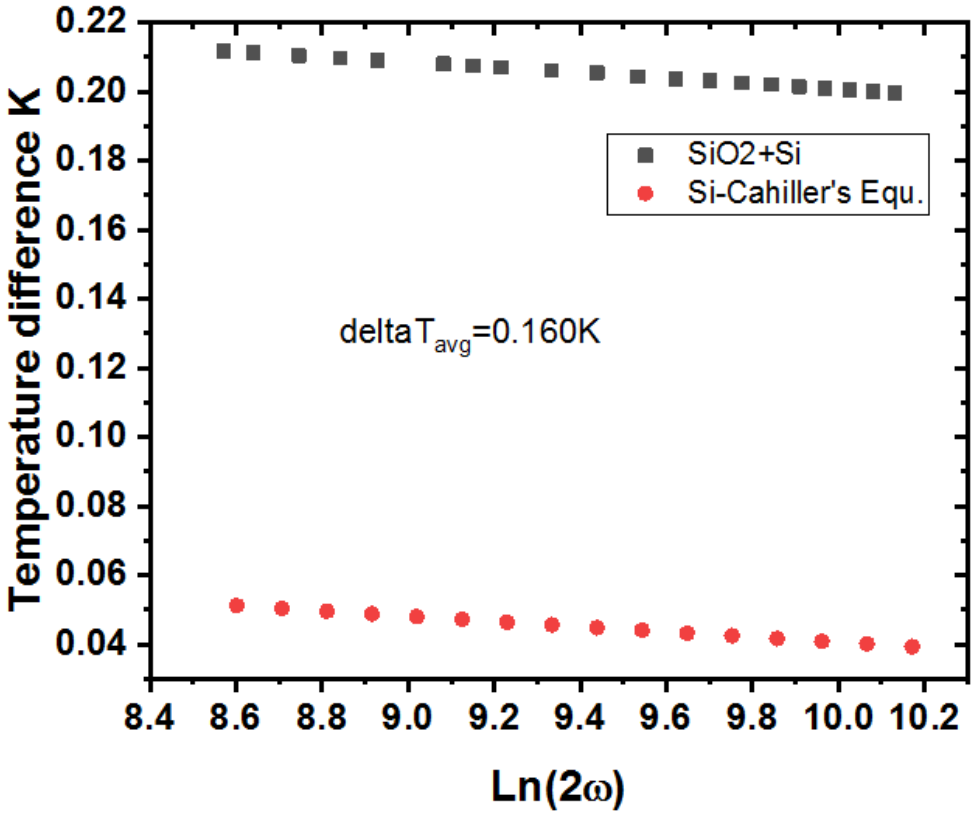


Figure 4.11 – Numerical test of the analytical film-extraction method for a SiO_2 film on a silicon substrate. The simulated response of the full SiO_2/Si system is compared with the calculated silicon substrate response. The difference between the two responses is used to estimate the temperature drop across the SiO_2 film.

The extracted values for the two virtual film/substrate systems are summarized in Table 4.12.

Table 4.12 – Summary of the FEM-based numerical test of the analytical single-film extraction method.

Film/substrate system	Input κ_f (W.m^{-1}.K^{-1})	Extracted κ_f (W.m^{-1}.K^{-1})	Relative error
Parylene C / $BrSiO_2$	0.13	0.119	8.46%
SiO_2 / Si	1.40	1.472	5.0%

The two tests show that the analytical film-extraction method can provide a reasonable estimate of the film thermal conductivity when applied to FEM-generated data. In both cases, the extracted values agree with the input values within approximately 10%. This confirms that the FEM model reproduces the expected thermal response of both low- and high-conductivity film/substrate systems.

At the same time, the remaining error is not negligible. It shows that the simplified analytical method introduces a systematic uncertainty. This uncertainty comes mainly from the one-dimensional approximation used for the film temperature drop, the finite width of the heater, and the way the substrate contribution is estimated. The error remains moderate for the two simple single-film cases considered here, but it can become larger for more complex stacks, especially when several layers and interfaces contribute to the measured thermal response.

Conclusion on the analytical film-extraction method This numerical study shows that the standard analytical film-extraction method can be useful for simple film/substrate systems, but it has a limited

accuracy. Even when the virtual data are generated under controlled numerical conditions, the extracted film thermal conductivity differs from the input value by several percent. Therefore, for complex multilayer systems, a direct analytical subtraction is not sufficient to separate the contributions of each layer and interface with high confidence.

This result provides an important transition toward the FEM-based inverse fitting approach used in Chapter 5. Instead of relying only on a simplified one-dimensional film correction, the inverse FEM method can include the real heater geometry, the finite thickness of the layers, the substrate influence, and the coupling between different thermal parameters.

4.2.4 Parametric Study: Influence of Substrate Thermal Conductivity

The previous subsection showed that the analytical film-extraction method gives reasonable results for two simple film/substrate configurations, but still introduces a systematic error of several percent. The next step is to understand how this error depends on the substrate thermal conductivity.

This point is important because the substrate controls how easily heat can be removed from the heater region. A high-conductivity substrate acts as an efficient heat sink and can help isolate the thermal resistance of a low-conductivity film. In contrast, when the substrate thermal conductivity is comparable to that of the film, the heat flow is more strongly coupled between the film and the substrate, and the simple analytical separation becomes less reliable.

To investigate this effect, an identical 1 µm SiO_2 film was simulated on three different substrates. The film thermal conductivity was fixed at: $\kappa_{f,\text{input}} = 1.40$ W.m^{-1}.K^{-1}. The substrate thickness was fixed at 380 µm. The three substrate thermal conductivities were:

$\kappa_{\text{sub}} = 10$, 50, and 131 W.m^{-1}.K^{-1}. The heater width was 20 µm, the heater thickness was 0.05 µm, and the injected RMS power per unit length was 12 W.m^{-1}.

The simulated in-phase temperature oscillations for the three cases are shown in Figure 4.12. Figure 4.12(a) compares the responses for all three substrates. Figures 4.12(b), 4.12(c), and 4.12(d) show the individual responses for the low-, medium-, and high-conductivity substrates, respectively.

The simulation results show that the temperature oscillation is strongly affected by the substrate thermal conductivity. When the substrate thermal conductivity is low, heat is removed less efficiently, and the temperature oscillation is larger. When the substrate thermal conductivity is high, heat is rapidly evacuated into the substrate, and the temperature oscillation becomes much smaller.

The extraction accuracy of the analytical film method was then evaluated for each case. The substrate contribution was subtracted from the total simulated response: $\Delta T_{\text{film}} \approx \Delta T_{\text{total}} - \Delta T_{\text{sub,analytical}}$. The film thermal conductivity was then calculated using Eq. (4.7). The quantitative results are summarized in Table 4.13.

Table 4.13 – Influence of substrate thermal conductivity on the analytical extraction of the SiO_2 film thermal conductivity. The input film thermal conductivity is fixed at $\kappa_{f,\text{input}} = 1.40$ W.m^{-1}.K^{-1}.

Case	κ_{sub} (W.m^{-1}.K^{-1})	Contrast ($\kappa_{\text{sub}}/\kappa_f$)	Extracted κ_f (W.m^{-1}.K^{-1})	Absolute error (W.m^{-1}.K^{-1})	Relative error (%)
(a)	10	7.1	1.58	+0.18	12.9
(b)	50	35.7	1.51	+0.11	7.9
(c)	131	93.6	1.47	+0.07	5.0

The calculated film temperature differences are shown in Figure 4.13. Figure 4.13(a) corresponds to the low-conductivity substrate, Figure 4.13(b) to the medium-conductivity substrate, and Figure 4.13(c) to the high-conductivity substrate.

The results show a clear trend. For the low-conductivity substrate, $\kappa_{\text{sub}} = 10$ W.m^{-1}.K^{-1}, the extracted film thermal conductivity is 1.58 W.m^{-1}.K^{-1}, corresponding to a relative error of 12.9%.

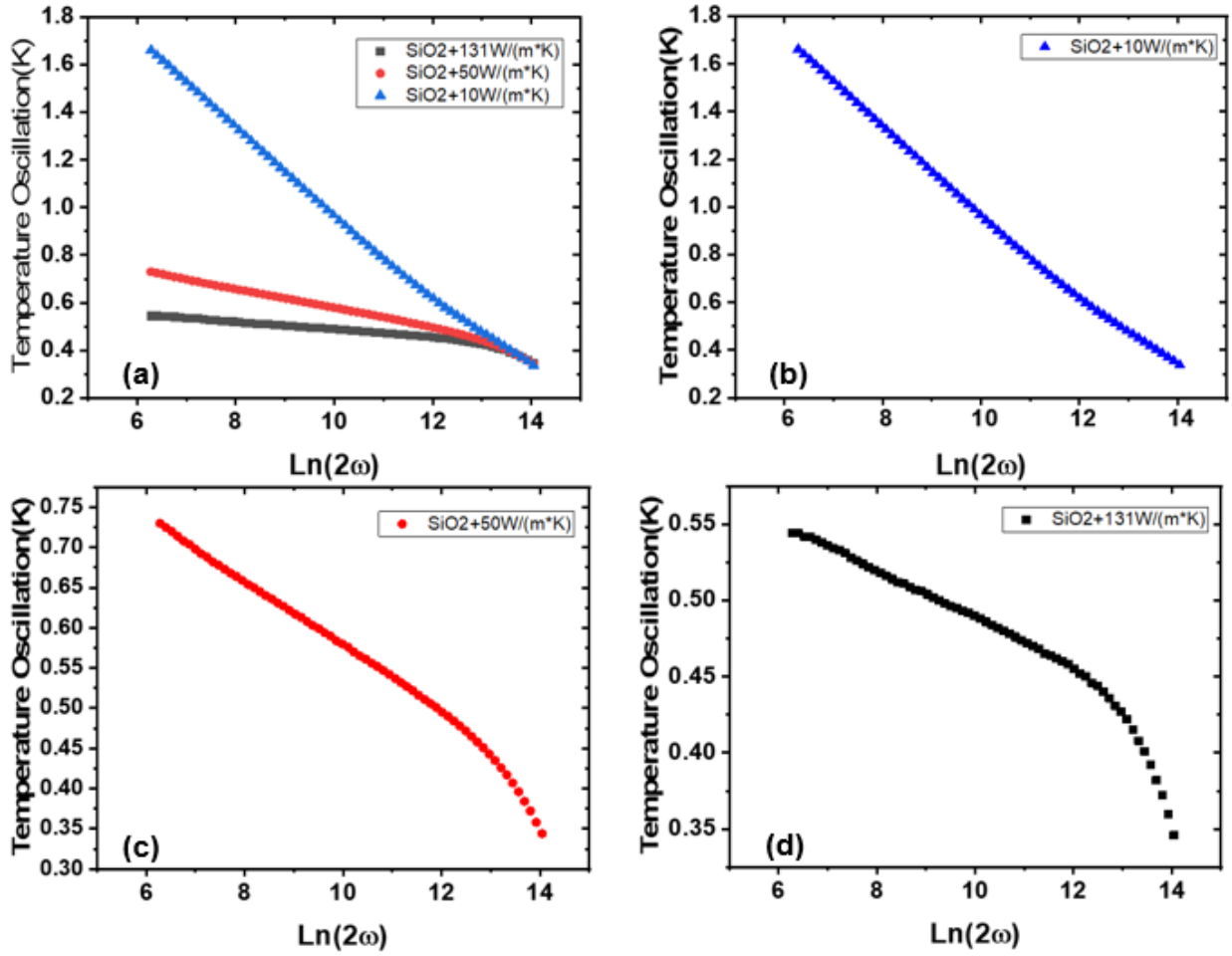


Figure 4.12 – Simulated in-phase temperature oscillations for an identical SiO_2 film on three different substrates with $\kappa_{sub} = 10, 50$, and 131 $W.m^{-1}.K^{-1}$. (a) Comparison of all three cases. (b) Low-conductivity substrate, $\kappa_{sub} = 10$ $W.m^{-1}.K^{-1}$. (c) Medium-conductivity substrate, $\kappa_{sub} = 50$ $W.m^{-1}.K^{-1}$. (d) High-conductivity substrate, $\kappa_{sub} = 131$ $W.m^{-1}.K^{-1}$. The signal amplitude decreases as the substrate thermal conductivity increases.

This larger error occurs because the substrate is not conductive enough to behave as an ideal heat sink. In this case, the film and substrate contributions are strongly coupled, and the assumption of a simple one-dimensional film temperature drop becomes less accurate.

For the medium-conductivity substrate, $\kappa_{sub} = 50\,W.m^{-1}.K^{-1}$, the extracted value is 1.51 $W.m^{-1}.K^{-1}$, corresponding to a relative error of 7.9%. The error is lower than in the previous case because the substrate removes heat more efficiently, but it remains significant.

For the high-conductivity substrate, κ_{sub}=131 $W.m^{-1}.K^{-1}$, and the extracted value is 1.47 $W.m^{-1}.K^{-1}$, corresponding to a relative error of 5.0%. This is the most favorable case among the three simulations. The high-conductivity substrate makes the film contribution easier to separate from the substrate response. However, a residual error remains because the analytical method still assumes one-dimensional heat flow through the film and an ideal line heat source. These assumptions are not exactly satisfied in the FEM geometry.

These simulations indicate that the analytical film-extraction method becomes more accurate when the substrate thermal conductivity is much higher than the film thermal conductivity. In other words, the condition $\kappa_f \ll \kappa_{sub}$ is favorable for the differential slope method. When this condition is not satisfied, the extracted film conductivity becomes more sensitive to the substrate response and to finite-geometry effects.

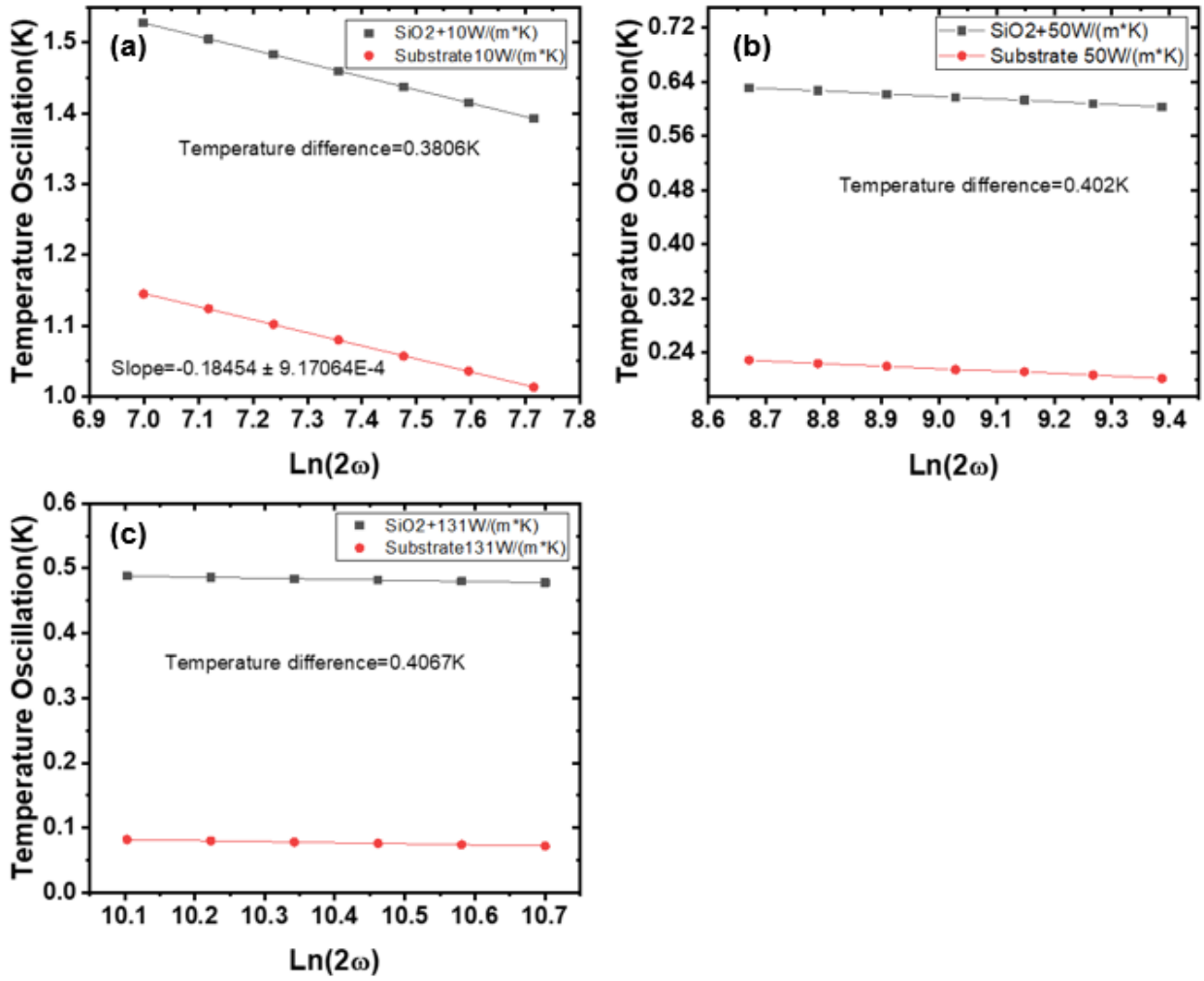


Figure 4.13 – Calculated film temperature contribution, ΔT_{film}, for an identical SiO_2 film on three different substrates. (a) Low-conductivity substrate, $\kappa_{\text{sub}} = 10$ W.m^{-1}.K^{-1}, showing the largest extraction error. (b) Medium-conductivity substrate, $\kappa_{\text{sub}} = 50$ W.m^{-1}.K^{-1}. (c) High-conductivity substrate, $\kappa_{\text{sub}} = 131$ W.m^{-1}.K^{-1}, showing the most accurate extraction among the three cases.

This result is directly relevant to the main multilayer sample studied in Chapter 5. In that case, the substrate thermal conductivity is approximately 1.287 W.m^{-1}.K^{-1}, which is comparable to the expected thermal conductivity of the dielectric layers. Therefore, the simple analytical subtraction method is not expected to provide a reliable separation between the film and substrate contributions. This supports the use of an FEM-based inverse fitting approach for the multilayer stack.

Conclusion The substrate thermal conductivity has a strong influence on the accuracy of the analytical film-extraction method. A highly conductive substrate improves the separation between the film resistance and the substrate response, whereas a low- or moderate-conductivity substrate increases the coupling between them. Even in the most favorable high-conductivity case, a residual error of about 5% remains because of finite heater geometry and the simplified one-dimensional approximation.

For the multilayer sample investigated in this thesis, where the substrate conductivity is close to that of the film stack, the analytical slope method is not sufficient. A more complete FEM-based inverse analysis is therefore required to include the real geometry, the substrate influence, and the coupled thermal response of the multilayer structure.

4.2.5 Further Discussion and Opportunities for Future Simulations

The numerical studies presented in this chapter provide useful guidance for future work. They show that the FEM model can be used not only to reproduce the 3-ω response, but also to test experimental conditions that are difficult to explore directly. Based on the results obtained in this chapter, three directions appear particularly relevant for future simulations.

— **Revisiting high-contrast systems, such as SiO_2/Si.**

The simulations performed on SiO_2/Si show that extracting the film thermal conductivity is theoretically possible when the film thermal conductivity is much lower than that of the substrate, namely when $\kappa_{\text{film}} \ll \kappa_{\text{sub}}$. In this configuration, the film introduces a distinct additional thermal resistance, and the numerical model predicts a measurable temperature drop associated with the film.

However, the corresponding experimental data obtained in this work were strongly affected by noise and signal instability. This prevented a reliable extraction of the film thermal conductivity. The main difficulty comes from the high thermal conductivity and high thermal diffusivity of the silicon substrate. With $\alpha \approx 8e-5$ m^2.s^{-1}, silicon acts as an efficient heat sink and strongly reduces the temperature oscillation of the heater. As a result, the useful 3-ω signal becomes close to the noise level of the present experimental setup.

Future simulations could include artificial electrical noise added to the thermal response in order to estimate the minimum signal-to-noise ratio required for reliable extraction on high-conductivity substrates. Such simulations could help define the required power level, heater geometry, or lock-in detection sensitivity. Other techniques, such as Time-Domain Thermoreflectance (TDTR), may also be more suitable for this type of high-conductivity substrate because they use high-frequency optical excitation and detection.

— **Studying anisotropy using different heater geometries.**

In this thesis, the films were treated as isotropic materials in the FEM model. However, PECVD thin films may present anisotropic thermal transport, meaning that the in-plane thermal conductivity $\kappa_{\parallel}$ can differ from the cross-plane thermal conductivity $\kappa_{\perp}$. This effect is especially relevant for thin films and multilayers, where growth direction, interfaces, density, and microstructure can influence heat transport differently along the in-plane and cross-plane directions.

The FEM model could be used in future work to study the sensitivity of the 3-ω signal to anisotropic thermal properties. In particular, simulations with different heater widths could help determine whether the measurement is more sensitive to $\kappa_{\parallel}$ or to $\kappa_{\perp}$. A narrow heater promotes stronger lateral heat spreading and may increase sensitivity to the in-plane thermal conductivity. In contrast, a wider heater tends to promote a more vertical heat-flow pattern and may be more sensitive to the cross-plane component.

Such a study would be useful for designing future heater geometries and for evaluating whether several heater widths can be combined to separate $\kappa_{\parallel}$ and $\kappa_{\perp}$.

— **Exploring the high-TBR limit.**

Another useful direction is the numerical study of very large thermal boundary resistance. This case is relevant because interface resistance can strongly modify the thermal response of multilayer systems. In the FEM model, this limit can be explored by increasing the interface resistance between the film and the substrate, or between different layers, until the heat transfer across the interface becomes strongly restricted.

In the limiting case, the interface behaves almost like an adiabatic boundary. The thermal wave is then partially confined near the heater and within the upper layers. This increases the local temperature oscillation and changes the spatial distribution of heat flow. Such simulations can provide a reference case for identifying when the measured response is mainly controlled by interface resistance rather than by the intrinsic thermal conductivity of the films.

This analysis also prepares the discussion developed in Chapter 5, where the possible role of high thermal boundary resistance is compared with the effective-medium interpretation of the multilayer stack.

4.3 Chapter Summary

This chapter validated the main experimental and numerical tools used in this thesis and clarified the range of applicability of the analytical methods.

First, the 3-ω experimental setup was tested on reference bulk materials. Measurements were performed on borosilicate glass and fused silica, two amorphous substrates with known thermal conductivities. The extracted values were close to literature values. For borosilicate glass, most reliable values were located around 1.14 – 1.21 $W.m^{-1}.K^{-1}$, close to the reference value of approximately 1.13 $W.m^{-1}.K^{-1}$. For fused silica, the two heater lines gave very close values, 1.409 $W.m^{-1}.K^{-1}$ and 1.414 $W.m^{-1}.K^{-1}$, leading to an average value of about 1.41 $W.m^{-1}.K^{-1}$. These results confirm that the experimental platform, the TCR calibration, and the slope-method data analysis provide reliable thermal conductivity measurements for bulk amorphous substrates.

Second, the FEM model was validated against analytical solutions. The analytical self-consistency test confirmed that the slope method correctly retrieves the input thermal conductivity when the assumptions of the analytical model are exactly satisfied. The FEM simulations of bulk substrates then showed good agreement with analytical results, with small deviations of a few percent. These deviations are mainly due to the finite heater geometry included in the FEM model, while the analytical model assumes an ideal line heat source. This comparison shows that the FEM model is consistent with the analytical theory while providing a more realistic description of the experimental geometry.

Third, parametric studies were used to examine the influence of input power, heater width, and substrate thermal conductivity. The power study confirmed that the temperature response is linear with input power as long as the temperature rise remains moderate. The heater-width study showed that narrower heaters better satisfy the line-source approximation, while wider heaters can introduce stronger finite-width effects. The substrate-conductivity study showed that the analytical film-extraction method is more accurate when the substrate thermal conductivity is much higher than the film thermal conductivity. When the substrate conductivity is comparable to that of the film stack, the film and substrate responses become strongly coupled, and the analytical subtraction method becomes less reliable.

Finally, the single-film numerical tests showed that the analytical film-extraction method can give reasonable estimates for simple film/substrate systems, but still introduces systematic errors of several percent. These errors arise from the one-dimensional approximation used for the film temperature drop, the finite heater geometry, and the difficulty of separating film and substrate contributions.

Overall, this chapter provides the basis for the analysis developed in Chapter 5. The experimental validation confirms that the 3-ω platform gives reliable results on reference materials. The numerical validation confirms that the FEM model can reproduce the expected 3-ω response. At the same time, the parametric studies show that simple analytical methods are not sufficient for the final Si_3N_4/SiO_2 multilayer stack, where several layers, interfaces, and the substrate contribute to the same measured signal. This motivates the use of the FEM-based inverse fitting and Effective Medium Approach developed in the next chapter.

Chapter 5

Methodology for the Thermal Characterization of Complex Multilayer Systems

This chapter presents the method used to extract the effective thermal conductivity of a complex five-layer Si_3N_4/SiO_2 stack. The first attempt was to use a detailed FEM model in which the thermal conductivity of each layer and the thermal boundary resistance (TBR) of each interface were treated as fitting parameters. However, this multi-parameter inverse problem did not lead to a unique and stable solution. The fitted parameters were strongly correlated, which made the direct extraction of individual layer and interface properties unreliable.

To understand this limitation, a frequency-dependent sensitivity analysis was performed. The results showed that, for the expected range of interface resistance values in high-quality PECVD dielectric stacks, the 3-ω signal is much more sensitive to the overall thermal response of the stack than to each individual interface resistance. This result explains why the independent extraction of all interface resistances is difficult with the present measurement configuration.

Based on this diagnosis, an Effective Medium Approach (EMA) was adopted. In this approach, the five-layer stack is replaced by one equivalent homogeneous layer with the same total thickness and an effective cross-plane thermal conductivity. The validity and limits of this approach were then tested using a series of numerical virtual samples. Finally, the EMA model was compared with an alternative high-TBR model using the real experimental data. This chapter therefore establishes a step-by-step procedure for extracting a reliable effective thermal conductivity from a complex multilayer stack.

5.1 Introduction: From a Simple Measurement to a Complex Inverse Problem

The initial objective of this work was to measure the effective cross-plane thermal conductivity of a five-layer Si_3N_4/SiO_2 thin-film stack prepared by plasma-enhanced chemical vapor deposition (PECVD). The 3-ω method was selected because it is widely used for measuring the thermal properties of thin films [84]. A cross-sectional schematic of the sample and a microscope image are shown in Figure 5.1.

The stack was deposited on a fused silica substrate. From the substrate to the top surface, the layer sequence is: SiO_2 (312 nm), Si_3N_4 (226 nm), SiO_2 (312 nm), SiO_2 (312 nm), and Si_3N_4 (126 nm). The total thickness of the dielectric stack is 1288 nm. Several metallic heaters with different sizes were patterned on the same wafer. Each heater consists of a 40 nm titanium (Ti) adhesion layer and a 500 nm gold (Au) layer. For the final analysis, two heater lines with the same length of 3 mm and different widths, 6 µm and 8 µm, were selected because they provided the most stable and consistent

datasets.

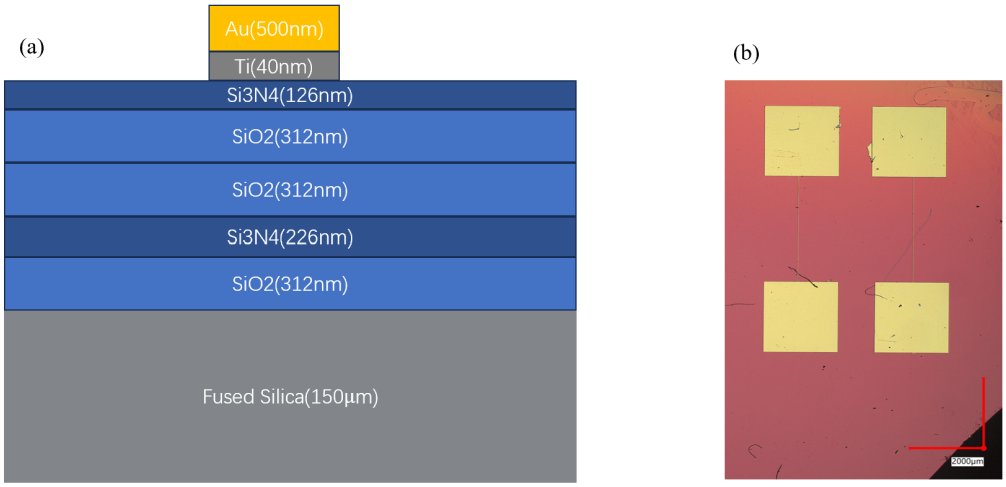


Figure 5.1 – Structure of the five-layer Si_3N_4/SiO_2 stack fabricated on a fused silica substrate. (a) Cross-sectional schematic showing the thickness of each layer. (b) Microscope image of the sample.

At first, a detailed FEM model was built to represent the full multilayer structure and all its interfaces. In this model, the thermal conductivities of Si_3N_4 and SiO_2, denoted by $\kappa_{Si_3N_4}$ and κ_{SiO_2}, and the thermal boundary resistances between layers were considered as unknown parameters. The aim was to extract all these parameters at the same time by fitting the simulated temperature oscillation $\Delta T(f)$ to the experimental 3-ω data [145].

However, this direct multi-parameter fitting procedure did not converge to a stable and unique solution in COMSOL Multiphysics® [146]. Depending on the initial values and parameter bounds, the fitted parameters either reached the imposed limits or changed strongly without giving a physically reliable result. This behavior indicates that the problem is not only a numerical difficulty, but an ill-posed inverse problem [147]. In such a problem, several different combinations of layer conductivities and interface resistances can produce very similar thermal responses.

This observation led to the main question of this chapter: what information can be reliably extracted from the measured 3-ω signal for this multilayer stack? To answer this question, the following points are examined:

— Why does the direct multi-parameter fit fail?

— Which parameters have the strongest influence on the measured 3-ω signal?

— Can the measurement separate the contributions of individual layers and interfaces?

— If this separation is not reliable, can a simpler effective model provide a meaningful thermal property for the whole stack?

— What are the limits of this effective model?

The rest of this chapter answers these questions step by step. First, the thermal conductivity of the substrate is determined from the low-frequency response. Then, a frequency-dependent sensitivity analysis is used to identify which parameters can be reliably probed by the measurement. Based on this analysis, an Effective Medium Approach is introduced and validated using virtual samples. Finally, the validated model is applied to the experimental data to extract the effective cross-plane thermal conductivity of the five-layer stack.

5.2 Measuring the Substrate: The First Step of the Decoupling Strategy

The first step of the analysis is to determine the thermal conductivity of the substrate, denoted by κ_{sub}. This step is necessary because the substrate strongly contributes to the measured 3-ω signal, especially at low frequency.

The reason is related to the thermal penetration depth. For a periodic heat source, the thermal penetration depth decreases when the frequency increases, following approximately:

$$L_p \propto \frac{1}{\sqrt{\omega}} \tag{5.1}$$

Therefore, at low frequency, the thermal wave penetrates deeply into the substrate. In this frequency range, the contribution of the thin-film stack is relatively small, and the measured response is mainly governed by the substrate. This property is used here to extract κ_{sub} before fitting the film properties. The frequency-dependent sensitivity analysis presented in Section 5.3 confirms this choice.

The thermal conductivity of the substrate was extracted from the low-frequency range between 71 Hz and 266 Hz. In this range, the in-phase temperature oscillation, ΔT_{in}, varies linearly with the natural logarithm of the angular heating frequency, $\ln(2\omega)$. According to the analytical solution of the 3-ω method for a line heat source on a semi-infinite substrate [84, 131], the substrate thermal conductivity can be obtained from the slope of this linear relation:

$$\kappa_{\text{sub}} = -\frac{P}{2\pi l \cdot B} = \frac{P}{2\pi l \cdot |B|} \tag{5.2}$$

where P is the time-averaged Joule power dissipated in the heater, l is the heater length, and B is the slope obtained from the linear fit:

$$S = \frac{d\Delta T_{\text{in}}}{d\ln(2\omega)} \tag{5.3}$$

Since ΔT_{in} decreases when the frequency increases, the fitted slope B is negative. The absolute value of the slope is therefore used in Eq. (5.2) to obtain a positive thermal conductivity.

In this work, the Joule power was calculated from the measured first-harmonic voltage and the heater resistance using the same voltage convention as defined in Chapter 3. When $V_{1\omega}$ is expressed as an RMS voltage, the average power is:

$$P = \frac{V_{1\omega,\text{rms}}^2}{R_0} \tag{5.4}$$

If a peak voltage amplitude is used instead, the corresponding average power is $P = V_{1\omega,\text{peak}}^2/(2R_0)$.

Figure 5.2 shows the experimental in-phase temperature oscillation plotted as a function of $\ln(2\omega)$ for the two selected heaters, with widths of 6 µm and 8 µm. In the selected low-frequency range, both datasets show a linear behavior, which supports the use of the slope method for extracting the substrate thermal conductivity.

The slopes obtained from the linear fits and the corresponding substrate thermal conductivity values are listed in Table 5.1.

The two heater geometries give close values: 1.266 ± 0.017 W.m^{-1}.K^{-1} for the 6 µm heater and 1.308 ± 0.025 W.m^{-1}.K^{-1} for the 8 µm heater. The average value is therefore:

$$\kappa_{\text{sub}} = 1.287 \pm 0.030 \text{ W.m}^{-1}\text{.K}^{-1}. \tag{5.5}$$

Here, the uncertainty of the average value is reported as the standard deviation between the two heater measurements. This value of κ_{sub} is then used as a fixed input parameter in the following steps, where the thermal properties of the thin-film stack are extracted.

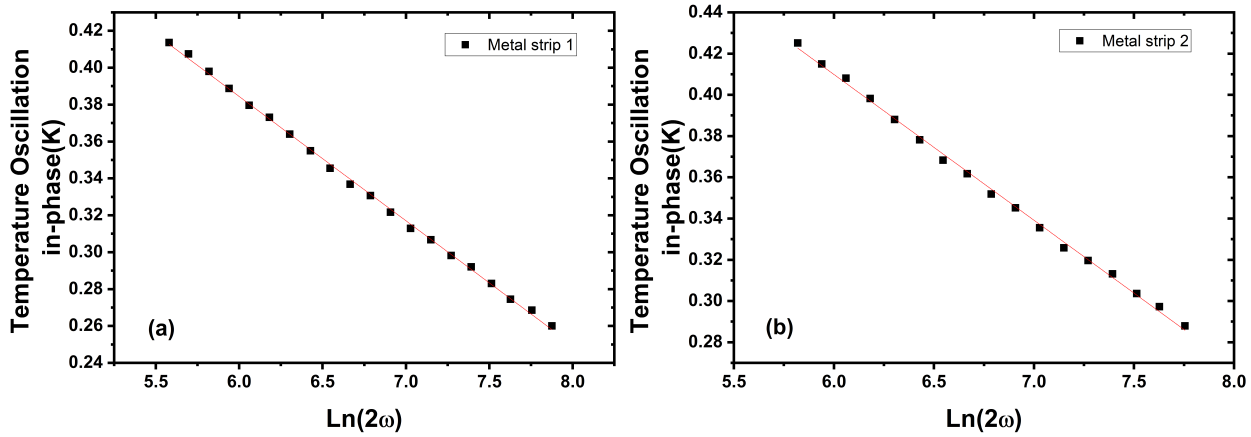


Figure 5.2 – Experimental in-phase temperature oscillation ΔT_{in} as a function of $\ln(2\omega)$ for the two heater geometries in the low-frequency range from 71 Hz to 266 Hz. (a) Heater width of 6 µm. (b) Heater width of 8 µm. The solid lines correspond to the linear fits used to extract the substrate thermal conductivity κ_{sub}.

Table 5.1 – Slope values obtained from the low-frequency linear fits and extracted substrate thermal conductivity values for the two heater geometries.

Heater width (µm)	Slope, B (K)	Extracted κ_{sub} $(W.m^{-1}.K^{-1})$
6	-0.02229	1.266 ± 0.017
8	-0.02145	1.308 ± 0.025

5.3 First Diagnostic Step: What Does Our Measurement Actually "See"? – Frequency-Dependent Sensitivity Analysis

After the direct multi-parameter fit failed to give a stable solution, the next step was to understand why this happened. The main question was: which parameters can be detected by the 3-ω signal, and which parameters have only a weak effect on the measured response?

To answer this question, a frequency-dependent sensitivity analysis was performed. This analysis quantifies how much the simulated temperature response changes when one input parameter is slightly modified. It is therefore a useful tool for identifying which parameters can be fitted reliably and which parameters cannot be extracted independently from the available data [148].

5.3.1 Principle of the Sensitivity Analysis

The idea of sensitivity analysis is simple. One input parameter is changed by a small percentage, while the other parameters are kept constant. The corresponding change in the model output is then calculated. In this work, the model output is the in-phase component of the heater temperature oscillation, denoted by ΔT_{in}.

For an input parameter X, the normalized sensitivity coefficient is defined as:

$$|S_X(f)| = \left| \frac{\left[\Delta T_{\text{in}}^{,\text{pert}}(f) - \Delta T_{\text{in}}^{,\text{base}}(f)\right] / \Delta T_{\text{in}}^{,\text{base}}(f)}{\left(X_{\text{pert}} - X_{\text{base}}\right) / X_{\text{base}}} \right| \tag{5.6}$$

where X_{base} is the baseline value of the input parameter, X_{pert} is its perturbed value, $\Delta T_{\text{in}}^{,\text{base}}(f)$ is the baseline in-phase temperature response, and $\Delta T_{\text{in}}^{,\text{pert}}(f)$ is the response after the perturbation.

The absolute value is used because the aim is to compare the magnitude of the response to different parameters, independently of whether the temperature increases or decreases. A large value of $|S_X|$ means that the 3-ω signal is strongly affected by the parameter X. Such a parameter can potentially be fitted with good reliability. In contrast, a value of $|S_X|$ close to zero means that the signal is weakly affected by this parameter. In that case, fitting this parameter is not reliable because different values may produce almost the same thermal response.

The sensitivity is expected to depend on frequency. This is because the thermal penetration depth of the 3-ω method depends on the heating frequency:

$$L_p = \sqrt{\frac{\alpha}{\pi f}} \tag{5.7}$$

where α is the thermal diffusivity and f is the heating frequency [84]. At low frequency, the thermal wave penetrates more deeply into the substrate. At higher frequency, the temperature field becomes more confined near the heater and the thin-film stack. Therefore, the sensitivity to the substrate, the film stack, and the interfaces changes with frequency.

5.3.2 Numerical Procedure

The sensitivity analysis was performed in COMSOL using the following procedure:

1. **Baseline model.** The full five-layer model, named Sample A, was used as the baseline structure. The model included the five dielectric layers and the six interfaces. The baseline material parameters were set to $\kappa_{\text{sub}} = 1.287\ \text{W.m}^{-1}\text{.K}^{-1}$, $\kappa_{\text{SiN}} = 2.5\ \text{W.m}^{-1}\text{.K}^{-1}$, and $\kappa_{\text{SiO}_2} = 1.3\ \text{W.m}^{-1}\text{.K}^{-1}$. For the baseline model, a thermal boundary resistance of $R_{\text{TBR}} = 5.0 \times 10^{-9}\ \text{m}^2\text{.K.W}^{-1}$ was assigned to the interfaces. This value represents a low interface resistance, close to the case of good thermal contact between PECVD layers [85, 88].
2. **Baseline frequency sweep.** A forward simulation was first performed over the frequency range from 6.9 Hz to 4300 Hz. This provided the baseline in-phase temperature response, $\Delta T_{\text{in}}^{\text{base}}(f)$.
3. **Individual parameter perturbation.** Each parameter was then increased by 5%, one at a time, while all other parameters were kept unchanged. Three types of perturbations were considered:
   — the substrate thermal conductivity, κ_{sub};
   — the film thermal conductivity, represented by a simultaneous 5% increase of the thermal conductivity of all film layers;
   — the interface resistance, represented by a simultaneous 5% increase of the TBR of all six interfaces.
4. **Calculation of sensitivity.** For each perturbed case, a new frequency sweep was performed. The normalized sensitivity coefficient was then calculated at each frequency using Eq. (5.6).

The resulting sensitivity curves are shown in Figure 5.3.

For clarity, the sensitivity values at a representative frequency of 163.4 Hz are summarized in Table 5.2. This frequency lies in the range where the film contribution becomes important.

5.3.3 Main Results of the Sensitivity Analysis

The sensitivity analysis gives three main results.

1. **The dominant contribution changes with frequency.** At low frequency, the signal is mainly sensitive to the substrate thermal conductivity. This is expected because the thermal penetration depth is large and the heat wave reaches deeply into the substrate. At higher frequency, the sensitivity to the film stack increases. This supports the two-step analysis used in this chapter: first, the substrate thermal conductivity is extracted from the low-frequency range; then, this value is fixed when extracting the effective thermal conductivity of the film stack.

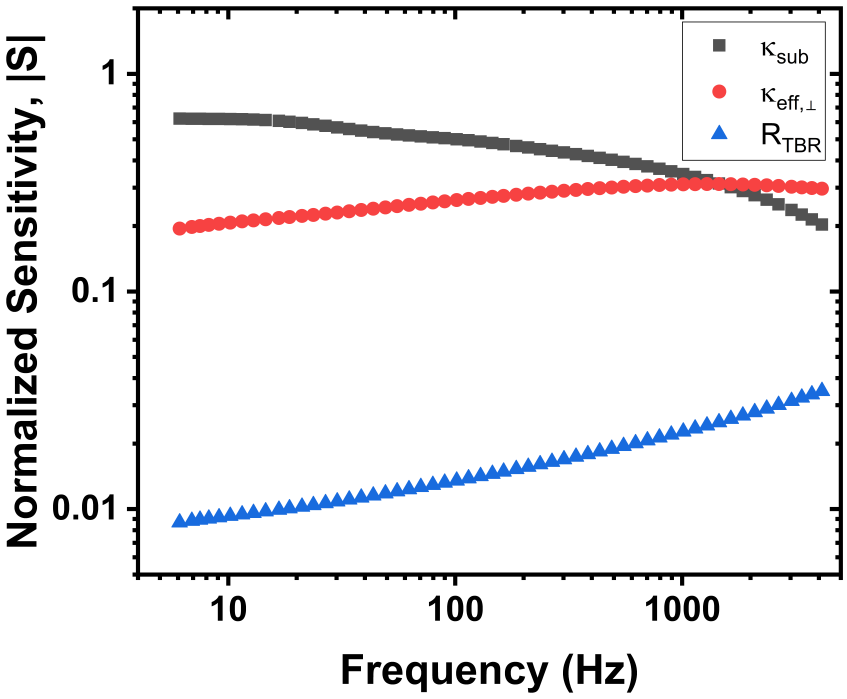


Figure 5.3 – Normalized sensitivity coefficients $|S_X|$ of the in-phase 3-ω temperature response with respect to the substrate thermal conductivity κ_{sub}, the effective film thermal conductivity κ_{eff}, and the interface thermal resistance R_{TBR}, as a function of frequency.

Table 5.2 – Normalized sensitivity coefficients $|S_X|$ of selected thermal parameters at 163.4 Hz.

Rank	Parameter	Normalized sensitivity $\lvert S_X \rvert$	Sensitivity level
1	κ_{SiN}	0.163	High
2	κ_{SiO_2}	0.077	Medium
3	$R_{\text{TBR,metal/SiN}}$	0	Insensitive
4	$R_{\text{TBR,SiN/SiO}_2}$	0	Insensitive
5	$R_{\text{TBR,SiO}_2/\text{SiO}_2}$	0	Insensitive
6	$R_{\text{TBR,SiO}_2/\text{glass}}$	0	Insensitive

2. **The sensitivity to low interface resistance is weak.** For the low interface resistance expected in the PECVD stack, around 5.0×10^{-9} m^2.K.W^{-1}, the sensitivity to R_{TBR} is much lower than the sensitivity to the film thermal conductivity. This means that, in this range, the 3-ω signal is not suitable for independently extracting each interface resistance. A very large interface resistance would be easier to detect, but this is not the expected case for the present sample.
3. **The direct multi-parameter fit is not reliable.** The weak sensitivity to the interfaces explains the failure of the initial fitting attempt. Several combinations of film thermal conductivity and interface resistance can lead to similar temperature responses. As a result, the optimization algorithm cannot uniquely separate the contribution of the films from the contribution of the interfaces. This parameter correlation makes the simultaneous extraction of several film and interface properties ill-posed for the present multilayer stack.

This result leads to a simpler and more reliable strategy. Instead of trying to extract all individual layer and interface properties at the same time, the multilayer stack is treated as one equivalent layer. This is the basis of the Effective Medium Approach introduced in the next section.

5.4 Building and Validating the Effective Medium Approach (EMA)

The sensitivity analysis showed that the 3-ω signal cannot reliably separate all individual layer and interface contributions in the present multilayer stack. However, it also showed that the signal is sensitive to the overall thermal response of the stack. This motivates the use of an Effective Medium Approach (EMA), in which the full multilayer structure is replaced by one equivalent layer.

5.4.1 Theoretical Basis of the EMA

The main idea of the EMA is to simplify the multilayer stack while preserving its total thermal response. Since the experimental signal cannot clearly resolve the contribution of each individual layer and each interface, the five dielectric layers and their interfaces are represented by one homogeneous layer with the same total thickness:

$$d_{\text{total}} = 1288\,\text{nm}.$$

This equivalent layer is described by two effective properties: an effective cross-plane thermal conductivity and an effective volumetric heat capacity.

Effective cross-plane thermal conductivity For heat flow normal to the layers, the different layers and interfaces act mainly as thermal resistances in series. The 1D effective cross-plane thermal conductivity is therefore written as:

$$\kappa_{\text{eff},\perp}^{\text{1D}} = \frac{d_{\text{total}}}{\sum_i (d_i/\kappa_i) + \sum_j R_{\text{TBR},j}} \tag{5.8}$$

where d_i and κ_i are the thickness and thermal conductivity of the i-th layer, and $R_{\text{TBR},j}$ is the thermal boundary resistance of the j-th interface.

This expression gives a 1D reference value for the cross-plane thermal conductivity of the stack. It includes both the resistance of the layers and the resistance of the interfaces.

Effective volumetric heat capacity The transient response also depends on the thermal mass of the stack. To conserve the total heat storage of the multilayer structure, the effective volumetric heat capacity is calculated using a thickness-weighted average:

$$(\rho c_p)_{\text{eff}} = \frac{\sum_i \rho_i c_{p,i} d_i}{d_{\text{total}}} \tag{5.9}$$

where $\rho_i c_{p,i}$ is the volumetric heat capacity of the i-th layer.

In the inverse fitting procedure, $(\rho c_p)_{\text{eff}}$ is fixed from the known material properties, while $\kappa_{\text{eff},\perp}$ is used as the fitting parameter. This reduces the initial multi-parameter problem to a single-parameter inverse problem.

It is important to note that Eq. (5.8) is a 1D series-resistance estimate. The actual 3-ω measurement has a three-dimensional temperature field, especially near the heater edges. For this reason, the value retrieved by a 3D FEM inverse fit may differ from the simple 1D estimate. The following virtual experiment is used to quantify this difference and to test whether the EMA can still reproduce the thermal response of the multilayer stack.

5.4.2 Virtual Experiment for EMA Validation

To test the EMA before applying it to real experimental data, a controlled virtual experiment was performed. In this test, the input parameters are known in advance. This makes it possible to

compare the value retrieved by the EMA fitting model with the reference value calculated from the full multilayer model.

The virtual experiment consists of two steps.

Step 1: Forward simulation with the full multilayer model
The complete five-layer structure is first built in COMSOL. Each layer and interface is assigned a known thermal property. A forward frequency sweep is then performed to calculate the in-phase temperature response $\Delta T_{\text{in}}(f)$. This simulated response is used as virtual experimental data.

Step 2: Inverse fit with the EMA model
The internal details of the multilayer structure are then replaced by one equivalent layer. The virtual data generated in Step 1 are fitted using this single-layer EMA model. The only fitted parameter is the effective cross-plane thermal conductivity, $\kappa_{\text{eff},\perp}^{\text{fit}}$. This inverse fit is performed with a 3D FEM model, so that lateral heat spreading near the heater is still included.

The comparison between the 1D reference value and the fitted value indicates how much the finite heater geometry and 3D heat spreading affect the extracted effective conductivity.

5.4.3 Validation on the Baseline Virtual Sample

The first validation was performed on the baseline virtual sample, named Sample A. Its layer structure is identical to that of the real sample.

Forward simulation The full five-layer model was built in COMSOL. The thermal conductivities were set to:

$$\kappa_{\text{SiN}} = 2.5 \text{ W.m}^{-1}\text{.K}^{-1}, \qquad \kappa_{\text{SiO}_2} = 1.3 \text{ W.m}^{-1}\text{.K}^{-1}$$

The substrate thermal conductivity was fixed at the experimentally measured value:

$$\kappa_{\text{sub}} = 1.287 \text{ W.m}^{-1}\text{.K}^{-1}.$$

A thermal boundary resistance of $R_{\text{TBR}} = 5.0 \times 10^{-9}$ m^2.K.W^{-1} was applied to all six interfaces. This value represents a low interface resistance, corresponding to good thermal contact between PECVD layers.

Using the 1D series-resistance formula in Eq. (5.8), the reference effective cross-plane thermal conductivity of Sample A is: $\kappa_{\text{eff},\perp}^{\text{1D}} \approx 1.45$ W.m^{-1}.K^{-1}. A forward simulation was then performed with the full multilayer model to generate the virtual in-phase temperature response $\Delta T_{\text{in}}(f)$.

Inverse fit The virtual data were then fitted with the single-layer EMA model. The fitting was performed in COMSOL using the Global Least-Squares Objective. Since the analysis in this chapter is based on the in-phase response, the objective function was defined as:

$$\Phi(\kappa_{\text{eff},\perp}) = \sum_{i=1}^{N} \left[\Delta T_{\text{in}}^{\text{data}}(f_i) - \Delta T_{\text{in}}^{\text{sim}}(f_i, \kappa_{\text{eff},\perp})\right]^2 \tag{5.10}$$

where N is the number of frequency points in the selected fitting range, $\Delta T_{\text{in}}^{\text{data}}$ is the virtual in-phase temperature response generated by the full multilayer model, and $\Delta T_{\text{in}}^{\text{sim}}$ is the response calculated by the single-layer EMA model.

The minimization was performed using the Levenberg–Marquardt algorithm. This algorithm is well suited for nonlinear least-squares problems. The optimality tolerance was set to 10^{-3}.

The fitting was carried out in the frequency range from 266 Hz to 898 Hz. The fitted curve is shown in Figure 5.4.

The fitted effective thermal conductivity was: $\kappa_{\text{eff},\perp}^{\text{fit}} \approx 1.996$ W.m^{-1}.K^{-1}.

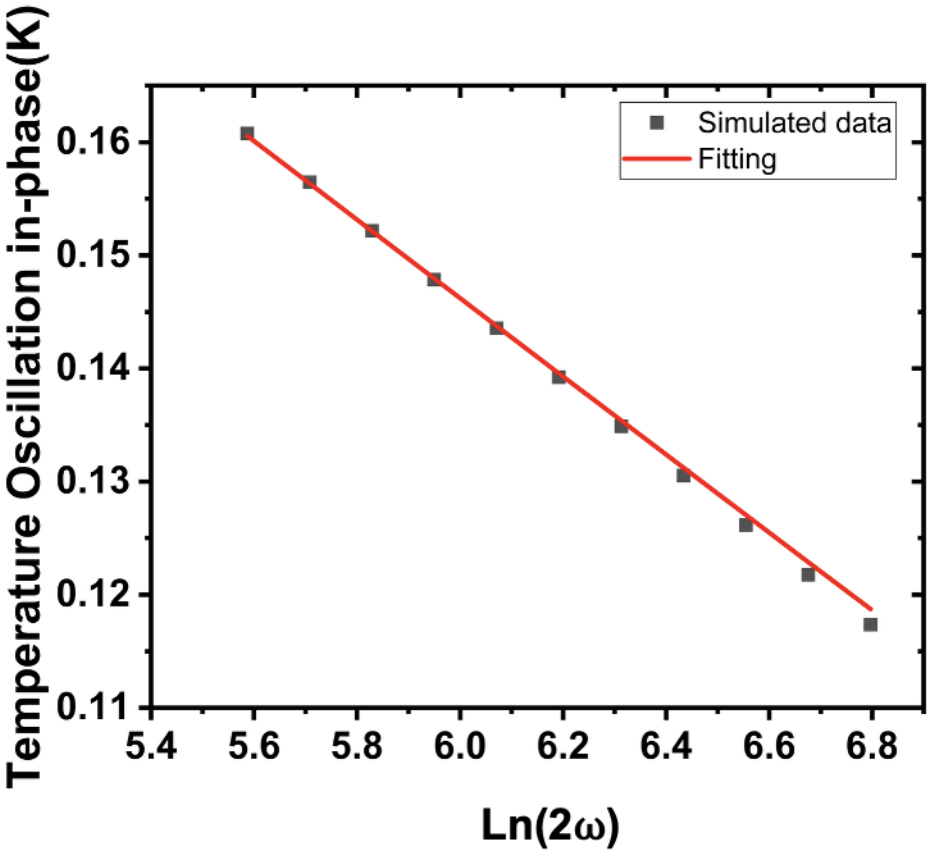


Figure 5.4 – EMA inverse fit applied to the virtual in-phase temperature response generated from the full multilayer model of Sample A. The single-layer EMA model reproduces the virtual data in the selected fitting range.

This value is about 37.4% higher than the 1D reference value of $\kappa^{1D}_{eff,\perp} \approx 1.45$ W.m^{-1}.K^{-1}.

This difference does not indicate a failure of the fit. Instead, it shows that the 1D series-resistance model does not fully capture the three-dimensional heat flow created by the finite-width heater. In the 3D FEM model, heat can also spread laterally in the upper layers before entering the substrate. This additional heat-spreading effect changes the apparent thermal response measured by the 3-ω method.

Therefore, the fitted value $\kappa^{fit}_{eff,\perp}$ should be understood as an effective parameter retrieved under the real 3D measurement geometry. It is not exactly the same as the simple 1D series-resistance value. This baseline test shows that the EMA model can reproduce the thermal response of the full multilayer structure with a single fitted parameter, while still accounting for the 3D geometry through the FEM simulation.

This result supports the use of the EMA model for the present analysis. The next section extends this validation to a wider set of virtual samples in order to define the range in which the fitted effective conductivity remains physically meaningful.

5.5 Testing the Applicability Range of the EMA

The validation on Sample A showed that the EMA model can reproduce the thermal response of the full multilayer structure in the baseline case. However, one successful case is not sufficient to define the range of validity of the method. The EMA must also be tested under different thermal conditions.

For this purpose, a virtual sample library was built. Eleven virtual samples, named Samples A to K, were defined by changing the film thermal conductivities, the interface thermal resistance, and,

in one case, the substrate thermal conductivity. The aim was to determine when the fitted EMA parameter can be interpreted as a meaningful effective cross-plane thermal conductivity, and when it should only be considered as an apparent fitting parameter.

5.5.1 Design of the Virtual Sample Library

The parameters of the eleven virtual samples are listed in Table 5.3. Sample A corresponds to the baseline case, whose structure and material values are close to those used for the real sample. Samples B and C test the influence of low interface resistance. Samples D, F, and G test the effect of higher film thermal conductivity. Samples H, I, and K test the effect of larger interface resistance. Sample J tests the effect of a higher substrate thermal conductivity.

Table 5.3 – Description of the virtual sample library used to test the applicability range of the EMA.

Sample	κ_{SiN} ($W.m^{-1}.K^{-1}$)	κ_{SiO_2} ($W.m^{-1}.K^{-1}$)	R_{TBR} ($m^2.K.W^{-1}$)	κ_{sub} ($W.m^{-1}.K^{-1}$)
A (Baseline)	2.5	1.3	5.0×10^{-9}	1.287
B	2.5	1.3	1.0×10^{-9}	1.287
C	2.5	1.3	1.0×10^{-8}	1.287
D	10.0	1.3	5.0×10^{-9}	1.287
E	0.5	1.3	5.0×10^{-9}	1.287
F	2.5	10.0	5.0×10^{-9}	1.287
G	10.0	10.0	5.0×10^{-9}	1.287
H	2.5	1.3	1.0×10^{-7}	1.287
I	0.5	0.5	1.0×10^{-7}	1.287
J	0.5	0.5	1.0×10^{-7}	10.0
K	0.5	0.5	1.0×10^{-5}	1.287

5.5.2 Results of the Virtual Sample Library

For each virtual sample, two values were compared. The first value, denoted by $\kappa^{1D}_{eff,\perp}$, was calculated using the 1D series-resistance model. The second value, denoted by $\kappa^{fit}_{eff,\perp}$, was obtained by fitting the virtual data with the 3D EMA model. The results are summarized in Table 5.4.

A general trend is observed: the value fitted by the 3D EMA model is larger than the 1D series-resistance value for all virtual samples. This difference is expected because the two values do not describe exactly the same physical situation. The 1D value only represents heat flow normal to the layers. In contrast, the 3D FEM fit includes the real heater geometry and the lateral spreading of heat near the heater. Therefore, $\kappa^{fit}_{eff,\perp}$ should be seen as the effective parameter measured under the actual 3-ω geometry.

For Samples A, B, C, and E, the difference between the 3D fitted value and the 1D reference value remains moderate, between about 37% and 50%. These samples correspond to cases where the film conductivity is comparable to, or lower than, that of the substrate, and where no layer acts as a strong lateral heat spreader. In this regime, the heat mainly penetrates downward into the substrate, while lateral spreading remains a secondary effect. This behavior is illustrated in Figure 5.5(a). Under these conditions, the EMA provides a useful effective description of the total thermal response seen by the 3-ω measurement.

A first limit of the EMA interpretation appears when the film contains highly conductive layers. This is observed for Samples D, F, and G. In these cases, the film can spread heat efficiently along the in-plane direction before heat enters the substrate. The fitted EMA value can still reproduce the

Table 5.4 – EMA validation results for the virtual sample library. The fitted value $\kappa_{\mathrm{eff},\perp}^{\mathrm{fit}}$ is obtained from the 3D EMA inverse fit and should be interpreted according to the thermal regime of each sample.

Sample	$\kappa_{\mathrm{eff},\perp}^{\mathrm{1D}}$ ($\mathrm{W.m^{-1}.K^{-1}}$)	$\kappa_{\mathrm{eff},\perp}^{\mathrm{fit}}$ ($\mathrm{W.m^{-1}.K^{-1}}$)	Difference (3D vs. 1D) (%)	Main thermal behavior
A	1.45	1.996	+37.4	Baseline case
B	1.49	2.09	+40.3	Low interface resistance
C	1.41	2.05	+45.4	Low interface resistance
D	1.65	3.52	+113.3	Strong lateral spreading
E	0.89	1.32	+48.3	Low-conductivity film
F	4.97	8.16	+64.2	Film-dominated spreading
G	8.38	10.47	+24.9	Strong film conduction
H	1.02	1.70	+66.7	Interface-related confinement
I	0.43	0.61	+41.9	Low-conductivity film with high TBR
J	0.43	0.55	+27.9	Low-conductivity film with higher-conductivity substrate
K	0.0303	0.0497	+64.0	Very high interface resistance

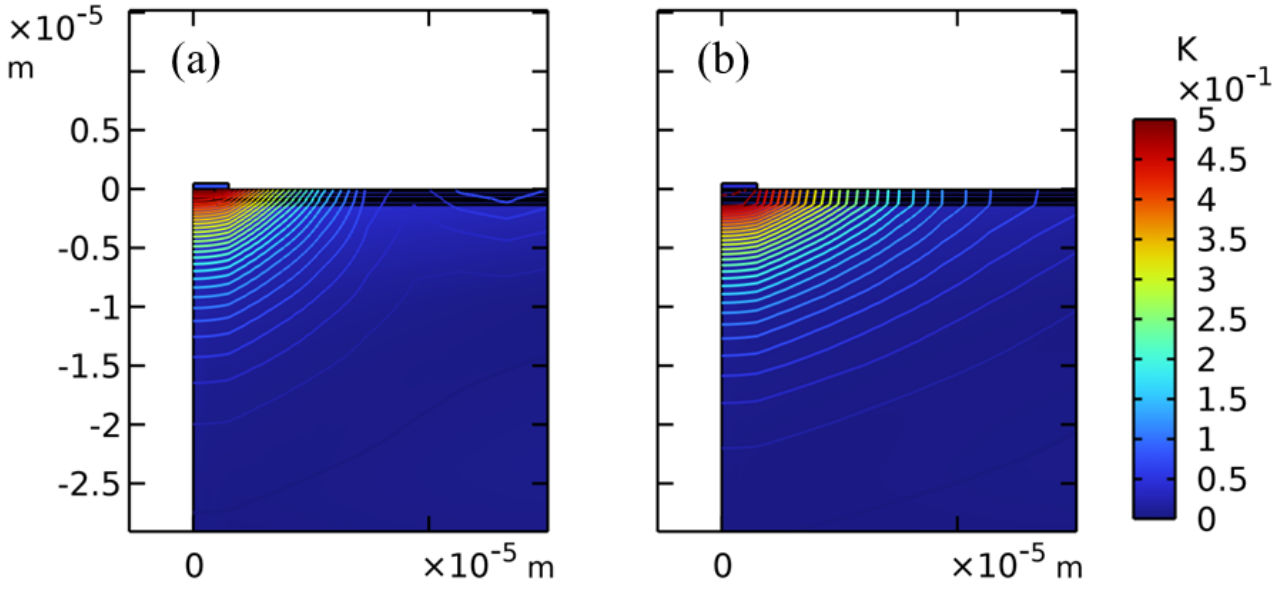


Figure 5.5 – Simulated temperature distribution illustrating the change in heat transport behavior. (a) For Sample A, where κ_{film} is comparable to κ_{sub}, heat mainly penetrates downward into the substrate. (b) When the film is much more conductive, the film spreads heat laterally before the heat enters the substrate. Both simulations are shown at 163 Hz.

numerical data, but it should no longer be interpreted as a strict cross-plane material property. It becomes an apparent effective parameter that describes the full heater-film-substrate response.

A second limit appears when the interface resistance is large enough to strongly affect the heat flow. This is the case for Samples H, I, and K. In this regime, the interfaces slow down heat transfer through the stack and create stronger thermal confinement near the heater. The upper part of the stack reaches a higher temperature, and lateral heat redistribution becomes more important. Again, the fitted EMA value remains useful for reproducing the thermal response, but its interpretation as a simple cross-plane conductivity becomes less direct.

Sample J shows the effect of increasing the substrate thermal conductivity while keeping the same

low-conductivity multilayer as Sample I. The fitted value decreases from 0.61 to 0.55 $W.m^{-1}.K^{-1}$, and the difference with the 1D reference value decreases from 41.9% to 27.9%. This shows that the substrate affects the fitted result, but in this case it does not completely dominate the response. The fitted value remains mainly controlled by the thermal resistance of the multilayer stack and its interfaces.

These results define the range in which the EMA can be used with a clear physical meaning. The EMA is most reliable when the film conductivity is comparable to or lower than the substrate conductivity, when no highly conductive layer dominates in-plane heat spreading, and when the interface resistance does not create strong thermal confinement near the heater. This regime corresponds to the real sample studied in this thesis.

In summary, the virtual sample library shows that the EMA is a useful and reliable reduced model within a defined range. Inside this range, $\kappa_{\mathrm{eff},\perp}^{\mathrm{fit}}$ can be used as a meaningful effective thermal conductivity of the multilayer stack under 3-ω measurement conditions. Outside this range, the fitted value may still reproduce the thermal response, but it should be interpreted as an apparent parameter rather than as a unique cross-plane material property.

5.5.3 Final Comment on the EMA Applicability

The virtual sample study shows that the EMA model can be used as a reliable reduced model within a defined range. It is most suitable when the film stack does not act as a strong in-plane heat spreader, when the substrate does not dominate the response in the selected frequency range, and when the interface resistance does not fully control the heat flow. These conditions correspond to the experimental case studied in this thesis. Therefore, the EMA provides a suitable way to extract an effective thermal conductivity for the present multilayer stack.

5.6 Testing an Alternative High-TBR Interpretation

After validating the EMA model, one remaining question had to be addressed. The low effective thermal conductivity measured for the real sample may be caused by low thermal conductivity inside the PECVD films. However, another possible explanation is that the interfaces have high thermal boundary resistance. In that case, the apparent low thermal conductivity would mainly come from the interfaces rather than from the films themselves.

To test this alternative explanation, the EMA model was compared with models that explicitly include thermal boundary resistance. The goal was not only to obtain a good fit, but also to check whether the fitted parameters have a clear physical meaning.

5.6.1 Sensitivity Analysis in a High-TBR Case

Before fitting a high-TBR model to the experimental data, an additional sensitivity analysis was performed. The aim was to check whether the 3-ω signal would be sensitive to the interface resistance if the real sample were controlled by a large TBR.

For this test, Sample H was used as a representative high-TBR case, with: $R_{\mathrm{TBR}} = 1.0 \times 10^{-7}$ $m^2.K.W^{-1}$.

As shown in Figure 5.6, the sensitivity to R_{TBR} becomes much larger than in the low-TBR case. It becomes comparable to the sensitivity to κ_{sub} and κ_{eff}. This means that, if the real sample were mainly controlled by a high interface resistance, the 3-ω signal should be able to detect this contribution.

5.6.2 Comparison Between the EMA Model and a Single Global TBR Model

The next step was to compare two models using the same experimental data from the 6 µm heater.

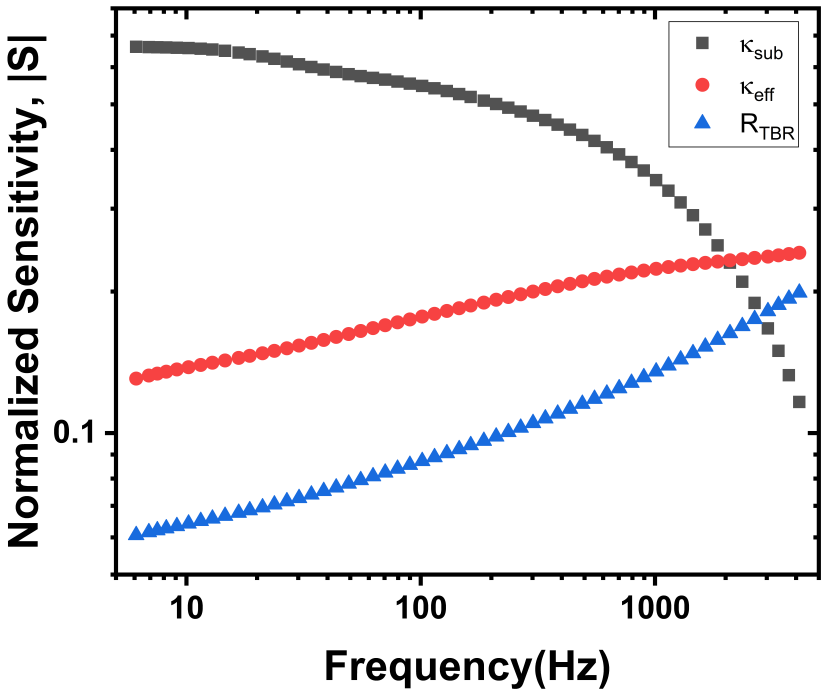


Figure 5.6 – Normalized sensitivity coefficients $|S_X|$ of the in-phase 3-ω response with respect to the substrate thermal conductivity κ_{sub}, the effective film thermal conductivity κ_{eff}, and a high interface thermal resistance $R_{\text{TBR}} = 1.0 \times 10^{-7}$ m^2.K.W^{-1}, as a function of frequency.

Model A: EMA model

This model replaces the multilayer stack with one equivalent layer and fits only one parameter, the effective cross-plane thermal conductivity $\kappa_{\text{eff},\perp}$. The fit gives:$\kappa_{\text{eff},\perp} \approx 0.62$ W.m^{-1}.K^{-1}. The residual sum of squares was approximately 1.02×10^{-4}.

Model B: single global TBR model

This model keeps the full five-layer structure. The intrinsic thermal conductivities of the films are fixed to literature values, and one global interface resistance $R_{\text{TBR,fit}}$ is fitted and applied to all six interfaces. This model also fits the experimental data. The residual sum of squares was much smaller, approximately 2.06×10^{-17}. However, this fit required a high interface resistance:$R_{\text{TBR,fit}} \approx 1.90 \times 10^{-7}$ m^2.K.W^{-1}.

From a purely numerical point of view, the single global TBR model gives a smaller residual. However, a smaller residual does not automatically mean that the fitted parameter is physically correct. The high-TBR model assumes that the film thermal conductivities are known and fixed. If these assumed values are not correct for the real PECVD films, the fitted interface resistance may compensate for this error. Therefore, a further test is needed to check whether interface resistances can be extracted independently.

5.6.3 Can Several TBR Values Be Fitted Independently?

To test whether several interface resistances can be determined independently, a virtual experiment was performed. In this test, the input data were generated numerically from a known multilayer structure. The true interface resistance values were therefore known in advance, and the data did not contain experimental noise.

Multi-TBR Inverse Fitting Test

The inverse problem was solved using the Parameter Estimation module in COMSOL Multiphysics. The Levenberg–Marquardt algorithm was used to minimize a nonlinear least-squares objective function. Since the analysis in this chapter is based on the in-phase response, the objective function was written as:

$$\Phi(\mathbf{p}) = \sum_{j=1}^{N} \left[\Delta T_{\text{in}}^{\text{model}}(f_j, \mathbf{p}) - \Delta T_{\text{in}}^{\text{data}}(f_j)\right]^2 \tag{5.11}$$

where $\mathbf{p}$ is the vector of fitted parameters, here corresponding to the unknown interface resistances, and N is the number of frequency points used in the fit.

1. **Creation of the reference virtual data.** A virtual sample with the same layer structure as Sample A was built. Three different TBR values were assigned to selected interfaces: $R_{\text{true},1} = 1.00 \times 10^{-7}$, $R_{\text{true},2} = 5.00 \times 10^{-6}$, $R_{\text{true},3} = 3.00 \times 10^{-7}$ m^2KW^{-1} .
   These values were used to generate noise-free virtual data.
2. **Multi-parameter inverse fitting.** The three interface resistances were then treated as unknown fitting parameters. The Levenberg–Marquardt algorithm was used to minimize Eq. (5.11). As shown in Figure 5.7, the fitted response is very close to the virtual data.
3. **Retrieved parameters.** Although the fitted curve matches the virtual data well, the retrieved interface resistances do not all match the input values. The fitted values were:

   $$R_{\text{fit},1} = 4.14 \times 10^{-7}, \quad R_{\text{fit},2} = 5.14 \times 10^{-6}, \quad R_{\text{fit},3} = 2.83 \times 10^{-7} \quad \text{m}^2\,\text{K}\,\text{W}^{-1}.$$

   The largest resistance, $R_{\text{true},2}$, is retrieved with reasonable accuracy because it dominates the thermal response. In contrast, $R_{\text{true},1}$ is strongly overestimated, increasing from 1.00×10^{-7} to 4.14×10^{-7} $\text{m}^2\,\text{K}\,\text{W}^{-1}$, corresponding to a relative error of about 314%.

This virtual experiment shows that the multi-TBR inverse problem is not unique. Even in a noise-free case, a good fit does not guarantee that all individual interface resistances can be retrieved correctly. The largest resistance controls most of the response, while the smaller resistances have weaker and correlated effects. As a result, the optimizer can compensate an error in one parameter by changing another parameter.

This result shows that, without independent information about the individual interfaces, fitting several thermal boundary resistances from the present 3-ω data is not reliable. It supports the use of the EMA model, where the stack is described by a single effective thermal conductivity instead of many strongly correlated layer and interface parameters.

5.6.4 Conclusion of the Comparison

The comparison between the EMA model and the high-TBR models leads to a clear conclusion. A high-TBR model can fit the experimental data, but this does not prove that the interfaces are the only cause of the low effective thermal conductivity. The result depends strongly on the film thermal conductivities that are fixed in the model. If the real PECVD films have lower thermal conductivities than the assumed literature values, the fitted TBR may become artificially high to compensate for this difference.

This is a parameter correlation problem. Different combinations of film thermal conductivity and interface resistance can produce similar 3-ω responses. Therefore, the interface resistance cannot be uniquely determined from the present data alone.

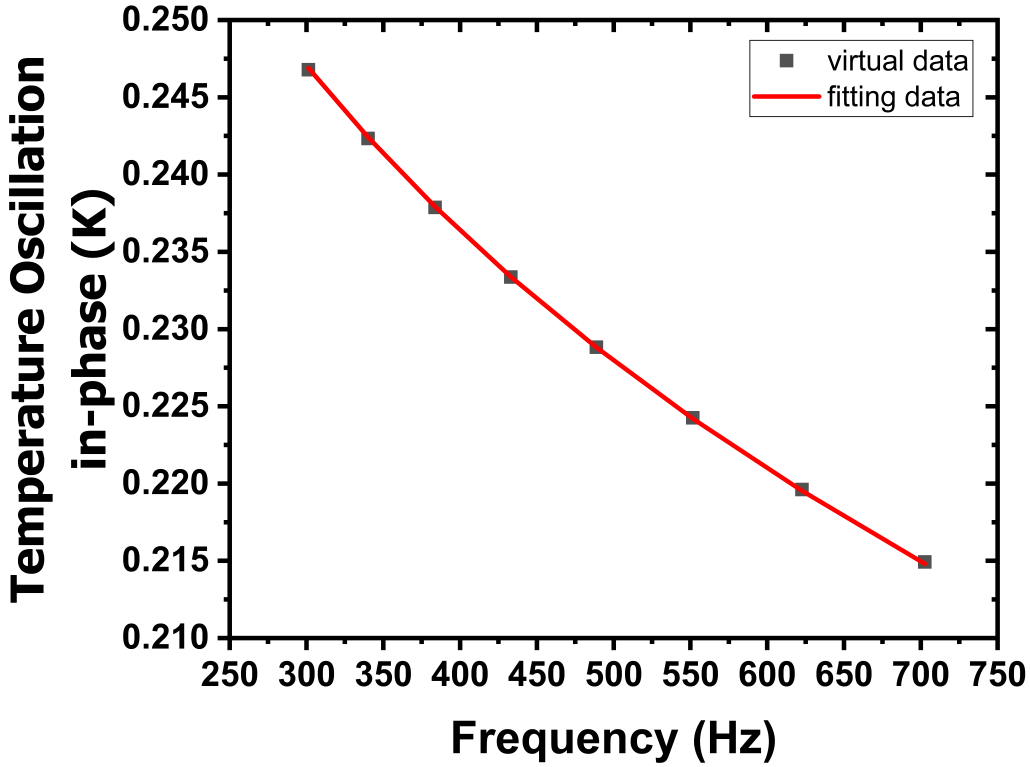


Figure 5.7 – Parameter correlation in the multi-TBR inverse fitting test. The fitted response obtained with the multi-TBR model closely matches the virtual data. However, the extracted interface resistances differ from the true input values, showing that a good fit does not necessarily give a unique set of physical parameters.

Verification calculation To compare the two interpretations, the effective thermal conductivity implied by the high-TBR model was calculated. The total thicknesses of the dielectric materials are: $d_{SiO_2} = 936nm$, $d_{SiN} = 352nm$. Using the fixed literature values: $\kappa_{SiO_2} = 1.3\ \mathrm{W.m^{-1}.K^{-1}}$, $\kappa_{SiN} = 2.5\ \mathrm{W.m^{-1}.K^{-1}}$, the intrinsic thermal resistance of the films is: $R_{film} \approx 8.61 \times 10^{-7}\ \mathrm{m^2.K.W^{-1}}$.

The high-TBR fit gives: $R_{TBR,fit} \approx 1.90 \times 10^{-7}\ \mathrm{m^2.K.W^{-1}}$.

Applied to six interfaces, this gives: $R_{int} \approx 11.40 \times 10^{-7}\ \mathrm{m^2.K.W^{-1}}$.

The total resistance is therefore: $R_{tot} = R_{film} + R_{int} \approx 20.01 \times 10^{-7}\ \mathrm{m^2.K.W^{-1}}$.

The corresponding effective thermal conductivity is:

$$\kappa_{eff,calc} = \frac{d_{total}}{R_{tot}} = \frac{1.288 \times 10^{-6}}{20.01 \times 10^{-7}} \approx 0.64\ \mathrm{W.m^{-1}.K^{-1}} \tag{5.12}$$

This calculated value is very close to the value obtained from the EMA fit, about $0.62\ \mathrm{W.m^{-1}.K^{-1}}$. This shows that the high-TBR model and the EMA model mainly describe the same total thermal resistance, but distribute this resistance differently between the films and the interfaces.

For this reason, reporting the effective thermal conductivity obtained from the EMA model is the most reliable choice for the present data. It gives the total thermal performance of the stack without requiring a unique separation between film resistance and interface resistance.

Conclusion For the present experimental data, reporting the effective thermal conductivity $\kappa_{eff,\perp}$ using the EMA model is the most reliable choice. This approach gives the overall thermal performance of the multilayer stack without requiring a unique separation between the film resistance and the interface resistance.

5.7 Final Extraction of the Effective Thermal Conductivity

After validating the EMA model and testing the alternative high-TBR interpretation, the final step is to apply the EMA model to the real experimental data. The objective is to extract the effective cross-plane thermal conductivity of the PECVD Si_3N_4/SiO_2 multilayer stack.

The final analysis was carried out in two steps:

1. **Substrate characterization.** The low-frequency part of the experimental response, from 71 Hz to 266 Hz, was used to extract the substrate thermal conductivity. This gave: $\kappa_{sub} = 1.287 \pm 0.030$ W.m^{-1}.K^{-1}. This value was then fixed in the following fitting step.
2. **Film-stack fitting.** The multilayer film stack was replaced by one equivalent layer with the same total thickness. The effective cross-plane thermal conductivity, $\kappa_{eff,\perp}$, was then fitted using the experimental in-phase data in the frequency range from 266 Hz to 898 Hz. This frequency range was selected because the sensitivity to the film stack is high while the influence of the substrate is reduced.

The FEM model used in COMSOL was configured with the same main geometrical, electrical, and thermal parameters as the experiment. These parameters are listed in Table 5.5. In the final EMA fit, the substrate thermal conductivity was fixed, while $\kappa_{eff,\perp}$ was used as the fitted parameter. The other parameters were used as fixed model inputs or as initial values required to run the simulation.

The value 1 Hz in Table 5.5 corresponds only to the initial value assigned to the COMSOL frequency parameter. During the inverse fitting procedure, the model was evaluated at the experimental frequency points imported in the selected range from 266 Hz to 898 Hz.

This fitting procedure was applied to two heater widths, 6 µm and 8 µm. Representative fits are shown in Figure 5.8. The model reproduces the experimental in-phase response well in the selected frequency range.

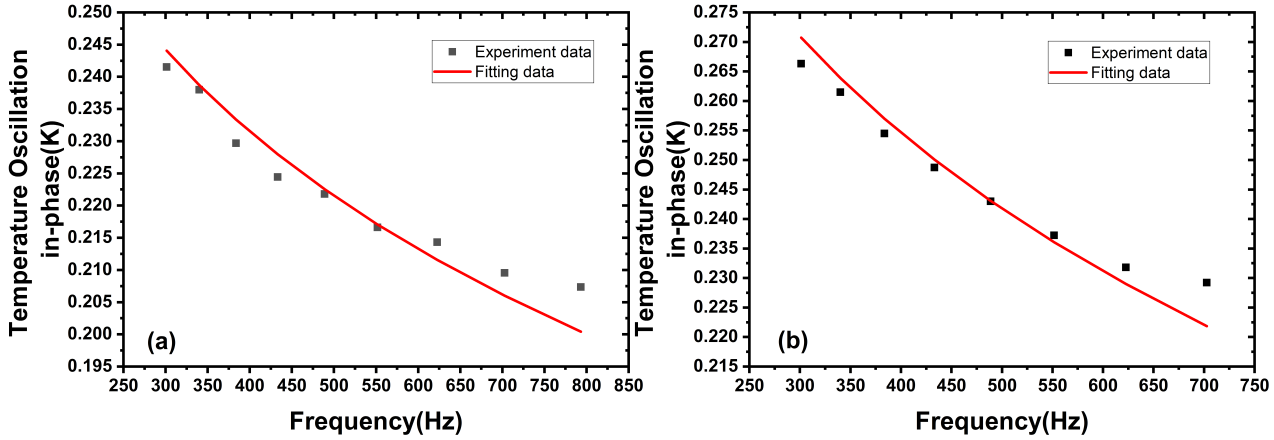


Figure 5.8 – Final EMA fits applied to the experimental in-phase data for two heater widths, 6 µm and 8 µm, in the selected fitting range from 266 Hz to 898 Hz.

The extracted effective thermal conductivity values are summarized in Table 5.6. The reported uncertainties correspond to the 95% confidence intervals obtained from the COMSOL parameter estimation procedure. The two heater geometries give close results: 0.624 W.m^{-1}.K^{-1} for the 6 µm heater and 0.615 W.m^{-1}.K^{-1} for the 8 µm heater. This agreement supports the repeatability of the extraction. The final effective cross-plane thermal conductivity of the multilayer stack is therefore reported as:

$$\kappa_{eff,\perp} = 0.62 \pm 0.03 \text{ W.m}^{-1}\text{.K}^{-1}$$

Table 5.5 – Main geometric, electrical, and thermal parameters used in the FEM model for the final EMA inverse fitting.

Symbol	Description	Value / Expression
Geometric parameters		
L	Length of the heater strip	3 mm
w	Width of the heater strip	6 µm and 8 µm
d_{sample}	Substrate thickness used in the model	150 µm
t_h	Thickness of the Au heater strip	0.5 µm
t_{Ti}	Thickness of the Ti adhesion layer	40 nm
d_f	Total thickness of the dielectric stack	1288 nm
Electrical parameters		
f	Frequency parameter	Initial COMSOL value: 1 Hz; fitting range: 266 Hz to 898 Hz
ω	Angular frequency	$2\pi f$
N	Number of dielectric layers	5
$V_{1\omega}$	First-harmonic voltage amplitude	0.255 V
R_0	Heater resistance	32.82 Ω and 25.25 Ω
β	Temperature coefficient of resistance	0.002 61 K^{-1}
P	Time-averaged Joule power	Calculated from $V_{1\omega}$ and R_0
ρ_{ref}	Reference electrical resistivity	Calculated from $R_0 w t_h / L$
Thermal parameters		
T_{ref}	Reference temperature	298 K
κ_{sub}	Substrate thermal conductivity	$1.287 W.m^{-1}.K^{-1}$
$(\rho c_p)_{\text{eff}}$	Effective volumetric heat capacity	Calculated from Eq. (5.9)
$\kappa_{\text{eff},\perp}$	Effective cross-plane thermal conductivity	Fitted parameter
$R^*_{\text{int},1}$	Interface resistance (Stripe/SiN)	1×10^{-9} m²·K/W
$R^*_{\text{int},2}$	Interface resistance (SiN/SiO_2)	1×10^{-7} m²·K/W
$R^*_{\text{int},2}$	Interface resistance (SiO_2/SiO_2)	5×10^{-9} m²·K/W
$R^*_{\text{int},2}$	Interface resistance (SiO_2/Glass)	8×10^{-8} m²·K/W

Table 5.6 – Final effective cross-plane thermal conductivity values extracted using the EMA model. The reported uncertainties correspond to the 95% confidence intervals obtained from the COMSOL parameter estimation procedure.

Heater width (µm)	$\kappa_{\text{eff},\perp}$ ($W.m^{-1}.K^{-1}$)	95% confidence interval
6	0.624	±0.027
8	0.615	±0.030
Average	**0.62**	±0.03

5.8 Final Discussion

The final extracted value, $\kappa_{\text{eff},\perp} = 0.62$ W.m^{-1}.K^{-1}, is much lower than the 1D reference value obtained for the idealized virtual Sample A: $\kappa^{\text{1D}}_{\text{eff},\perp} \approx 1.45$ W.m^{-1}.K^{-1}.

This difference does not indicate a failure of the method. Instead, it shows that the real PECVD-grown multilayer stack has a higher thermal resistance than the idealized model based on literature material values. Several physical factors may contribute to this reduction, including amorphous

structure, non-ideal stoichiometry, lower film density, defects, and rough or imperfect interfaces. All these factors can increase phonon scattering and reduce the effective thermal conductivity of the stack.

The result is also consistent with the applicability range of the EMA defined in Section 5.5. The extracted value is lower than the substrate thermal conductivity: $0.62 < 1.287$ W.m^{-1}.K^{-1}. This means that the real sample lies in the regime where the film stack remains the main thermal resistance and where the EMA can provide a meaningful effective description of the multilayer response.

Therefore, the final value of $\kappa_{\text{eff},\perp}$ should be interpreted as the effective cross-plane thermal conductivity of the complete PECVD multilayer stack under the present 3-ω measurement conditions. It describes the total thermal response of the stack, including the combined effects of the individual layers and their interfaces.

5.9 Summary and Outlook

This chapter presented the analysis used to extract the effective thermal conductivity of the five-layer Si_3N_4/SiO_2 stack. The first direct attempt to fit several layer and interface parameters did not give a unique solution. A frequency-dependent sensitivity analysis was therefore used to identify which parameters could be reliably detected by the 3-ω signal.

The sensitivity analysis showed that the signal is mainly sensitive to the substrate at low frequency and to the film stack at higher frequency. It also showed that, for the expected range of interface resistance in the present PECVD stack, individual interface resistances cannot be extracted independently. This justified the use of the Effective Medium Approach.

The EMA model was then tested using virtual samples. This study showed that the fitted effective conductivity is meaningful when the film stack does not act as a strong lateral heat spreader and when the interface resistance does not fully dominate the heat flow. The alternative high-TBR interpretation was also tested. Although a high-TBR model can fit the data, it does not provide a unique separation between film resistance and interface resistance.

Using the validated EMA model, the final effective cross-plane thermal conductivity of the PECVD multilayer stack was extracted as: $\kappa_{\text{eff},\perp} = 0.62 \pm 0.03$ W.m^{-1}.K^{-1}. This value provides a useful thermal parameter for modeling similar multilayer dielectric stacks.

Future work could combine this thermal characterization with structural analysis, such as transmission electron microscopy, density measurements, or composition analysis. This would help connect the measured effective thermal conductivity with the microstructure of the PECVD films and the quality of their interfaces.

General Conclusion and Perspectives

This thesis focused on the thermal characterization of dielectric thin films and multilayer structures using the 3-ω technique combined with finite element modeling. The motivation comes from the increasing importance of thermal management in microelectronic and optoelectronic devices, where dielectric layers such as SiO_2 and SiN_x are widely used for insulation and passivation. Although these materials are electrically useful, they can also limit heat dissipation, especially when their thickness is reduced to the nanoscale and when several layers and interfaces are combined in a stack.

The main difficulty addressed in this work is that the thermal response measured at the surface of a multilayer system contains the coupled contribution of the substrate, the individual thin films, and the interfaces. As a result, extracting a single material property from the measured 3-ω signal is not straightforward. Simple analytical models provide useful physical insight, but they become limited when the heater geometry is finite, when the substrate strongly influences the signal, or when several thin layers and interfaces contribute simultaneously.

The objective of this thesis was therefore to develop and validate a combined experimental and numerical methodology able to interpret the 3-ω response of complex dielectric multilayer systems. The work progressed from analytical modeling and experimental validation to numerical simulations, sensitivity analysis, and finally effective-medium inverse fitting for the real multilayer stack.

Summary of the Main Contributions

The contributions of this thesis are both experimental and numerical. They concern the development of a 3-ω measurement platform, the validation of the FEM model, the analysis of the limits of analytical methods, and the extraction of an effective thermal conductivity for a five-layer SiN_x/SiO_2 stack.

Development and Validation of the 3-ω Experimental Platform

A first contribution of this work is the development and validation of a 3-ω experimental platform dedicated to thin films and multilayer structures. The metallic strip deposited on the sample was used both as a heater and as a resistance thermometer. Its temperature coefficient of resistance was calibrated before each thermal measurement, allowing the measured third-harmonic voltage to be converted into the temperature oscillation of the heater.

The experimental platform was validated using reference bulk materials. Measurements on borosilicate glass and fused silica gave thermal conductivity values close to literature values. For borosilicate glass, the most reliable values were located around $1.14\,\mathrm{W\,m^{-1}\,K^{-1}}$ to $1.21\,\mathrm{W\,m^{-1}\,K^{-1}}$, close to the reference value of about $1.13\,\mathrm{W\,m^{-1}\,K^{-1}}$. For fused silica, two independent heater geometries gave values of $1.409\,\mathrm{W\,m^{-1}\,K^{-1}}$ and $1.414\,\mathrm{W\,m^{-1}\,K^{-1}}$. These results confirmed that the measurement setup, the TCR calibration, and the analytical slope method can provide reliable results for homogeneous amorphous substrates.

An attempted measurement on a SiO_2/Si sample also highlighted a practical limitation of the setup. Because silicon has a high thermal conductivity and a high thermal diffusivity, the temperature

oscillation of the heater becomes very small and approaches the noise level. This result showed that the success of a 3-ω measurement depends not only on the theoretical validity of the method, but also on the accessible signal level, the heater geometry, and the selected frequency window.

Development and Validation of the FEM Model

A second contribution is the development of a FEM model able to reproduce the 3-ω thermal response under controlled numerical conditions. A two-dimensional cross-sectional model was first used for validation, diagnostic simulations, and parametric studies. This 2D model was useful for comparing FEM results with analytical solutions and for understanding how parameters such as input power, heater width, and substrate thermal conductivity affect the measured response.

The FEM model was validated by comparison with analytical solutions for bulk substrates. The analytical self-consistency test showed that the slope method retrieves the input thermal conductivity when the assumptions of the analytical model are exactly satisfied. The FEM simulations of bulk borosilicate glass and silicon then showed deviations of only a few percent from the input values. These small differences are mainly explained by finite heater geometry, which is included in the FEM model but neglected in the ideal line-source analytical model.

The numerical study also showed that the input power does not affect the extracted thermal conductivity as long as the system remains in the linear regime. However, it affects the signal-to-noise ratio and must therefore be chosen carefully in experiments. The heater-width study confirmed that narrower heaters better satisfy the line-source approximation, while wider heaters can introduce stronger finite-width effects.

Limits of the Analytical Film-Extraction Method

The FEM model was then used to test the analytical extraction of a single film on a substrate. Two film/substrate systems were simulated: Parylene C on borosilicate glass and SiO_2 on silicon. In both cases, the analytical film-extraction method gave values close to the input film conductivity, with errors within approximately 10%. This confirmed that the method can be useful for simple film/substrate systems.

However, the simulations also showed that the error is systematic and originates from the assumptions of the analytical method. In particular, the film temperature drop is treated as one-dimensional, the heater is treated as an ideal line source, and the substrate response must be estimated separately. These assumptions become less accurate when the film and substrate responses are strongly coupled.

A parametric study on substrate thermal conductivity further clarified this point. The analytical film-extraction method becomes more accurate when the substrate thermal conductivity is much higher than the film thermal conductivity. In contrast, when the substrate conductivity is comparable to that of the film stack, the film and substrate contributions cannot be easily separated. This result is directly relevant to the final multilayer sample, where the fused-silica substrate has a thermal conductivity close to that of the dielectric layers. Therefore, the simple analytical subtraction method is not sufficient for the final sample.

Diagnosis of the Multilayer Inverse Problem

The core part of the thesis concerned the thermal characterization of a five-layer SiN_x/SiO_2 stack deposited on a fused-silica substrate. The stack contains several thin dielectric layers and multiple internal interfaces. A direct inverse approach, in which the thermal conductivity of each layer and the thermal boundary resistance of each interface are fitted independently, was first considered.

The frequency-dependent sensitivity analysis showed that this direct multi-parameter fitting problem is not well posed for the present data. The 3-ω signal is sensitive to the global thermal impedance

of the stack, but it does not contain enough independent information to uniquely separate all individual layer and interface contributions. In particular, different combinations of film thermal conductivity and interface resistance can produce similar surface temperature responses.

This result led to the use of an Effective Medium Approach (EMA). Instead of trying to extract several strongly correlated parameters, the multilayer stack was replaced by one equivalent layer with the same total thickness. The fitted parameter is then the effective cross-plane thermal conductivity of the complete stack, denoted by $\kappa_{\text{eff},\perp}$.

Validation of the Effective Medium Approach

The EMA was tested using virtual samples generated with FEM. A full multilayer model was first used to generate virtual data, and this data was then fitted using a single-layer EMA model. This virtual experiment showed that the EMA model can reproduce the thermal response of the full multilayer structure with one fitted effective parameter.

The virtual sample library further defined the range of applicability of the EMA. The fitted effective conductivity remains physically meaningful when the film stack does not act as a strong in-plane heat spreader, when the substrate does not dominate the response in the selected frequency range, and when the interface resistance does not completely control the heat flow. Outside this range, the fitted value may still reproduce the thermal response, but it should be interpreted more carefully as an apparent parameter describing the global heater-film-substrate response.

The alternative high-TBR interpretation was also tested. A high-TBR model can fit the experimental data, but this does not prove that the interfaces alone are responsible for the low effective conductivity. The result depends strongly on the film conductivities fixed in the model. The multi-TBR virtual fitting test showed that even in a noise-free numerical case, several interface resistances cannot all be retrieved uniquely. This supports the use of the EMA for the present dataset.

Final Effective Thermal Conductivity of the Multilayer Stack

Using the validated EMA model, the effective cross-plane thermal conductivity of the five-layer SiN_x/SiO_2 stack was extracted from the experimental data. The final value obtained from the two heater geometries is:

$$\kappa_{\text{eff},\perp} = 0.62 \pm 0.03 \text{ W.m}^{-1}\text{.K}^{-1}. \tag{5.13}$$

The uncertainty corresponds to the 95% confidence intervals obtained from the COMSOL parameter estimation procedure. The two heater widths gave close values, which supports the repeatability of the extraction.

This value is lower than the thermal conductivities generally reported for bulk or dense single-layer SiO_2 and SiN_x. The reduction is consistent with the combined influence of nanoscale effects, non-ideal PECVD film microstructure, possible density or stoichiometry variations, defects, and internal interfaces. The present measurement does not separate these contributions individually. Instead, it provides the effective thermal response of the complete multilayer stack under the present 3-ω measurement conditions.

Limitations of the Present Work

The methodology developed in this thesis provides a consistent way to characterize the effective thermal response of the studied multilayer stack. However, several limitations must be clearly stated.

— **Effective rather than layer-by-layer extraction.** The final reported value is an effective cross-plane thermal conductivity of the complete stack. It should not be interpreted as the intrinsic thermal conductivity of one individual layer. The 3-ω signal in the selected frequency range

does not provide enough independent information to uniquely separate the thermal conductivity of each layer and the thermal resistance of each interface.

— **Parameter correlation.** The film thermal conductivities and interface thermal resistances are strongly correlated in the inverse problem. A good numerical fit does not necessarily guarantee a unique physical parameter set. This limitation was confirmed by the multi-TBR virtual fitting test.

— **Model dimensionality and geometry.** The 2D FEM model was used for validation and parametric studies, while the final multilayer inverse fitting was performed using a 3D FEM model. Nevertheless, both models rely on idealized geometries, nominal layer thicknesses, and simplified descriptions of the heater and interfaces. Small deviations between the real sample and the modeled geometry may contribute to uncertainty in the extracted value.

— **Interface description.** Interfaces were represented using thermal boundary resistance values or, in the final EMA model, through their contribution to the effective stack response. The actual microscopic structure of the interfaces was not measured directly in this thesis. Therefore, the role of individual interfaces cannot be quantified independently from the present data alone.

— **Isotropic material assumption.** The dielectric films were treated as thermally isotropic. This assumption is reasonable as a first approximation for amorphous PECVD films, but deposition conditions may still induce anisotropy or depth-dependent properties. The present measurement mainly probes the cross-plane thermal response.

— **Room-temperature characterization.** The measurements were performed at room temperature. Since thermal conductivity can depend on temperature, additional measurements over a wider temperature range would be required to fully characterize the phonon transport mechanisms in the films.

— **Signal-to-noise limitation.** The attempted SiO_2/Si measurement showed that high-conductivity substrates can reduce the temperature oscillation to a level close to the noise floor. This limits the applicability of the present experimental setup for certain high-diffusivity substrates unless the signal level or detection sensitivity is improved.

Perspectives for Future Research

The results of this thesis suggest several directions for future work.

Application to Other Multilayer Dielectric Systems

The methodology developed here can be applied to other dielectric multilayer systems used in microelectronics and photonics. Potential examples include low-κ interlayer dielectrics, passivation stacks, oxide/nitride multilayers, and other insulating films used in device fabrication. For such systems, the EMA-based 3-ω analysis can provide an effective thermal parameter useful for device-level thermal modeling.

The approach may also be adapted to materials whose thermal properties change with processing conditions, such as PECVD films deposited at different temperatures, pressures, or gas compositions. Comparing their effective thermal conductivity could help connect deposition parameters with thermal performance.

Combination with Microstructural Characterization

A key next step would be to combine the thermal measurement with structural and chemical characterization. Techniques such as transmission electron microscopy, X-ray reflectometry, ellipsometry,

density measurements, or composition analysis could provide information on film thickness, density, stoichiometry, roughness, and interface quality.

Such information would help interpret the measured reduction in effective thermal conductivity. It would also make it possible to distinguish more clearly between different possible origins of the thermal resistance, such as low intrinsic film conductivity, imperfect interfaces, roughness, or density variations.

Temperature-Dependent 3-ω Measurements

Future work could extend the measurements to a wider temperature range. Temperature-dependent measurements would provide additional information on the dominant heat transport mechanisms in the PECVD films. For example, they could help identify whether the films behave like typical amorphous solids and whether a low-temperature plateau or other characteristic behavior appears in the thermal conductivity.

Such experiments would require adapting the current setup to a cryostat or a temperature-controlled stage while maintaining stable electrical contacts and low-noise 3-ω detection.

Improved Interface-Sensitive Test Structures

Although individual interface resistances could not be extracted uniquely from the present multi-layer sample, future test structures could be designed to improve interface sensitivity. One possibility is to fabricate a series of samples with the same materials but different numbers of interfaces, for example two-layer, four-layer, and six-layer stacks. Comparing their effective thermal responses could provide additional constraints on the average contribution of a given interface type.

Another possibility is to combine several heater widths or several frequency windows in a joint inverse fitting procedure. This may increase the amount of independent information available in the data and help reduce parameter correlation.

Extension to Anisotropic Thermal Conductivity

The methodology can also be extended to anisotropic thermal conductivity measurements. In thin films and multilayers, the in-plane thermal conductivity $\kappa_{\parallel}$ may differ from the cross-plane thermal conductivity $\kappa_{\perp}$. Heater width is an important parameter in this context. Narrow heaters enhance lateral heat spreading and therefore increase the influence of the in-plane thermal conductivity, whereas wider heaters promote a more one-dimensional heat-flow pattern through the film, making the extracted response predominantly governed by the cross-plane thermal conductivity.

By fabricating several heater widths on the same sample and fitting the data with an anisotropic FEM model, it may become possible to estimate both $\kappa_{\parallel}$ and $\kappa_{\perp}$. This would be particularly useful for crystalline films, textured layers, polymers, and multilayer systems with strong structural anisotropy.

Improvement of Measurements on High-Conductivity Substrates

The unsuccessful extraction from the SiO_2/Si sample showed that high-conductivity substrates require careful experimental design. Future work could focus on improving the signal-to-noise ratio for such systems. This may involve optimizing the heater geometry, increasing the stability of the bridge and lock-in detection, reducing parasitic harmonic distortion from the source, or improving shielding and grounding.

Numerical simulations including artificial noise could also be used to estimate the minimum signal level required for reliable extraction. This would help define the experimental conditions needed for thin films deposited on silicon or other high-diffusivity substrates.

Final Remarks

This thesis developed and validated a combined 3-ω and FEM methodology for the thermal characterization of dielectric thin films and multilayer systems. The main result is the extraction of an effective cross-plane thermal conductivity of: $\kappa_{\text{eff},\perp} = 0.62 \pm 0.03$ W.m^{-1}.K^{-1} for the studied five-layer SiN_x/SiO_2 stack.

This value should be understood as the effective thermal response of the complete multilayer stack, including the combined effects of the films and their interfaces. The work also shows that, for such complex structures, simple analytical methods and direct multi-parameter inverse fitting are not sufficient. A validated FEM-based effective-medium strategy provides a more reliable way to extract a physically meaningful thermal parameter from the measured 3-ω response.

The methodology developed in this thesis can serve as a basis for future studies of dielectric multilayers and other complex thin-film systems where heat transport is governed by the combined effects of nanoscale films, interfaces, and substrate coupling.

Appendix A

Numerical Verification of Effective Medium Theory (EMT)

1.1 Theoretical Background and Research Objectives

Effective Medium Theory (EMT) is a cornerstone for describing the macroscopic transport properties of composite materials based on their constituent phases. The treatment of electrical conductivity (σ) and thermal conductivity (κ) is well-established through Bruggeman-type symmetric models, A version of this relationship for a two-phase system is often expressed as:

$$\phi_1 \frac{P_1 - P_{eff}}{P_1 + (d-1)P_{eff}} + \phi_2 \frac{P_2 - P_{eff}}{P_2 + (d-1)P_{eff}} = 0, \tag{A.1}$$

where ϕ_i is the volume fraction of phase i, P_{eff} is the effective physical transport parameter of the whole composite, and P_i is the physical transport parameter of a constituent phase. For spherical inclusions in a three-dimensional matrix, the dimensionality factor is $d = 3$. There is no debate concerning the determination of thermal and electrical conductivities where the transport parameter is $P = \kappa$ and $P = \sigma$ respectively. The determination of the composite's effective Seebeck coefficient (S_{eff}) in the framework of the Effective Medium Theory remains a subject of theoretical refinement and ongoing discussion. The primary entry point for this study is the analytical framework derived by J. Sonntag [149, 150], which describes how the individual properties of each phase contribute to the total thermopower. As highlighted in recent academic commentary [151], a critical nuance in applying Eq. A.1 lies in the physical interpretation of the thermal conductivity parameter κ_i. According to the paper [150], the relevant physical parameter to describe the effective Seebeck coefficient is $P = \kappa/S$ where κ is the total thermal conductivity and the S the Seebeck coefficient.

In his response to the work of Vaney et al. [151], J. Sonntag argues that only the electronic contribution to the thermal conductivity (κ_e) should be utilized in the formula (A.1) instead, as it directly relates to the local coupling of electronic component of heat and electrical charge carriers. The corresponding transport parameter is then written $P = \kappa_e/S$ where κ_e corresponds to the electronic component of the thermal conductivity. The inclusion of the lattice thermal component (κ_L), which does not carry electric charge, is proposed as a primary source of discrepancy between EMT predictions and experimental observations in certain composite systems. This view was reiterated in a more recent article [92]. The objective of this appendix is to provide a rigorous numerical cross-validation of these transport parameters using the Finite Element Method (FEM). By implementing a 3D representative volume elements (RVE) in COMSOL Multiphysics ®, we aim to provide an objective assessment of the theory without pre-existing bias toward a specific analytical assumption. The goals of this study are:

— **Extract "Ground Truth" Values:** Simulate the effective transport parameters (σ_{eff}, κ_{eff}, and S_{eff}) of a composite through direct calculation of local flux densities.

— **Conduct Parameter Sensitivity Analysis:** Compare the numerical FEM results against EMT models calculated using both the total thermal conductivity (κ_{tot}) and the electronic component only (κ_e).

— **Validate Mixture Laws:** Assess the accuracy of classical analytical limits (such as series and parallel models) in describing the behavior of heterogeneous thermoelectric materials.

Through this side-by-side presentation of analytical and numerical results, we aim to document the predictive limits and the sensitivity of Effective Medium Theory in the context of phase-separated thermoelectric alloys.

1.2 Structure of the Model

The numerical verification was implemented using the Finite Element Method (FEM) within the COMSOL Multiphysics ® software environment. The primary objective of the FEM model is to simulate local flux densities to extract effective transport parameters—namely the Seebeck coefficient, thermal conductivity, and electrical conductivity—for comparison with Effective Medium Theory (EMT) predictions. The detailed implementation steps are described below.

Geometry and Stochastic Modeling: To accurately represent a phase-separated alloy, a 3D Representative Volume Element (RVE) containing random, non-overlapping spherical inclusions was constructed. The generation of this sphere layer was automated using Java programming within the COMSOL Application Builder, ensuring a truly stochastic distribution of the filler phase. This sphere structure was then imported into the respective simulation modules. Additional components, such as gold coatings placed at the top and bottom boundaries, were modeled using COMSOL's CAD capabilities to act as ideal thermal and electrical contractors.

Materials and Parameters: The material properties for the matrix and filler were defined based on the high-contrast parameters required for rigorous EMT validation, as summarized in Table A.1. The chosen parameters are those used in ref. [91] to model the thermoelectric parameters with a Random Resistor Network, except for the thermal conductivity where a larger span was selected. The gold electrodes utilized standard values from the COMSOL Material Library.

Table A.1 – Parameters used in the FEM simulation and in the EMT model.

Parameters	**Matrix**	**Filler**
Electrical conductivity (S/m)	1×10^{4}	1×10^{-4}
Seebeck coefficient (V/K)	1×10^{-6}	1×10^{-4}
Thermal conductivity (W/(m·κ))	34	1.13

Physics and Multiphysics Coupling: The model accounts for the coupled transport of heat and charge. Depending on the specific property under investigation, simulations utilized the *Heat Transfer in Solids* and *Electric Currents* interfaces, coupled through the *Thermoelectric Effect* multiphysics node. This allows for the simultaneous resolution of Fourier's law and Ohm's law, incorporating the cross-coupling terms necessary for Seebeck coefficient extraction.

1.2.1 The Size of the Model

The geometry consists of a bulk matrix with dimensions of 1000 µm × 1000 µm × 500 µm. Two gold probes (1000 µm × 1000 µm × 50 µm) are located at the top and bottom surfaces to serve as

interface contractors. Inside the matrix, spherical filler particles with a radius of 50 µm are randomly distributed. The number of particles is dictated by the specific volume fraction (ϕ) being studied. The distribution of these random and non-overlapping spheres is shown in Figure A.1. For the 3D domain, a Free Tetrahedral mesh was employed. To capture the steep potential and temperature gradients at the phase interfaces, a custom-decided refinement was applied to the mesh size (Figure A.2).

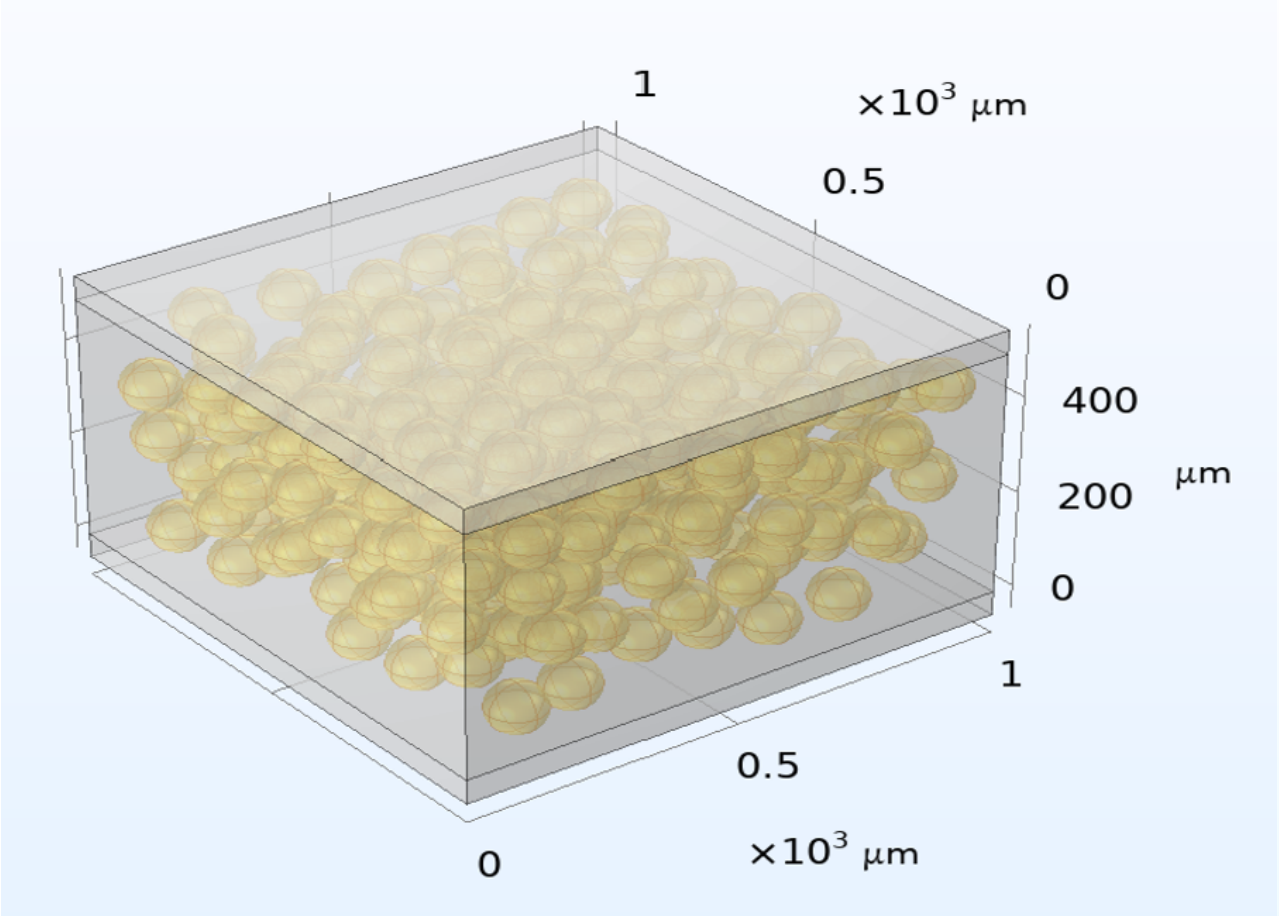


Figure A.1 – The random and non-overlapping spheres inside the bulk.

1.2.2 Seebeck Coefficient Simulation

The method used to determine the effective Seebeck coefficient (S_{eff}) was based on simulating the open-circuit voltage difference induced by a temperature gradient across the random sphere structure (Figure A.3).

Boundary Conditions: A stationary study was performed where a temperature gradient was established between the two gold probes. The top probe temperature was set to $T_{hot} = 343.15\,\text{K}$, while the bottom probe was maintained at $T_{cold} = 293.15\,\text{K}$, resulting in a ΔT of 50 K. To ensure the measurement of the Seebeck effect under open-circuit conditions, the Normal Current Density was set to zero on the top terminal, while the bottom terminal was grounded ($V = 0$). The lateral sides of the RVE were set to be thermally and electrically insulated to enforce a one-dimensional macroscopic flux.

Data Extraction and Calculation: The simulation utilized the *Heat Transfer in Solids* and *Electric Currents* physics nodes, coupled via the thermoelectric effect. All results were obtained at a steady

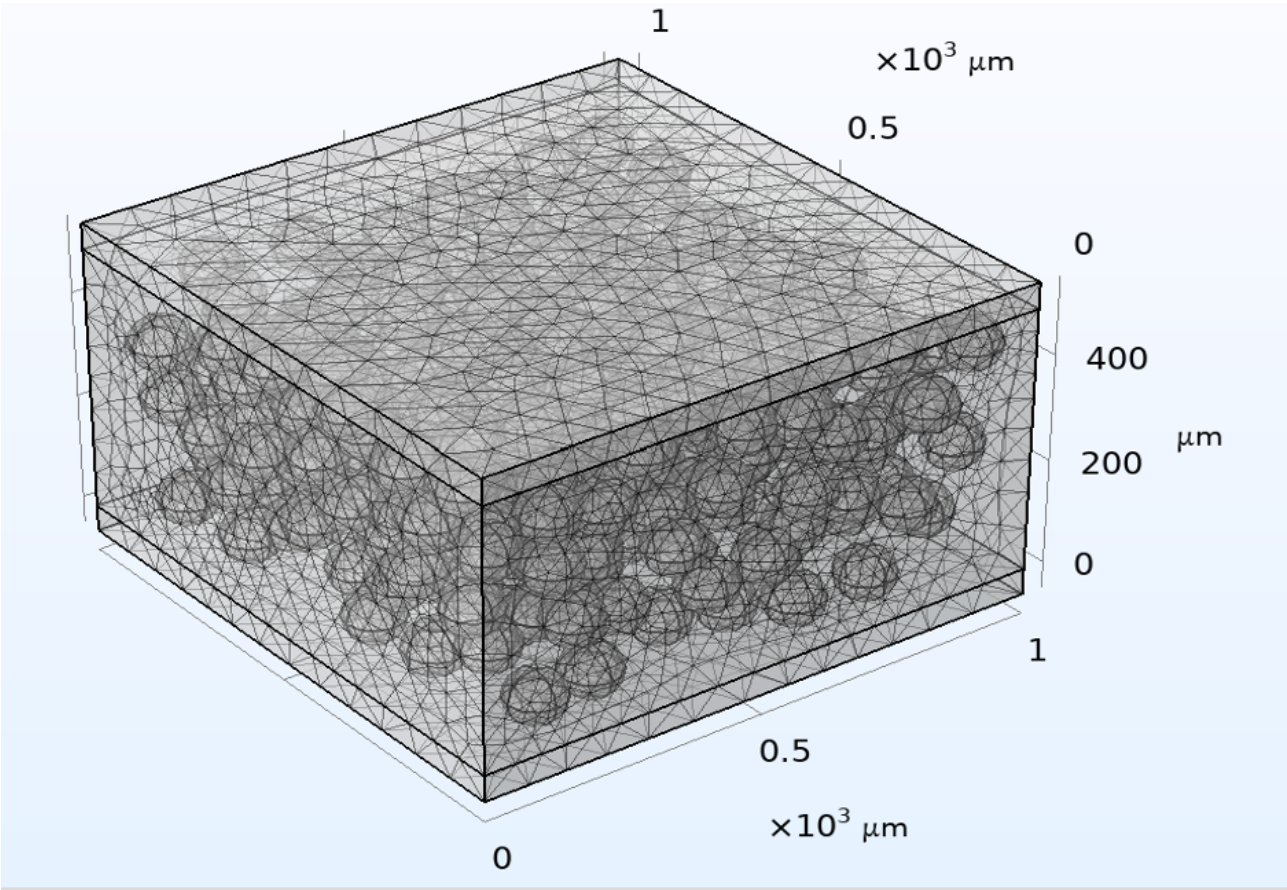


Figure A.2 – The meshing of random and non-overlapping spheres inside the bulk.

state. To calculate the effective Seebeck coefficient, data sets for the electric potential (V) and temperature (T) were extracted along the longitudinal axis from the top to the bottom of the bulk matrix.As shown in Figure A.4, a linear relationship between the local electric potential and temperature was observed. The effective Seebeck coefficient was then determined from the slope of this distribution using Equation A.2:

$$S_{eff} = -\frac{\Delta V}{\Delta T} \tag{A.2}$$

where ΔV is the induced voltage difference and ΔT is the applied temperature difference. This numerical approach provides a direct measure of the composite's thermopower without requiring a priori assumptions about the weighting of the constituent phases.

1.2.3 Thermal Conductivity Simulation

The method used to determine the effective thermal conductivity (κ_{eff}) was based on simulating the steady-state heat flux through the composite structure (Figure A.5). A known heat flux was applied to the RVE, and the resulting temperature gradient was used to back-calculate the effective conductivity.

Boundary Conditions and Physics: The simulation utilized the *Heat Transfer in Solids* physics node. A constant Heat Flux of $q = 3000\,\mathrm{W/m^2}$ was applied to the top probe. For the bottom probe, a Convective Heat Flux boundary condition was implemented with a heat transfer coefficient of $h = 3\,\mathrm{W/(m^2{\cdot}K)}$. The lateral sides of the structure were set to be thermally insulated to ensure that the heat flow remains parallel to the vertical axis.The simulation accounts for the total thermal conductivity of each phase. It is worth noting that while FEM calculates the total heat transport,

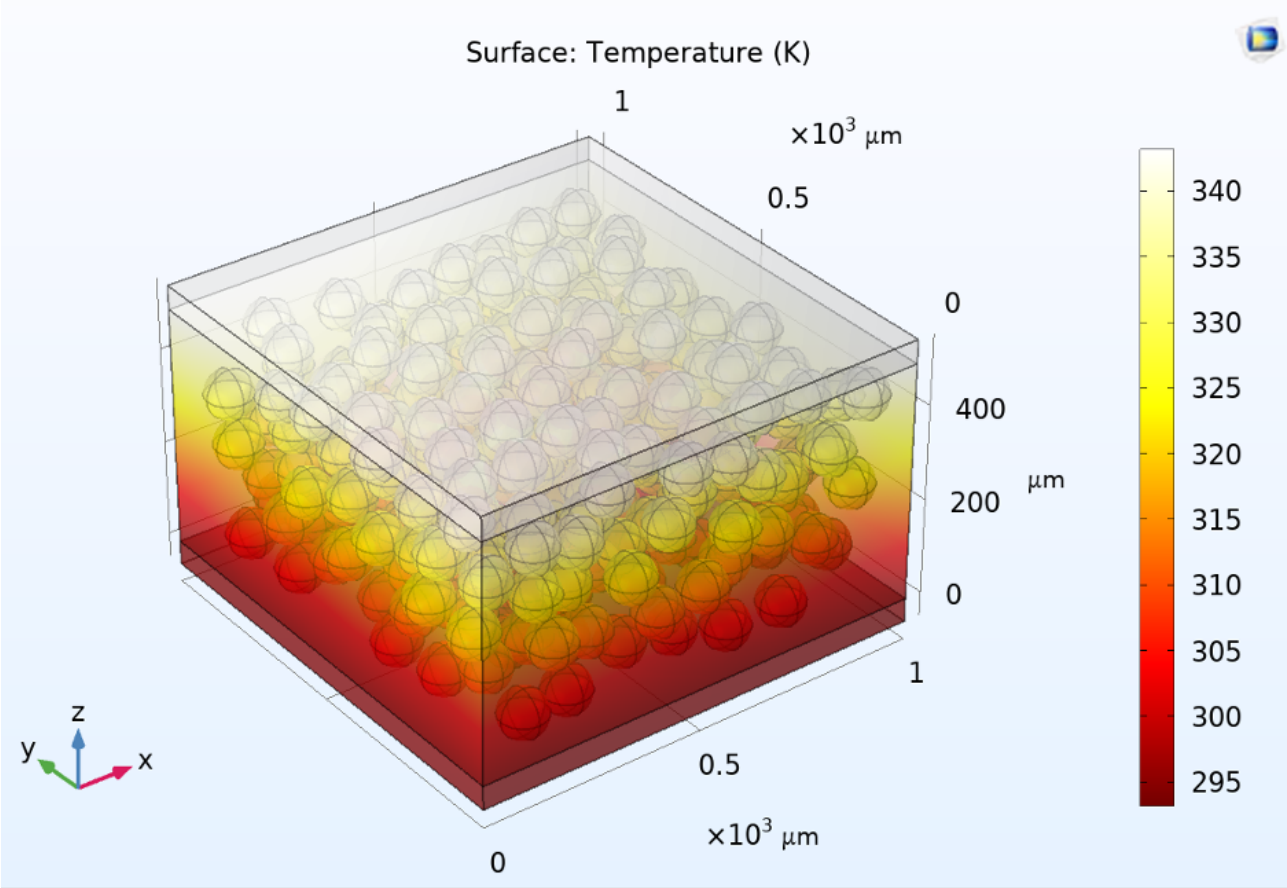


Figure A.3 – 3D geometry and boundary condition setup for the Seebeck coefficient simulation.

the resulting κ_{eff} serves as the benchmark to evaluate the EMT models discussed in Section A, particularly regarding the role of electronic vs. lattice contributions.

Observation and Calculation: As shown in Figure A.5, the core temperature of the spherical inclusions reflects their spatial proximity to the heat source; spheres closer to the top edge exhibit higher temperatures. The temperature distribution remains relatively uniform within the core of each sphere due to the local thermal equilibrium. All results were obtained at a steady state. Temperature data was extracted along the depth of the bulk, and Figure A.6 shows the temperature variation per unit length. The effective thermal conductivity was extracted from the slope of this distribution using the 1D Fourier's Law expression (Equation A.3):

$$\kappa_{eff} = \frac{Q}{A \cdot (\Delta T / \Delta L)} \tag{A.3}$$

where Q is the total heat flux in Watts, A is the cross-sectional area, and $\Delta T/\Delta L$ represents the temperature gradient across the depth of the bulk matrix.

1.2.4 Electrical Conductivity Simulation

The method used to determine the effective electrical conductivity (σ_{eff}) was based on simulating the steady-state current density and electric potential distribution through the random sphere structure.

Boundary Conditions and Physics: The simulation was performed using the *Electric Currents* physics node. To establish a controlled potential gradient, the top probe was defined as a Terminal with a specified current of $I = 1\,\text{A}$. The bottom probe was set as the Ground ($V = 0$). Similar

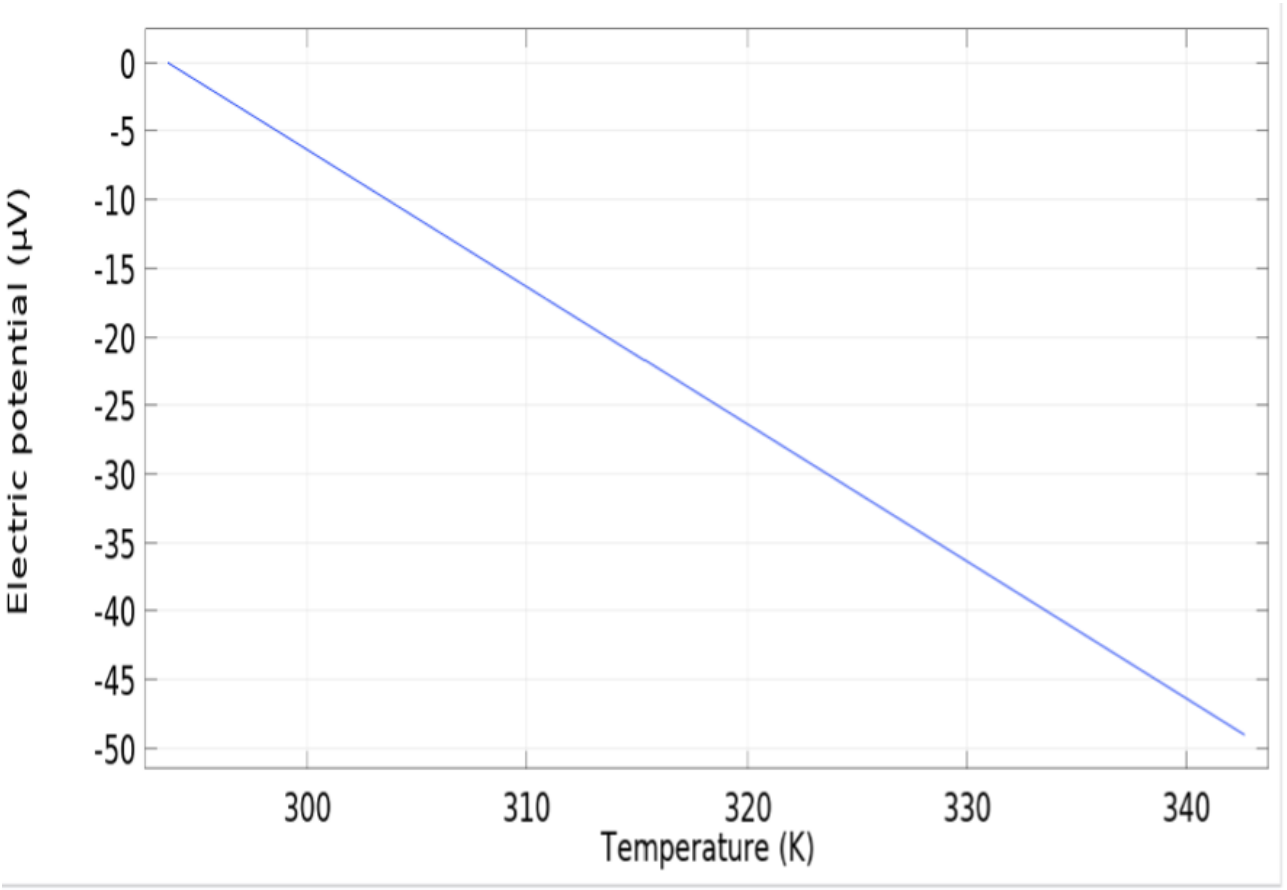


Figure A.4 – FEM simulated effective electric potential vs. temperature. The linear slope represents the extracted effective Seebeck coefficient.

to the previous simulations, the lateral boundaries of the RVE were set to electrical insulation to ensure a one-dimensional current flow along the longitudinal axis. Figure A.7 illustrates the resulting distribution of electric potential within the composite.

Data Extraction and Calculation: The electrical resistance (R) of the entire structure was obtained by evaluating the global voltage at the terminal using COMSOL's Derived Values and Global Evaluation tools. Once the resistance was extracted, the effective electrical conductivity was calculated by substituting the geometric parameters and the resistance value into the following equation:

$$\sigma_{eff} = \frac{L}{R \cdot A} \tag{A.4}$$

where σ_{eff} is the effective electrical conductivity in S/m, R is the extracted resistance in Ohms, L is the length of the bulk matrix in meters, and A is the cross-sectional area in m^2. This method allows for a direct correlation between the internal microstructural distribution and the macroscopic electrical response.

1.3 Data Analysis and Discussion

In this section, the effective parameters calculated via EMT using Scilab are compared against the numerical results obtained from the FEM simulations as a function of the filler loading fraction (ϕ).

Conductivity Comparison (κ and σ): Figure A.8 illustrates the evolution of the effective thermal conductivity. Due to the high computational cost associated with resolving a large number of stochastic

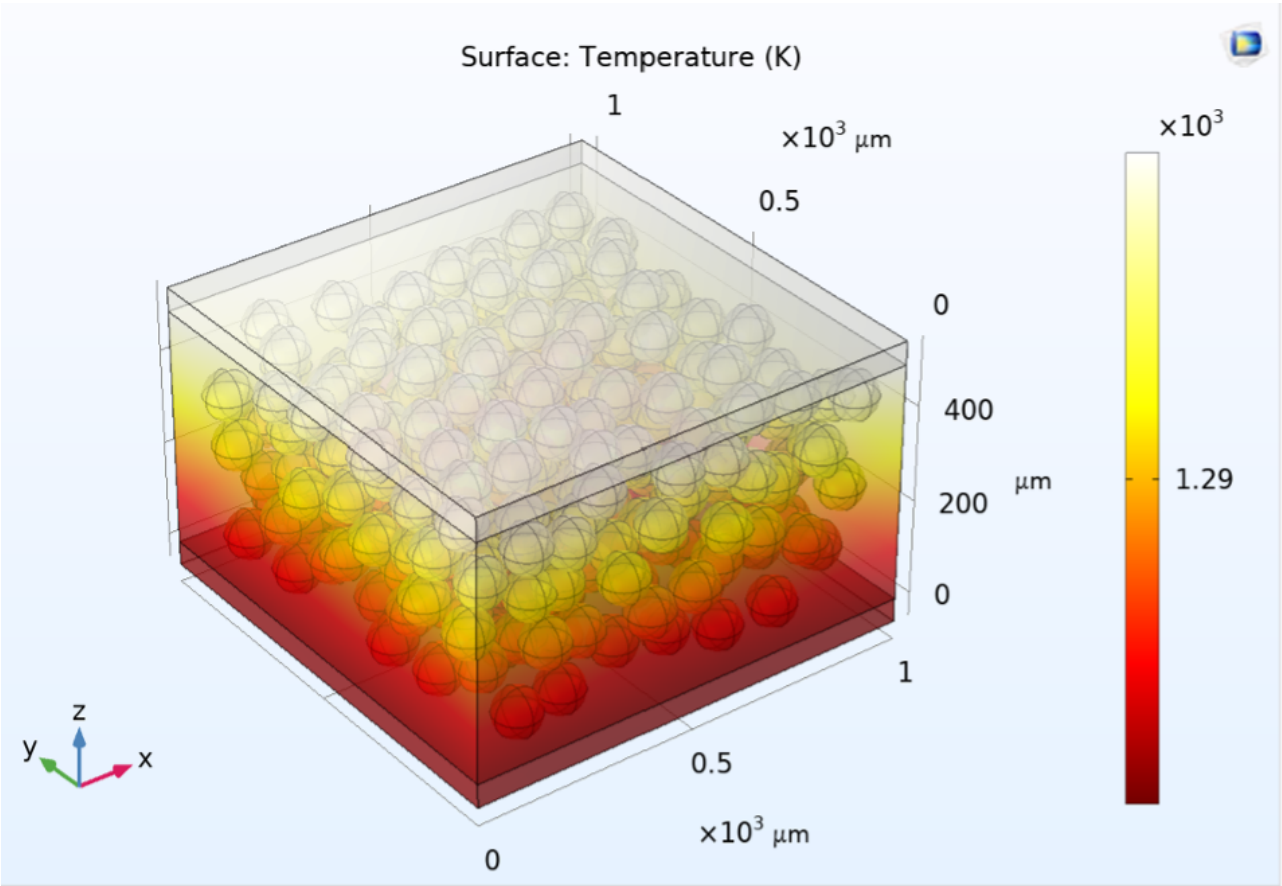


Figure A.5 – 3D temperature distribution simulation for the effective thermal conductivity calculation.

inclusions, direct simulations were performed for volume fractions up to $\phi = 0.3$. For the high-loading regime ($\phi = 0.7$ to 1.0), a property-exchange method was employed. As shown in the zoom-in views (Figure A.9) and the corresponding difference plots (Figure A.10), the discrepancy between the FEM and EMT results for thermal conductivity appears to be randomly distributed. In contrast, the electrical conductivity results (Figures A.11–A.13) show that the deviation between the two methods tends to increase with the filler loading fraction, suggesting a higher sensitivity of the electrical flux close to the percolation of the filler phase.

Seebeck-Related Ratios and Modeling Uncertainties: The core of the investigation involves the ratios σ/S and κ/S, which serve as the weighting factors in the Sonntag EMT formulation. The term σ/S is used in place of κ_e/S because κ_e is direcly proportional to σ according to the Wiedmann-Franz law. The comparison between FEM and EMT for these ratios is presented in Figures A.14–A.19. Our analysis reveals that the discrepancy observed for the σ/S ratio is almost entirely dominated by the underlying deviations in electrical conductivity. Similarly, the variations in the κ/S ratio are dominated by the thermal conductivity deviations. One solution to reduce the effect of FEM simulated conductivity errors on Seebeck coefficient calculation is plotting directly this quantity as obtained by FEM and from EMT formulas. Figure A.20 shows loading fraction dependence of the Seebeck coefficient simulated by FEM compared to the value calculated by EMT. This operation was processed in two fold. First, the ratio σ/S is calculated from eq. A.1 as a function of the loading fraction. Secondly, filler fraction dependence of the electrical conductivity σ is also obtained from eq. A.1. Finally, effective Seebeck coefficient values are obtained from the ratio of σ by σ/S. The same approach was followed considering κ/S as the relevant transport parameter for calculating the Seebeck coefficient, the results are depicted fig.A.21. Both evolutions depict a steep increase of the Seebeck coefficient at 2/3 loading fraction, called later "transition". Relative errors between FEM and

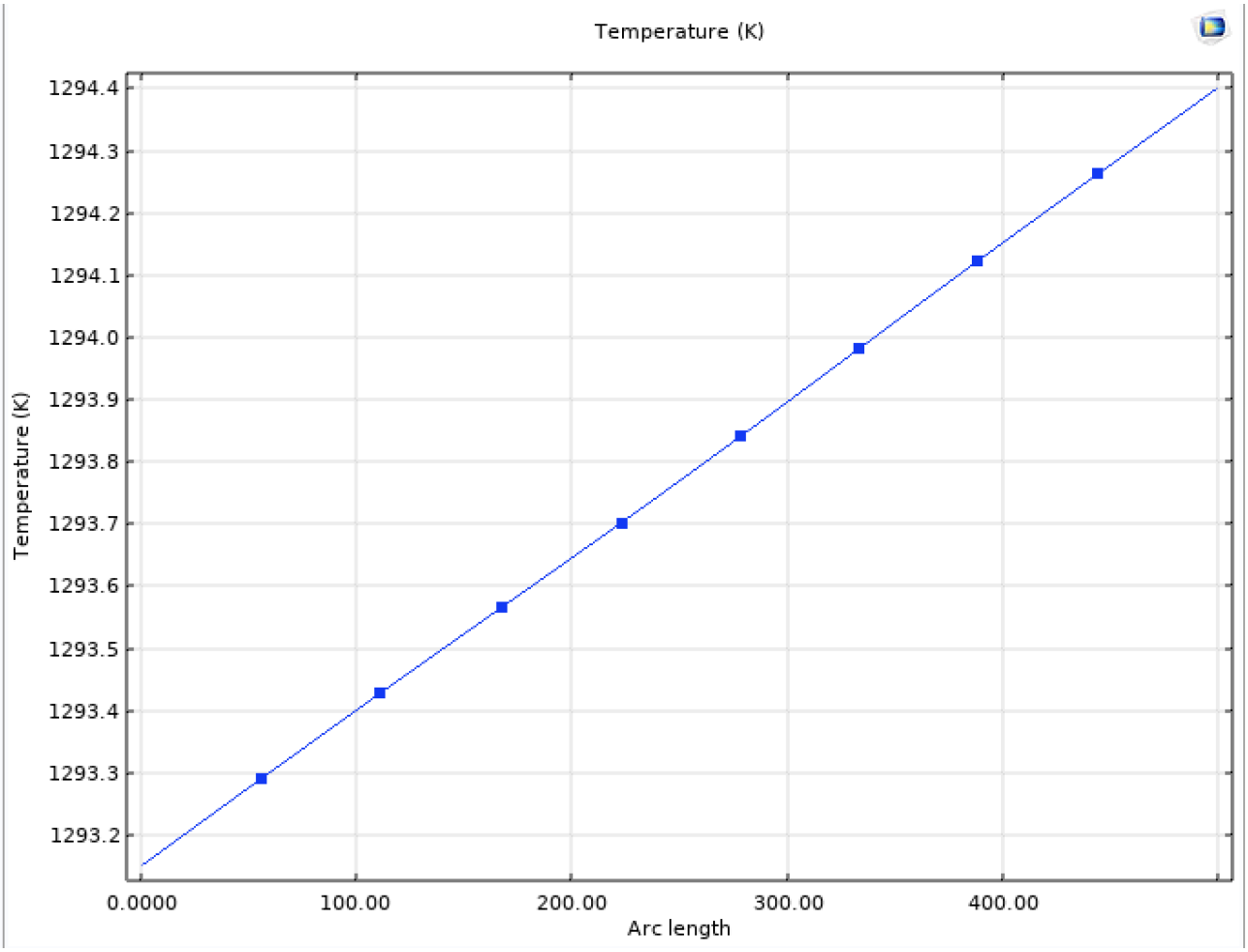


Figure A.6 – The extracted temperature vs. length profile from the thermal conductivity simulation. The slope is used to determine the effective thermal conductivity.

EMT, assuming σ/S, then κ/S as relevant transport parameters for simulating the Seebeck coefficient are shown fig. A.22.

Based on these preliminary results, using the ratio σ/S as written by Sonntag in references [151] and [92] give the most reliable results in comparison with the FEM approach, (at least for this set of thermoelectric parameters) given in table A.1, at low loading fraction and at the vicinity of the Seebeck coefficient "transition". For the highest loading fraction κ/S gave a better results as compared to FEM predictions. EMT model gives its highest relative error close to the transition.

Future Work and Computational Outlook: This appendix presents a preliminary verification of the complex transport behavior in composites. Future research will focus on the following enhancements:

— **Geometric Optimization:** Transitioning from spherical inclusions to ellipsoidal models to better represent the real morphology of phase-separated fillers and especially highlighting the percolation phenomena.

— **Computational Expansion:** Utilizing high-performance computing (HPC) clusters to bridge the current simulation gap in the mid-range volume fractions ($\phi = 0.3$ to 0.7).

— **Dimensionality Analysis:** Exploring 2D simulations as an alternative to further investigate the sensitivity of the three thermoelectric parameters.

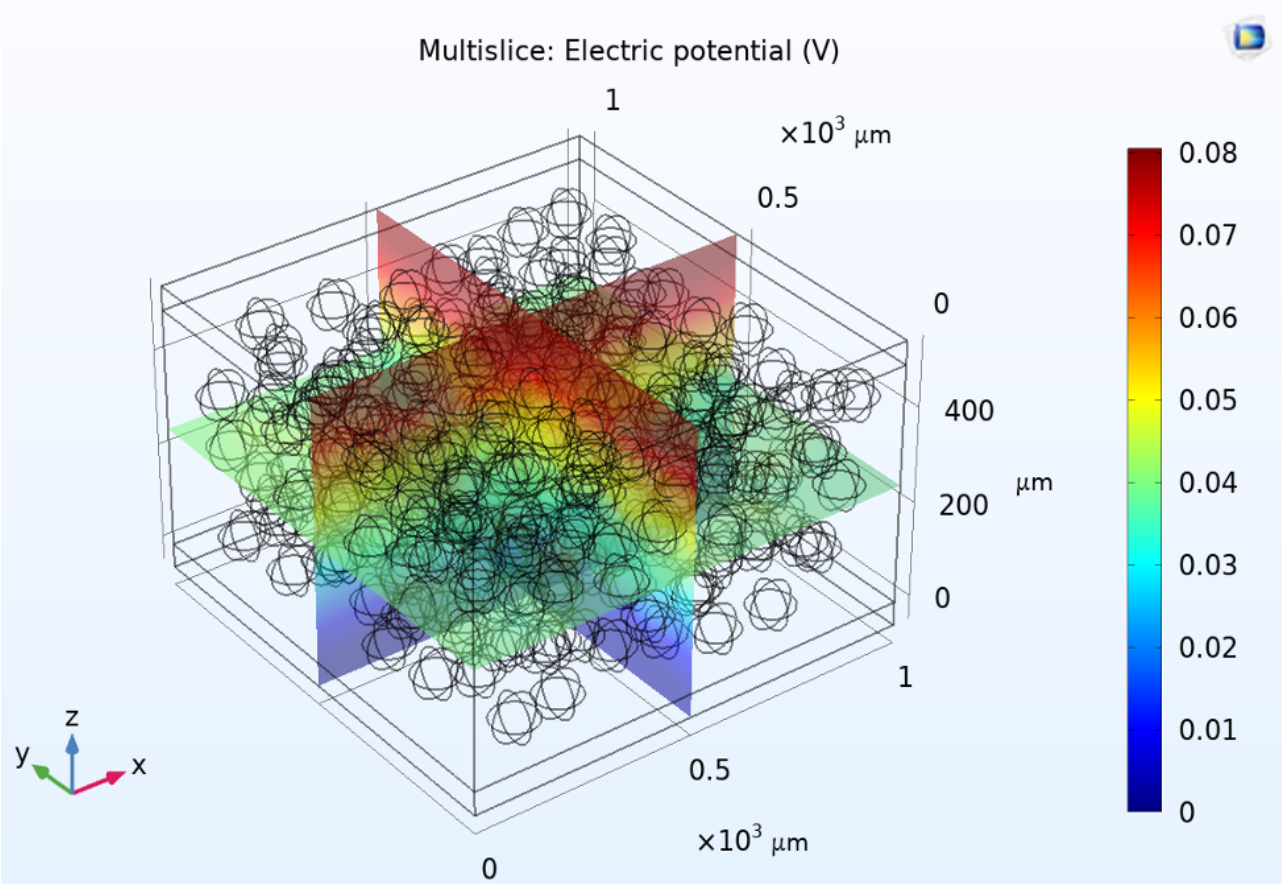


Figure A.7 – 3D electric potential simulation profile for the effective electrical conductivity calculation.

1.4 Summary of Preliminary Work

The COMSOL simulations of Effective Medium Theory presented in this appendix highlight the inherent challenges in modeling large-scale, stochastic composite systems. While the current data provides a clear visualization of the potential deviations in EMT weighting factors, the results in the $\phi \in [0.3, 0.7]$ range remain necessary for a complete reliable conclusion. Nonetheless, this work establishes a robust numerical framework for the ongoing validation of thermoelectric transport theories in heterogeneous media.

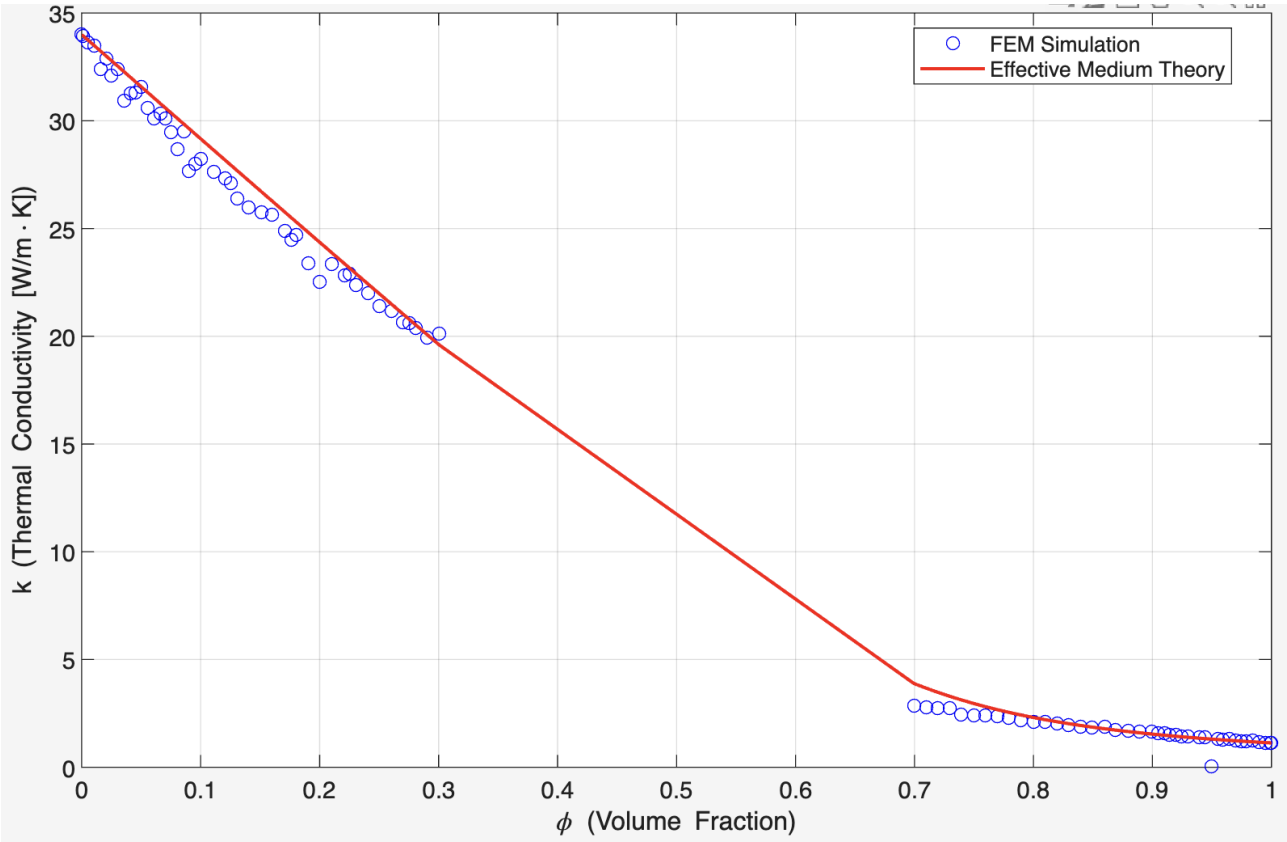


Figure A.8 – Filler loading fraction of the effective thermal conductivity calculated by FEM (blue circle) and by EMT (red line).

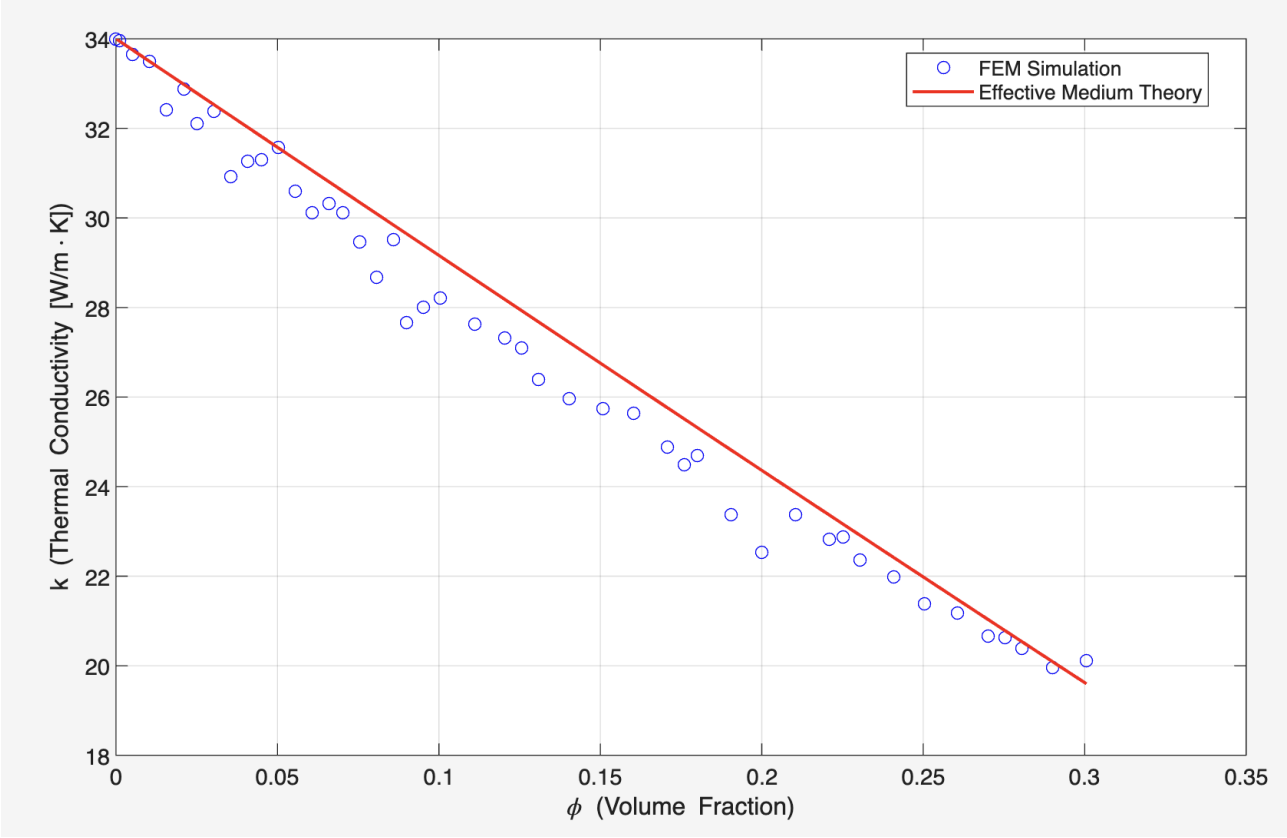


Figure A.9 – A zoom of Figure A.8.

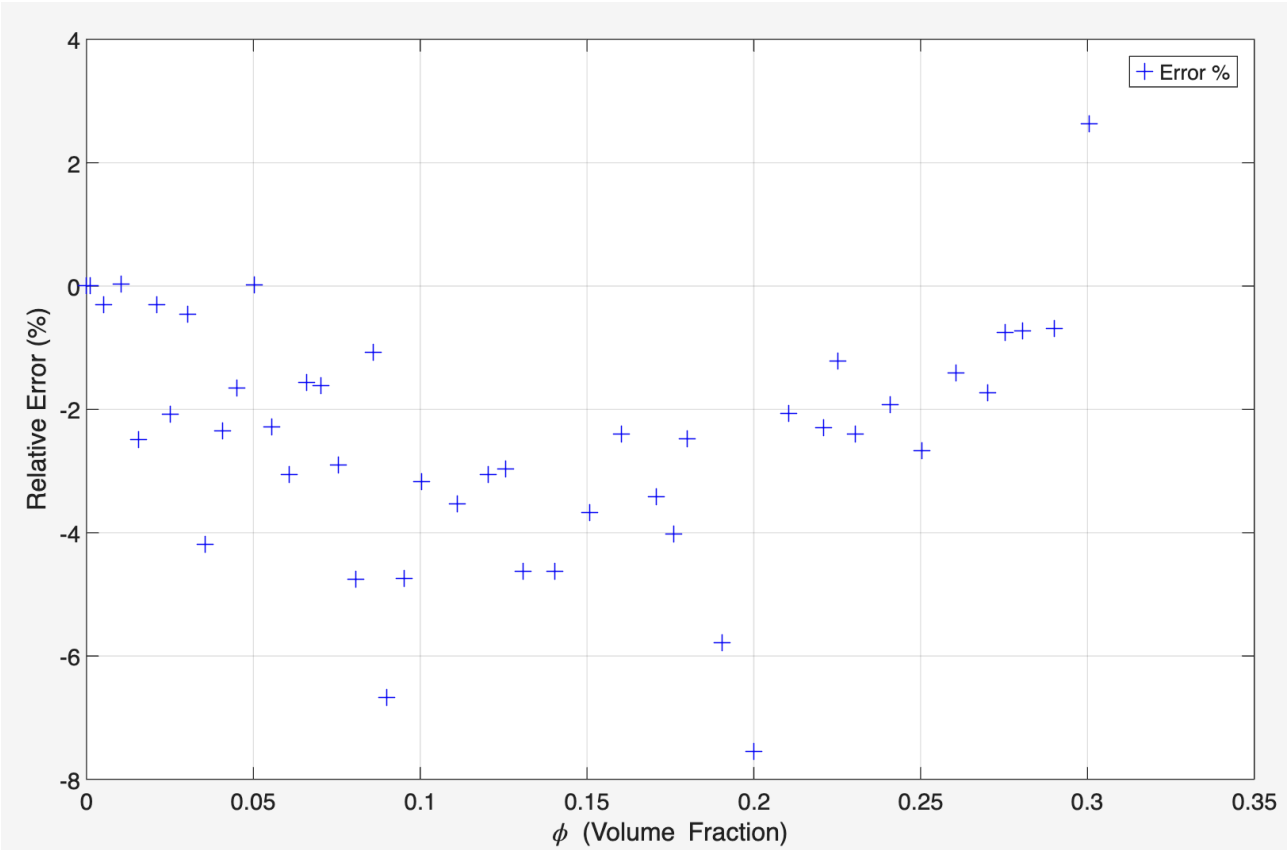


Figure A.10 – Difference calculated from Figure A.9 between the effective thermal conductivity calculated by FEM and EMT.

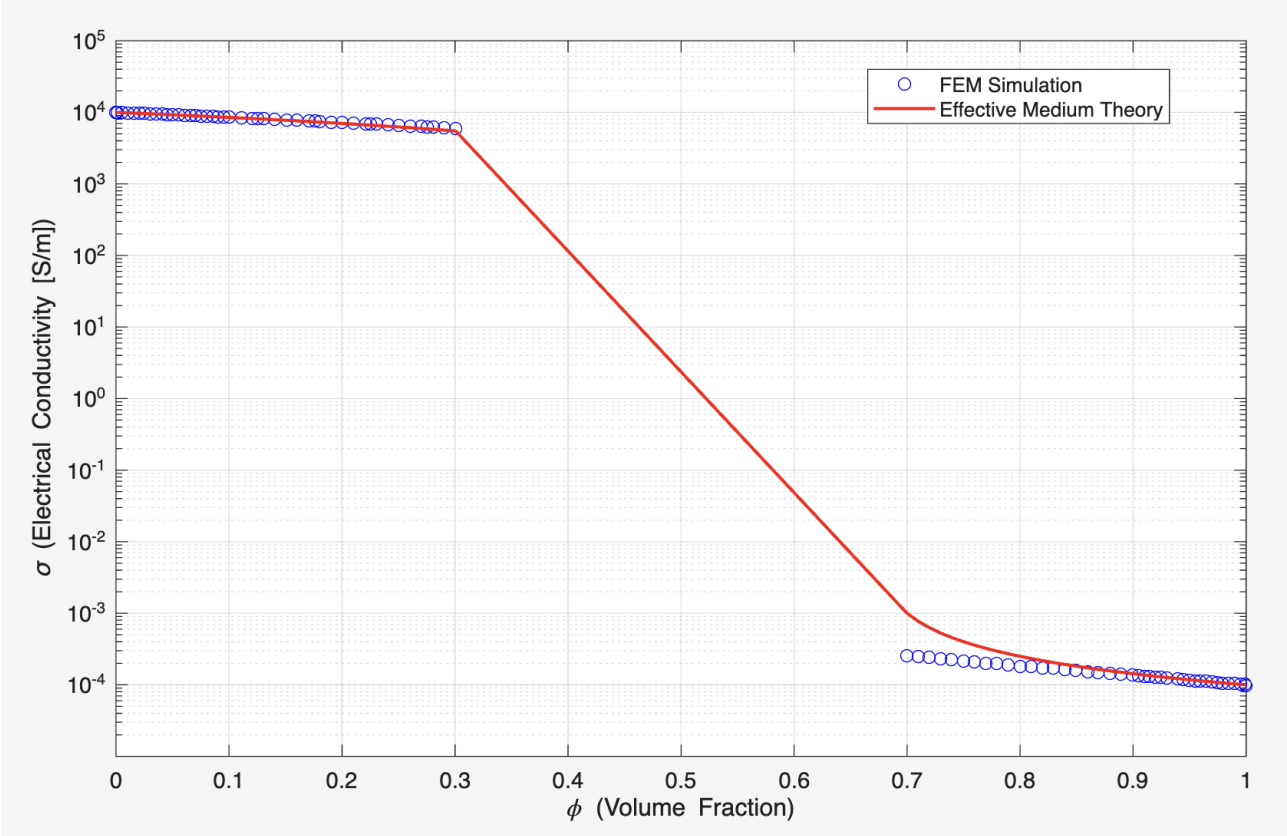


Figure A.11 – Filler loading fraction of the effective electrical conductivity calculated by FEM (blue circle) and by EMT (red line).

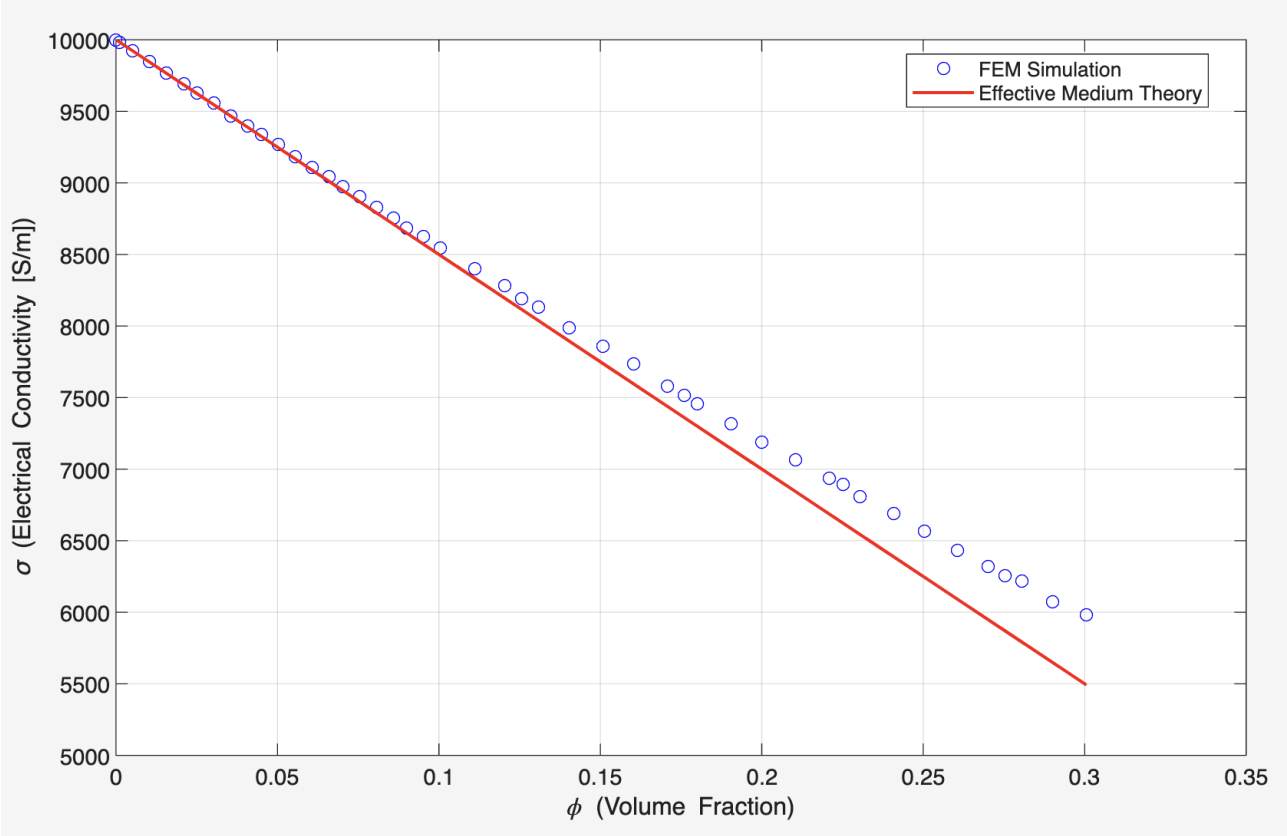


Figure A.12 – A zoom of Figure A.11.

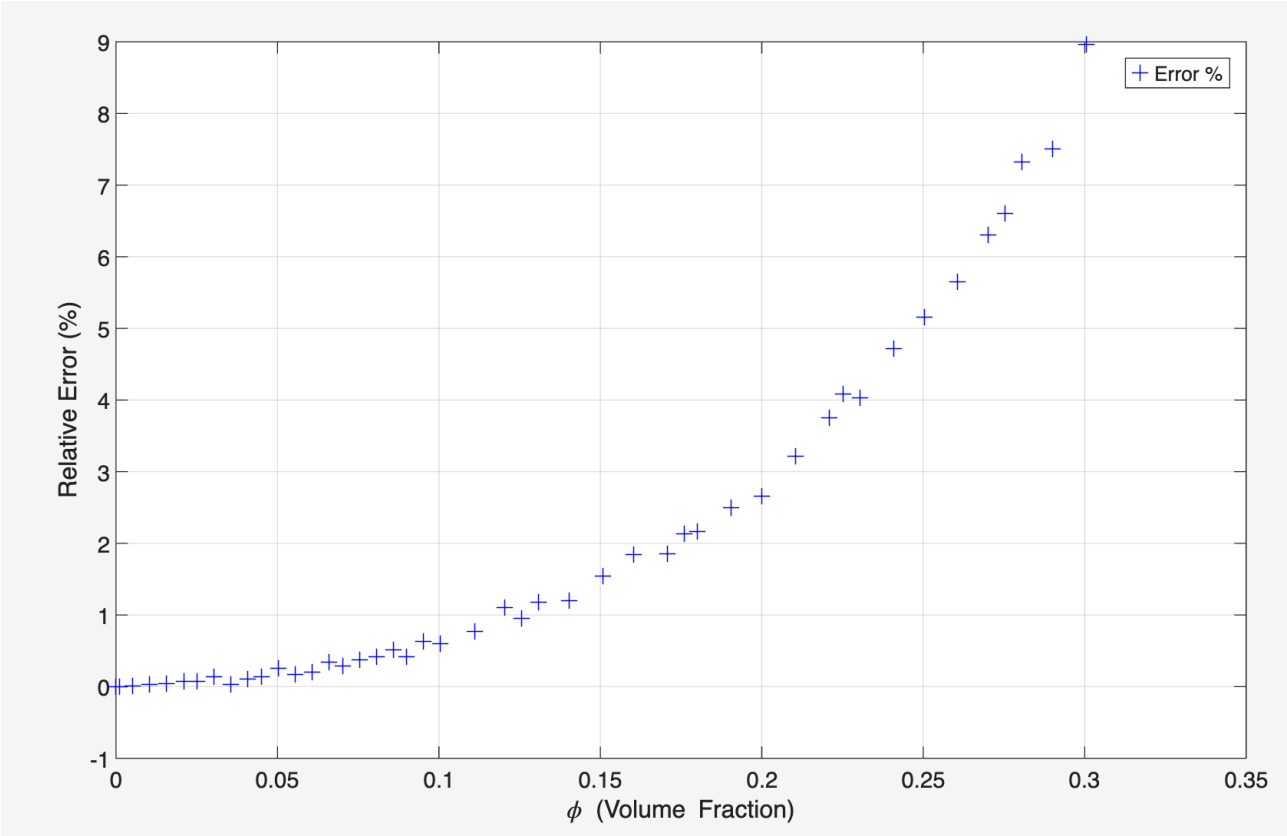


Figure A.13 – Difference calculated from Figure A.12 between the effective electrical conductivity calculated by FEM and EMT.

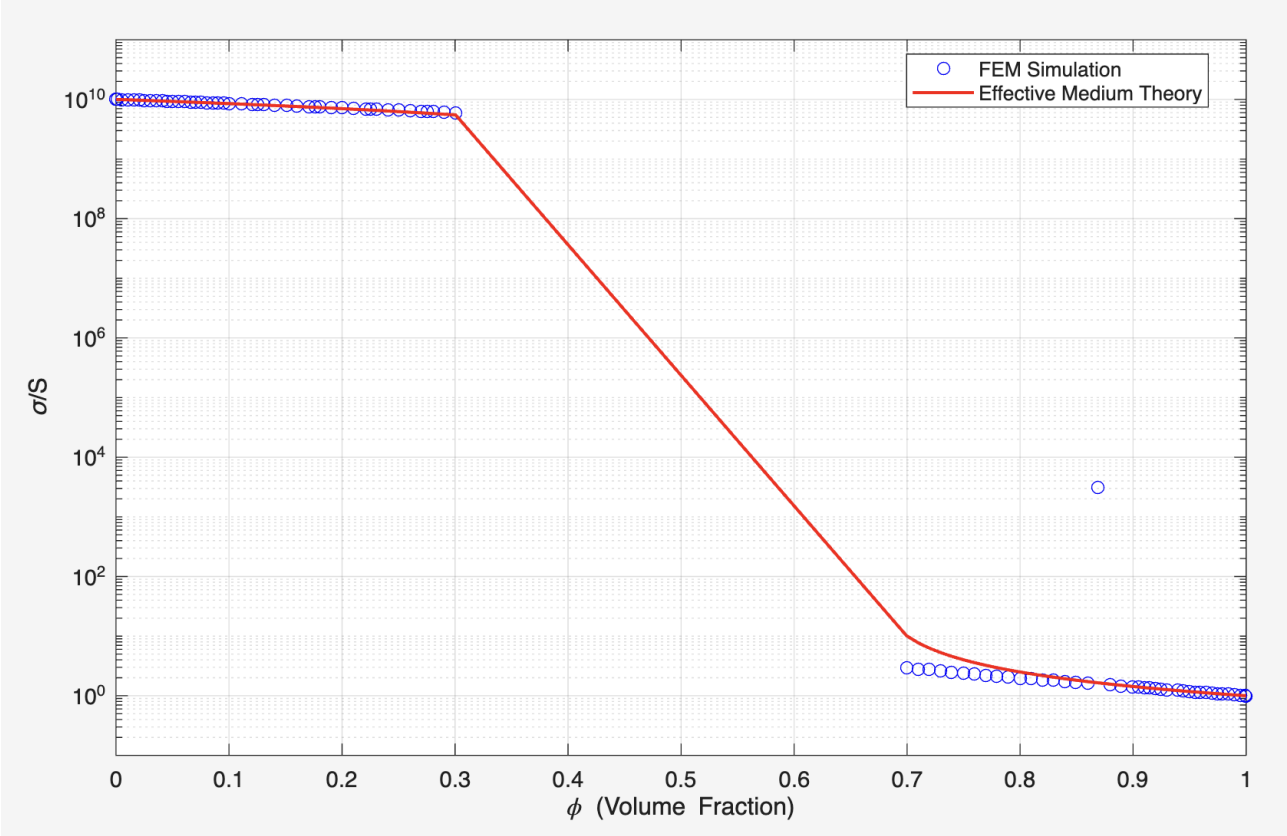


Figure A.14 – Filler loading fraction of the effective ratio electrical conductivity by Seebeck coefficient calculated by FEM(blue circle) and EMT(red line).

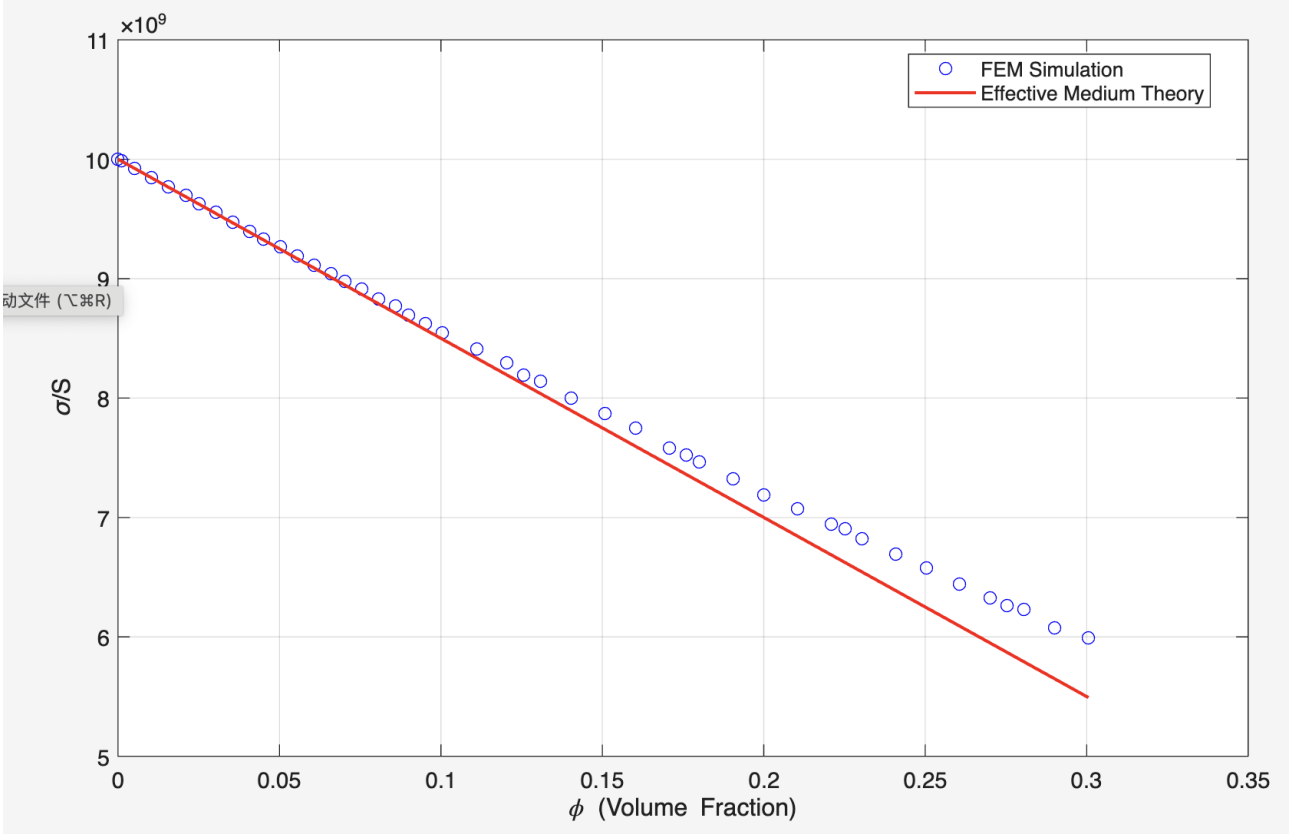


Figure A.15 – A zoom figure of A.14.

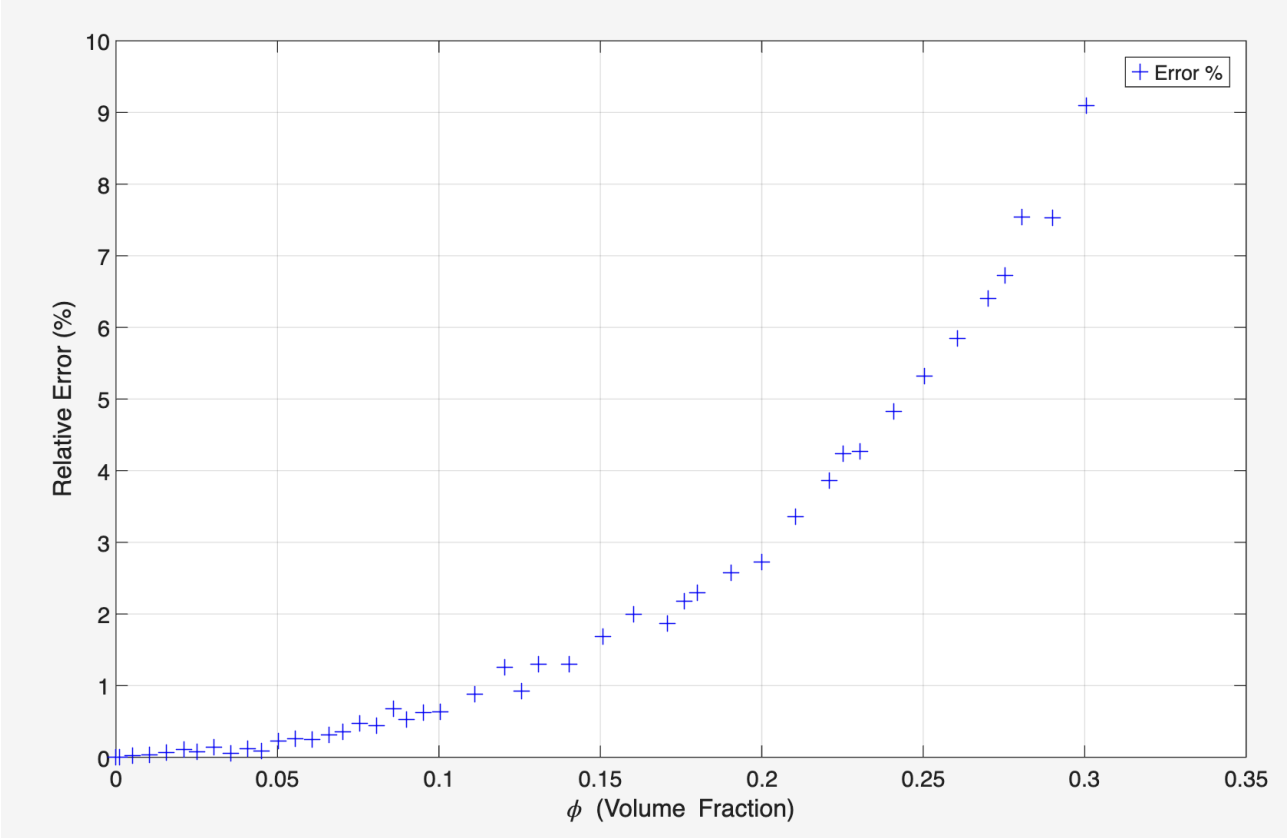


Figure A.16 – Difference calculated from Figure A.15 between the effective ratio electrical conductivity by Seebeck coefficient calculated by FEM and EMT.

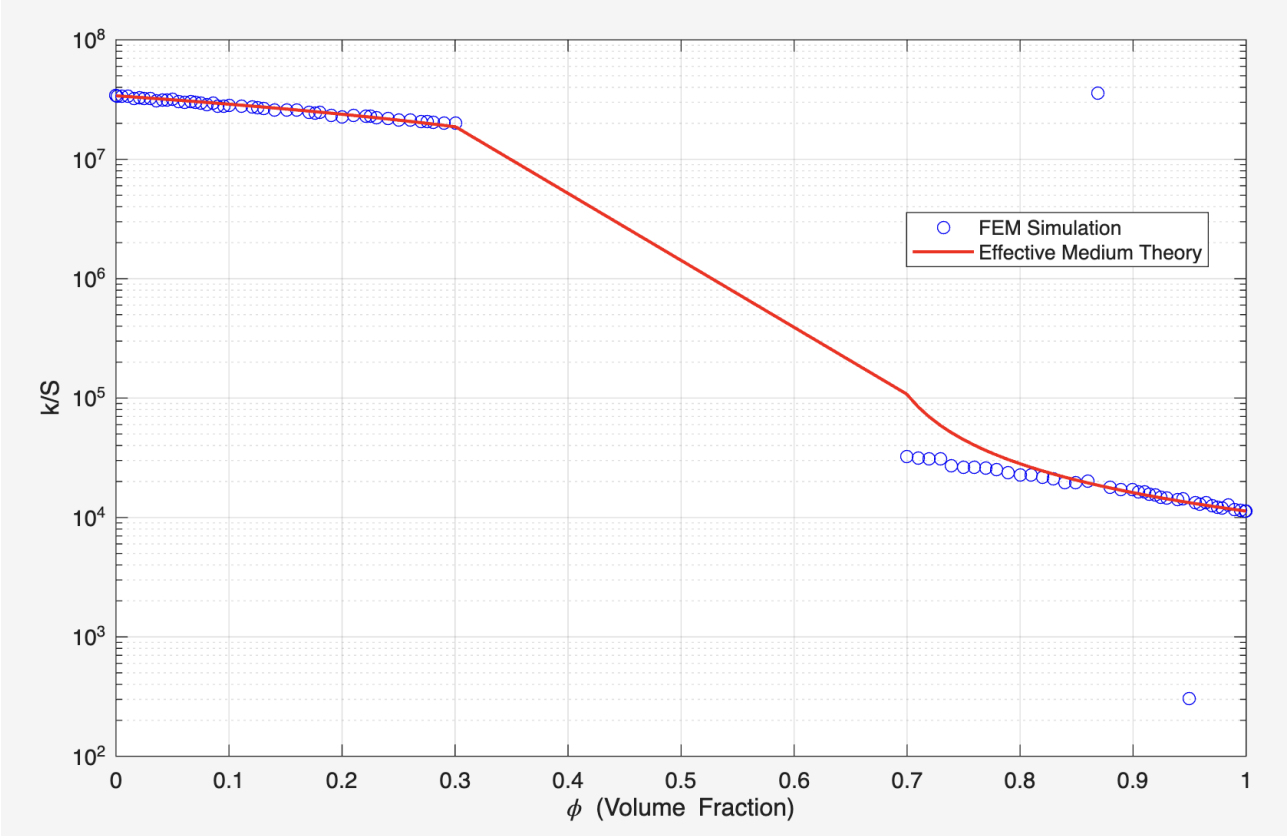


Figure A.17 – Filler loading fraction of the effective ratio thermal conductivity by Seebeck coefficient calculated by FEM(blue circle) and EMT(red line).

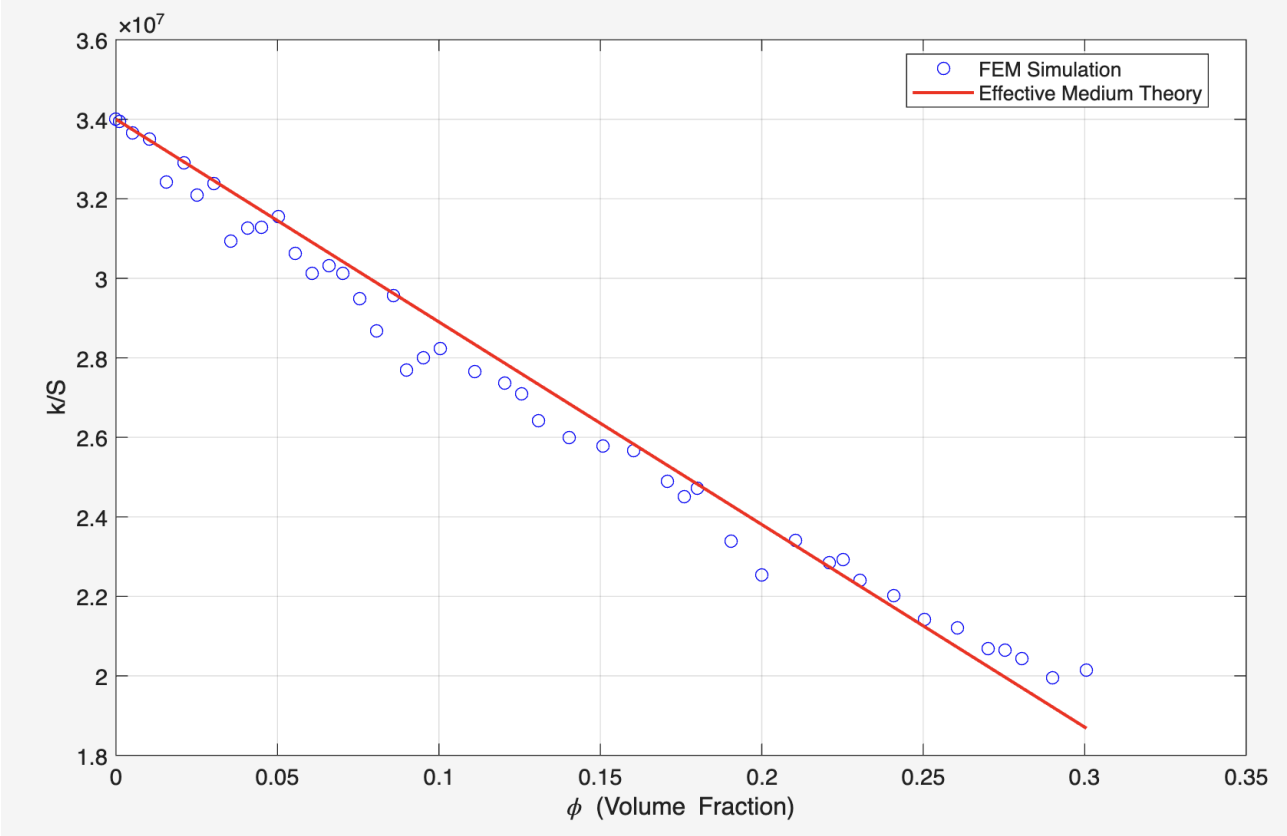


Figure A.18 – A zoom figure of A.17 .

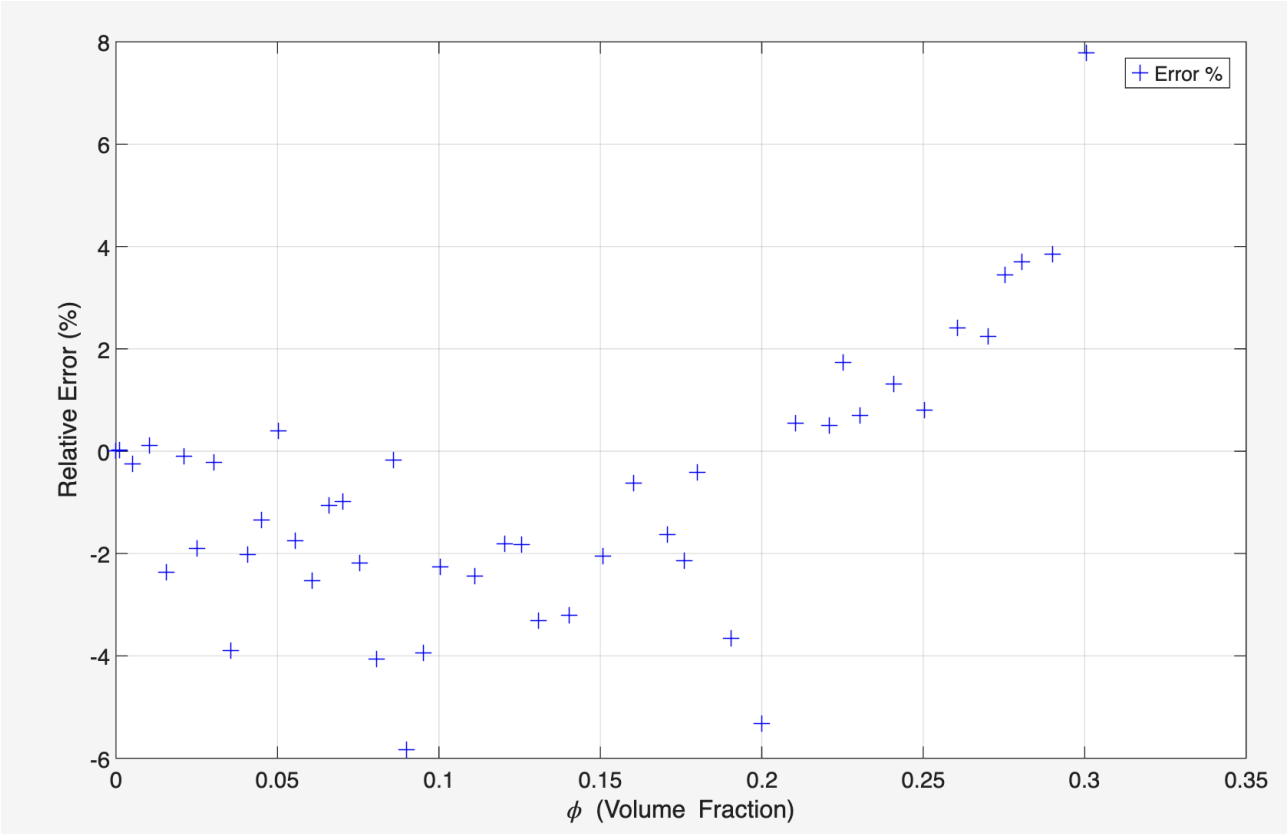


Figure A.19 – Difference calculated from Figure A.18 between the effective thermal conductivity/Seebeck coefficient ratio calculated by FEM and EMT.

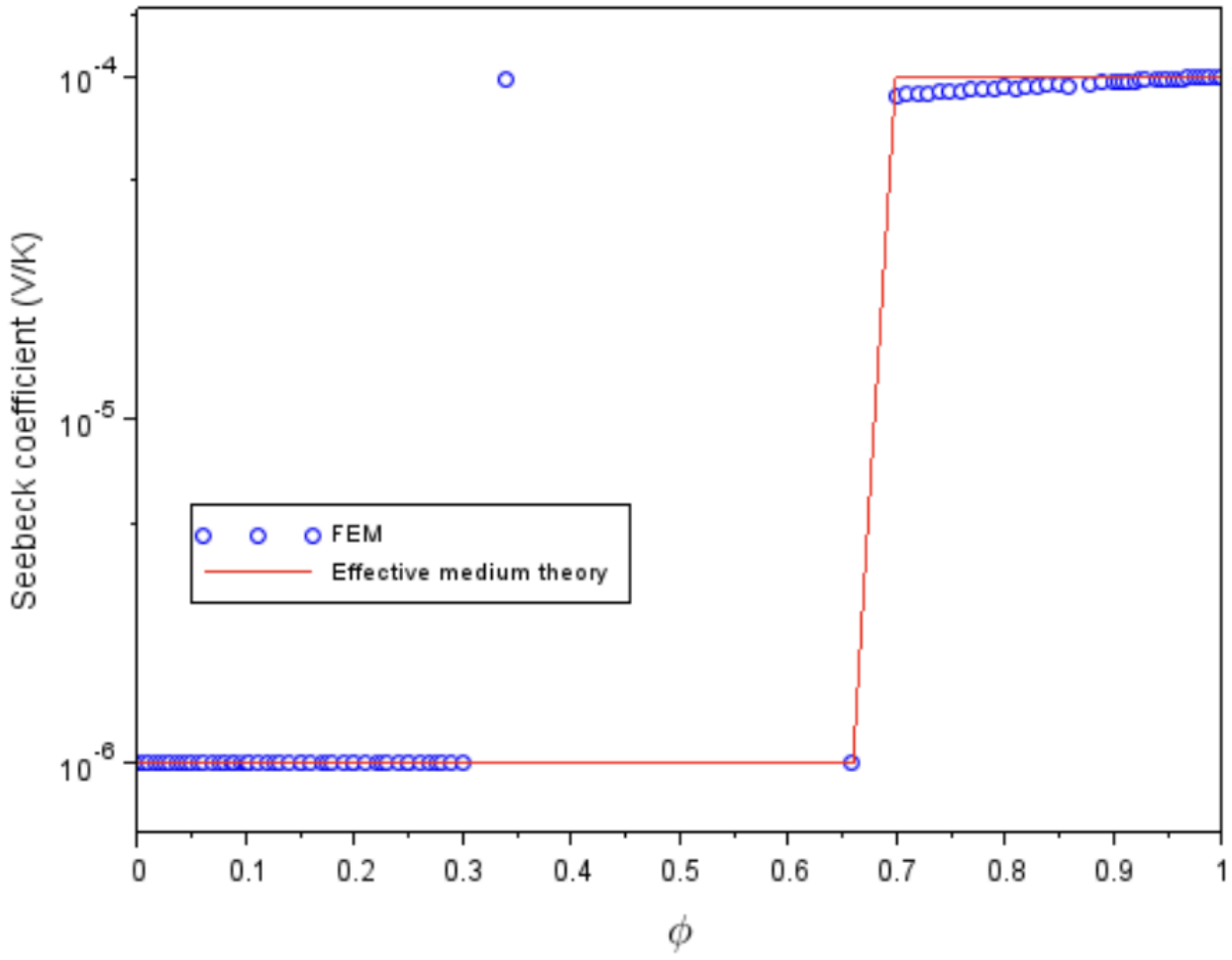


Figure A.20 – Comparison between the effective Seebeck coefficient calculated by FEM and by EMT, assuming the relevant transport parameter is σ/S.

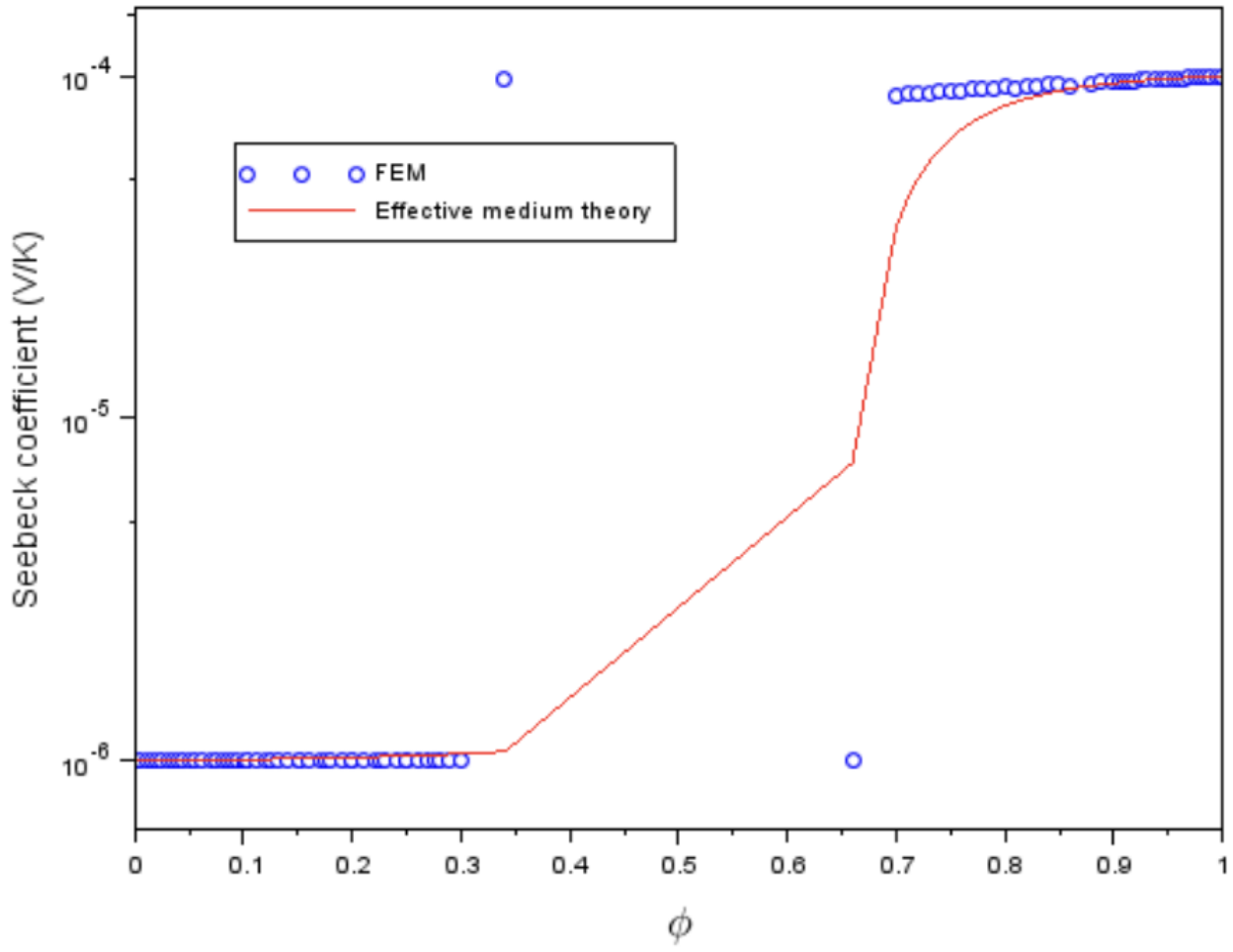


Figure A.21 – Comparison between the effective Seebeck coefficient calculated by FEM and by EMT, assuming the relevant transport parameter is κ/S.

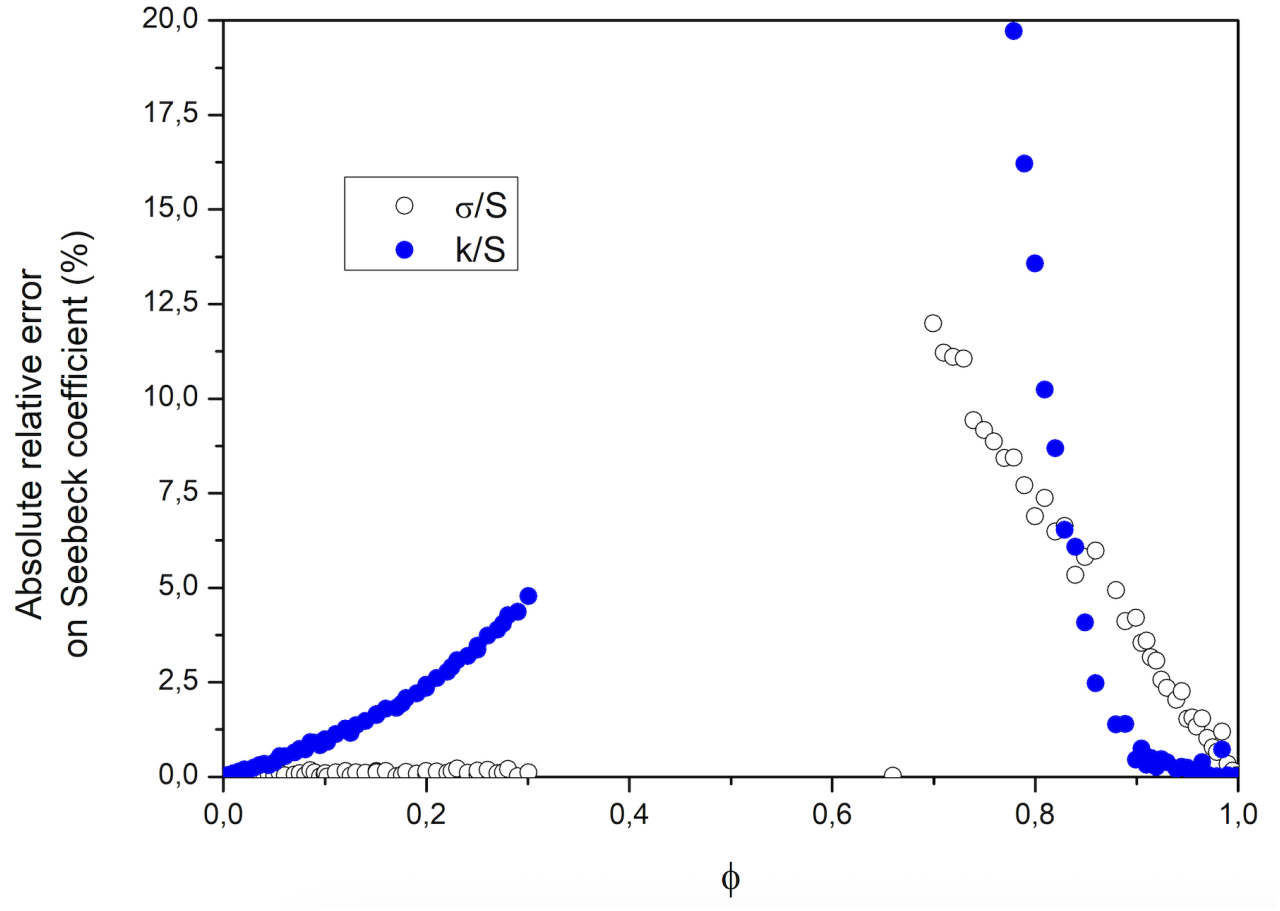


Figure A.22 – Absolute relative error between the effective Seebeck coefficient calculated by FEM and by EMT, assuming two different assumptions: the relevant transport parameter is σ/S, then κ/S.

Bibliography

[1] Eric Pop. « Energy dissipation and transport in nanoscale devices ». In: *Nano Research* 3.2 (2010), pp. 147–169. DOI: 10.1007/s12274-010-1019-z.

[2] B. Shi, A. Srivastava, and A. Bar-Cohen. « Co-design of micro-fluidic heat sink and thermal through-silicon-vias for cooling of three-dimensional integrated circuit ». In: *IET Circuits, Devices & Systems* 7.5 (2013), pp. 223–231. DOI: 10.1049/iet-cds.2013.0026. URL: https://doi.org/10.1049/iet-cds.2013.0026.

[3] Kenneth E. Goodson. « Ordering Up the Minimum Thermal Conductivity of Solids ». In: *Science* 315.5810 (2007), pp. 342–343. DOI: 10.1126/science.1138067. URL: https://doi.org/10.1126/science.1138067.

[4] Eric Pop, Sanjiv Sinha, and Kenneth E. Goodson. « Heat Generation and Transport in Nanometer-Scale Transistors ». In: *Proceedings of the IEEE* 94.8 (2006), pp. 1587–1601. DOI: 10.1109/JPROC.2006.879794. URL: https://doi.org/10.1109/JPROC.2006.879794.

[5] Miyuru Dayarathna, Yonggang Wen, and Rui Fan. « Data Center Energy Consumption Modeling: A Survey ». In: *IEEE Communications Surveys & Tutorials* 18.1 (2016), pp. 732–794. DOI: 10.1109/COMST.2015.2481183.

[6] Jungwoo Joh and Jesús A. del Alamo. « Critical Voltage for Electrical Degradation of GaN High-Electron Mobility Transistors ». In: *IEEE Electron Device Letters* 31.4 (2010), pp. 297–299. DOI: 10.1109/LED.2010.2041838.

[7] Andrei Sarua et al. « Integrated Micro-Raman/Infrared Thermography Probe for Monitoring of Self-Heating in AlGaN/GaN Transistor Structures ». In: *IEEE Transactions on Electron Devices* 53.10 (2006), pp. 2438–2447. DOI: 10.1109/TED.2006.882274.

[8] Gaudenzio Meneghesso et al. « Reliability of GaN High-Electron-Mobility Transistors: State of the Art and Perspectives ». In: *IEEE Transactions on Device and Materials Reliability* 8.2 (2008), pp. 332–343. DOI: 10.1109/TDMR.2008.923743.

[9] Gordon E. Moore. « Cramming More Components Onto Integrated Circuits ». In: *IEEE Solid-State Circuits Society Newsletter* 11.3 (2006). Reprinted from Electronics, vol. 38, no. 8, Apr. 19, 1965, pp. 33–35. DOI: 10.1109/N-SSC.2006.4785860.

[10] Karl Rupp. *Microprocessor Trend Data*. Accessed: 2026-03-23. 2022. URL: https://github.com/karlrupp/microprocessor-trend-data.

[11] Wikipedia contributors. *Transistor count — Wikipedia, The Free Encyclopedia*. [Online; accessed 23-March-2026]. 2022. URL: https://en.wikipedia.org/wiki/Transistor_count.

[12] Apple Inc. *Apple unveils M1 Ultra—the world's most powerful chip for a personal computer*. Apple Newsroom. Mar. 2022. URL: https://www.apple.com/newsroom/2022/03/apple-unveils-m1-ultra-the-worlds-most-powerful-chip-for-a-personal-computer/.

[13] Robert H. Dennard et al. « Design of Ion-Implanted MOSFET's with Very Small Physical Dimensions ». In: *IEEE Journal of Solid-State Circuits* 9.5 (1974), pp. 256–268. DOI: 10.1109/JSSC.1974.1050511.

[14] Shekhar Borkar. « Thousand Core Chips: A Technology Perspective ». In: *Proceedings of the 44th Annual Design Automation Conference (DAC)*. New York, NY, USA: ACM, 2007, pp. 746–749. DOI: 10.1145/1278480.1278667.

[15] Hadi Esmaeilzadeh et al. « Dark Silicon and the End of Multicore Scaling ». In: *Proceedings of the 38th Annual International Symposium on Computer Architecture (ISCA)*. San Jose, CA, USA, June 2011, pp. 365–376. DOI: 10.1109/ISCA.2011.5955230.

[16] Michael Bedford Taylor. « Is Dark Silicon Useful? Harnessing the Four Horsemen of the Coming Dark Silicon Apocalypse ». In: *Proceedings of the 49th Annual Design Automation Conference (DAC)*. San Francisco, CA, USA: ACM, 2012, pp. 1131–1136. DOI: 10.1145/2228360.2228567.

[17] National Research Council. *The Future of Computing Performance: Game Over or Next Level?* Ed. by Samuel H. Fuller and Lynette I. Millett. Includes data adapted from M. Horowitz et al. Washington, DC: The National Academies Press, 2011. ISBN: 978-0-309-15951-7. DOI: 10.17226/12980. URL: https://www.nap.edu/catalog/12980/the-future-of-computing-performance-game-over-or-next-level.

[18] E. Fred Schubert. *Light-Emitting Diodes*. 2nd. Cambridge, UK: Cambridge University Press, 2006. ISBN: 9780521865388. DOI: 10.1017/CBO9780511754029.

[19] Joachim Piprek. « Efficiency droop in nitride-based light-emitting diodes ». In: *physica status solidi (a)* 207.10 (2010), pp. 2217–2225. DOI: 10.1002/pssa.201026149.

[20] Matteo Meneghini et al. « A Review on the Reliability of GaN-Based LEDs ». In: *IEEE Transactions on Device and Materials Reliability* 8.2 (2008), pp. 323–331. DOI: 10.1109/TDMR.2008.921527.

[21] Y. C. Shen et al. « Auger recombination in InGaN measured by photoluminescence ». In: *Applied Physics Letters* 91.14 (2007), p. 141101. DOI: 10.1063/1.2785135.

[22] J. Hader et al. « On the importance of radiative and Auger losses in GaN-based quantum wells ». In: *Applied Physics Letters* 92.26 (2008), p. 261103. DOI: 10.1063/1.2953543.

[23] H. D. Sun et al. « Thermal quenching mechanism of photoluminescence in 1.55 μm GaInNAsSb / Ga(N)As quantum-well structures ». In: *Applied Physics Letters* 89.10 (2006), p. 101909. DOI: 10.1063/1.2345240. URL: https://doi.org/10.1063/1.2345240.

[24] Yukio Narukawa et al. « White light emitting diodes with super-high luminous efficacy ». In: *Journal of Physics D: Applied Physics* 43.35 (2010), p. 354002. DOI: 10.1088/0022-3727/43/35/354002.

[25] Nadarajah Narendran and Yimin Gu. « Life of LED-Based White Light Sources ». In: *Journal of Display Technology* 1.1 (2005), pp. 167–171. DOI: 10.1109/JDT.2005.852510.

[26] F. Patrick McCluskey, Thomas Podlesak, and Richard Grzybowski. *High Temperature Electronics*. 1st. Boca Raton, FL, USA: CRC Press, 1997. ISBN: 9780849396236. DOI: 10.1201/9780203751978.

[27] Zongtao Li. « A review on thermal management of light-emitting diodes: From package-level to system-level ». In: *Applied Thermal Engineering*, 124145 (2024). DOI: 10.1016/j.applthermaleng.2024.124145. URL: https://doi.org/10.1016/j.applthermaleng.2024.124145.

[28] Andras Poppe and Clemens J.M. Lasance. « On the standardization of thermal characterization of LEDs ». In: *25th Annual IEEE Semiconductor Thermal Measurement and Management Symposium (SEMI-THERM)*. IEEE, 2009, pp. 151–158. DOI: 10.1109/STHERM.2009.4810757.

[29] Shunsuke Nishiura et al. « Properties of transparent Ce:YAG ceramic phosphors for white LED ». In: *Optical Materials* 33.4 (Feb. 2011), pp. 688–691. DOI: 10.1016/j.optmat.2010.06.005. URL: https://doi.org/10.1016/j.optmat.2010.06.005.

[30] Govind P. Agrawal and Niloy K. Dutta. *Semiconductor Lasers*. 2nd. Originally published by AT&T, 1993. Springer New York, NY, 2013. ISBN: 978-1-4613-0481-4. DOI: 10.1007/978-1-4613-0481-4.

[31] Joachim Piprek. *Semiconductor Optoelectronic Devices: Introduction to Physics and Simulation*. San Diego, CA, USA: Academic Press, 2003. ISBN: 9780080469782. DOI: 10.1016/C2009-0-22633-X.

[32] Larry A. Coldren, Scott W. Corzine, and Milan L. Mašanović. *Diode Lasers and Photonic Integrated Circuits*. 2nd. Hoboken, NJ, USA: John Wiley & Sons, 2012. ISBN: 9780470484128. DOI: 10.1002/9781118148167.

[33] Ken-ichi Mizuishi et al. « Reliability of InGaAsP/InP Buried Heterostructure Lasers ». In: *Japanese Journal of Applied Physics* 21.S1 (1982), p. 359. DOI: 10.7567/JJAPS.21S1.359.

[34] D. Botez and D. R. Scifres, eds. *Diode Laser Arrays*. Cambridge University Press, 1994.

[35] B. Jayant Baliga. *Fundamentals of Power Semiconductor Devices*. 2nd. New York, NY, USA: Springer Cham, 2019. ISBN: 978-3-319-93988-9. DOI: 10.1007/978-3-319-93988-9.

[36] Xu She et al. « Review of Silicon Carbide Power Devices and Their Applications ». In: *IEEE Transactions on Industrial Electronics* 64.10 (2017), pp. 8193–8205. DOI: 10.1109/TIE.2017.2652401.

[37] Fang Luo et al. « A Review of SiC Power Module Packaging: Layout, Material System and Integration ». In: *CPSS Transactions on Power Electronics and Applications* 2.3 (2017), pp. 170–186. DOI: 10.24295/CPSSTPEA.2017.00017.

[38] Katja Puschkarsky et al. « Understanding BTI in SiC MOSFETs and Its Impact on Circuit Operation ». In: *IEEE Transactions on Device and Materials Reliability* 18.2 (2018), pp. 144–153. DOI: 10.1109/TDMR.2018.2819003.

[39] H. Julian Goldsmid. *Introduction to Thermoelectricity*. 2nd. Springer Series in Materials Science. Springer Berlin, Heidelberg, 2016. ISBN: 978-3-662-49256-7. DOI: 10.1007/978-3-662-49256-7.

[40] David Michael Rowe, ed. *CRC Handbook of Thermoelectrics*. 1st. Boca Raton, FL, USA: CRC Press, 1995. ISBN: 9781315219691. DOI: 10.1201/9781420049718.

[41] G. Jeffrey Snyder and Eric S. Toberer. « Complex thermoelectric materials ». In: *Nature Materials* 7.2 (2008). PMID: 18219332, pp. 105–114. DOI: 10.1038/nmat2090.

[42] L. D. Hicks and M. S. Dresselhaus. « Effect of quantum-well structures on the thermoelectric figure of merit ». In: *Physical Review B* 47.19 (May 1993), pp. 12727–12731. DOI: 10.1103/PhysRevB.47.12727.

[43] Rama Venkatasubramanian et al. « Thin-film thermoelectric devices with high room-temperature figures of merit ». In: *Nature* 413.6856 (2001). PMID: 11595940, pp. 597–602. DOI: 10.1038/35098012.

[44] T. C. Harman et al. « Nanostructured thermoelectric materials ». In: *Journal of Electronic Materials* 34.5 (May 2005), pp. L19–L22. DOI: 10.1007/s11664-005-0083-8.

[45] Kanishka Biswas et al. « High-performance bulk thermoelectrics with all-scale hierarchical architectures ». In: *Nature* 489.7416 (2012). PMID: 22996556, pp. 414–418. DOI: 10.1038/nature11439.

[46] Brian C. Sales, David Mandrus, and Richard K. Williams. « Filled Skutterudite Antimonides: A New Class of Thermoelectric Materials ». In: *Science* 272.5266 (1996), pp. 1325–1328. DOI: 10.1126/science.272.5266.1325. URL: http://www.jstor.org/stable/2889796.

[47] George S. Nolas et al. « Semiconducting Ge clathrates: Promising candidates for thermoelectric applications ». In: *Applied Physics Letters* 73.2 (1998), pp. 178–180. DOI: 10.1063/1.121747. URL: https://doi.org/10.1063/1.121747.

[48] Yanzhong Pei et al. « Convergence of electronic bands for high performance bulk thermoelectrics ». In: *Nature* 473.7345 (2011). PMID: 21544143, pp. 66–69. DOI: 10.1038/nature09996.

[49] Joseph P. Heremans et al. « Enhancement of thermoelectric efficiency in PbTe by distortion of the electronic density of states ». In: *Science* 321.5888 (2008). PMID: 18653890, pp. 554–557. DOI: 10.1126/science.1159725.

[50] Charles Kittel. *Introduction to Solid State Physics*. 8th. Hoboken, NJ, USA: John Wiley & Sons, 2004, p. 704. ISBN: 978-0-471-41526-8.

[51] David G. Cahill et al. « Nanoscale thermal transport ». In: *Journal of Applied Physics* 93.2 (2003), pp. 793–818. DOI: 10.1063/1.1524305.

[52] David G. Cahill et al. « Nanoscale thermal transport. II. 2003–2012 ». In: *Applied Physics Reviews* 1.1 (2014), p. 011305. DOI: 10.1063/1.4832615.

[53] Gang Chen. *Nanoscale Energy Transport and Conversion: A Parallel Treatment of Electrons, Molecules, Phonons, and Photons*. Online edition, Oxford Academic, 31 Oct. 2023. New York, NY, USA: Oxford University Press, 2005. ISBN: 9780195159424. DOI: 10.1093/oso/9780195159424.001.0001.

[54] Arun Majumdar. « Microscale Heat Conduction in Dielectric Thin Films ». In: *Journal of Heat Transfer* 115.1 (Feb. 1993), pp. 7–16. DOI: 10.1115/1.2910673.

[55] Chang-Lin Tien and Gang Chen. « Challenges in Microscale Conductive and Radiative Heat Transfer ». In: *Journal of Heat Transfer* 116.4 (Nov. 1994), pp. 799–807. DOI: 10.1115/1.2911450.

[56] G. Chen. « Thermal conductivity and ballistic-phonon transport in the cross-plane direction of superlattices ». In: *Physical Review B* 57.23 (June 1998), pp. 14958–14973. DOI: 10.1103/PhysRevB.57.14958.

[57] A. A. Joshi and A. Majumdar. « Transient ballistic and diffusive phonon heat transport in thin films ». In: *Journal of Applied Physics* 74.1 (July 1993), pp. 31–39. DOI: 10.1063/1.354111.

[58] Yongho Sungtaek Ju and Kenneth E. Goodson. « Phonon scattering in silicon films with thickness of order 100 nm ». In: *Applied Physics Letters* 74.20 (1999), pp. 3005–3007. DOI: 10.1063/1.123994. URL: https://doi.org/10.1063/1.123994.

[59] Keivan Esfarjani, Gang Chen, and Harold T. Stokes. « Heat transport in silicon from first-principles calculations ». In: *Physical Review B* 84.8 (Aug. 2011), p. 085204. DOI: 10.1103/PhysRevB.84.085204.

[60] Ho-Ki Lyeo and David G. Cahill. « Thermal conductance of interfaces between highly dissimilar materials ». In: *Physical Review B* 73.14 (Apr. 2006), p. 144301. DOI: 10.1103/PhysRevB.73.144301.

[61] Keith T. Regner et al. « Broadband phonon mean free path contributions to thermal conductivity measured using frequency domain thermoreflectance ». In: *Nature Communications* 4.1 (2013), p. 1640. DOI: 10.1038/ncomms2630.

[62] Mark E. Siemens et al. « Quasi-ballistic thermal transport from nanoscale interfaces observed using ultrafast coherent soft X-ray beams ». In: *Nature Materials* 9.1 (Jan. 2010). PMID: 19898462, pp. 26–30. DOI: 10.1038/nmat2568.

[63] Jeremy A. Johnson et al. « Direct Measurement of Room-Temperature Nondiffusive Thermal Transport Over Micron Distances in a Silicon Membrane ». In: *Physical Review Letters* 110.2 (Jan. 2013), p. 025901. DOI: 10.1103/PhysRevLett.110.025901.

[64] A. J. Minnich et al. « Thermal Conductivity Spectroscopy Technique to Measure Phonon Mean Free Paths ». In: *Physical Review Letters* 110.9 (Aug. 2011), p. 095901. DOI: 10.1103/PhysRevLett.107.095901.

[65] J. M. Ziman. *Electrons and Phonons*. Oxford University Press, 1960.

[66] P. G. Klemens. « The Scattering of Low-Frequency Lattice Waves by Static Imperfections ». In: *Proceedings of the Physical Society. Section A* 68.12 (Dec. 1955), pp. 1113–1133. DOI: 10.1088/0370-1298/68/12/303.

[67] E. H. Sondheimer. « The mean free path of electrons in metals ». In: *Advances in Physics* 50.6 (2001). Originally published in 1952, reprinted in the 50th anniversary issue, pp. 499–537. DOI: 10.1080/00018730110102187.

[68] M. V. Simkin and G. D. Mahan. « Minimum Thermal Conductivity of Superlattices ». In: *Physical Review Letters* 84.5 (Jan. 2000), pp. 927–930. DOI: 10.1103/PhysRevLett.84.927.

[69] Maria N. Luckyanova et al. « Coherent Phonon Heat Conduction in Superlattices ». In: *Science* 338.6109 (2012), pp. 936–939. DOI: 10.1126/science.1225549.

[70] J. Ravichandran et al. « Crossover from incoherent to coherent phonon scattering in epitaxial oxide superlattices ». In: *Nature Materials* 13.2 (Feb. 2014). PMID: 24317186, pp. 168–172. DOI: 10.1038/nmat3826.

[71] Piotr Leonidovich Kapitza. « The Study of Heat Transfer in Helium II ». In: *Collected Papers of P. L. Kapitza*. Ed. by D. ter Haar. Original research conducted in 1941. Pergamon Press, 1971, pp. 581–624. DOI: 10.1016/B978-0-08-015840-2.50015-4.

[72] W. A. Little. « The Transport of Heat Between Dissimilar Solids at Low Temperatures ». In: *From High-Temperature Superconductivity to Microminiature Refrigeration*. Ed. by B. Cabrera, H. Gutfreund, and V. Kresin. Boston, MA: Springer, 1996, pp. 27–53. DOI: 10.1007/978-1-4613-0411-1_3.

[73] Gerald L. Pollack. « Kapitza Resistance ». In: *Reviews of Modern Physics* 41.1 (Jan. 1969), pp. 48–81. DOI: 10.1103/RevModPhys.41.48.

[74] E. T. Swartz and R. O. Pohl. « Thermal boundary resistance ». In: *Reviews of Modern Physics* 61.3 (July 1989), pp. 605–668. DOI: 10.1103/RevModPhys.61.605.

[75] Patrick E. Phelan. « Application of Diffuse Mismatch Theory to the Prediction of Thermal Boundary Resistance in Thin-Film High-T_c Superconductors ». In: *Journal of Heat Transfer* 120.1 (Feb. 1998), pp. 37–43. DOI: 10.1115/1.2830060.

[76] M. L. Huberman and A. W. Overhauser. « Electronic Kapitza conductance at a diamond-Pb interface ». In: *Physical Review B* 50.5 (Aug. 1994), pp. 2865–2873. DOI: 10.1103/PhysRevB.50.2865.

[77] R. J. Stevens, A. N. Smith, and P. M. Norris. « Measurement of Thermal Boundary Conductance of a Series of Metal-Dielectric Interfaces by the Transient Thermoreflectance Technique ». In: *Journal of Heat Transfer* 127.3 (Mar. 2005), pp. 315–322. DOI: 10.1115/1.1857944.

[78] Patrick E. Hopkins. « Thermal Transport across Solid Interfaces with Nanoscale Imperfections: Effects of Roughness, Disorder, Dislocations, and Bonding on Thermal Boundary Conductance ». In: *International Scholarly Research Notices* 2013 (2013), p. 682586. DOI: 10.1155/2013/682586.

[79] Christian Monachon, Ludger Weber, and Chris Dames. « Thermal Boundary Conductance: A Materials Science Perspective ». In: *Annual Review of Materials Research* 46.1 (2016), pp. 433–463. DOI: 10.1146/annurev-matsci-070115-031719.

[80] Simon M. Sze and Kwok K. Ng. *Physics of Semiconductor Devices*. 3rd. Hoboken, NJ: John Wiley & Sons, 2006. ISBN: 9780471143239. DOI: 10.1002/0470068329.

[81] Stanley M. Wolf and Richard N. Tauber. *Silicon Processing for the VLSI Era*. Vol. 1: Process Technology. Sunset Beach, CA: Lattice Press, 1986. ISBN: 9780961672133.

[82] B. E. Deal and A. S. Grove. « General Relationship for the Thermal Oxidation of Silicon ». In: *Journal of Applied Physics* 36.12 (Dec. 1965), pp. 3770–3778. DOI: 10.1063/1.1713945.

[83] Shyam P. Murarka. *Metallization: Theory and Practice for VLSI and ULSI*. Boston, MA: Butterworth-Heinemann, 1993. ISBN: 9780750690010.

[84] David G. Cahill. « Thermal conductivity measurement from 30 to 750 K: the 3ω method ». In: *Review of Scientific Instruments* 61.2 (Feb. 1990), pp. 802–808. DOI: 10.1063/1.1141498.

[85] S.-M. Lee and David G. Cahill. « Heat transport in thin dielectric films ». In: *Journal of Applied Physics* 81.6 (Mar. 1997), pp. 2590–2595. DOI: 10.1063/1.363923.

[86] Scott E. Thompson et al. « A 90-nm logic technology featuring strained-silicon ». In: *IEEE Transactions on Electron Devices* 51.11 (Nov. 2004), pp. 1790–1797. DOI: 10.1109/TED.2004.836648.

[87] Joohyung Lee and Yogesh B. Gianchandani. « A temperature-dithering closed-loop interface circuit for a scanning thermal microscopy system ». In: *Journal of Microelectromechanical Systems* 14.1 (Feb. 2005), pp. 44–53. DOI: 10.1103/JMEMS.2004.839011.

[88] L. Griffin et al. « Phonon scattering in amorphous solids and at interfaces ». In: *Physical Review B* 83 (2011), p. 195414.

[89] H. Duan. « From MOSFET to FinFET to GAAFET: The evolution, challenges, and future prospects ». In: *Applied and Computational Engineering* 50 (2024), pp. 113–120. DOI: 10.54097/ace.v50i1.09.

[90] James V. Beck and Kenneth J. Arnold. *Parameter Estimation in Engineering and Science*. New York, NY: John Wiley & Sons, 1977. ISBN: 9780471061854.

[91] Andres Georg Rösch et al. « Improved Electrical, Thermal, and Thermoelectric Properties Through Sample-to-Sample Fluctuations in Near-Percolation Threshold Composite Materials ». In: *Advanced Theory and Simulations* 4.1 (2021), p. 2000284. DOI: 10.1002/adts.202000284.

[92] J. Sonntag, B. Lenoir, and P. Ziolkowski. « Electronic Transport in Alloys with Phase Separation (Composites) ». In: *Open Journal of Composite Materials* 9.1 (2019), pp. 21–56. DOI: 10.4236/ojcm.2019.91002.

[93] Jean-Baptiste-Joseph Fourier. *Théorie analytique de la chaleur*. Paris: Firmin Didot, 1822.

[94] H. S. Carslaw and J. C. Jaeger. *Conduction of Heat in Solids*. 2nd. Oxford University Press, 1959.

[95] Frank P. Incropera, David P. DeWitt, et al. *Fundamentals of Heat and Mass Transfer*. 6th. John Wiley & Sons, 2007.

[96] I. Tamm. « Über die Quantentheorie der molekularen Lichtzerstreuung ». In: *Zeitschrift für Physik* 60 (1930), p. 345.

[97] J. Frenkel. *Wave Mechanics: Elementary Theory*. Clarendon Press, 1932.

[98] Neil W. Ashcroft and N. David Mermin. *Solid State Physics*. Holt, Rinehart and Winston, 1976.

[99] Peter Debye. « Zur Theorie der spezifischen Wärmen ». In: *Annalen der Physik* 344.14 (1912), pp. 789–839. DOI: 10.1002/andp.19123441404.

[100] Rudolf Peierls. « Zur kinetischen Theorie der Wärmeleitung in Kristallen ». In: *Annalen der Physik* 395.8 (1929), pp. 1055–1101. DOI: 10.1002/andp.19293950803.

[101] C. T. Walker and R. O. Pohl. « Phonon Scattering by Point Defects ». In: *Physical Review* 131.4 (Aug. 1963), pp. 1433–1445. DOI: 10.1103/PhysRev.131.1433.

[102] P. W. Anderson. « Absence of Diffusion in Certain Random Lattices ». In: *Physical Review* 109.5 (Mar. 1958), pp. 1492–1505. DOI: 10.1103/PhysRev.109.1492.

[103] David G. Cahill and R. O. Pohl. « Heat flow and lattice vibrations in glasses ». In: *Solid State Communications* 70.10 (1989), pp. 927–930. DOI: 10.1016/0038-1098(89)90630-3.

[104] Albert Einstein. « Eine Beziehung zwischen dem elastischen Verhalten und der spezifischen Wärme bei festen Körpern mit einatomigem Molekül ». In: *Annalen der Physik* 339.1 (1911). Archiv-Link: https://www.db-thueringen.de/receive/dbt_mods_00003539, pp. 170–172. DOI: 10.1002/andp.19113390110.

[105] Glen A. Slack. « The Thermal Conductivity of Nonmetallic Crystals ». In: *Solid State Physics*. Ed. by Henry Ehrenreich, Frederick Seitz, and David Turnbull. Vol. 34. Academic Press, 1979, pp. 1–71. ISBN: 9780126077346. DOI: 10.1016/S0081-1947(08)60359-8.

[106] David G. Cahill and R. O. Pohl. « Thermal conductivity of amorphous solids above the plateau ». In: *Physical Review B* 35.8 (Mar. 1987), pp. 4067–4073. DOI: 10.1103/PhysRevB.35.4067.

[107] A. F. Ioffe and A. R. Regel. « Non-crystalline, amorphous and liquid electronic semiconductors ». In: *Progress in Semiconductors* 4 (1960), pp. 237–291.

[108] David G. Cahill et al. « Thermal conductivity of thin films: Measurements and understanding ». In: *Journal of Vacuum Science & Technology A: Vacuum, Surfaces, and Films* 7.3 (May 1989), pp. 1259–1266. DOI: 10.1116/1.576265.

[109] C. J. Glassbrenner and Glen A. Slack. « Thermal Conductivity of Silicon and Germanium from 3°K to the Melting Point ». In: *Physical Review* 134.4A (May 1964), A1058–A1069. DOI: 10.1103/PhysRev.134.A1058.

[110] R. C. Zeller and R. O. Pohl. « Thermal Conductivity and Specific Heat of Noncrystalline Solids ». In: *Physical Review B* 4.6 (Sept. 1971), pp. 2029–2041. DOI: 10.1103/PhysRevB.4.2029.

[111] H. B. G. Casimir. « Note on the conduction of heat in crystals ». In: *Physica* 5.6 (1938), pp. 495–500. ISSN: 0031-8914. DOI: 10.1016/S0031-8914(38)80162-2.

[112] Joseph Callaway. « Model for Lattice Thermal Conductivity at Low Temperatures ». In: *Physical Review* 113.4 (Feb. 1959), pp. 1046–1051. DOI: 10.1103/PhysRev.113.1046.

[113] K. Fuchs. « The conductivity of thin metallic films according to the electron theory of metals ». In: *Mathematical Proceedings of the Cambridge Philosophical Society* 34.1 (1938), pp. 100–108. DOI: 10.1017/S0305004100019952.

[114] Deyu Li et al. « Thermal conductivity of individual silicon nanowires ». In: *Applied Physics Letters* 83.14 (Oct. 2003), pp. 2934–2936. DOI: 10.1063/1.1616981.

[115] M. Asheghi et al. « Temperature-Dependent Thermal Conductivity of Single-Crystal Silicon Layers in SOI Substrates ». In: *Journal of Heat Transfer* 120.1 (Feb. 1998), pp. 30–36. DOI: 10.1115/1.2830059.

[116] Zhun-Yong Ong and Eric Pop. « Molecular dynamics simulation of thermal boundary conductance between carbon nanotubes and SiO_2 ». In: *Physical Review B* 81.15 (Apr. 2010), p. 155408. DOI: 10.1103/PhysRevB.81.155408.

[117] I. M. Khalatnikov. « Heat exchange between a solid and Helium II ». In: *Zh. Eksp. Teor. Fiz.* 22 (1952), p. 687.

[118] Takafumi Yao. « Thermal properties of AlAs/GaAs superlattices ». In: *Applied Physics Letters* 51.22 (Nov. 1987), pp. 1798–1800. DOI: 10.1063/1.98526.

[119] C. Colvard et al. « Folded acoustic and quantized optic phonons in (GaAl)As superlattices ». In: *Physical Review B* 31.4 (Feb. 1985), pp. 2080–2091. DOI: 10.1103/PhysRevB.31.2080.

[120] S.-M. Lee, David G. Cahill, and Rama Venkatasubramanian. « Thermal conductivity of Si–Ge superlattices ». In: *Applied Physics Letters* 70.22 (June 1997), pp. 2957–2959. DOI: 10.1063/1.118755.

[121] ASTM C177-19. *Standard Test Method for Steady-State Heat Flux Measurements and Thermal Transmission Properties by Means of the Guarded-Hot-Plate Apparatus*. Tech. rep. West Conshohocken, PA: ASTM International, 2023. URL: https://www.astm.org/c0177-19.html.

[122] G. F. C. Searle. « A method of determining the thermal conductivity of copper ». In: *Philosophical Magazine* 9.50 (1905), pp. 125–129. DOI: 10.1080/14786440509463260.

[123] David G. Cahill. « Analysis of heat flow in layered structures for time-domain thermoreflectance ». In: *Review of Scientific Instruments* 75.12 (Dec. 2004), pp. 5119–5122. DOI: 10.1063/1.1819431.

[124] M. Kuball et al. « Measurement of temperature in active high-power AlGaN/GaN HFETs using Raman spectroscopy ». In: *IEEE Electron Device Letters* 23.1 (Jan. 2002), pp. 7–9. DOI: 10.1109/55.974795.

[125] B. L. Zink, R. Pietri, and F. Hellman. « Thermal Conductivity and Specific Heat of Thin-Film Amorphous Silicon ». In: *Physical Review Letters* 96.5 (Feb. 2006), p. 055902. DOI: 10.1103/PhysRevLett.96.055902.

[126] A. Jacquot et al. « Numerical simulation of the 3ω method for measuring the thermal conductivity ». In: *Journal of Applied Physics* 91.7 (Apr. 2002), pp. 4733–4738. DOI: 10.1063/1.1459611.

[127] Chris Dames. « Measuring the Thermal Conductivity of Thin Films: 3ω and Related Electrothermal Methods ». In: *Annual Review of Heat Transfer*. Vol. 16. Begell House, 2013, pp. 7–49. DOI: 10.1615/AnnualRevHeatTransfer.v16.20.

[128] Jung Hun Kim, Albert Feldman, and Donald Novotny. « Application of the three omega thermal conductivity measurement method to a film on a substrate of finite thickness ». In: *Journal of Applied Physics* 86.7 (Oct. 1999), pp. 3959–3963. DOI: 10.1063/1.371314.

[129] Tao Tong and Arun Majumdar. « Reexamining the 3-omega technique for thin film thermal characterization ». In: *Review of Scientific Instruments* 77.10 (Oct. 2006), p. 104902. DOI: 10.1063/1.2349601.

[130] T. Borca-Tasciuc et al. « Anisotropic Thermal Conductivity of A Si/Ge Superlattice ». In: *MRS Proceedings*. Vol. 545. Cambridge University Press, 1998, p. 473. DOI: 10.1557/PROC-545-473.

[131] T. Borca-Tasciuc, A. R. Kumar, and G. Chen. « Data reduction in 3ω method for thin-film thermal conductivity determination ». In: *Review of Scientific Instruments* 72.4 (Apr. 2001), pp. 2139–2147. DOI: 10.1063/1.1353189.

[132] D. K. Schroder. *Semiconductor Material and Device Characterization*. 3rd. Wiley-Interscience, 2006.

[133] W. (Lord Kelvin) Thomson. « On the dynamical theory of heat ». In: *Transactions of the Royal Society of Edinburgh* 20 (1851), p. 261.

[134] A. F. Mayadas and M. Shatzkes. « Electrical-Resistivity Model for Polycrystalline Films: The Case of Arbitrary Reflection at External Surfaces ». In: *Physical Review B* 1.4 (Feb. 1970), pp. 1382–1389. DOI: 10.1103/PhysRevB.1.1382.

[135] C. R. Tellier, C. P. Pichard, and A. J. Tosser. « Statistical model of electrical conduction in polycrystalline metals ». In: *Thin Solid Films* 61.3 (1970), pp. 349–354. ISSN: 0040-6090. DOI: 10.1016/0040-6090(79)90480-2.

[136] J. R. Sambles. « The resistivity of thin metal films—Some critical remarks ». In: *Thin Solid Films* 106.4 (Aug. 1983), pp. 321–331. ISSN: 0040-6090. DOI: 10.1016/0040-6090(83)90344-9.

[137] Ijaz-ur-Rahman and Kamaluddin Ahmed. « Electron mean free path in a thin metal film ». In: *Journal of Applied Physics* 49.6 (June 1978), pp. 3625–3626. DOI: 10.1063/1.325257.

[138] W. F. Smith. « Principles of Materials Science and Engineering ». In: *McGraw-Hill* (1995).

[139] H. G. Tompkins et al. « Spectroscopic ellipsometry and reflectometry: A user's perspective ». In: *2000 Digest of the LEOS Summer Topical Meetings*. IEEE, 2000, pp. II27–II28. DOI: 10.1109/LEOSST.2000.869717.

[140] Marc J. Madou. *Fundamentals of Microfabrication and Nanotechnology*. 3rd. CRC Press, 2011.

[141] O. C. Zienkiewicz, R. L. Taylor, and J. Z. Zhu. *The Finite Element Method: Its Basis and Fundamentals*. Seventh. Oxford: Butterworth-Heinemann, 2013. ISBN: 978-1-85617-633-0. DOI: 10.1016/C2009-0-24909-9.

[142] J. N. Reddy. *An Introduction to the Finite Element Method*. Third. New York: McGraw-Hill Education, 2005. ISBN: 978-0072466850.

[143] Robert D. Cook et al. *Concepts and Applications of Finite Element Analysis*. Fourth. New York: John Wiley & Sons, 2001. ISBN: 978-0-471-35605-9.

[144] Jörg Schröder and Paulo Pimenta, eds. *Novel Finite Element Technologies for Solids and Structures*. Vol. 91. Lecture Notes in Applied and Computational Mechanics. Cham, Switzerland: Springer Nature, 2020. ISBN: 978-3-030-33519-9. DOI: 10.1007/978-3-030-33520-5.

[145] A. Jacquot et al. « Fabrication and modeling of an in-plane thermoelectric micro-generator ». In: *Twenty-First International Conference on Thermoelectrics, 2002. Proceedings ICT '02.* IEEE, 2002, pp. 561–564. DOI: 10.1103/10.1109/ICT.2002.1190380.

[146] COMSOL AB. *COMSOL Multiphysics User's Guide v. 6.1*. Stockholm, Sweden, 2023.

[147] Helcio R. B. Orlande. *Inverse Heat Transfer: Fundamentals and Applications*. Second. Boca Raton, FL: CRC Press, 2021. DOI: 10.1201/9781003155157.

[148] Andrea Saltelli et al. *Global Sensitivity Analysis: The Primer*. Chichester, UK: John Wiley & Sons, Ltd, 2008. ISBN: 978-0-470-05997-5. DOI: 10.1002/9780470725184.

[149] Joachim Sonntag. « Disordered electronic systems. III. Thermoelectric power in alloys with phase separation ». In: *Physical Review B* 73.4 (2006), p. 045126. DOI: 10.1103/PhysRevB.73.045126.

[150] Joachim Sonntag. « Thermoelectric power in alloys with phase separation (composites) ». In: *Journal of Physics: Condensed Matter* 21.17 (2009), p. 175703. DOI: 10.1088/0953-8984/21/17/175703.

[151] Joachim Sonntag. « Comment on "Effective medium theory based modeling of the thermoelectric properties of composites: comparison between predictions and experiments in the glass-crystal composite system $Si_{10}As_{15}Te_{75}$–$Bi_{0.4}Sb_{1.6}Te_3$" ». In: *Journal of Materials Chemistry C* 4.43 (2016), pp. 10390–10393. DOI: 10.1039/C6TC03140D.

Titre: Étude thermique d'un système multicouches : modélisation par la méthode des éléments finis et caractérisation expérimentale par la technique 3ω (en français).

Mots clefs: Méthode 3-oméga, Conductivité thermique, Couches minces diélectriques, Simulation FEM, Résistance d'interface, Approche du Milieu Effectif (EMA).

Résumé: La gestion thermique est passée d'un aspect secondaire à un verrou critique déterminant la fiabilité et les performances des dispositifs microélectroniques modernes. La réduction continue des dimensions des composants a conduit à des densités de puissance très élevées, accentuant les effets d'auto-échauffement dans des technologies telles que les transistors logiques FinFET et les amplificateurs de puissance à base de nitrure de gallium (GaN). Dans ces systèmes, les couches minces diélectriques, telles que le dioxyde de silicium SiO_2 et le nitrure de silicium SiN_x, jouent un rôle essentiel comme couches de passivation et d'isolation. Cependant, à l'échelle nanométrique, leur conductivité thermique peut être fortement réduite par rapport aux matériaux massifs, en raison de la diffusion des phonons aux frontières, des effets de taille, ainsi que des résistances thermiques d'interface, également appelées résistances de Kapitza. La caractérisation précise de ces propriétés thermiques effectives constitue donc une condition nécessaire pour une modélisation fiable des dispositifs et pour la prédiction de leur durée de vie.

Cette thèse propose un cadre métrologique complet combinant la méthode expérimentale 3-oméga (3ω) et des simulations numériques par la méthode des éléments finis (FEM). Sur le plan expérimental, nous avons développé et optimisé un banc de mesure 3ω conçu pour les couches minces diélectriques et les structures multicouches, pour lesquelles la réponse thermique est faible et fortement influencée par le substrat et les interfaces. Ce dispositif permet de détecter de faibles oscillations de température à partir du signal de tension 3ω mesuré, sur une plage de fréquences contrôlée. Sur le plan numérique, une stratégie de modélisation FEM hiérarchisée a été mise en place. Un modèle bidimensionnel en coupe transversale a d'abord été utilisé pour la validation, les études paramétriques et l'analyse des limites des approches analytiques simplifiées. Pour l'analyse finale de l'empilement multicouche, cette approche a été étendue à un modèle FEM tridimensionnel incluant des domaines d'éléments infinis, afin de reproduire plus fidèlement la géométrie expérimentale et de réduire les effets artificiels liés aux frontières du domaine de calcul. Par rapport aux modèles analytiques unidimensionnels simplifiés, l'approche FEM prend en compte l'étalement latéral de la chaleur, la géométrie finie du ruban chauffant et la réponse thermique complexe des structures multicouches, améliorant ainsi la fiabilité de l'interprétation des données.

La méthodologie a été validée à l'aide de substrats de référence et de couches minces diélectriques simples. La contribution principale de ce travail réside dans l'étude d'un empilement diélectrique complexe composé de cinq couches alternées de SiN_x et de SiO_2. Nous avons ainsi abordé le défi fondamental du problème inverse de conduction thermique dans de tels systèmes multicouches. Les premières tentatives visant à extraire simultanément la conductivité thermique intrinsèque de chaque couche et la résistance thermique spécifique de chaque interface se sont révélées être un problème mathématiquement mal posé, en raison d'une forte corrélation entre les paramètres.

Pour résoudre cette difficulté, nous avons réalisé une analyse systématique de sensibilité en fonction de la fréquence. Ce diagnostic a montré que le signal 3ω est fortement sensible à l'impédance thermique globale de l'empilement, mais qu'il ne possède pas une sensibilité suffisante pour déconvoluer de manière unique les résistances thermiques d'interface individuelles (R_{TBR}) dans des empilements multicouches de bonne qualité. Par conséquent, nous avons adopté une approche du milieu effectif (Effective Medium Approach, EMA). Cette approche a été validée au moyen d'un protocole d'expérience virtuelle, reposant sur une bibliothèque d'échantillons générés numériquement, qui a également permis de définir les limites de son domaine d'applicabilité. Grâce à ce cadre validé, nous avons extrait, à partir des données expérimentales, la conductivité thermique effective transverse de l'empilement à cinq couches, obtenant $k_{\mathrm{eff},\perp} = 0.62 \pm 0.03$ $\mathrm{W.m^{-1}.K^{-1}}$, où l'incertitude correspond à l'intervalle de confiance de la procédure d'ajustement inverse.

Les résultats montrent que la conductivité thermique effective de l'empilement multicouche est significativement inférieure aux valeurs intrinsèques généralement rapportées pour les matériaux massifs correspondants. Cette réduction est cohérente avec l'impact cumulé des mécanismes de diffusion des

phonons à l'échelle nanométrique, incluant la diffusion aux frontières, la microstructure non idéale des films et les multiples interfaces internes. Cette thèse établit ainsi un protocole rigoureux pour caractériser des systèmes nanostructurés complexes lorsque les inversions analytiques classiques ne sont plus suffisantes, et fournit des données et des éléments d'interprétation utiles pour l'ingénierie thermique des futurs composants électroniques.

Title: Thermal study of a multilayer system: finite element modeling and experimental characterizations by the 3ω technique (in English).

Keywords: 3-omega method, Thermal conductivity, Dielectric thin films, FEM simulation, Interface resistance, Effective Medium Approach (EMA).

Abstract: Thermal management has evolved from a secondary consideration to a critical bottleneck determining the reliability and performance of modern microelectronic devices. The relentless scaling of device dimensions has led to extreme power densities, exacerbating self-heating effects in technologies such as FinFET logic and Gallium Nitride (GaN) power amplifiers. In these systems, dielectric thin films, such as silicon dioxide SiO_2 and silicon nitride SiN_x, serve as essential passivation and isolation layers. However, their thermal conductivity at the nanoscale can be significantly degraded compared with bulk materials due to phonon scattering at boundaries, size effects, and thermal boundary resistance, also known as Kapitza resistance, at interfaces. Precise characterization of these effective thermal properties is therefore a prerequisite for accurate device modelling and lifetime prediction.

This thesis proposes a comprehensive metrology framework that combines the experimental 3-omega (3ω) method with Finite Element Method (FEM) numerical simulations. Experimentally, we developed and optimized a 3ω measurement setup designed for dielectric thin films and multilayer structures, where the thermal response is weak and strongly affected by the substrate and interfaces. The setup enables the detection of small temperature oscillations through the measured 3ω voltage signal over a controlled frequency range. Numerically, a hierarchical FEM modelling strategy was established. A two-dimensional cross-sectional model was first used for validation, parametric studies, and analysis of the limitations of simplified analytical approaches. For the final analysis of the multilayer stack, this framework was extended to a three-dimensional FEM model including infinite element domains, in order to reproduce the experimental geometry more accurately and reduce artificial boundary effects. Compared with simplified one-dimensional analytical models, the FEM approach accounts for lateral heat spreading, finite heater geometry, and the complex thermal response of multilayer structures, thereby improving the reliability of data interpretation.

The methodology was validated using standard substrates and single-layer dielectric thin films. The core contribution of this work lies in the investigation of a complex five-layer dielectric stack comprising alternating SiN_x and SiO_2 films. We addressed the fundamental challenge of the inverse heat conduction problem for such multilayer systems. Initial attempts to simultaneously extract the intrinsic thermal conductivity of individual layers and the specific thermal resistance of each interface proved to be an ill-posed mathematical problem due to strong parameter correlation.

To resolve this issue, we performed a systematic frequency-dependent sensitivity analysis. This diagnosis revealed that the 3ω signal is highly sensitive to the overall thermal impedance of the stack but lacks sufficient sensitivity to uniquely deconvolve individual interface resistances (R_{TBR}) in high-quality multilayer stacks. Consequently, we adopted an Effective Medium Approach (EMA). This approach was validated through a virtual experiment protocol using a library of numerically generated samples, which also allowed the boundaries of its applicability to be defined. Using this validated framework, we retrieved the effective cross-plane thermal conductivity of the five-layer stack from experimental data, obtaining $k_{\mathrm{eff},\perp} = 0.62 \pm 0.03$ W.m^{-1}.K^{-1}, where the uncertainty corresponds to the confidence interval of the inverse fitting procedure.

The results show that the effective thermal conductivity of the multilayer stack is significantly lower than the intrinsic values generally reported for the corresponding bulk constituent materials. This reduction is consistent with the cumulative impact of nanoscale phonon scattering mechanisms, including boundary scattering, non-ideal film microstructure, and multiple internal interfaces. This thesis establishes a rigorous protocol for characterizing complex nanostructured systems where standard analytical inversions fail, offering valuable insights and data for the thermal engineering of future electronic components.